Advanced Optoelectronic Characterisation of Solar Cells

Shawn Willis

Oriel College

A thesis submitted for the degree of

DPhil in Materials

University of Oxford

Abstract

Optoelectronic characterisation techniques are assessed in their application to three solar cell systems.

Charge injection barriers are found in PbS/ZnO colloidal quantum dot solar cells through the use of temperature dependent current-voltage and capacitance-voltage measurements. The injection barriers are shown to complicate the Mott-Schottky capacitance analysis which determines built-in bias and doping density. A model that incorporates depletion capacitance and a constant capacitance arising from the injection barriers is given to explain the Mott-Schottky plots. The junction mechanism at the PbS/ZnO interface is found to transition from excitonic to *p-n* behaviour based on the amount of UV photodoping the cell has received. External quantum efficiency analysis at different photodoping times reveals a growing charge collection region within the material, demonstrating the shift to *p-n* behaviour. This is further supported by the observance of depletion capacitance behaviour after, but not before, UV photodoping.

Defects within GaAs cells containing InAs quantum dots are found to enhance the sub-bandgap performance of the cell using external quantum efficiency analysis. This is verified by illuminated current-voltage analysis using a 1000 nm high pass optical filter to block photons of larger energy than the bandgap. Using capacitance-voltage analysis, high temperature rapid thermal annealing is shown to induce defects in dilute nitride cells, which explains the drop in open circuit voltage compared to lower temperature annealed cells.

The doping level of polymer solar cells exposed to air is found to increase with continued exposure using Mott-Schottky capacitance analysis. Current-voltage measurements show the formation of an Al_2O_3 barrier layer at the polymer/aluminium interface. The usefulness of capacitance-voltage measurements to probe the polymer/fullerene interface is investigated in thermally evaporated thiophene/C_{60} cells.

Acknowledgements

I would like to thank my supervisors, Dr Andrew Watt and Dr Hazel Assender, for their guidance and discussions. I also thank them for the exceptional work atmosphere they have fostered in the group. It has been a pleasure to work with you both. I thank my collaborators, Dr Ian Sellers from Sharp Electronics and fellow DPhil students Cheng Cheng and Peter Kovacik for providing me solar cells to study and for the scientific discussions. Also, thanks to Dr Huiyun Liu and Mr Frank Tutu at University College London for growing the GaAs quantum cells. I thank Dr Kanad Mallik and Dr Jason Smith for sitting down with me and discussing measurement techniques and results interpretation. Thank you to Dr Richard Beal and Dr Alexandros Stavrinadis for showing me around the lab when I arrived. I thank Dr Johnny Moghal for providing me solar cells to test my experimental setups and Dr Andrew Cook for providing me access to test equipment. Thanks goes to Laurie Walton for all the help in the machine shop. Also thank you to Richard Turner and Dr John Topping for help with odds-and-ends around the lab. I thank Dr Paul Warren for setting up all the computers I needed to run tests. I also thank the rest of my fellow DPhil students as well for making the work environment enjoyable: Laura Droessler, Elva Zou, Jenna Holder, Simon Fairclough, and Chris Cattley. I thank the Department of Materials for accepting me into the program and providing this great opportunity. Finally, I thank my wife Amy and son Kaz for supporting me and making this all worthwhile. This is for you both.

Declaration of Originality

This thesis is an account of work carried out by the author in the Department of Materials, University of Oxford under the supervision of Dr Andrew Watt and Dr Hazel Assender. Any work of others that has been drawn upon is duly acknowledged in the text, and a list of references is presented at the end of the thesis. No part of this thesis has been submitted towards the completion of another degree at the University of Oxford or elsewhere. Parts of this thesis have been submitted to or published in the following scientific journals or conference presentations:

Willis, S. M.; Assender, H. E.; Watt, A. A. R. Polymer/Fullerene Solar Cell Interfaces Studied with Impedance Spectroscopy. *Conference Proceedings: 6th Photovoltaic Science Applications and Technology (PVSAT-6)*. Oral presentation, March **2010**. 17-21.

Willis, S. M.; Assender, H. E.; Watt, A. A. R. Polymer/Fullerene Solar Cell Interfaces Studied with Capacitance. *Conference Proceedings: First International Conference on Materials for Energy*. Poster presentation, July **2010**. A436-A438.

Willis, S. M.; Sellers, I. R.; Cheng, C.; Liu, H. Y.; Assender, H. E.; Watt, A. A. R. Electrical Characterisation of Quantum Dot Solar Cells. *Conference Proceedings: 7th Photovoltaic Science Applications and Technology (PVSAT-7)*. Oral presentation. April **2011**. 83-86.

Kovacik, P.; **Willis, S. M.**; Sforazzini, G.; Assender, H. E.; Watt, A. A. R. Vacuum Deposition of Conjugated Polymers for Solar Cells. *Conference Proceedings: 7th Photovoltaic Science Applications and Technology (PVSAT-7)*. Poster presentation. April **2011**. 29-30.

Cheng, C.; **Willis, S. M.**; Walton, T.; Cattley, C. A.; Assender, H. E.; Watt, A. A. R. Lead Sulfide Nanocrystals for Photovoltaic Applications. *Conference Proceedings: 7th Photovoltaic Science Applications and Technology (PVSAT-7)*. Poster presentation. April **2011**. 137-140.

Kovacik, P.; Sforazzini, G.; Cook, A. G.; **Willis, S. M.**; Grant, P. S.; Assender, H. E.; Watt, A. A. R. Vacuum-Deposited Planar Heterojunction Polymer Solar Cells. *Appl. Mater. Interf.* **2011**. 3, 11-15.

Kovacik, P.; **Willis, S. M.**; Matichak, J. D.; Assender, H. E.; Watt, A. A. R. Effect of side Groups on the Vacuum Thermal Evaporation of Polythiophenes for Organic Electronics. Submitted to ACS Macromolecules.

Table of Contents

Table of Figures

List of Abbreviations

6T	Sexithiophene
A	Area
Ag	Silver
Al	Aluminium
Al_2O_3	Aluminium oxide
AlGaAs	Aluminium gallium arsenide
Alq3	aluminium tris(8-hydroxyquinoline)
AM1.5, AM0	Air Mass1.5, Air Mass0
AODF	Amino-oxadiazole-fluorene
Au	Gold
BHJ	Bulk heterojunction
C	Capacitance
CdTe	Cadmium telluride
CIGS	Copper indium gallium (di)selenide
CQD	Colloidal quantum dot
CV	Capacitance-voltage
CZTS	Copper zinc tin sulfide
E_F	Fermi energy level
E_g	Bandgap energy
EQE	External quantum efficiency
E_{vac}	Vacuum energy level
FET	Field effect transistor
FF	Fill factor
GaAs	Gallium arsenide
GaInNAs	Gallium indium nitrogen arsenide, dilut nitride
Ge	Germanium
GRL	Graded recombination layer
HOMO	Highest occupied molecular orbital
IBSC	Intermediate band solar cell
InAs	Indium arsenide
In(Ga)As	Indium arsenide grown on gallium
InP	Indium phosphide
ITO	Indium tin oxide
IV	Current-voltage
J_0	Reverse saturation current density
J_{mpp}	Current density at the maximum power point
J_{sc}	Short circuit current
JV	Current density-voltage
k_B	Boltzmann constant
LED	Light emitting diode
LiF	Lithium fluoride
LUMO	Lowest unoccupied molecular orbital
MEG	Multiple exciton generation
n	Ideality factor
N_A	Doping density
P	Power

P3HT	Poly(3-hexylthiophene)
PbS	Lead sulphide
PbSe	Lead selenide
PCBM	[6,6]-phenyl-C_{61} butric acid methyl ester
PCE	Power conversion efficiency
PEDOT:PSS	Poly(3,4-ethylenedioxythiophene) poly(styrenesulfonate)
P_s	Incident light power density
Pth	Polythiophene
PV	Photovoltaic
q	Elemntary charge
QD	Quantum dot
R	Resistance
R_s	Series resistance
R_{sh}	Shunt resistance
T	Temperature
TEM	Transmission electron microscope
TiO_2	Titanium dioxide
V	Bias voltage
V_{bi}	Built-in bias
V_{mpp}	Voltage at the maximum power point
V_{oc}	Open circuit voltage
w_{dw}	Width of the depletion region
X	Reactance
Z	Impedance
ZnO	Zinc oxide
ε_0	Permittivity of free space
εs	Dielectric permittivity of the semiconductor
Φ	Work function
χ	Electron affinity
ω	Angular frequency

Chapter 1

Introduction

1.1 Motivation

The development of renewable energy sources is one of the most pressing challenges the world currently faces. Proven coal reserves are estimated to last about another 120 years at current production rates while proven oil and gas reserves work out to near 45 and 60 years respectively[1]. Of course if these numbers are correct, as each reserve runs out, consumption of the remaining types of fuel will increase, shortening the time remaining until depletion. These numbers are also based on current production rates, and it would be unrealistic for production to remain at these levels with growing populations and rapid technological development in large countries such as China. The main point is that without replacing these energy sources before they run out, the world could face an energy catastrophe.

Although it is the subject of fierce debate, climate change should also be mentioned since CO_2 emissions from fossil fuels are a major contributor[2,3]. The world is in the biggest experiment mankind has seen, and the results could be disastrous if changes are not made. Clean energy from renewable sources is a path to making these changes.

Of all the energy sources available, the sun is the most abundant. One hour of sunlight provides more energy than mankind consumes in a year[4]. Yet even with such a huge potential, solar energy contributes less than 0.1% to the world's energy production[4,5,6]. The major reason for such a low contribution is the high cost of solar photovoltaics compared to fossil fuels and even other renewable energy sources[4,6]. Two different technological paths are presented here. In one direction are colloidal quantum dot[7] and polymer[8] solar cells which follow the low efficiency, but low cost[9] route. In the other direction are GaAs cells with quantum dots which follow the high cost, but high efficiency route. In both cases, the goal is to reduce the overall cost per Watt of solar power.

Continued research and improved understanding is needed in each of the three systems before they are ready to compete in the energy, or even solar cell, market. This thesis utilises and develops a number of electrical characterisation techniques (described in chapter 2) as metrology methods for the different cell technologies. Chapters 3 - 5 assesses these techniques applied to the different solar cells and investigates, among other things, contact injection barriers, material junctions, and materials degradation.

1.2 Thesis Organisation

The remainder of this chapter discusses the basic solar cell principles with special consideration given to junctions, since they are essential for the photovoltaic behaviour and many of the electrical characterisations in chapter 2 derive from the physics of junctions. Following an explanation of the different experimental techniques in chapter 2, each cell is examined and the experimental results and

conclusions are presented in chapters 3 - 5. Finally, overall conclusions are given in chapter 6.

1.3 Solar Cell Basics

The basic goal of a photovoltaic device is to convert energy in the form of light to energy in the form of electricity. The processes by which this occurs can be sub-categorised in multiple different ways, but for the discussion here they will be divided into three main areas, charge generation, charge separation, and charge transport. The focus of this thesis is not to provide an in-depth discussion of every solar cell mechanism, however a brief overview of the charge generation and transport processes is given in this section. A more in-depth description of junctions, the mechanism for charge separation, is given in section 1.4 since many of the characterisation techniques employed in this thesis require an understanding of junction physics within a solar cell. For a more complete description of the other processes, see any of the many books or websites describing solar cell physics, for example[10,11,12,13,14].

1.3.1 Charge Generation

Charge generation occurs when the semiconducting material absorbs photons and excites electrons to higher energy states creating electron-hole pairs. Photon absorption depends both on the solar spectrum and the absorbing semiconductor material. In order to achieve the best efficiency in a solar cell, a balancing act must be carried out. A larger semiconductor bandgap produces charge carriers with higher energy leading to a higher possible open circuit voltage for the cell. However, this reduces the amount of photons converted to excited electrons since photons below the bandgap are not absorbed which results in less photocurrent. Smaller bandgaps absorb

more photons, leading to larger photocurrents, but the excess energy of the excited electron above the bandgap is lost to thermalisation and the electron energy is reduced to that of the bandgap.

The optimum solar cell bandgap can be determined through the principle of detailed balance[10]. Not only does the cell absorb solar radiation, it exchanges thermal radiation with its environment[10]. When the solar spectrum, cell absorption, and cell emission are taken into account, the detailed balance process yields an optimum semiconductor bandgap near 1.4 eV, resulting in a maximum efficiency near 33%. This is based on the standard AM1.5 solar spectrum (defined so the integrated irradiance of the spectrum is 1000 Wm^{-2}) which accounts for absorption and scattering by the atmosphere[10]. Using the extra-terrestrial spectrum (AM0), the optimum bandgap is near 1.3 eV and the maximum efficiency is about 31%[15]. If the temperature difference between the cell and the source is increased, the efficiency increases. The ultimate solar cell efficiency for illumination by the sun (6000 K black body temperature) and a cell temperature of 0 K, is near 44% with an optimum bandgap of 2.2 eV[16]. Of course this requires energy to cool the cell which would lower the overall efficiency. Another way to improve the efficiency is to concentrate the light, which has the effect of increasing the angular range of absorbed light. For a concentration factor of 1000, the optimum bandgap is 1.1 eV and the maximum efficiency is near 37%[17]. The maximum concentration factor of 4.6×10^4 occurs when the illuminating radiation from every angle incident on the solar cell is the same temperature as the sun. Under less than maximum concentration conditions, the cell is partly illuminated from the sun and the remaining illumination comes from a source with the same temperature as the earth[14]. The efficiency limit for maximum concentration is over 40%[10]. However,

this doesn’t account for the heat generated by high concentration which leads to stronger emission from the cell.

The efficiencies and bandgaps calculated by the detailed balance process in the preceding paragraph are all for single junction cells (no tandem cells). There are also a few assumptions in the calculations. First, the cells were assumed to have perfect absorption (all light with energy above the bandgap is absorbed) and each absorbed photon created exactly one electron-hole pair. Second, radiative recombination was the only recombination process. And third, there was perfect charge transport through the cell and perfect charge collection.

1.3.2 Charge Separation

Following charge generation, the excited electron-hole pair needs to be separated before they recombine and give up their energy. Recombination can happen through different processes. Radiative recombination, which is a result of spontaneous emission, leads to the generation of a photon. Interaction between the excited carriers can result in one excited carrier giving up its energy to another excited carrier. This results in the decay of one of the carriers across the bandgap and an increase in the kinetic energy of the other carrier, which later loses the excess energy through thermalisation. This is known as Auger recombination. Finally, recombination can occur through relaxation into trap states due to impurities or defects in the semiconductor. The first two processes are due to fundamental physical processes. The last process, which is mainly due to imperfect material, can be affected by the quality of the semiconductor.

Junctions between materials with different properties are used to separate the excited charges. An in-depth discussion of junctions is presented in section 1.4 which covers

the different types of junctions and the diode behaviour that leads to solar cell behaviour.

1.3.3 Charge Transport

Charge transport through the semiconductor is hindered by recombination. Photon absorption creates minority carriers that need to reach a junction before they recombine with a majority carrier through one of the processes mentioned in section 1.3.2. The minority carrier diffusion length is a parameter that describes, on average, how far minority carriers can diffuse before recombining. This places a limit on the thickness of the absorbing material which must be balanced with the thickness needed for photon absorption. There are architectures, such as the bulk heterojunction described in section 1.4.3, that are designed to aid absorption and reduce the distance minority carriers need to travel. This is especially needed in organic solar cells where the exciton diffusion length is very short.

The central mechanism for charge separation, a junction of two materials, is also important in charge transport. Once minority carriers diffuse to the junction they are transported to the other material becoming majority carriers. This action spatially separates the electrons and holes. Finally, when an external circuit is connected across the terminals, the photocurrent can flow through the circuit providing power to the system. Further discussion of the different types of junctions and their application to solar cells is given in section 1.4.

1.4 Junction Physics

Junctions play an important role in solar cells as the mechanism to separate charge carriers. They are also exploited in many of the characterisation techniques central to the work presented in this thesis and described in chapter 2. Therefore, special

consideration is given to junctions in this section. Reference material for this section comes from references [10, 14, 18, 19, 20]. In some cases references outside these sources are used and the reference is given in the normal fashion.

1.4.1 Semiconductor-Metal Junctions

When a semiconductor and metal are brought into electrical contact, electrons diffuse from regions of higher concentration to regions of lower concentration. This happens by an exchange of charge carriers from one material to the other. In the case of an *n*-type semiconductor with a work function (explained in the next paragraph) less than that of the metal ($\Phi_n < \Phi_m$), electrons flow from the semiconductor to the metal leaving behind a region of fixed positive charges, and for a *p*-type semiconductor with $\Phi_p > \Phi_m$ electrons flow from the metal into the semiconductor resulting in a region of negative net charge in the semiconductor. The flow of charge results in a region within the semiconductor depleted of mobile charge carriers, called the depletion region. For an *n*-type material, the flow of electrons into the metal leaves behind fixed positive charges, and for a *p*-type material the electrons that flow into the semiconductor combine with positive holes. Metals have such a large amount of free charge that any flow of electrons into or out of the metal is easily compensated and the depletion region within the metal is negligible.

This process, shown in Figure 1.1, can also be explained with an energy description. Before coming in contact, the semiconductor and metal have independent Fermi levels (electron energy state that has a 50% probability of being occupied). When the two come in contact, the Fermi levels must line up, which results in the vacuum energy level changing between the two materials by the difference in work functions.

The work function is the potential required to remove the least tightly bound electron and is defined by[10]

$$\Phi_w = \left(E_{vac} - E_F\right) \tag{1.1}$$

where Φ_w is the work function, E_{vac} is the vacuum energy level and E_F is the Fermi level. In a metal the work function is always the same as the electron affinity (the least amount of energy required to remove an electron from a solid). In a semiconductor the electron affinity, χ, is the difference in energy between the vacuum energy and conduction band energy, and is therefore different than its work function.

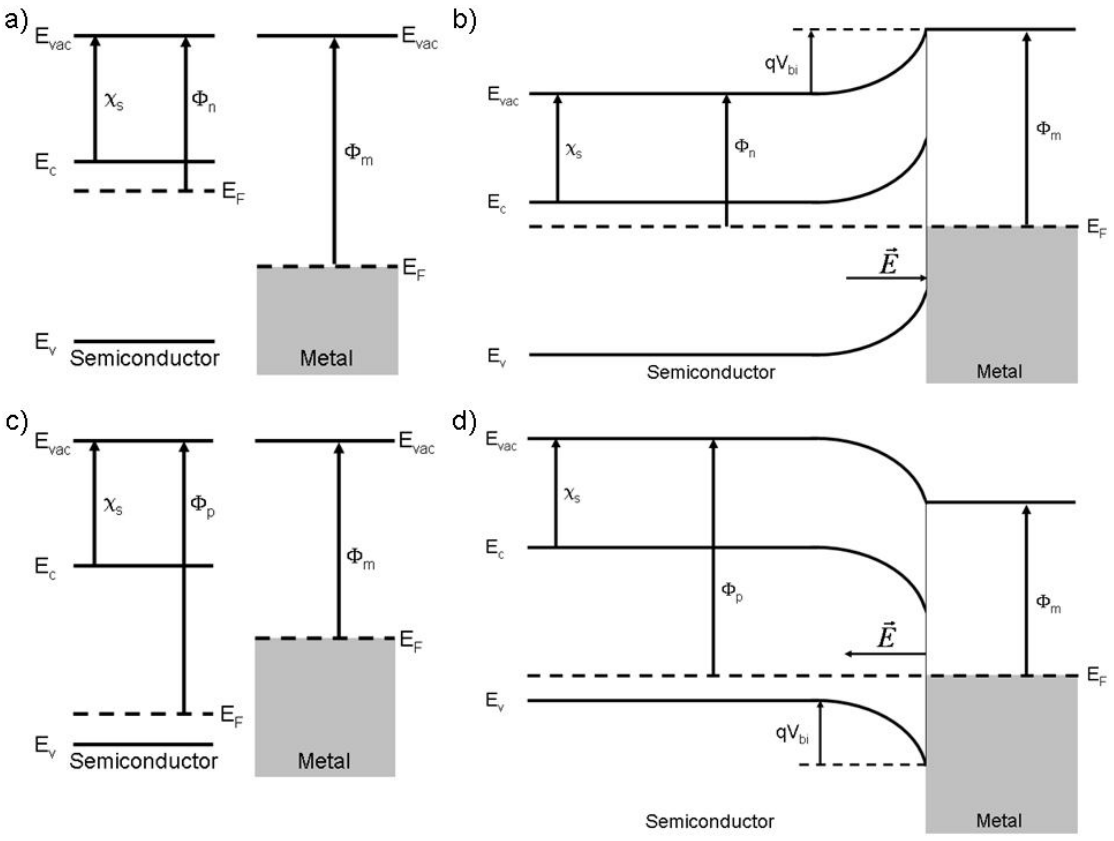

Figure 1.1. a) Energy levels of an *n*-type semiconductor and a metal in isolation. b) Energy level diagram of the metal-semiconductor (Schottky) junction in equilibrium for an *n*-type semiconductor. c) Energy levels of a *p*-type semiconductor and a metal in isolation. d) Energy level diagram of the metal-semiconductor (Schottky) junction in equilibrium for a *p*-type semiconductor.

The flow of electrons from one material to the other described in the preceding paragraph results in an electric field. Once the electric field balances the initial potential energy difference, charge stops flowing leaving a region of net charge in the semiconductor near the junction. Basically none of the charged region lies within the metal, since metals are much worse at storing charge than semiconductors. Away from the junction the potential energy becomes constant and the electric field goes to zero. This happens very quickly in the metal and the distance is negligible. In the semiconductor however, this is not the case. The region of charged semiconductor is known as the space charge region which is the same as the depletion region in the preceding paragraph. The conduction and valence band energy levels bend in the same way as the vacuum energy level since the electron affinity and bandgap in a semiconductor are constant. The built in bias, V_{bi}, describes the amount of total band bending given by qV_{bi}.

This type of junction is known as a Schottky junction. The characteristic that makes the junction so important for photovoltaic behaviour is the junction's asymmetric response to applied bias (rectification) demonstrated in Figure 1.2 for an *n*-type semiconductor with $\Phi_n < \Phi_m$. An analogous situation applies to a p-type semiconductor with $\Phi_p > \Phi_m$, but is not shown. In the dark, at equilibrium, a small amount of majority carriers in the semiconductor have enough thermal energy to overcome the barrier created at the junction. This is balanced however, by a leakage current of minority carriers that drift from the semiconductor to the metal resulting in no net charge flow. Under forward bias (metal more positive for an *n*-type semiconductor, and semiconductor more positive for a *p*-type semiconductor), the barrier height is reduced and majority carriers flow into the metal easier. The resulting current increases nearly exponentially with applied forward bias. Under reverse bias

the barrier height is increased reducing the thermally activated current of majority carriers. This leaves the small leakage current in the reverse direction. However, due to the low density of minority carriers, this current is small.

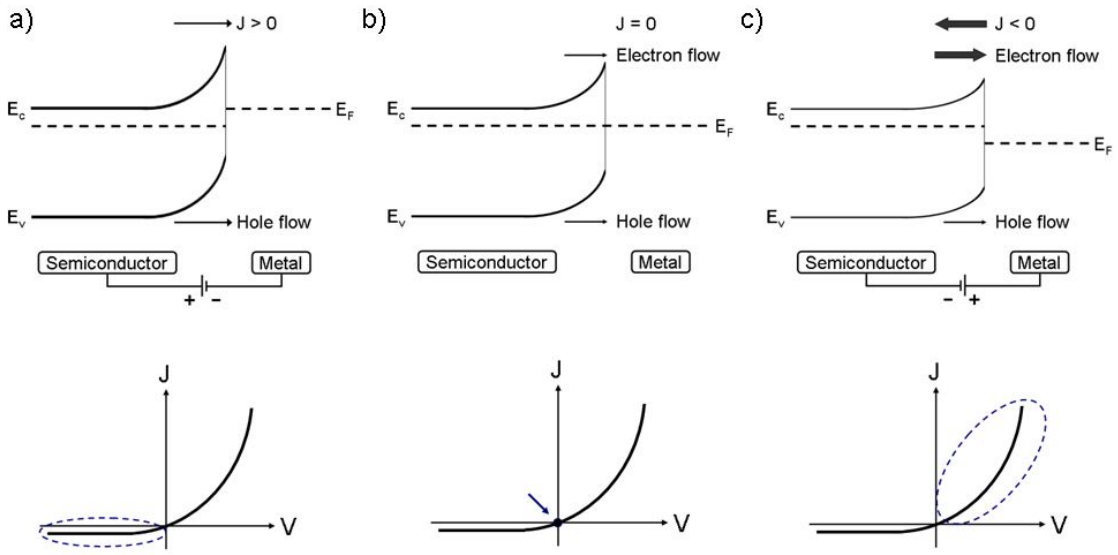

Figure 1.2. Energy band diagrams for a Schottky junction with an *n*-type semiconductor at different biases. The net current density, *J*, is defined here as positive for net positive charge flow from left to right. The corresponding location on the *JV* curve is shown below each diagram. a) Reverse bias. Minority hole drift across the depletion region is the only charge flow which results in a small positive net current. b) Equilibrium. Hole drift and electron diffusion currents combine for zero net current. c) Forward bias. The reduced barrier height greatly increases the majority electron diffusion across the junction resulting in a large negative net current. The hole drift current remains similar to the previous two cases.

When the semiconductor is illuminated with photons of energy greater than the bandgap, the electric field in the space charge region sweeps minority carriers into the metal leaving the semiconductor to become charged by the remaining majority carriers. This results in a shift of the majority carrier quasi Fermi level in the semiconductor. As an example, for an *n*-type semiconductor the electron quasi Fermi level far from the junction increases under illumination becoming higher than the metal's Fermi level. This Fermi level splitting is what creates the photovoltage. The ability of a semiconductor to sustain the difference in quasi Fermi levels when

illuminated is imperative for photovoltaic energy conversion[10]. Biased junctions are discussed more in section 1.4.5.

In the preceding discussion only *n*-type materials with $\Phi_n < \Phi_m$ and *p*-type materials with $\Phi_p > \Phi_m$ were considered in examining how the metal-semiconductor junction formed. If the relative values of the work functions are reversed such that $\Phi_n < \Phi_m$ or $\Phi_p > \Phi_m$, the junction is no longer rectifying. Figure 1.3 shows the resulting band bending for the two situations. In this case, majority carriers are assisted (instead of blocked) across the junction from the semiconductor to the metal and minority carriers have a barrier in this direction. Since majority carriers flow from the metal into the semiconductor when the junction is formed, there is an accumulation of majority carriers near the junction which allows majority carriers to flow easily in either direction. This is known as an Ohmic contact. If this junction is illuminated, any charges separated by the junction can flow back into the semiconductor without much difficulty, making the photovoltage insignificant.

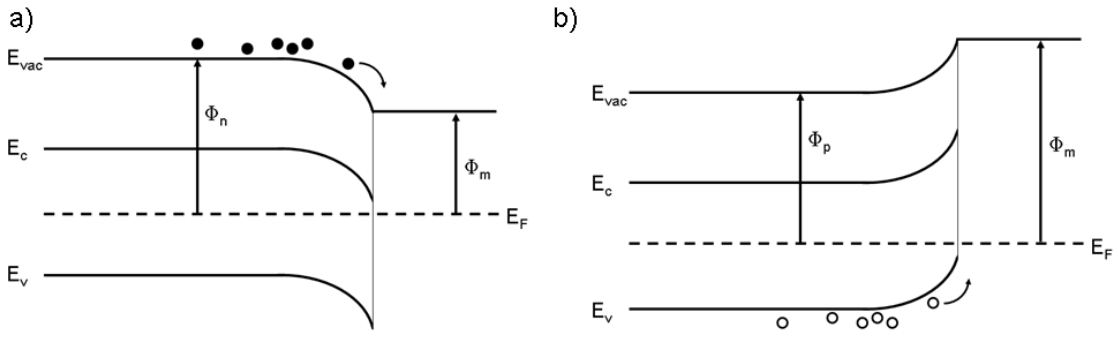

Figure 1.3 Ohmic Schottky junction band diagrams for an *n*-type semiconductor (a) and a *p*-type semiconductor (b). Majority carriers are assisted across the junction instead of blocked.

There are a few limitations when using Schottky junctions as the mechanism to separate charge and create a photovoltage. First, the useful barrier height is limited to about half of the bandgap, E_g. If the barrier height is greater than $E_g/2$, minority

carriers outnumber majority carriers near the interface and an inversion layer is formed. The junction becomes dense with carriers and cannot sustain the photovoltage. Second, highly doped semiconductors can result in very thin barrier layers that allow majority carriers to tunnel through the junction. Finally, interface states can exist at the metal-semiconductor interface which trap charge and limit the photovoltage. These limitations can be overcome by using a semiconductor-semiconductor junction.

1.4.2 Semiconductor-Semiconductor Junctions

1.4.2.1 *p-n* Junction

The most widely used structure for solar cells is the *p-n* junction[10]. It is similar to the Schottky junction described in section 1.4.1, except now the junction is composed of oppositely doped semiconductors. In the *p-n* homojunction (same semiconductor material oppositely doped), electrons flow from the *n*-type material into the *p*-type material and holes from the *p*-type material to the *n*-type material when the two semiconductors come in contact. This creates a region near the junction of negative charge in the *p*-type material and positive charge in the *n*-type material that is depleted of mobile charge carriers. An electric field is created at the junction due to the flow of charges which points from the *n*-type material to the *p*-type material. Photogenerated electrons are swept to the *n*-type material and holes to the *p*-type material where they each become majority carriers. Figure 1.4 illustrates the *p-n* junction.

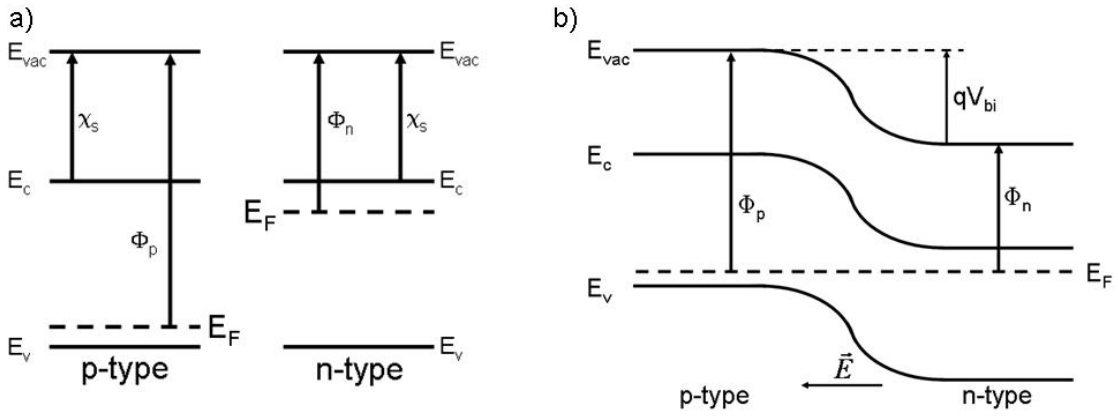

Figure 1.4. a) Energy levels of *p*- and *n*-type semiconductor in isolation. b) Energy level diagram of the *p*-*n* junction in equilibrium.

1.4.2.2 *p*-*i*-*n* junction

A layer of intrinsic (undoped) semiconductor can be placed between the *p*- and *n*-type semiconductor materials changing it to a *p*-*i*-*n* junction. The concept is the same as that of the *p*-*n* junction and the same built-in bias is created. However the depletion region, and hence electric field, extends across a wider region. The advantage of this structure is seen in materials with short minority carrier diffusion lengths. The extended depletion region is able to collect more charge to contribute to the photocurrent. There are disadvantages to the *p*-*i*-*n* junction though. Since the middle layer is undoped, the conductivity is lower than the doped regions and can increase the series resistance. Also, charged impurities within the intrinsic region can cause the electric field to vanish.

1.4.2.3 *p*-*n* Heterojunction

A *p*-*n* heterojunction is formed from two different semiconductor materials (rather than the same material) that are oppositely doped. Again the concept is the same as the *p*-*n* homojunction, but in this case there are discontinuities in the conduction and valence bands between the two materials due to the different bandgaps of the

materials. This also leads to different effective fields, and hence driving forces, for holes and electrons at the junction. Figure 1.5 shows an example of the band structure of a *p*-*n* heterojunction. However, the exact band alignment must be addressed case-by-case since it depends on the work function and electron affinity of the two materials. In the example, the effective field driving the electrons to the *n*-type material is enhanced by the conduction band offset. However, for holes a barrier is formed in the valence band that hinders hole transport to the *p*-type material which can lead to carrier recombination.

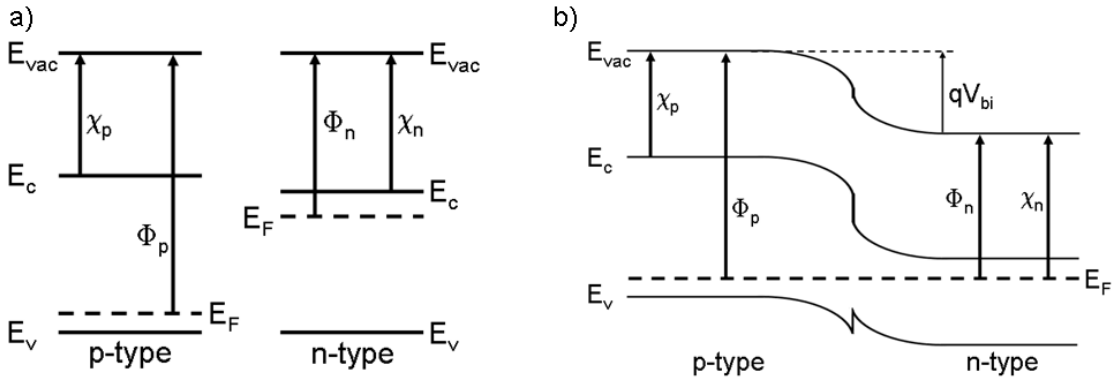

Figure 1.5. a) Energy levels of different material *p*- and *n*-type semiconductors in isolation. b) Energy level diagram of the *p*-*n* heterojunction in equilibrium. The exact band alignment must be addressed case-by-case since it depends on the work function and electron affinity of the two materials

1.4.3 Excitonic Junction

The charge separation mechanism in polymer solar cells is somewhat different than the *p*-*n* and Schottky junctions described in sections 1.4.1 and 1.4.2 due to a much larger exciton (electron-hole pair) binding energy in organic semiconductors. In an inorganic semiconductor, very weakly bound Wannier excitons (electron-hole pair) are formed upon absorbing a photon[21]. These generally have a binding energy of only a few meV and are likely to be ionised at room temperature producing a free electron-hole pair[10]. On the other hand, photon absorption in an organic semiconductor creates

strongly bound Frenkel excitons[22] with binding energies ranging from 0.1-1.4 eV[23]. The reason for such a large binding energy is due to localised electron and hole wavefunctions and low dielectric constants[23] (ε ~3-4 compared to ε ~10 for inorganic semiconductors[24]).

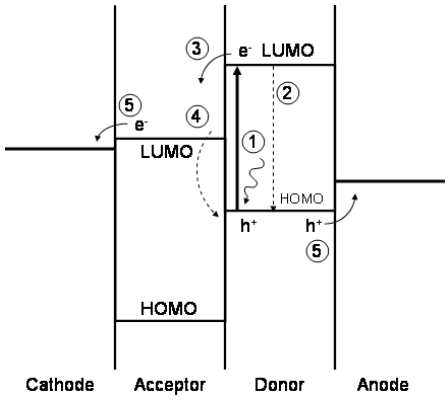

Figure 1.6. Charge generation and extraction in an organic heterojunction solar cell. (1) A photon is absorbed creating a bound electron-hole pair known as an exciton. The exciton can either (2) recombine, or (3) dissociate at the donor-acceptor interface. The electron and hole can (4) recombine, or (5) be extracted at their respective electrode.

With such large binding energies, the electric field created by the difference in electrode work functions is not enough to separate the exciton, as in an inorganic semiconductor. In order to overcome the strong attraction between the electron and hole in organic solar cells, a heterojunction architecture is used. In this architecture, two organic materials with different electron affinities and ionization potentials are used instead of a single organic material[25]. One material, generally a polymer, acts as an electron donor and the other material, a fullerene or polymer, acts as an electron acceptor. The benefit of the heterojunction comes from the energy band offset between the donor and acceptor materials. When an exciton diffuses to the interface, it rapidly dissociates (time scale of about 45 fs) injecting the electron into the acceptor material while leaving the hole in the donor material[26]. The process is shown in Figure 1.6.

The key for electron-hole separation lies in the exciton reaching the interface before it recombines. Since the exciton is a neutral species, it moves by diffusion through the donor material. The distance it travels before recombining is known as the exciton diffusion length and depends on trap density, degree of disorder in the material, and the dielectric of the material[27,28]. The typical diffusion length in various organic semiconductors is around 5 – 20 nm[25,29,30]. Therefore, the exciton must be created within about 10 nm of the donor-acceptor interface if the charge carriers are to be harvested for the photocurrent. However, the absorption depth in most organic materials is much larger than the exciton diffusion length[25]. Therefore the planar heterojunction architecture (donor and acceptor materials side-by-side) has a severely limited width for effectively converting photons into charge carriers. To overcome this, a bulk heterojunction architecture is used. In this type of device the donor and acceptor materials are blended together creating a dispersed interface throughout the active region of the device. If the blended regions are similar in length to the exciton diffusion length, exciton extinction is considerably reduced since there is a high probability the exciton will diffuse to an interface where it will dissociate.

1.4.4 Depletion width

To determine the thickness of the depleted regions in the *p*- and *n*-type materials at a *p*-*n* junction, some simplifying approximations can be made. The depletion region is assumed to be completely free of majority carriers leaving a region of ionised impurity atoms of positive charge in the *n*-type material and negative charge in the *p*-type material. Also, these regions are assumed to be discrete. In other words, outside the depletion region, there is an abrupt change to neutral semiconducting material. Poisson's equation can then be used with these boundary conditions to determine the width of the depletion region in each material, resulting in depletion widths of[10]

$$w_{p,n} = \frac{1}{N_{a,d}} \sqrt{\frac{2\varepsilon_s V_{bi}}{q\left(\frac{1}{N_a} + \frac{1}{N_d}\right)}} \quad \textbf{(1.2)}$$

where $w_{p,n}$ is the depletion region in the *p*- and *n*-type material respectively, $N_{a,d}$ is the density of acceptor and donor impurity atoms respectively, ε_s is the dielectric permittivity of the semiconductor (incorporates permittivity of free space, ε_0), V_{bi} is the built in voltage, and q is the elementary charge. Equation (1.2) highlights a couple items of interest. First the width of the depletion region increases as the doping density decreases. This means a large depletion region, which helps with carrier collection, must be balanced against the need for high doping, which aids conductivity. Second, the relative depletion region width and the amount of V_{bi} dropped in each layer depend on the relative doping levels. The layer with lower doping will have a wider depletion region and more of the V_{bi} will be dropped in that layer. If one layer is doped much more heavily than the other, the depletion width can be approximated to lie completely in the lower doped layer. This gives the depletion region width to be[10]

$$w_{dw} \approx w_{p,n} = \sqrt{\frac{2\varepsilon_s}{qN_{a,d}} V_{bi}} \quad \textbf{(1.3)}$$

where w_{dw} is the width of the depletion region. For Schottky junctions, equation (1.3) gives the depletion region width in the semiconductor, since the metal can be considered to be much more heavily doped.

Finally, the junction is voltage dependent. If a voltage, *V*, is applied across the *p*-*n* junction such that the *p*-type layer is at a more positive bias under forward bias conditions, the built-in bias in equation (1.3) is replaced with ($V_{bi} - V$). The bias-

dependent nature of the junction is exploited by measuring the capacitance at different biases to determine V_{bi} and N_a. This is covered in 2.2.3.

1.4.5 Ideal Diode Behaviour

The junction within a solar cell gives the device its rectifying (diode) behaviour that enables charge separation. As a point of reference the current density of an ideal diode in the dark, J_{dark}, (no illumination) is given by[10]

$$J_{dark}(V) = J_0\left(e^{\frac{qV}{k_BT}} - 1\right) \quad \textbf{(1.4)}$$

where J_0 is the dark saturation current density (explained later in this section), V is the applied bias, k_B is the Boltzmann constant, and T is the temperature. From the equation it can be seen that a positive applied bias results in an exponential increase in current, while a negative bias yields a very small current. This is described physically in the following paragraphs.

In a *p-n* junction with zero applied bias and in the dark, it is still possible that majority carriers can diffuse across the junction even though the established electric field at the junction opposes this action. Once a majority carrier diffuses across the boundary, it becomes a minority carrier and eventually recombines after travelling, on average, its diffusion length. Minority carriers that are thermally generated within a diffusion length from the junction have a good probability of reaching the junction where they are swept across to become majority carriers. In equilibrium these two currents (diffusion and drift) are equal and the net current flow is zero. Figure 1.7b demonstrates this process.

When a forward bias is applied to the junction as in Figure 1.7c (positive bias at the *p*-type material and negative at the *n*-type), an electric field results that is in opposition to the electric field created by the space charge region at the junction. Since the space charge region is depleted of mobile charge carriers, its resistivity is much higher than the rest of the device and the applied bias is dropped almost entirely across this region. The net electric field at the junction is reduced since the applied electric field is in opposition to the built-in field which reduces the barrier height and increases the diffusion current across the junction. Very little effect is seen in the drift current since it still depends on the number of minority carriers thermally generated within a diffusion length of the depletion region, which doesn't increase as much as the diffusion current does. The increased diffusion current means there is increased minority carrier injection at the junction and therefore increased recombination with majority carriers which are supplied by the external circuit. The removal of minority carriers by recombination allows more majority carriers to diffuse across the junction to become minority carriers, sustaining the current. The diffusion current can then be thought of as a recombination current where a greater recombination results in a larger current across the junction. The parameter J_0 from equation (1.4) is a measure of this recombination in a diode, where a larger J_0 corresponds to larger recombination. It depends on the material quality and temperature, increasing as T increases and decreasing as the material quality increases.

Figure 1.7d shows the *p*-*n* junction under reverse bias. This time the applied electric field is in the same direction as the built-in field which increases the barrier to diffusion of majority carriers across the junction. This leaves the drift current slightly higher than the diffusion current resulting in a small current under reverse bias. As with the forward bias case, the drift current doesn't change much.

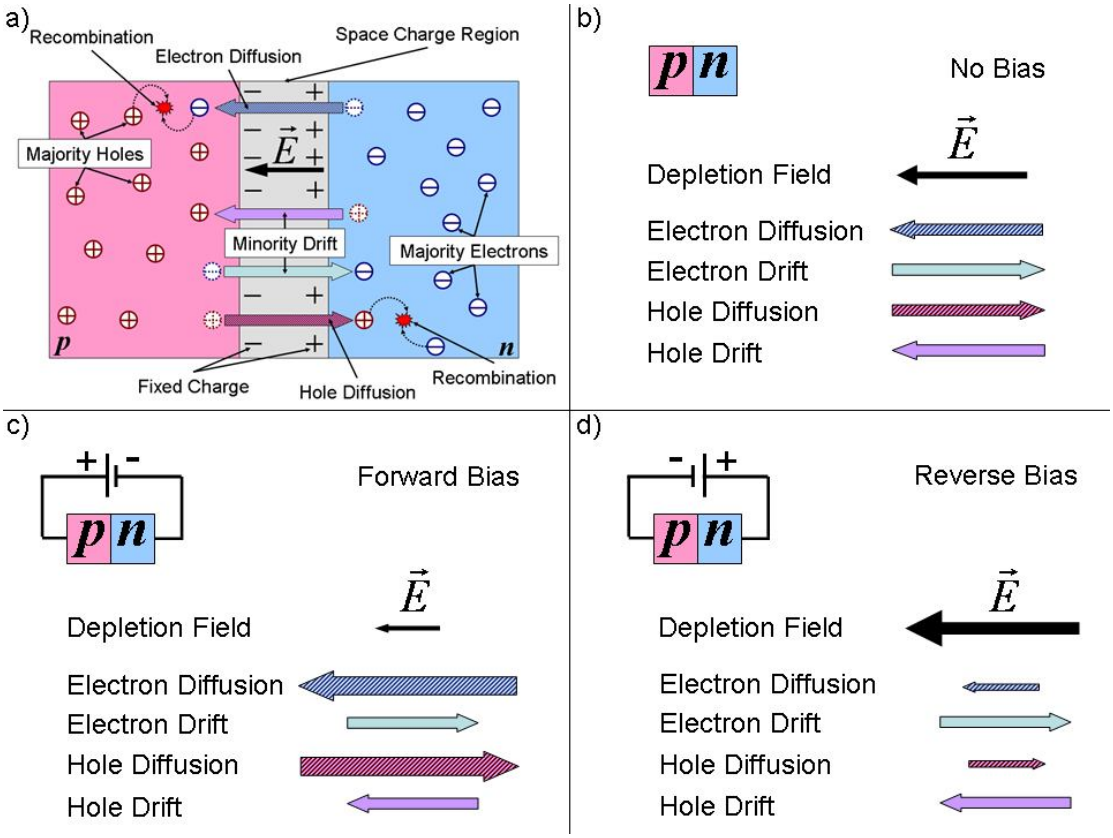

Figure 1.7. a) Majority carrier diffusion and minority carrier drift at a p-n junction. b) Drift and diffusion currents cancel out to zero with no bias applied to the junction. c) The majority carrier diffusion is larger under forward bias due to the reduced junction barrier height. d) There is very little majority carrier diffusion under reverse bias, leaving the drift current to be larger.

1.4.6 Ideal Solar Cell Behaviour

An ideal solar cell can be modelled as current generator in parallel with a diode as seen in Figure 1.8a. The resistance of the load across the terminals and the illumination intensity determine how much current flows through the load versus the diode. A higher load resistance results in more current through the diode and a higher potential across the terminals.

Two important characterisation points are the short circuit current density, J_{sc}, and the open circuit voltage, V_{oc}. The short circuit current is the current under illumination when the resistance between the terminals is zero (terminals are shorted together). The voltage at the terminals in this case is zero. The open circuit voltage is the voltage

under illumination when the terminals are disconnected (resistance is infinite). In this case the current from one terminal to the other is zero. Outside this voltage range (V = 0 V and $V = V_{oc}$ at the terminals) the device no longer acts as a solar cell. If a voltage is applied across the terminals such that $V < 0$ or $V > V_{oc}$, the device consumes power. In the first case, the cell acts as a photodetector. The second case is the regime where light emitting diodes operate.

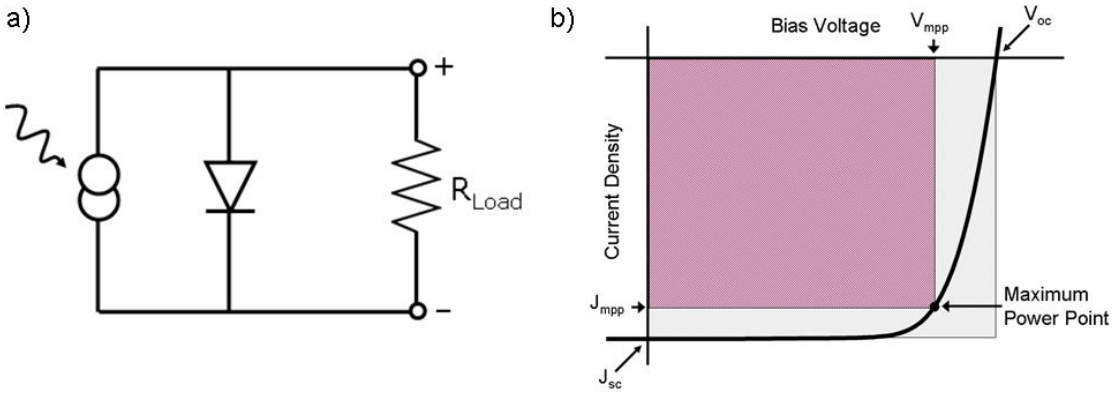

Figure 1.8. a) Equivalent circuit for the ideal solar cell. The resistance of the load determines how much current flows through the load and how much flows through the diode. b) Solar cell *JV* curve showing V_{oc} and J_{sc}. The fill factor is a ratio of the area of the square determined by the maximum power point to the area of the square determined by V_{oc} and J_{sc}.

There are two other important characterisation parameters beside J_{sc} and V_{oc} for solar cells. The first is the fill factor, FF, which is defined as[10]

$$FF = \frac{J_{mpp} V_{mpp}}{J_{sc} V_{oc}} \qquad \textbf{(1.5)}$$

where J_{mpp} and V_{mpp} are the current density and voltage at the maximum power point. Different resistive loads across the terminals produce different currents and voltages at the terminals. J_{mpp} and V_{mpp} correspond to the load where the power ($P = JV$) is maximised. Figure 1.8b gives an example of the relationship between the current and voltage at different resistive load values. The figure also demonstrates how the

maximum power achievable from the cell relates to a "non-real" power determined by J_{sc} and V_{oc}. The fill factor then provides a quantification of the shape of the *JV* curve. Although the points along the *JV* curve correspond to different resistive loads, actual measurements are done by applying different voltages across the terminal and measuring the current. This is discussed in section 2.1.

Finally, the power conversion efficiency, PCE, relates the energy output from the cell to the incident light power density, P_s. It is given by

$$PCE = \frac{J_{sc} V_{oc} FF}{P_s}. \tag{1.6}$$

The photocurrent for the ideal solar cell is given by

$$J(V) = J_{sc} - J_{dark}(V) \tag{1.7}$$

where $J_{dark}(V)$ is given by equation (1.4).

1.4.7 Non-Ideal Solar Cell Behaviour

The previous section discussed an ideal solar cell. In reality there are parasitic resistances that degrade the performance of the cell. Figure 1.9 shows how the series and shunt resistances, R_s and R_{sh}, are included in the equivalent solar cell circuit and the effects they have on the *JV* curves. The series resistance is a result of the material's resistance to current flow. Much of the R_s contribution can come from the resistance between the semiconductor surface and the contact and from resistive contacts. Leakage current through "shunt" pathways in the cell and around the edges of the cell contributes to R_{sh}. As is demonstrated in Figure 1.9, low R_s and high R_{sh} are needed for the best performance.

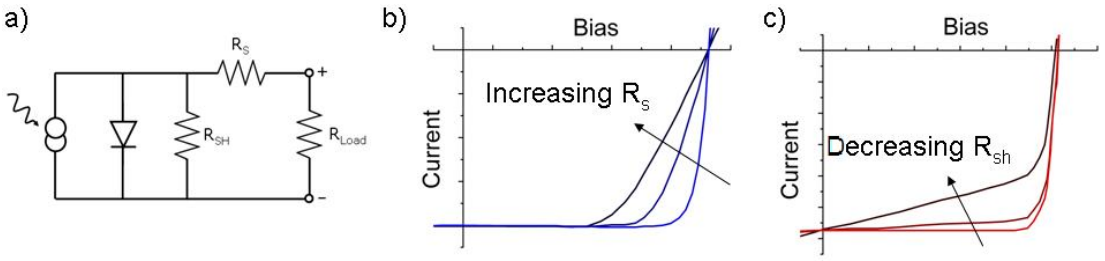

Figure 1.9. a) Solar cell equivalent circuit with series and shunt resistances included. b) The effect of increasing series resistance on the *JV* curve. c) The effect of increasing shunt resistance on the *JV* curve.

When the parasitic resistances are taken into account, the full diode equation becomes

$$J = J_{sc} - J_0\left(e^{\frac{q(V+JAR_s)}{k_BT}} - 1\right) - \frac{V + JAR_s}{R_{sh}} \qquad \textbf{(1.8)}$$

where A is the cell area. The dark diode equation, equation (1.4), is also modified with the addition of an ideality factor, n, to become

$$J = J_0\left(e^{\frac{qV}{nk_BT}} - 1\right). \qquad \textbf{(1.9)}$$

In inorganic solar cells the ideality factor generally has a value between 1 and 2, and describes the recombination in the cell[31].

1.5 Current Solar Cell Technology

Most solar cells operate based on a *p*-*n* junction[10]. This is also the junction that produces the highest performing cells. Table 1.1 lists the current state of the art single junction solar cells for both *p*-*n* and excitonic junctions under the AM1.5G spectrum. This is not an exhaustive list, but it provides a good overview of cells based on the junctions presented in section 1.4. Silicon received its own category here since it currently has the dominant share (~80%)[32] of the PV market. Not included in this list are the lead-salt colloidal quantum dots (CQD) solar cells. There is still debate about

the junction mechanism of these cells. However, PbS CQD cells are the focus of chapter 3, and a study of the junction mechanism is presented there. The current state of CQD solar cells is also given in chapter 3. Multi-junction and concentrator solar cells have also been left out of the table. Although the end goal of the dilute nitride cells in chapter 4 is for use in a multi-junction cell, the multi-junction architecture itself is not investigated in this thesis.

Table 1.1. Current confirmed record performance of single junction solar cells[128]. The majority of the cells operate based on a *p-n* junction. The last two cells listed are based on an excitonic junction.

Category	Cell	V_{oc} (V)	J_{sc} (mAcm^{-2})	FF	PCE	Ref
p-n						
Silicon	Crystalline	0.696	42.0	0.836	24.4%	33
Silicon	Multicrystalline	0.664	37.7	0.809	20.3%	34
Silicon	Amorphous	0.886	16.7	0.670	10.1%	35
III-V	GaAs thin film	1.111	29.4	0.859	28.1%	36
III-V	GaAs multicrystalline	0.994	23.2	0.797	18.4%	37
III-V	InP crystalline	0.878	29.5	0.854	22.1%	38
Thin Film	CIGS	0.690	35.5	0.812	19.9%	39
Thin Film	CdTe	0.845	26.1	0.755	16.7%	40
Thin Film	CZTSS	0.516	28.6	0.654	9.7%	41
Excitonic						
	Dye-sensitized	0.736	21.7	0.736	10.9%	42
	Organic polymer	0.816	14.4	0.702	8.3%	43

Since crystalline silicon is such an established technology, the end product advances in efficiency are generally accomplished through incremental improvements to the production line instead of revolutionary advances[44]. This is because of the cost and risk of making large changes to the production line. Even though the efficiency of III-

V solar cells is quite high, the fabrication cost is restrictive. Therefore much of the focus on III-V solar cells is on multi-junction, concentrator, and third generation solar cells[45]. Chapter 4 investigates two III-V based technologies ultimately looking to be used in third generation and multi-junction cells. Thin film CIGS cells offer high efficiencies at a lower cost than silicon, but the future of this technology may run into difficulty due to the use of scarce and toxic materials[46,47]. The same is true for CdTe[48,49]. The development of thin film Cu_2ZnSnS_4-type cells looks to address these two issues[46,47]. Dye-sensitized solar cells have efficiencies comparable to amorphous silicon, but can be produced at a lower cost[45]. However, the long-term stability still needs to be addressed before they enter the market[45]. Finally, organic materials offer the possibility of low-cost, flexible solar cells. However, longer device lifetimes need to be achieved in these as well[45].

Chapter 2

Electrical Characterisation Techniques

2.1 Current-Voltage Measurements

Current-voltage (*IV*) or current density-voltage (*JV*) measurements are the most fundamental solar cell characterisation technique since the four key solar cell parameters (V_{oc}, J_{sc}, FF, PCE) are determined through these measurements. However, these are not the only parameters that can be determined using *JV* measurements. The diode ideality factor, *n*, and dark saturation current, J_0, are determined from *IV* curves taken in the dark, and the parasitic resistances can be determined from illuminated *IV* curves.

2.1.1 *IV* Experimental Setup

IV measurements were taken using a Keithley 2400 SourceMeter Instrument. A Newport 67005 solar simulator was used to simulate AM1.5 illumination. Figure 2.1 shows a comparison of the simulator spectrum with that of the ASTM G173-03 AM1.5 global spectrum at 100 mW/cm^2. The solar cells were located such that the incident power density from the solar simulator was 100 mW/cm^2 which was calibrated with a Thorlabs D3MM thermal sensor. The PbS colloidal quantum dot

solar cells in chapter 3 and the polymer solar cells in chapter 5 were all mounted in a custom built cell holder (Figure 2.2) that allowed nitrogen to be continuously flushed through the system. Nitrogen was flushed through the holder to ensure the cells were maintained in an oxygen-free environment, if the cells were mounted in an environment with oxygen present. The In(Ga)As quantum dot and GaInNAs cells in chapter 4 were mounted in an Oxford Instruments DNV cryostat, even when just room temperature measurements were taken, for ease of making connection to the cells.

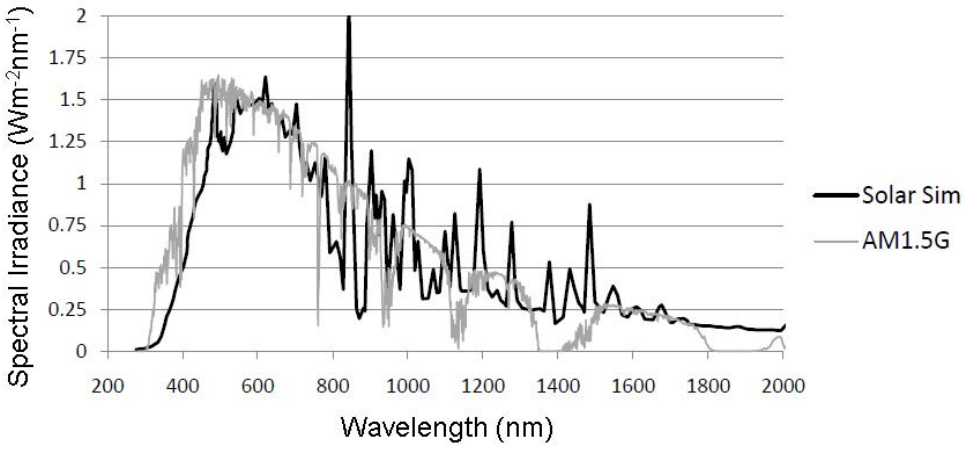

Figure 2.1. Comparison of the Newport 67005 solar simulator spectrum with the ASTM G173-03 AM1.5 global spectrum at 100 mW/cm^2.

2.1.2 Key Solar Cell Parameter Determination

Figure 1.8b shows a typical *JV* curve (current divided by the cell area gives the current density) with J_{sc} and V_{oc} marked. Both of these values can be taken directly from the *JV* curve. J_{sc} is the current when the voltage is zero and V_{oc} is the voltage when the current is zero. To determine the fill factor, the power is calculated ($P = IV$) at each point along the curve between J_{sc} and V_{oc} and the maximum power point is found. The current and voltage at the maximum power point (J_{mpp}, V_{mpp}) along with J_{sc} and V_{oc} are used in equation (1.5) to determine the fill factor. Finally, the power

conversion efficiency is determined by equation (1.6) with an incident illumination power density of 100 mWcm^{-2}.

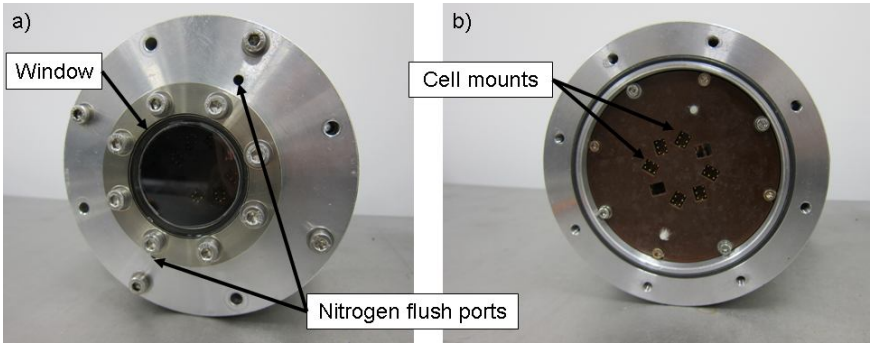

Figure 2.2. Custom-built cell holder. a) The holder with the cover mounted showing the illumination window and ports used to flush nitrogen through the holder. b) The holder with the cover removed showing where the cells are mounted. Up to eight substrates can be mounted at one time. Each position has two contacts for the ITO strip and each aluminium strip.

2.1.3 Parasitic Resistances Determination

The illuminated *IV* curves are also used to determine the series and shunt resistances. If the series and shunt resistances are both large (a valid approximation for the CQD and polymer cells), the term with R_{sh} can be neglected in equation (1.8) giving

$$I(V) = I_{sc} - I_0\left(e^{\frac{q(V+IR_s)}{k_BT}} - 1\right) \quad \textbf{(2.1)}$$

where the current, *I*, has been used instead of the current density, *J*. Algebraically solving for the voltage gives

$$V = \frac{k_BT}{q}\ln\left(\frac{I_{sc} + I_0 - I}{I_0}\right) - IR_s. \quad \textbf{(2.2)}$$

This can be differentiated with respect to *I* to get

$$\frac{dV}{dI} = -\frac{k_BT}{q}\left(\frac{1}{I_{sc} + I_0 - I}\right) - R_s. \quad \textbf{(2.3)}$$

At open circuit between the terminals the current is zero and $V = V_{oc}$ leading to

$$R_s = -\left.\frac{dV}{dI}\right|_{V=V_{oc}} - \frac{k_B T}{q}\left(\frac{1}{I_{sc} + I_0}\right). \quad \textbf{(2.4)}$$

Now ($k_B T/q$) is much smaller than V_{oc}. Therefore, if R_s is large compared to ($k_B T/qI_0$), it can be approximated as

$$R_s \approx \left.\frac{dV}{dI}\right|_{V=V_{oc}}. \quad \textbf{(2.5)}$$

The shunt resistance can also be approximated if the series and shunt resistances are both small. In this case R_s can be neglected in equation (1.8), which then becomes

$$I(V) = I_{sc} - I_0\left(e^{\frac{qV}{k_B T}} - 1\right) - \frac{V}{R_{sh}} \quad \textbf{(2.6)}$$

where again the current is used in place of the current density. This can be differentiated with respect to V to get

$$\frac{dI}{dV} = -\frac{q}{k_B T} I_0 e^{\frac{qV}{k_B T}} - \frac{1}{R_{sh}}. \quad \textbf{(2.7)}$$

At short circuit between the terminals the voltage is zero and $I = I_{sc}$ which gives

$$\frac{1}{R_{sh}} = -\left.\frac{dI}{dV}\right|_{V=0} + \frac{qI_0}{k_B T}. \quad \textbf{(2.8)}$$

If R_{sh} is small, then ($qI_0/k_B T$) is comparatively negligible and R_{sh} can be approximated as

$$\frac{1}{R_{sh}} \approx \left.\frac{dI}{dV}\right|_{V=0}. \quad \textbf{(2.9)}$$

2.1.4 Ideality Factor and Reverse Saturation Current Determination

To determine the ideality factor, n, and reverse saturation current, J_0, the diode equation (equation (1.9)) is fitted to the diode portion of the dark *IV* curve[50] as seen in Figure 2.3.

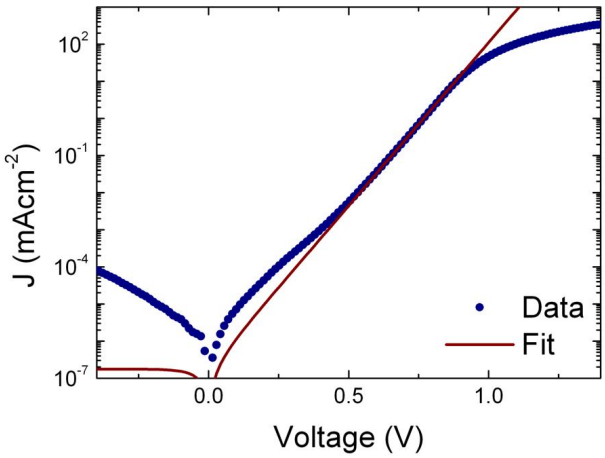

Figure 2.3. Example dark *JV* curve showing equation (1.9) fitted to the diode portion on the curve to determine *n* and J_0.

2.2 Impedance Measurements

2.2.1 Impedance Experimental Setup

Impedance and capacitance measurements were taken with either a Solartron 1260 Impedance Gain Phase Analyzer or an Agilent E4980A option 001 Precision LCR Meter. The Solartron was used for the impedance and capacitance measurements reported in chapters 4 and 5, and the Agilent for the measurements in chapter 3. The Solartron had noise problems at certain bias ranges. However, valid measurements could still be taken. Once the Agilent became available, it was used instead. Both systems are all-in-one measuring units that provide the stimulating signal and measure the response. All capacitance and impedance measurements were taken with the cell in the dark. The experimental setup is shown in Figure 2.4

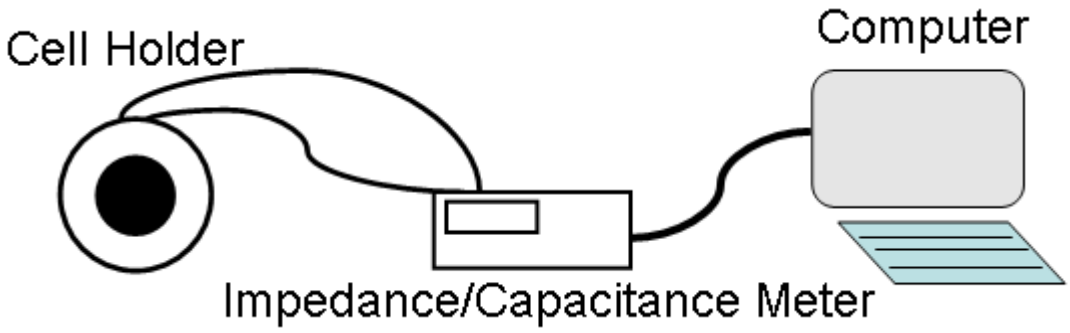

Figure 2.4. Capacitance and impedance experimental setup.

2.2.2 Brief Impedance Measurement Theory

As a simple description of the measurement process, the device under test is stimulated with a small amplitude, single-frequency voltage (or current), and the phase shift and amplitude of the resulting current (or voltage) is measured[51]. Impedance is defined within linear systems theory[52], which requires a small perturbing signal to maintain an electrically linear response[51]. Figure 2.5 demonstrates the importance of the small perturbing signal at forward DC bias for a system with an exponential current response, such as a diode.

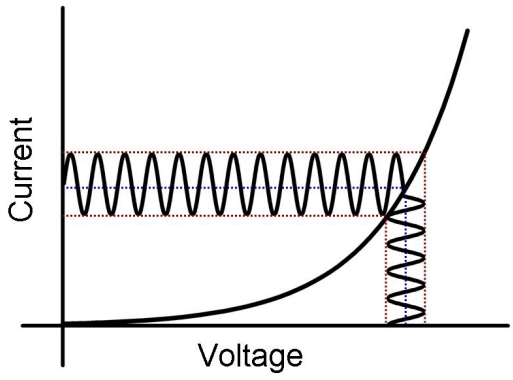

Figure 2.5. The perturbation amplitude in voltage causes a larger amplitude response in current due to the exponential relationship. Therefore it is necessary to use small perturbation amplitudes.

A change in voltage results in a non-linear change in current. However, if the perturbation is small, the change can be approximated as linear. The perturbation amplitude was 25 mV for all measurements performed in this thesis.

The response signal amplitude and phase with respect to the stimulating signal determine the device's impedance at the particular perturbation frequency and DC bias. Although the impedance and capacitance could be directly taken from both the Solartron and Agilent machines, this resulted in incorrect capacitance results since the machines make assumptions about the configuration of the external circuit under measurement. In order to avoid this problem, the real and imaginary impedance components were recorded ($Z = R + iX$, where Z is the impedance, R is the real component, and X is the imaginary component) and the real component of the complex capacitance was found. The impedance of a capacitor is given by

$$Z_{cap} = \frac{1}{i\omega C} \tag{2.10}$$

where ω is the angular frequency of the perturbation signal and C is the capacitance. Rearranging for C, substituting $R + iX$ for Z, and rationalizing gives the complex capacitance as

$$C = \frac{-X}{\omega\left(R^2 + X^2\right)} - i\frac{R}{\omega\left(R^2 + X^2\right)}. \tag{2.11}$$

All capacitance values were determined by the real component of equation (2.11), which gives the capacitance as

$$C = \frac{-X}{\omega\left(R^2 + X^2\right)}. \tag{2.12}$$

2.2.3 Capacitance-Voltage Measurements

As mentioned in section 1.4.4, the depletion width at a Schottky junction is bias dependent. For reverse and small forward bias values such that there is still a barrier to diffusion current across the junction (see section 1.4.5), the Schottky junction behaves analogous to a parallel-plate capacitor with plate spacing equal to the depletion width. This can be seen by looking at the dynamic capacitance of the junction, which is defined as the amount of charge moving in or out of the device with changing bias and is written as[53]

$$C \equiv \frac{dQ}{dV} \tag{2.13}$$

where Q is the charge. The amount of charge in a *p*-type semiconductor at the junction is[53]

$$Q = -A\sqrt{2q\varepsilon_s N_a \left(V_{bi} - V\right)} \tag{2.14}$$

giving the capacitance to be

$$C(V) = A\sqrt{\frac{q\varepsilon_s N_a}{2(V_{bi} - V)}}\,. \tag{2.15}$$

The depletion width at a Schottky junction was given in equation (1.3). Incorporating the depletion width, the capacitance can be expressed as

$$C = \frac{A\varepsilon_s}{w} \tag{2.16}$$

where the bias dependency, ($V_{bi} - V$), was substituted for V_{bi} in equation (1.3). This is similar to the expression for the capacitance of a parallel-plate capacitor with plate spacing equal to the depletion width. Since the depletion width is bias dependent, so is

the capacitance. This can be exploited to determine V_{bi} and N_a. Equation (2.15) can be re-written as

$$\frac{1}{C^2} = \frac{2(V_{bi} - V)}{A^2 q \varepsilon_s N_a}. \quad \textbf{(2.17)}$$

From this it can be seen that in a plot of C^{-2} versus bias voltage, a linear response is observed for regions of capacitance determined by the depletion capacitance. Fitting equation (2.17) to this region reveals the doping density and built-in bias.

This analysis is also valid for a *p-n* junction if the doping on one side of the material is much larger than the doping on the other. In that case, the depletion region is almost entirely in only one of the semiconductor layers (see section 1.4.4). If the doping densities are similar, then this approximation is no longer valid and the doping density in equation (2.17) needs to incorporate the doping in both junction materials. Assuming the relative permittivity is the same in each material, the full form of equation (2.17) is

$$\frac{1}{C^2} = \frac{2(V_{bi} - V)}{A^2 q \varepsilon_s}\left(\frac{1}{N_a} + \frac{1}{N_d}\right) \quad \textbf{(2.18)}$$

for similar material doping densities at a *p-n* junction.

Section 2.2.2 mentioned the importance of using a small modulation amplitude to maintain the linearity of the response. Choosing the correct modulation frequency is also important. For inorganic crystalline material such as the material studied in chapter 4, frequencies in the range of 10 kHz to 1 MHz are typically used in order to prevent losses due to shunt pathways[54]. However, in materials that have slower responding charge carriers such as those in chapters 3 and 5, it is important to use a low modulation frequency (typically around 100 Hz) to ensure all the charge carriers

can respond to the modulation signal and contribute to the capacitance[53,55]. Generally inorganic crystalline material has faster responding charges than organic material which means the capacitance results are consistent over a wider range of frequencies.

2.2.4 CV Depletion Width Determination

The width of the depletion region can be determined by a couple of methods. First, equation (2.16) shows the form of the capacitance for a parallel-plate capacitor with spacing *w*. This also represented the depletion capacitance where *w* was the depletion width. Therefore in the depletion capacitance regime, the depletion width can be found as function of bias by measuring the capacitance and using equation (2.16). The built-in bias and doping density values can also be used to determine the depletion width using equation (1.3) with ($V_{bi} - V$) in the place of V_{bi} for the bias-dependent depletion width.

2.2.5 Diffusion Capacitance

The technique described in section 2.2.4 was based on the depletion capacitance. At forward biases such that flat-band or near flat-band conditions are reached, minority carriers are injected into the semiconductor from the metal and the capacitance becomes dominated by the excess minority carriers[56,57]. This is known as the diffusion capacitance[53]. This happens in a *p*-*n* junction as well when majority carriers diffuse across the reduced barrier becoming minority carriers[58] (see section 1.4.5). The capacitance can be found by considering the layer with thickness equal to *L* of accumulated minority carriers at the junction. Using Boltzmann statistics, for electron minority carriers the capacitance is[59,60]

$$C_{\mu} = \frac{q^2 L n_0}{k_B T} e^{\frac{qV_F}{\eta k_B T}} \quad \textbf{(2.19)}$$

where n_0 is the minority carrier concentration in equilibrium, η is a factor that accounts for departure from Boltzmann statistics, and V_F is the potential associated with splitting the carrier Fermi levels related to the accumulation of minority carriers[59,61]. This capacitance is also commonly referred to as the chemical capacitance, since it is an equilibrium property[58,59]. According to equation (2.19), the capacitance should increase with increasing forward bias. However, minority carrier injection can be limited (for example by barriers at metal semiconductor junctions[62,63]) which causes the capacitance to go negative above a given forward bias, departing from the chemical capacitance[62].

Injected minority carriers are governed by diffusion and recombination, which leads to an impedance model based on diffusion coupled with recombination in the chemical (diffusion) capacitance regime[64,65]. The process can be modelled with a transmission line equivalent circuit[65,66] shown in Figure 2.6.

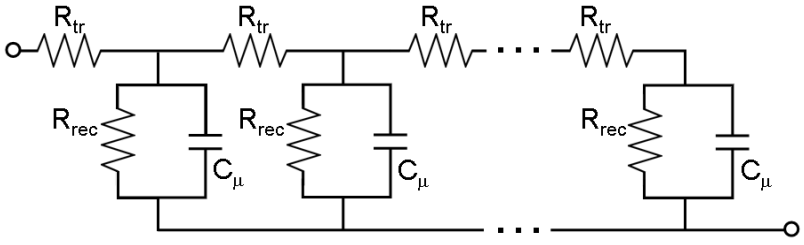

Figure 2.6. Transmission line equivalent circuit representation of diffusion and recombination

In the equivalent circuit model shown in Figure 2.6 R_{rec} represents the recombination resistance, R_{tr} represents the transmission resistance, and C_{μ} represents the chemical capacitance. The minority carrier lifetime, τ, is then given by[56]

$$\tau = R_{rec} C_{\mu} . \quad \textbf{(2.20)}$$

The recombination resistance and transmission resistance are related by[65]

$$R_{tr} = \left(\frac{d}{L_n} \right)^2 R_{rec} \quad \textbf{(2.21)}$$

where d is the distance from the junction to the electrode that minority carriers must travel to be extracted at the electrode and L_n is the minority carrier diffusion length. If the diffusion length is large compared to d, R_{rec} is much larger than R_{tr} and the transmission line can be reduced to an RC circuit. The resulting description of the entire process to include series resistance is shown in Figure 2.7. Impedance measurements in the chemical capacitance regime (forward bias above the flat-band bias) are taken over a broad range of frequencies to create a complex plane representation of the impedance[67]. The impedance spectrum for the circuit shown in Figure 2.7 is a semi-circular arc shifted on the real axis by an amount equal to R_s as seen in Figure 2.8a.

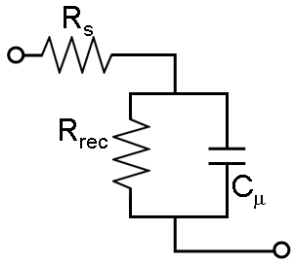

Figure 2.7. Reduced equivalent circuit for cells with a large diffusion length compared to the material thickness.

Fitting the measured impedance spectra data with the circuit in Figure 2.7 leads to the minority carrier lifetime using equation (2.20). The minority carrier lifetime, τ, can also be found by the frequency at the top of the arc (highlighted in Figure 2.8a) since

it corresponds to the RC time constant, and therefore to the minority carrier lifetime such that $\tau = 1/\omega$.

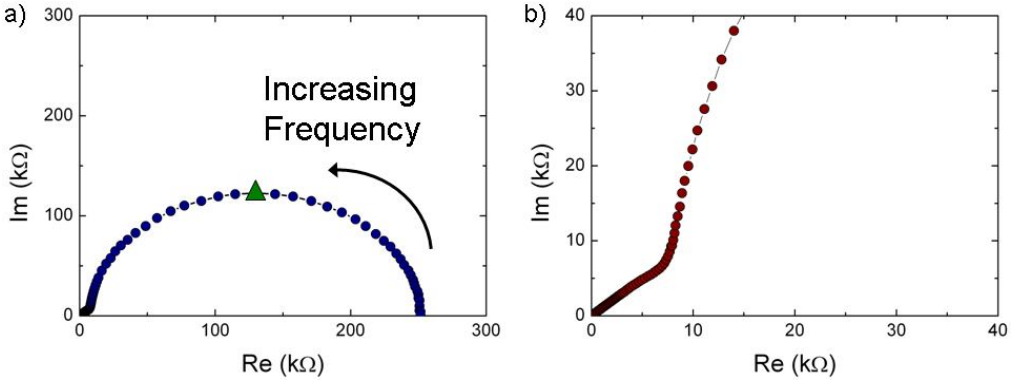

Figure 2.8. a) Impedance spectra corresponding to recombination. The minority carrier lifetime is determined by the RC time constant or the characteristic peak frequency (green triangle). b) Warburg feature at high perturbing frequencies corresponding to diffusion.

Diffusion effects are seen in the impedance spectra by a 45^0 "Warburg" feature at high frequencies as demonstrated in Figure 2.8b. However for cells that are thin compared to the diffusion length, the transmission resistance is a small fraction of the recombination resistance and the Warburg part becomes very small to the point of not seeing it[58]. The Warburg part can also be masked by the presence of other high-frequency components such as inductance of the connecting leads or chemical capacitance of majority carriers[56]. If the minority carrier lifetime is small, the RC arc is reduced and the Warburg part becomes larger with respect to the rest of the curve[64].

2.3 External Quantum Efficiency Measurements

2.3.1 EQE Experimental Setup

Illumination for the external quantum efficiency (EQE) measurements was provided by a halogen lamp and Oriel Cornerstone 130 monochromator. High-pass cut off filters of 400, 610, and 1000 nm were used to block harmonics when illuminating at

longer wavelengths. The light intensity at each wavelength was calibrated using a Newport 818 UV enhanced silicon photodetector and a Newport 918 IR germanium photodetector. The current signal from the solar cell was measured with a Keithley 6845 picoammeter. The entire system was controlled via a labView virtual instrument. Figure 2.9 shows the EQE experimental setup.

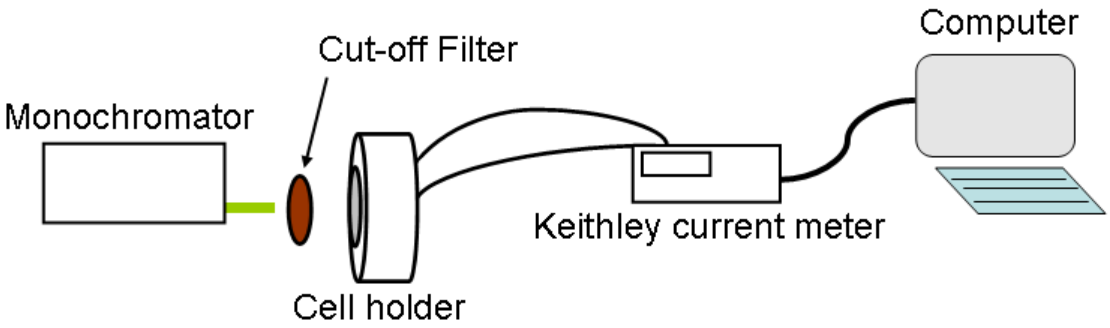

Figure 2.9. External quantum efficiency experimental setup.

2.3.2 EQE Method

EQE is the ratio of the number of collected charge carriers to the number of incident photons. This value is wavelength dependent and gives a description of how well the cell converts solar energy to electrical energy. For example, if every incident photon at a given wavelength is absorbed and all the carriers are collected, the EQE at that wavelength is one.

In order to measure EQE, the solar cell is illuminated with a single wavelength (in reality the line width depends on the monochromator) and the photocurrent is measured. The photocurrent is equal to J_{sc} (in reality the measured current is slightly less than J_{sc} since the meter has a very small resistance). This process is then repeated over a broad spectrum of wavelengths to build the wavelength dependent EQE graph.

Once the EQE across the solar spectrum wavelengths is determined, it can be integrated with the solar spectral irradiance to determine J_{sc}. This allows a comparison to be made with the measured J_{sc} from *JV* measurements. However, the illumination intensity of the EQE system needs to be considered. For example, quantum efficiency measurements on P3HT:PCBM solar cells show little intensity dependence at intensities near one sun, but at intensities below 1 $mWcm^{-2}$ the results become very intensity dependent[68]. The J_{sc} determined from the EQE measurements also provides a method for adjustments. In the preceding analysis, the measured optical power was assumed to be incident entirely within the solar cell. This was true for the cells in chapter 4. However, the cells in chapter 3 were much smaller and the incident photons could not be completely focused onto the cell. Therefore for these cells, an overall correction factor was applied to the EQE measurements such that the J_{sc} determined from integration matched that of the *JV* determined J_{sc}. The correction factor was applied equally to all wavelength values, so the shape of the EQE response remained unaltered.

2.4 Temperature Dependent Measurements

Temperature dependent measurements were taken with the solar cells mounted in an Oxford Instruments DNV cryostat controlled by an Oxford Instruments ITC 502 temperature controller. Figure 2.10a shows the cell mount inside the cryostat for the cells studied in chapter 3. Figure 2.10b shows a cell from chapter 4 mounted on the cryostat mount.

Temperature dependent measurements were conducted by first lowering the temperature to 77 K and letting the cell stabilize for 1 hour. After each measurement, the temperature was raised to the next temperature and allowed to stabilize for 5

minutes once the new temperature was reached before taking the next measurement. Temperature dependent measurements were performed with dark and illuminated *JV*, CV, and EQE measurements. The temperature dependent experimental setups are shown in Figure 2.11.

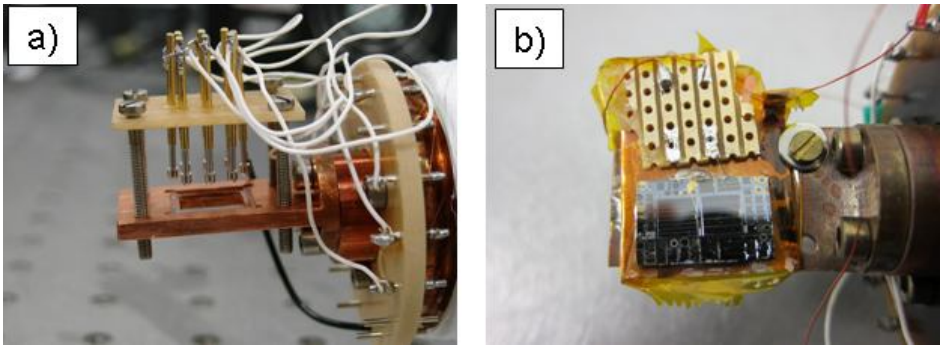

Figure 2.10. a) Cryostat cell mount for cells in chapter 3. b) A cell from chapter 4 mounted on the cryostat cold finger.

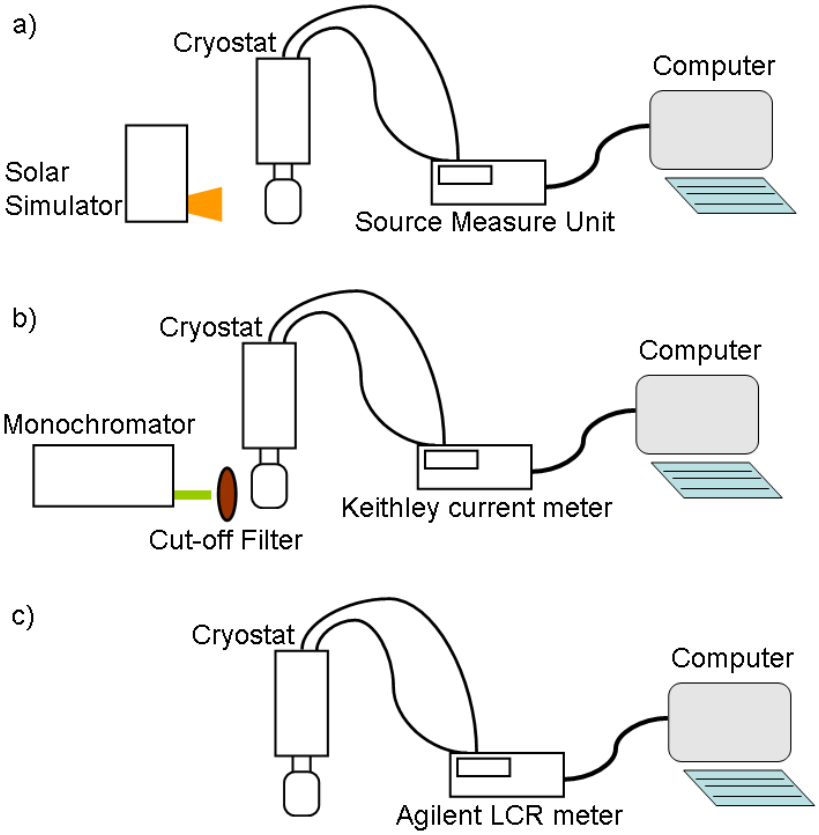

Figure 2.11 Temperature dependent experimental setups for a) *JV* measurements, b) CV measurements, and c) EQE measurements.

Chapter 3

Interface Analysis of Colloidal Quantum Dot Solar Cells

3.1 Introduction

The major drawback solar PV currently faces is that it is too costly to compete with other sources of electricity[69]. Solution processed colloidal quantum dot (CQD) solar cells have recently made significant progress in this regard and offer a promising route towards low-cost solar cells with the added benefit of bandgap tunability leading to solar cells that harvest photons over a large portion of the solar spectrum[69,70,71,72,73]. Advances in chemistry and nanotechnology allow easy manufacturing of uniform semiconductor nanocrystal quantum dots (QD)s without the need of a clean room, high temperature processing, or ultra-high vacuum equipment leading to large quantum dot production at competitive prices[72]. Fabrication of the solar cell itself also promises to be low-cost using cheap manufacturing processes such as spray-coating and inkjet printing combined with roll-to-roll processing[70,71, 74, 75].

The other major reason CQD solar cells are so attractive is because they can be spectrally tuned by controlling the size of the QD material due to the quantum size

effect[18,70,71,76]. If a semiconductor is fabricated into a small enough crystallite, electrons become more tightly confined resulting in the continuous structure within each band becoming discrete[77]. The size where this occurs is the effective Bohr radius of an exciton (electron-hole pair) within the semiconductor, since an exciton is analogous to a hydrogen atom, and can be viewed as the bulk semiconductor's lowest excited state[77]. Therefore, when a particle is made smaller than the Bohr radius, quantum confinement of the electron and hole wave functions produces an increase in the bandgap[78, 79]. For example, PbS which has an exciton Bohr radius of 18 nm[71,80] can be tuned to have an absorption onset from ~ 600 nm to over 1800 nm[71,81]. The benefit of such bandgap tunability coupled with cheap solution processing is in the application to multi-junction solar cells.

An optimised triple-junction solar has an efficiency limit near 49%[70]. However the drawbacks of single-crystal multi-junction cells are high material cost leading to high energy payback time, the necessity of crystal lattice matching, and the need to make physically rigid cells[70]. On the other hand, solution processed CQD solar cells avoid these problems. In fact, they open the possibility to fabricate a low-cost, multi-junction cell from a single material composed of layers of different sized QDs that harvest photons over a large portion of the solar spectrum[70,72]. Figure 3.1 illustrates this idea. In this example the first QD layer is composed of 2.6 nm diameter PbS CQDs with an absorption onset at 680 nm, the second layer has 3.6 nm PbS CQDs with an onset at 1070 nm, and the final layer has 7.2 nm PbS CQDs with an onset at 1750 nm[71].

One final phenomenon worth mentioning (although it is not investigated in this thesis) is multiple exciton generation (MEG), since this is often cited as a possible advantage

of CQD solar cells. Due to strong confinement by the QDs, interactions between incident photons and charges in the QDs may lead to the generation of multiple excitons from a single photon[82,83]. Application in a solar cell could then be a path to increasing the power conversion efficiency beyond the Schockley-Queisser limit[73]. Already, MEG has been observed in both PbS and PbSe QDs[84,85,86]. However, MEG in solar cells has yet to be proven and the efficiency of the process, fundamental mechanism, and application to solar cells are still areas of debate[73,87,88,89,90,91,92].

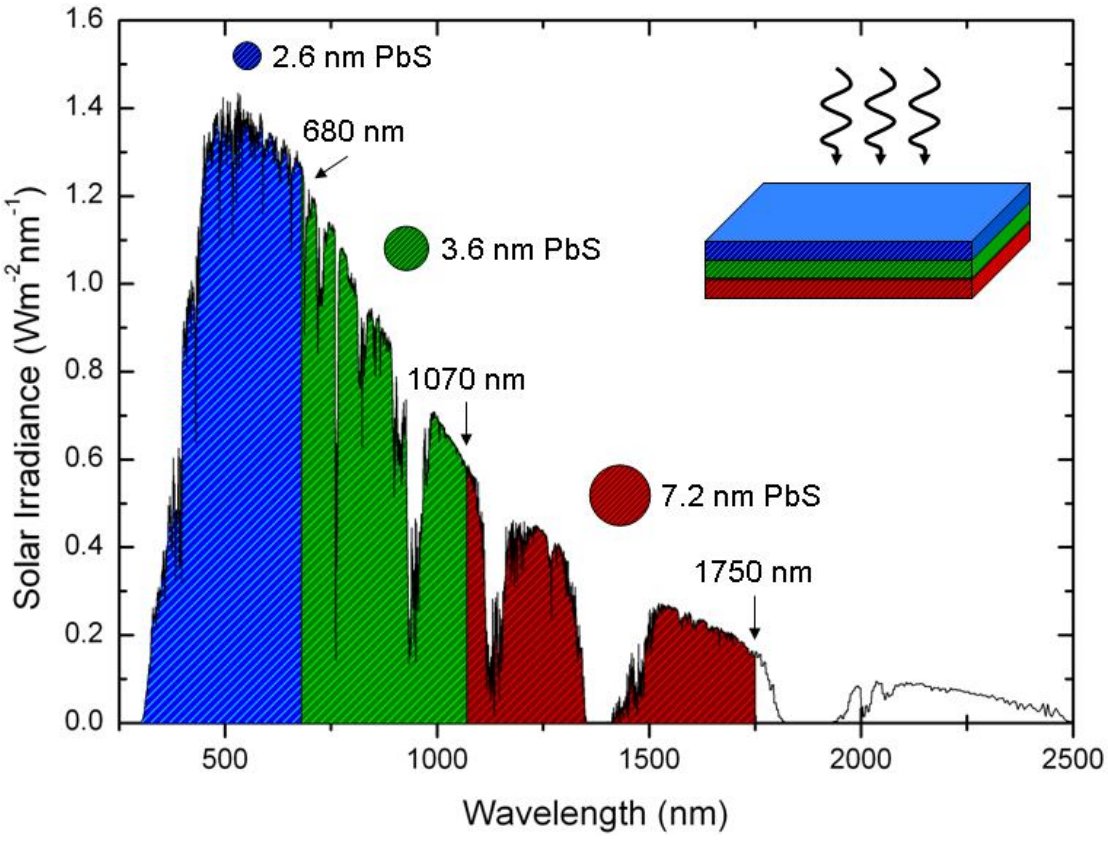

Figure 3.1. Multi-layer PbS CQD solar cell absorption for CQD sizes of 2.6, 3.6, and 7.2 nm. Light is incident on the small dot layer first, harvesting high energy photons. Each subsequent layer harvests a different portion of the spectrum.

3.2 Current State of CQD Solar Cells

In the past four years CQD solar cell architecture has progressed from Schottky barriers[50] to heterojunctions[93] and even on to the more complex architectures of bulk

heterojunction[94] and tandem[95,96] cells. The power conversion efficiency for CQD solar cells has also seen rapid progress with the current record at 5.5% for a bulk heterojunction solar cell fabricated from lead sulphide (PbS) quantum dots and titanium dioxide (TiO_2) nanocrystals[94]. The appearance of the tandem cell this year (2011), while currently lower in efficiency than the single and bulk heterojunction cells, demonstrates clear progress towards realizing a highly efficient multi-junction CQD solar cell like the one illustrated in Figure 3.1. In addition, novel charge transport has been reported this year in CQD cells employing quantum funnels (graded layer of CQD sizes) that direct minority carriers toward an electron acceptor material[97].

A brief summary of some of the highest performing PbS and PbSe solar cells is given in Table 3.1. This is not meant to be a complete catalogue, but rather is intended to give a general idea of the current state of PbS and PbSe CQD solar cells. For a more complete list of infrared CQD solar cells, see reference 71. The top section of Table 3.1 presents the CQD highlights for each type of device architecture while the bottom section is focused on single, planar heterojunctions with ZnO since that structure is closely related to the cell architecture investigated in this chapter.

Table 3.1. CQD solar cell highlights. Bottom half – ZnO specific heterojunctions

Architecture	Material	V_{oc} (V)	J_{sc} (mAcm^{-2})	FF	AM1.5G PCE	Ref.
Schottky	ITO/PbS/LiF/Al	0.51	14.0	0.51	3.6%	98
Heterojunction	FTO/TiO_2/PbS/Au	0.51	16.2	0.58	5.1%	93
Bulk Heterojunction	FTO/TiO_2/PbS:TiO_2/Au	0.48	20.6	0.56	5.5%	94
Tandem	ITO/TiO_2/PbS(1.6 eV) /GRL/PbS (1.0 eV)/Au	1.06	8.3	0.48	4.2%	96
PbS and PbSe Heterojunctions with ZnO						
PbSe/ZnO Film	ITO/ZnO/PbSe/α-NPD/Au	0.39	15.7	0.27	1.6%	99
PbSe/ZnO QD	ITO/PEDOT:PSS/PbSe/ZnO/Al	0.44	24.0	0.32	3.4%	100
PbS/ZnO	ITO/ZnO/PbS/Au	0.59	8.9	0.56	2.9%	80

The last architecture listed in Table 3.1 is very similar to the devices studied in this chapter, only inverted. It has been reported that a Schottky junction forms at the PbS/metal junction without careful selection of the metal electrode that creates an opposing diode to the PbS/ZnO diode[101]. By moving the PbS to the transparent conductor side, that problem is alleviated. However, as will be seen in the thickness-dependent EQE section (3.7.2.1), this moves the charge separating junction to the back side of the photon absorbing PbS layer which may inhibit exciton separation.

3.3 Work Presented in this Thesis

The work presented in this chapter was carried out in collaboration with a fellow DPhil student (Cheng Cheng). All QD synthesis and cell fabrication (section 3.5) was carried out by Cheng. The electrical characterisations and analysis were performed by the author.

The field of CQD solar cells is relatively young compared to other solar cell technologies. As a result, there are still many new device structures, in terms of materials and architectures, to investigate. The main focus of this chapter is an electrical characterisation (using the techniques presented in chapter 2) of the first reported CQD heterojunction solar cell of the architecture ITO/PEDOT:PSS/PbS/ZnO/Al. In addition, specific areas of interest are investigated. The heterojunction operating mechanism is still not fully understood with suggestions of both *p-n* and excitonic behaviour (see section 3.6). Specific attention is given to this topic using capacitance and quantum efficiency methods. The charge dynamics at the electrode contacts also receives special consideration in terms of charge injection barriers.

3.4 UV Photodoping the ZnO QDs

A problem with using ZnO as an *n*-type material to form the heterojunction with PbS is that it has low conductivity which restricts the current output from the solar cell[100]. However, the conductivity can be increased by UV photodoping which is thought to passivate electron traps on the ZnO surface[102,103]. ZnO is intrinsically *n*-type[104], but mobile electrons can become trapped when gas molecules such as O_2, NO_2, and CO are adsorbed on the ZnO surface[105]. In order to free the electrons, oxygen desorption from the nanocrystal surface can be induced by the introduction of holes from the anode through applying a high forward bias or UV illumination in an O_2-free environment[106,107]. Using this explanation, Lakhwani *et al*. suggest the ZnO nanocrystals can be considered an intrinsic, wide-bandgap semiconductor before UV illumination[104]. After full UV illumination, they measured the doping density to be on the order of 10^{18} to 10^{19} cm^{-3} depending on the method of measurement.

3.5 CQD Solar Cell Fabrication

The first step was to synthesize PbS nanocrystals with a bandgap of 1.3 – 1.4 eV using the process described by Luther *et al*[80]. A mixture of 0.47 g PbO, 10 mL 1-octadecene, and 2 mL oleic acid was mixed and heated in a flask to 120^0C under N_2 for 2 hours. During this process the PbO dissolved and produced a clear solution. In a separate vial, 180 µL hexametyldisilathiane (TMS_2S) was mixed with 3 mL 1-octadecene and degassed under N_2 flow. The TMS_2S solution was loaded into a syringe and swiftly injected into the PbO solution at 100°C. The resulting mixture turned from clear to dark, indicating rapid nucleation. The nanocrystals were allowed to grow for 1 minute at which point the growth was halted by quenching the flask in an ice water bath. The solution temperature dropped to room temperature in less than

1 minute. The solution was then transferred to a 50 mL centrifuge tube and 35 mL 1:1 ethyl aceate: methanol was added to precipitate the nanocrystals. The solids were separated by centrifuging at 4000 rpm for 5 minutes. The supernatant was decanted and 5 mL hexane was used to re-disperse the nanocrystals. The nanocrystals were washed with methane twice, and then re-dispersed in 5 mL hexane. Finally, the nanocrystals (in hexane) were driven through a 0.45 μm PTFE filter.

A butylamine ligand exchange was performed by adding 5 mL butylamine to dissolve the precipitated nanocrystals. This process was assisted by ultrasonication for 30 minutes. The nanocrystals were precipitated again by adding isopropanol and re-dispersed in 5 mL butylamine. After another 30 minutes of ultrasonication, the nanocrystals were transferred to a N_2-filled dry box. The next day the nanocrystals were precipitated by isopropanol, centrifuged, and dried under N_2 flow. The dry weight was then calculated. Hexane was used to disperse the nanocrystals to 25 mg/mL for device fabrication. The solution was stored in a nitrogen dry-box.

The ZnO nanocrystals (larger than the Bohr radius) were synthesized using the method described by Pacholski *et al*[108]. A zinc precursor was prepared by dissolving 0.002 mol zinc acetate dihydrate in 100 mL methanol. Potassium hydroxide in 50 mL methanol was added by drops to the zinc precursor at 60°C while stirring. The solution turned cloudy at first and then became clear. After 2 hours, the ZnO nanoparticles started to precipitate from the solution. The precipitates were collected by centrifugation, and re-dispersed in methanol. The nanoparticles were washed with methanol 3 times, dried, and then re-dispersed in chloroform to 40 mg/mL. The nanoparticle solution was then transferred to a N_2-filled dry-box.

Next, the cells themselves were fabricated using the following procedure. PEDOT:PSS was spin cast onto cleaned, pre-patterned ITO substrates. PbS QDs were spin cast next using a layer-by-layer method[100]. The PbS layer thicknesses of the test cells measured by DEKTAK were 50 nm, 125 nm, 190 nm, and 230 nm. During each layer iteration, the cell was immersed in 1,2-ethanedithiol (EDT) to perform a ligand exchange of butylamine to EDT[109]. The residual EDT was washed off by spinning the substrate while dropping methanol and hexane onto the surface. After this, ZnO was spin cast on top of the PbS layer to create a ~100 nm thick ZnO layer. Finally, Al electrodes were evaporated through a shadow mask producing cells with an area of 0.03 cm^2. Figure 3.2 illustrates the cell structure. Each substrate produces three "pixel" solar cells determined by the overlap of ITO and Al.

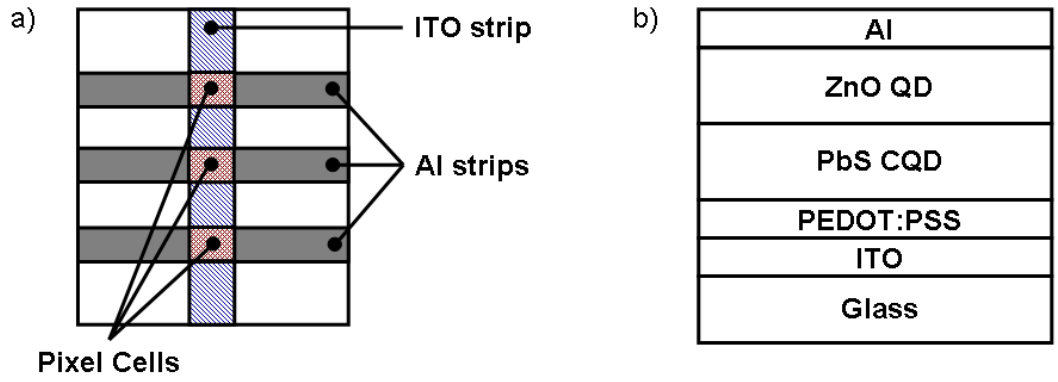

Figure 3.2. a) Three solar cells (termed pixel cells) per substrate are determined by the ITO and Al overlap. The area for each pixel cell is 0.03 cm^2. b) The solar cell layer structure. The layers are not to scale.

3.6 CQD Solar Cell Junction Interface Processes

An area of considerable discussion in CQD cells is the operating mechanism at heterojunction interfaces. Solar cells fabricated from PbS and PbSe QDs have both been shown to form Schottky barriers that separate electron and hole charge carriers when in contact with a metal electrode[50,110,111,112,113]. However, when forming a

heterojunction with an *n*-type material there has been much debate as to whether the operating mechanism of the junction is depleted *p*-*n*[93,94,101] or excitonic[99,100,114]. This is important because thick PbS layers would improve absorption of photons with energy greater than the quantum confined bandgap, but thicker layers reduce the charge separation efficiency due to the extra distance they must travel to the heterojunction[70]. In an excitonic junction, the charge harvesting ability is determined by the exciton diffusion length[22]. However, a *p*-*n* junction creates a depletion region that extends out from the junction increasing the charge collection distance within the material. Minority carriers only need to diffuse to the depletion region in order to be swept into the other material due to the electric field in the depletion region, becoming majority carriers.

In support of excitonic junction behaviour, Leschkies *et al*. argue that the V_{oc} dependence on QD size (smaller QDs produce larger V_{oc}) in PbSe QD/ZnO thin film solar cells provides evidence of an excitonic junction[99]. Their argument focuses on the position of the Fermi level within the PbSe material in relation to the ZnO Fermi level. The ZnO thin film is *n*-type and has a Fermi level near the conduction band. For each case of doped PbSe (intrinsic, *n*-type, *p*-type), the PbSe Fermi level should be below the ZnO Fermi level. The location of the PbSe Fermi level can be changed by decreasing the PbSe QD size which increases the bandgap, and therefore changes the Fermi level position. Each doping case should respond differently to the change in bandgap. For their argument, they assume the conduction and valence bands both increase by the same amount when the bandgap increases[99]. This results in the Fermi level staying in the same location for intrinsic PbSe (always in the middle of the bandgap), moving toward the ZnO Fermi level (smaller Fermi level difference between the materials) for *n*-type PbSe, and moving away from the ZnO Fermi level

(larger Fermi level difference between the materials) for *p*-type PbSe. They conclude then that when the PbSe QD size is decreased, the V_{bi} and hence V_{oc} should stay the same in the intrinsic case, decrease in the *n*-doped case, and increase in the *p*-doped case. The final piece of evidence is their conclusion that the PbSe is not *p*-type based on FET transfer characteristics which show ambipolar conduction and high electron current in the dark and under illumination. Therefore, they conclude the junction cannot behave like a traditional *p*-*n* solar cell since the PbSe would need to be *p*-type to exhibit an increasing V_{oc} with decreasing QD size[99].

There are a couple items to consider with regards to the conclusions made by Leschkies *et al.* discussed in the previous paragraph. First, they follow the PbSe QD synthesis method described by Luther *et al*[109]. Field effect transistors were indeed found to have ambipolar conduction when fabricated from PbSe QDs that had been synthesised with that method. However, broad band illumination caused the material to become *p*-type[109]. Any exposure to oxygen was also found to *p*-dope the PbSe[109]. Also, it has been shown that PbSe synthesised in this manner can be used to fabricate *p*-type Schottky solar cells[113]. Based on the argument of Leschkies *et al.*, *p*-type PbSe would result in the Fermi level shifting in the right direction to produce an increase in the V_{oc} with decreasing QD size. This brings into question the conclusion of Leschkies *et al*. that the PbSe QDs are not *p*-type.

The second thing to consider is the proposed response of the V_{bi} and V_{oc} with changing bandgap. Their argument is based on a *p*-*n* homojunction response. In a heterojunction, Fermi level alignment determines the amount of band bending, but there are also conduction and valence band offsets due to the different bandgap sizes between the two materials[115]. The offsets must also be considered along with the

Fermi level difference when determining the energy level difference between extracted carriers. Therefore a change in the bandgap changes the Fermi, conduction band, and valence band energy levels which all must be considered in the analysis.

Another argument for excitonic junction behaviour comes from Choi *et al*[100]. They found two distinct regimes based on PbSe QD size in PbSe QD/ZnO QD solar cells. For QD diameters smaller than ~3.8 nm the V_{oc} was found to increase with decreasing PbSe QD diameter. For QD diameters larger than ~3.8 nm no significant photovoltaic effect was seen. The small diameter QDs were correlated to a type II heterojunction that provides a positive driving force for charge transfer from the PbSe to ZnO, and the large diameter QDs were correlated to a type I heterojunction where charge transfer at the interface is energetically unfavourable. Based on the size dependence of the photovoltaic behaviour, they concluded the most likely mechanism was not Fermi level alignment of a *p-n* junction. To test this further they fabricated cells with the PbSe and ZnO layer reversed (ITO/ZnO/PbSe/Al). In this configuration the PbSe is expected to make a Schottky contact with the Al electrode that opposes the PbSe/ZnO junction. In the dark, the device was expected to show forward rectification dominated by the PbSe/Al Schottky contact. However, under illumination the PbSe/ZnO should transfer electrons into the ZnO leading to a photo-induced chemical potential energy gradient that lowers or reverses the rectification. The tests resulted in forward rectification in the dark, no rectification at 100 $mWcm^{-2}$ illumination, and reverse rectification at 150 $mWcm^{-2}$ illumination. They conclude that only excitonic behaviour could account for this effect[100].

In considering the conclusions from Choi *et al*. the ZnO doping state needs to be considered. When fabricating functioning solar cells (not the inverted PbSe/ZnO

devices), Choi mentions the importance of UV photodoping the ZnO layer. However, there is no indication that the cells used to test the rectification reversal behaviour in the preceding paragraph were photodoped. As will be shown in sections 3.7.2.2 and 3.7.3.2, the ZnO doping level is important to the junction characteristics.

On the depleted *p-n* side of the argument, Pattantyus-Abraham *et al*. first show results of photovoltaic behaviour (J_{sc} ~ 10 mAcm^{-2}, V_{oc} ~ 0.38 V) for PbS QDS that have a negligible conduction band offset with the electron accepting material (TiO_2)[93]. The PbS QD size in this case was 5.5 nm (bandgap of 0.9 eV) producing a conduction band energy of 4.1 eV which is the same as the TiO_2 conduction band energy level. The built-in electric field of a depletion region created at the PbS/TiO_2 interface is concluded to be the mechanism that prevents electron back flow from the TiO_2 to PbS, creating the photovoltaic behaviour[93]. They also point out that this result is in opposition to conclusions from photoluminescence measurements that suggested only PbS QDs with bandgaps greater than 1 eV could transfer electrons to TiO_2[116]. Pattantyus-Abraham *et al*. also examine the charge transfer characteristics in the PbS CQD film[93]. Reports of excitonic behaviour have described the energy transport through the CQD film as bound electron-hole pairs that diffuse through Forster transfer to the charge separating heterojunction[114]. For PbS CQD with a bandgap of 1.3 eV, the Forster transfer time is estimated to be ~200 to 400 ns[117]. Coupled with an exciton radiative lifetime of 1 – 2 μs[117,118], efficient Forster transfer is expected only over a few dot-to-dot transfers[93]. However, devices with PbS thickness of 200 – 250 nm (requiring over ~50 Forster transfers) demonstrated high internal and external quantum efficiencies[93]. Since Forster transfer cannot account for the energy transfer, a depletion region that separates excitons is concluded as the junction operating mechanism.

In the work presented in this thesis, capacitance-voltage and external quantum efficiency measurements are used to investigate the operating mechanism at the PbS/ZnO interface. Capacitance-voltage measurements are presented in the supporting material of reference [94] as indication of fully depleted junctions in bulk heterojunction PbS/TiO_2 solar cells. However, the supporting information offers no explanation as to how that conclusion was drawn from the data. No depletion widths are calculated and no C^{-2} versus voltage curves are shown. The work presented here shows a much more complete study, concluding both excitonic and *p-n* mechanisms are possible depending on the ZnO doping density.

One final area of disagreement is differences in the energy levels reported for the PbS QDs. Figure 3.3a shows the reported values determined by cyclic voltammetry[116,119] and Figure 3.3b shows the values determined by Kelvin probe[101].

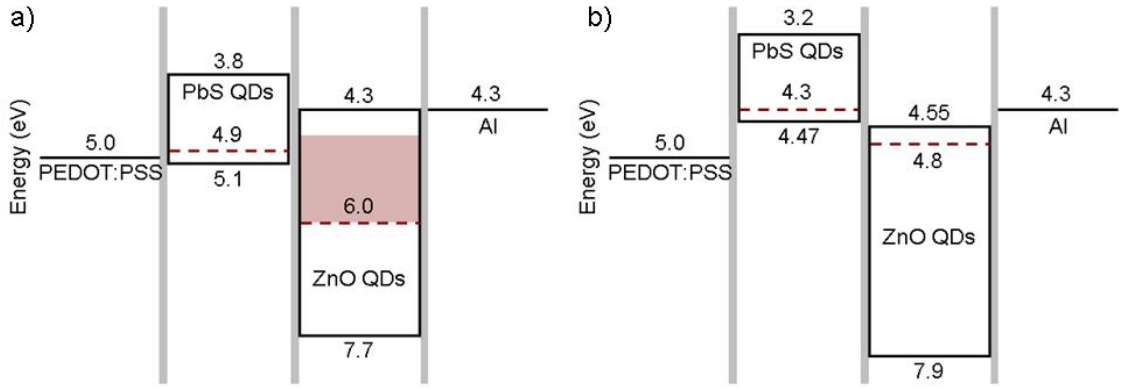

Figure 3.3. Energy level diagrams determined by cyclic voltammetry (a) and Kelvin probe (b). The energy levels are shown for isolated materials. The red dashed lines indicate the Fermi levels. The shaded area in the ZnO bandgap shown in (a) represents a range of possible ZnO Fermi levels based on the amount of doping.

The shaded area in the ZnO bandgap represents a range of possible Fermi levels based on photodoping that is discussed in sections 3.4 and 3.7.2.2. For this work, the energy diagram in Figure 3.3a is used. This was chosen since the energy level difference

between the PbS HOMO and ZnO LUMO in that case can support a sizeable photovoltage, whereas the difference in Figure 3.3b cannot.

3.7 CQD Solar Cell Results and Discussion

The experimental work on these cells began as an electrical characterisation encompassing current-voltage, impedance, and quantum efficiency measurements. Variations to the cell included different thicknesses of the PbS CQD layer, different UV photodoping levels, and cell temperatures ranging from 77 to 300 K. Many of the conclusions derived from the experimental work are based on the analysis of results from more than one type of characterisation or cell variation which makes compartmentalised results discussion difficult. Therefore in an effort to present the clearest picture and highlight focus areas, this section is organised by characterisation technique with a discussion of the results included in each technique section followed by further discussion with an emphasis on the analysis of results that are interrelated between techniques and cell variations in the conclusion section.

Before presenting the results, a description of the different cell variations is given including the labelling system that will be used for the rest of the section. Two different UV photodoping methods were performed. In the first method, photodoping was conducted on the fully fabricated cell in a purpose-built cell holder with a continuous flow of nitrogen flushed through the holder. The UV source was a xenon lamp in a quartz housing. The cell was illuminated with UV radiation while monitoring the increase in J_{sc}. When the J_{sc} saturated (no longer increased with continued UV illumination), the cell was considered fully doped. For this doping method, the UV radiation had to pass through the holder window, ITO coated glass substrate, PEDOT:PSS, and PbS layer before reaching the ZnO layer as shown in

Figure 3.4a. That path is expected to severely limit the amount of UV radiation reaching the ZnO layer. However with long enough photodoping, the J_{sc} was observed to increase and saturated after about 10 minutes of illumination. The cells photodoped by this method were also tested prior to any UV photodoping, which is given the label $Cell_{pre}$. After complete doping (J_{sc} saturated), the cells are labelled $Cell_{post}$. Hence the $Cell_{pre}$ and $Cell_{post}$ labels correspond to the same cells before (pre) and after (post) photodoping.

The second method, illustrated in Figure 3.4b, of photodoping was conducted inside a nitrogen environment glovebox with a mercury lamp prior to depositing the aluminium electrode. In this case the illumination was incident directly on the ZnO layer, but on the side opposite to the PbS/ZnO junction. Cells photodoped in this manner are labelled $Cell_{GB}$.

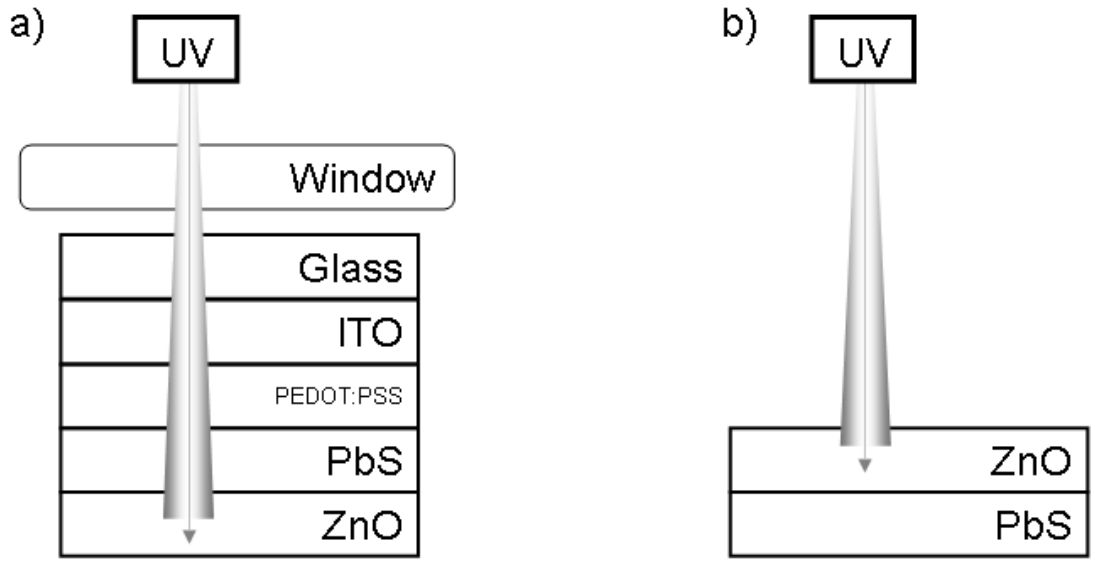

Figure 3.4. a) Post-dope method. UV radiation passes through the holder window, glass, ITO, PEDOT:PSS, and PbS before reaching the ZnO. b) Pre-dope method. UV radiation is incident directly on the ZnO. However, it is the side opposite the PbS/ZnO interface. Layer thicknesses are not to scale.

Besides the two doping methods, cells were fabricated with four different PbS CQD layer thicknesses (50, 125, 190, and 230 nm). The thickness is designated following the doping method. For example, the 50 nm-thick PbS layer cell tested before doping is labelled $Cell_{pre,50}$. For all cells the ZnO layer was kept at 100 nm.

3.7.1 *JV* Analysis

This section explores the *JV* characteristics of PbS/ZnO CQD heterojunction cells under various conditions. In section 3.7.1.1, *JV* results from the four different PbS layer thicknesses are presented and discussed for all three cell photodoping variations (pre, post, GB). The section ends with the temperature dependent *JV* results and discussion in section 3.7.1.2.

3.7.1.1 PbS-Layer Thickness Dependent *JV* Results

Figure 3.5 shows the four basic solar cell parameters for each batch of cells as functions of the PbS layer thickness. The uncertainties shown are one standard deviation of the measurements from three different pixel cells (see section 3.5) measured at each thickness.

The trends are similar between the batches for all thicknesses except 50 nm, in which case $Cell_{post,50}$ has a sharp increase in efficiency. This is due to an increase in J_{sc} and FF at 50 nm compared to a decrease in these two parameters in the other two batches at 50 nm. It is unclear at right now whether this is an effect of the device processing or the photodoping method.

A first look at the trends of the solar cell parameters in Figure 3.5 shows the power conversion efficiency, PCE, follows closely to the trend in the short circuit current,

J_{sc}. There are variations in open circuit voltage, V_{oc}, and fill factor, FF, but they are small and the effects on PCE are masked by the J_{sc} trends.

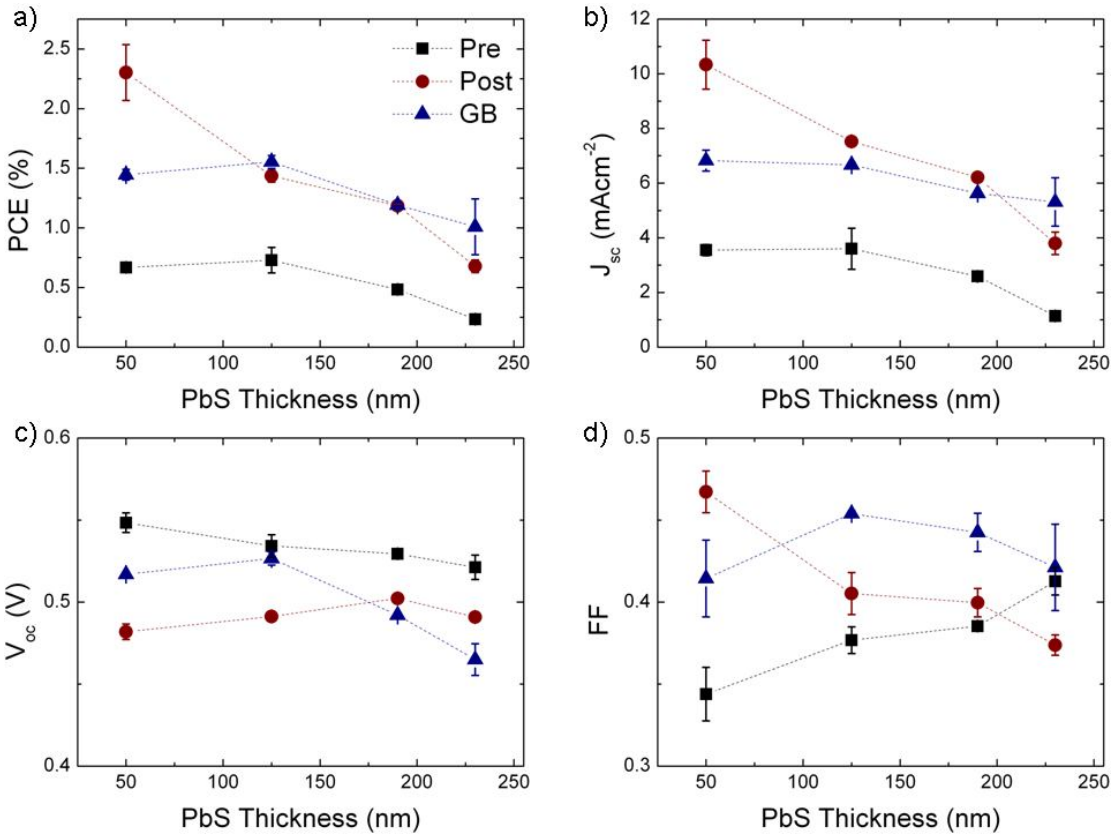

Figure 3.5. Solar cell parameters as a function of PbS layer thickness. a) PCE. b) J_{sc}. c) V_{oc}. d) FF.

The effect of UV photodoping is seen by comparing $\text{Cells}_{\text{pre}}$ and $\text{Cells}_{\text{post}}$. For all thicknesses, J_{sc} increases and V_{oc} decreases. The increase in J_{sc} is likely due to increased conductivity of the ZnO QDs with UV photodoping as discussed in section 3.4. The series resistance, R_s, shown in Figure 3.6c supports this idea as well.

Photodoping decreases R_s and the J_{sc} trend over PbS thickness matches well with that of R_s (lower R_s produces higher J_{sc}) for all three doping variations (pre-, post-, and GB-doped). The slight decrease in V_{oc} with photodoping has been reported and attributed to changes in the ZnO surface potential[104].

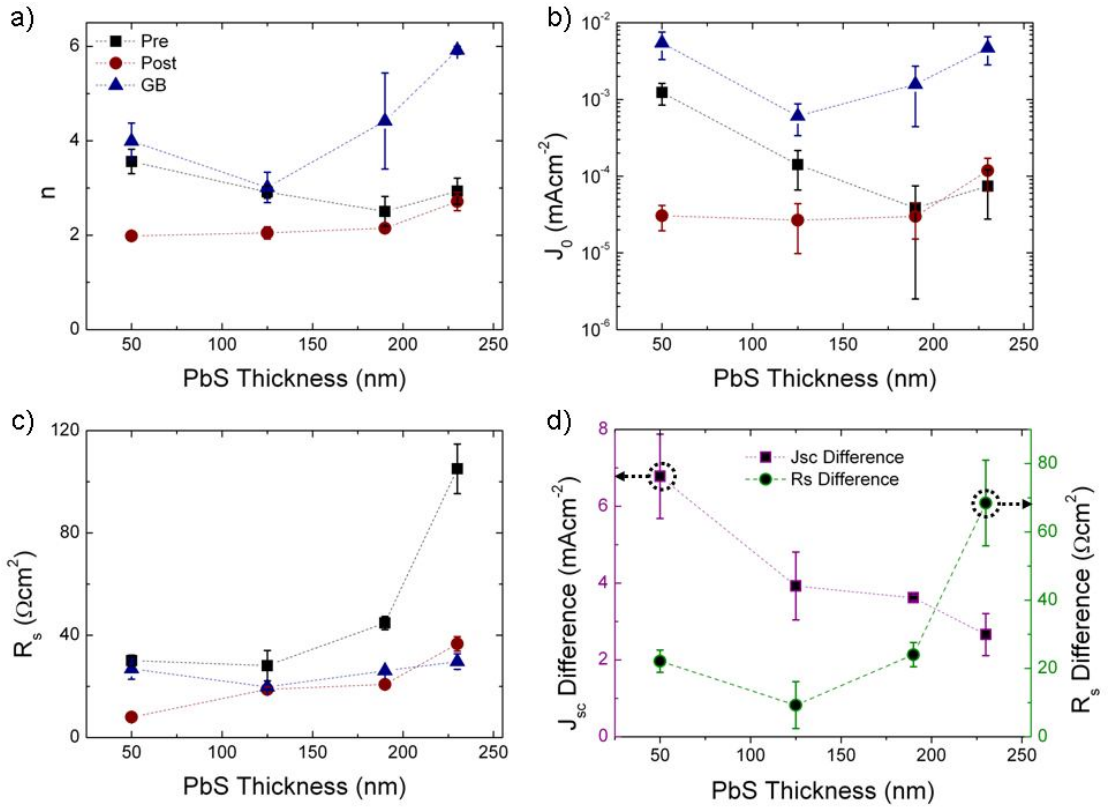

Figure 3.6. PbS layer thickness dependence of a) diode ideality factor, b) reverse saturation current, and c) series resistance. The ideality factor and series resistance differences between the pre- and post-doped cases are shown in (d).

The difference in J_{sc} between $\text{Cells}_{\text{pre}}$ and $\text{Cells}_{\text{post}}$ shown in Figure 3.6d is largest for the thinnest device and decreases with increasing PbS thickness. This suggests better ZnO doping is seen when the UV radiation passes through thinner PbS amounts. However as Figure 3.6d also shows, the difference in R_s behaves in the opposite manner with the largest difference seen for the thickest PbS layer cells. The apparent contradiction between the two is resolved by considering the effect of exciton separation in conjunction with the increase in ZnO conductivity. The J_{sc} depends not only on the material conductivity, but also on how many excitons are separated (followed by charge collection). For thick PbS layers, more excitons are created further from the PbS/ZnO junction, which reduces the number of excitons that are separated due to the increased distance they must travel to the junction. Hence, the J_{sc}

is also reduced. Therefore, even though the change in R_s is largest for the thickest PbS layer, the increase in J_{sc} is limited by the amount of excitons that are actually harvested.

The diode ideality factor, n, and reverse saturation current, J_0, shown in Figure 3.6a-b provide more insight into the PbS/ZnO interface. There is a drop in n after photodoping between $Cells_{pre}$ and $Cells_{post}$ and an increase in J_0 (except for the 230 nm PbS thickness). The changes in n and J_0 are more pronounced for the two thinner PbS layers and the uncertainty is large for the two thicker PbS layers, so the focus will be on the thinner two devices. Information about the type of recombination is gleaned from n. However, this is generally for values of n between 1 and 2. Therefore the conclusion here is that the recombination method after doping looks to be different and moves closer to the ideal diode case (for an ideal diode $n = 1$). The ideality factor for the $Cell_{GB}$ batch is higher at every thickness than the other two batches. However, since it was not possible to measure this batch before photodoping, the effect of doping on n and J_0 in these cells is not directly known.

A reduction in the recombination is seen by the drop in J_0 from the pre-doped to post-doped measurements (again, no pre-doped measurements were possible for the $Cell_{GB}$ batch). Since photodoping causes oxygen to be released from the ZnO surface[102,106,107], it is possible that adsorbed oxygen creates recombination pathways at the junction interface which are removed during photodoping. The effect on V_{oc} from photodoping also needs to be considered if this is the case. Lower recombination should raise the V_{oc}[10,14]. However, the change in surface potential could be great enough that any increases in V_{oc} are overshadowed by the decrease due to the surface potential change[104] producing the overall drop in V_{oc} after photodoping.

3.7.1.2 Temperature Dependent *JV* Results

Temperature dependent *JV* measurements were performed on $Cell_{post,125}$. Figure 3.7 displays the temperature dependent illuminated (a) and dark (b) *JV* curves. The most obvious feature is that the behaviour at 77 K is clearly delineated from the rest.

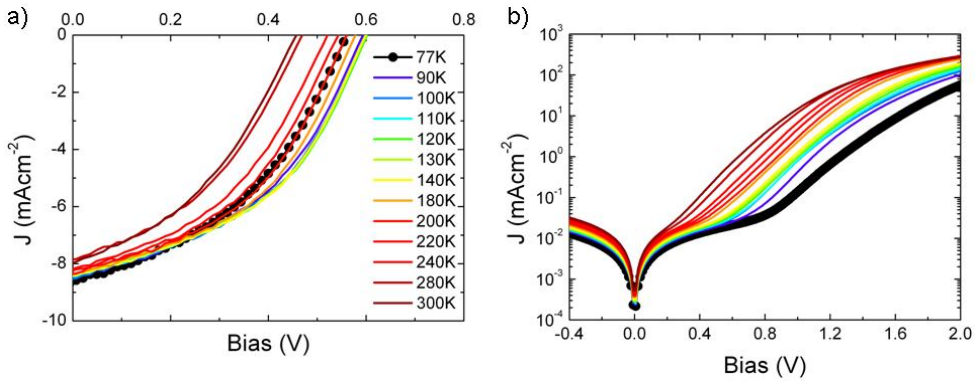

Figure 3.7. Temperature dependent *JV* curves. a) Under AM1.5 illumination. b) In the dark.

It is easier to spot trends in the data by looking at the parameters as a function of temperature as seen in Figure 3.8. Unlike the PbS-layer thickness experiment in section 3.7.1.1 where the efficiency followed closely to J_{sc}, for temperature changes the efficiency follows the V_{oc} trend. The J_{sc} does vary with temperature, but the variation is small and any effect it has on efficiency is masked by the V_{oc} temperature dependency. The variation in FF across the range of temperatures is also small as seen in Figure 3.8d, but it is close to the V_{oc} and PCE behaviour. The trend of more interest is that seen in the V_{oc}. A near linear increase is seen with temperatures decreasing from 300 K to ~160 K. With further temperature decrease, the V_{oc} saturates and begins to drop again. Trends similar to this have been reported in organic bulk heterojunction solar cells and have been attributed to charge injection barriers at the electrodes[120].

Rauh *et al*. report very similar V_{oc} temperature dependence to the results seen here (increasing V_{oc} with decreasing temperature until the V_{oc} levels off and then decreases with further temperature decrease) in organic bulk heterojunction solar cells[120]. They were able to match the trend using a model that incorporates different injection barrier heights at the anode and cathode contacts[120]. However, they show only qualitative results with matching trends and do not show fits of the model[121] applied directly to their data. In the cells studied here, injection barriers are a good explanation for the V_{oc} behaviour since there is more evidence for them based on the temperature dependent CV results in section 3.7.3.3.

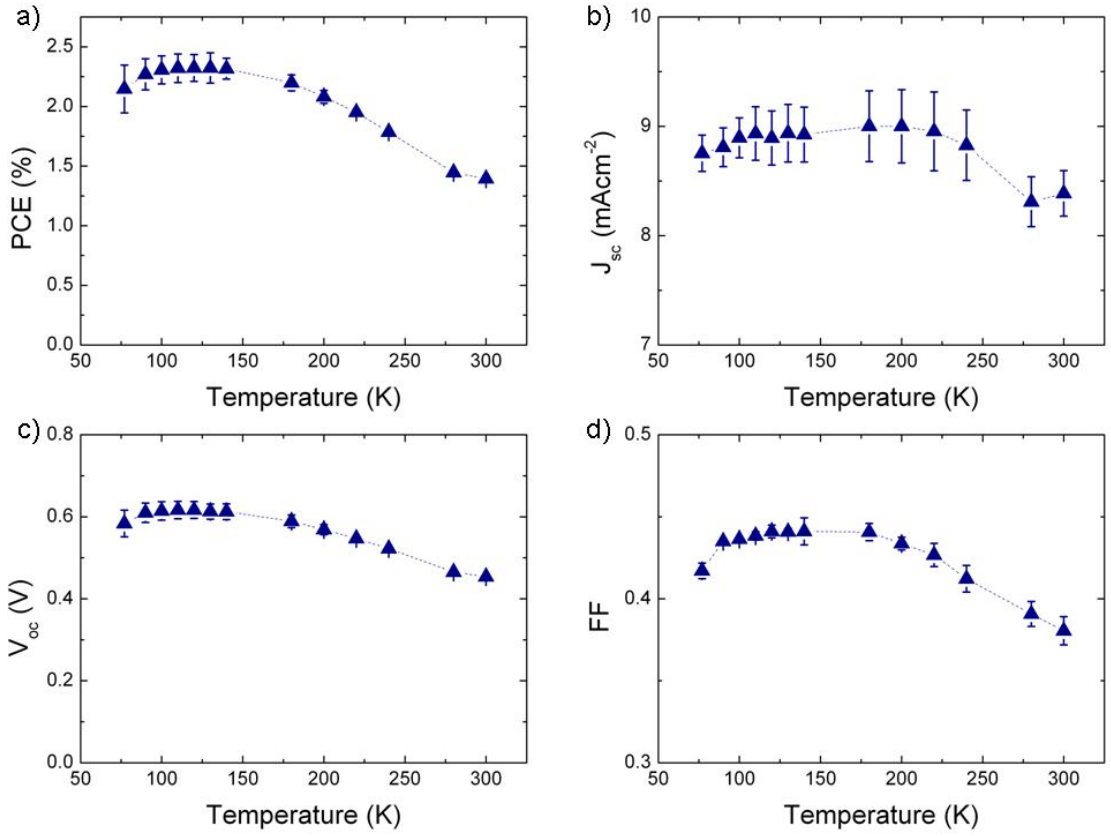

Figure 3.8. Temperature dependent solar cell parameters. a) PCE. b) J_{sc}. c) V_{oc}. d) FF.

The decrease in J_{sc} with increasing temperature from ~180 K is unexpected since at higher temperatures charge carriers have more thermal energy. However, similar trends of J_{sc} increasing with decreasing temperature to a maximum near 200 K have

been reported by Ju *et al*. in titanium oxide PbS CQD solar cells[122]. They attribute the increase in J_{sc} at temperatures down to 200 K to increased coupling between the quantum dots due to thermal contraction of the ligands. Near 200 K the ligands no longer contract and the J_{sc} then decreases with further temperature decrease[122]. Such a model fits with our results.

An idea of the amount of recombination can be seen from the reverse saturation current (Figure 3.9b) where higher J_0 corresponds to higher recombination. In this regard, J_0 is seen to decrease with decreasing temperature as V_{oc} increases. Larger recombination leads to a drop in V_{oc} and the two values correspond well down to about 140 K at which point J_0 continues to decrease but V_{oc} levels off. The deviation in trend between J_0 and V_{oc} at low temperatures suggests the injection barrier explanation provides a better reason for the observed V_{oc} behaviour. However, the outlying temperature of 77 K does correlate again between V_{oc} and J_0 with a sudden increase in J_0 and decrease in V_{oc}.

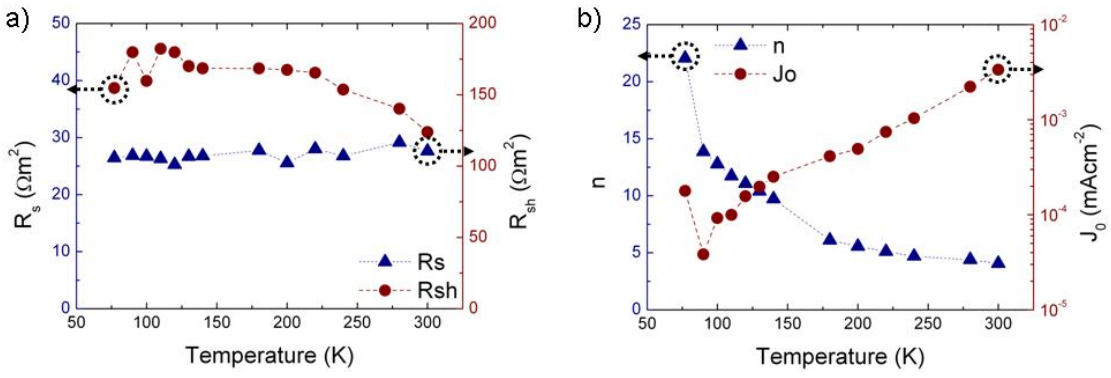

Figure 3.9. Temperature-dependent values. a) R_s and R_{sh}. c) n and J_0.

3.7.2 EQE Analysis

This section focuses on the external quantum efficiency, EQE, characteristics of the PbS/ZnO CQD heterojunction solar cell under various conditions. In section 3.7.2.1

the EQE is examined in cells having different thicknesses of the CQD PbS layer leading to a discussion on photon harvesting. Section 3.7.2.2 examines the EQE as a function of the amount of UV photodoping, and presents evidence for the type of junction at the PbS/ZnO interface. The last parameter dependency in the EQE analysis is temperature which is presented in section 3.7.2.3.

Absorption measurements of the different PbS thicknesses were attempted, but due to scattering the measurements were not valid. Therefore the PbS absorption is not included with the EQE results.

3.7.2.1 PbS-Layer Thickness Dependent EQE Results

This section begins with a general description of the different regions in the PbS layer in terms of charge absorption and extraction. It is approached from both the *p-n* junction and excitonic models with the purpose of aiding in the EQE results interpretation. Following this, the results are given with a discussion of the EQE features of interest.

In a general sense, it is possible for two regions to exist in the PbS layer. Photons are either absorbed in a region where the excited charge carriers have a good probability of being collected or they are absorbed in a region where there is little probability for charge collections. In the *p-n* model the region of high charge collection probability consists of two pieces. First is the depletion region (see section 1.4.4) which sweeps minority carriers across the junction, separating the electron-hole pair. Outside the depletion region, up to a distance given by the exciton diffusion length, is an area where excitons have a high probability of diffusing to the depletion region and dissociating. Beyond this region, excitons will most likely recombine before they are separated. For the discussion here, this is termed the dead zone. In the excitonic

model, excitons must diffuse to an interface to be separated. Therefore, the region of high charge collection probability in the excitonic model consists only of a region defined by the exciton diffusion length (no depletion region). Outside of this region is the dead zone. The different regions for the *p-n* model applied to the cells studied here are illustrated in Figure 3.10. For the excitonic model, the depletion region is absent and the photon harvesting region is controlled by the diffusion length.

Both the *p-n* and excitonic junction models were given in the previous paragraph. Section 3.7.2.2 will offer evidence of a transition from a purely excitonic junction before photodoping to a *p-n* junction during and after photodoping. The width of the depletion region extending into each material (PbS and ZnO) under the *p-n* model depends on the doping density of the ZnO layer which is again presented in section 3.7.2.2. However for the discussion right now, it is enough to say that the depletion region should lie almost entirely in the PbS layer when the ZnO layer has been fully photodoped.

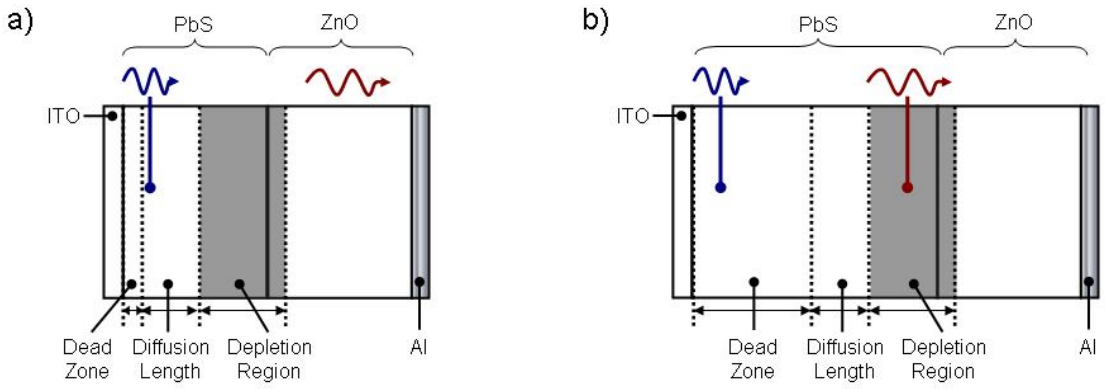

Figure 3.10. Charge harvesting regions and photon absorption for a) thin PbS layer and b) thick PbS layer. a) Thin PbS layer - short wavelength photons are absorbed in a collection region but long wavelength photons pass through before being absorbed. b) Thick PbS layer – short wavelength photons are absorbed in the dead zone and are not collected but long wavelength photons are absorbed in a collection region. For an excitonic junction there is no depletion region. The charge collection region is determined by the diffusion length.

There is also an assumption that has been made concerning the two general regions (charge carriers harvested versus recombination). This is that excitons are not dissociated at the PEDOT:PSS/PbS interface. If excitons are dissociated at the PEDOT:PSS/PbS interface, the dead zone would transition back to a charge collection region near this interface. This is discussed in more detail later in this section.

Photon absorption also needs to be considered in conjunction with the two PbS regions. High energy photons have shorter absorption lengths than lower energy photons[10,101,123]. This means short wavelength photons are absorbed near the front (PEDOT) surface of the PbS layer while long wavelength propagate further into the material before being absorbed. For a thin device, short wavelength photons create excitons in the extraction region (either the depletion region under the *p-n* model or within an exciton diffusion length of the junction for the excitonic model) while longer wavelength photons propagate further and possibly through the PbS without being absorbed (shown in Figure 3.10). In conjunction with the wavelength dependent absorption length, the minority carrier diffusion length is also wavelength dependent with higher energy photons creating higher energy carriers that have a longer diffusion length. The ZnO layer is not expected to contribute to photon harvesting due to its large bandgap (3.4 eV[99,104]) which means only high energy photons can be absorbed in the ZnO layer. However, the high energy photons are expected to be absorbed near the front of the PbS layer and therefore don't reach the ZnO layer. Hence there is a peak in the EQE spectrum: photons of lower energy than the peak are not absorbed, and photons of higher energy than the peak are absorbed too far from the interface for their charges to be extracted. As the PbS layer is made thicker, the longer wavelength photons have a better chance of being absorbed, but absorption of short wavelength photons moves into the dead zone (Figure 3.10). This means fewer

excitons from high energy photons are extracted. The expected peak in the EQE spectrum then shifts to longer wavelengths as the PbS layer is made thicker. Figure 3.11 shows the EQE results for two batches of four different PbS layer thicknesses (50, 125, 190, and 230 nm) and the shifting peak (labelled 1) is clearly visible. This effect has been reported in PbS Schottky cells of variable thicknesses with the conclusion that absorption in the dead zone accounts for the drop in quantum efficiency at the short wavelengths[112].

There are also a few other features of interest in the EQE spectra. The peak at 920 nm (labelled 2) is the easiest to explain and reflects the bandgap of the PbS QDs, associated with the peak in the absorptivity of the PbS at this wavelength. 920 nm corresponds to a bandgap of 1.35 eV giving further evidence of the size of the PbS QDs and the increased bandgap compared to bulk PbS due to quantum confinement. As expected, this peak is visible in all of the cells.

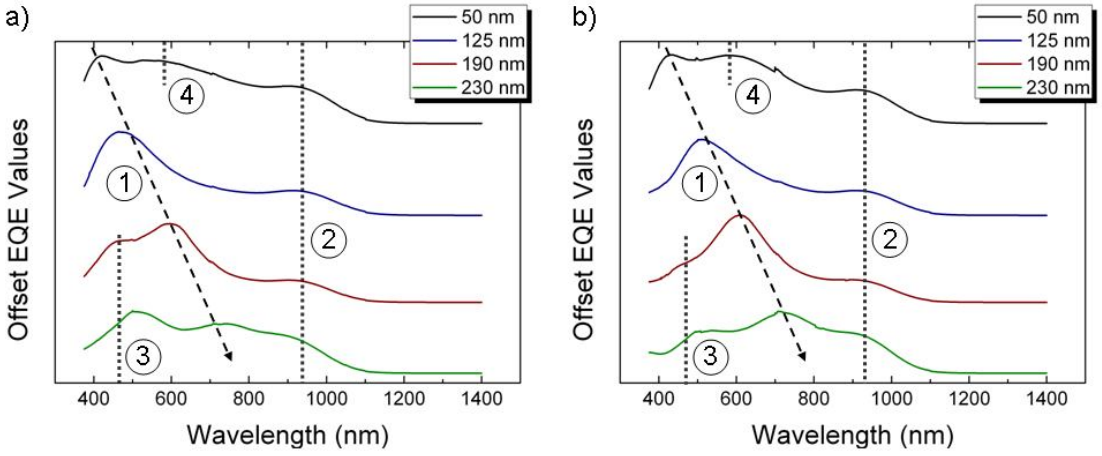

Figure 3.11. External quantum efficiency for four PbS thickness values. Two different batches are shown. Batch 1 is shown in (a) and batch 2 in (b). The four indicated features are discussed in the text.

Next is a peak near 470 nm and 500 nm that is visible in the two thickest cells (labelled 3). This peak is also possibly in the two thinnest cells, but is overshadowed

by the larger main peak. A couple of explanations are possible for this peak. First, Fermi level alignment between PbS and PEDOT creates an Ohmic extraction path for holes from PbS into PEDOT and a barrier to electrons in this direction. Excitons created near the PEDOT/PbS interface by high energy photons could dissociate at this interface by hole extraction into the PEDOT layer followed by minority carrier diffusion of the electron through the PbS layer to the ZnO layer. However, there is a high probability of the electron recombining with a hole majority carrier in this case. Another possibility is due to the longer diffusion length of higher energy excitons that result from the absorption of high energy photons. This extra diffusion length must then be considered with the increased absorption length of longer wavelengths which create lower energy excitons closer to the depletion region. Here the *p-n* model has been used for fully doped cells. The validity of this will be discussed in section 3.7.2.2. The interplay between these two factors could produce the dip that is observed between the short wavelength peak and the main peak in the two thickest cells.

Another interesting feature of the short wavelength peak is the relative magnitude compared to the main peak of the two thickest cells. In the first batch the short wavelength peak has a much larger relative magnitude compared to the main peak than in the second batch, and is actually larger than the main peak for the thickest cell. This suggests different doping levels for the ZnO layer which is discussed in the following section (3.7.2.2) on doping dependent EQE measurements. Photodoping increases the conductivity of the ZnO as discussed in 3.4, but as will be shown in section 3.7.2.2, it also affects the depletion region.

Finally, there is a peak near 580 nm in the 50 nm thick PbS layer cells (labelled 4). This is possibly due to reflection of long wavelength photons from the aluminium contact back into the PbS layer followed by absorption. However, this needs further investigation.

3.7.2.2 UV Photodoping Dependent EQE Results

EQE measurements were taken at incremental times during UV photodoping from no doping until fully doped using the post-fabricated doping method. This was done on a 190 nm-thick-PbS-layer cell. The results are shown in Figure 3.12.

Under the *p*-*n* model, a depletion region should form at the PbS/ZnO junction. As mentioned in section 3.4, UV photodoping transitions the ZnO from an intrinsic semiconductor (or nearly intrinsic) to an *n*-type semiconductor[104]. Since the ZnO nanocrystals were all synthesised in air, they are expected to be very nearly intrinsic due to oxygen adsorption. This means the depletion region transitions from being located mainly in the ZnO layer when the ZnO doping density is much lower than the PbS doping density to being located mainly in the PbS when the ZnO doping density is much higher than the PbS doping density[10]. Using the discrete boundary approximation, the depletion region extending into the PbS layer is given by equation (1.2). The depletion region in the PbS layer is of interest since, as mentioned in section 3.7.2.1, the ZnO layer is not expected to contribute much to photon absorption. Assuming a fully photodoped cell with a ZnO doping density of 10^{19} cm^{-3} and a built-in bias of 0.1 V (V_{bi} was chosen based on the difference in Fermi level values between materials from literature[101,93]), the depletion region within the PbS layer varies from 50 nm to 120 nm for PbS doping densities of 6 to 1 x 10^{16} cm^{-3} respectively (70 nm for 3 x 10^{16} cm^{-3}). If V_{bi} is 0.2 V, the depletion region goes up to

170 nm in the PbS layer for a PbS doping density of 10^{16} cm^{-3}. For ZnO doping densities on the order of 10^{14} cm^{-3}, the depletion region in the PbS layer becomes negligible. It is conceivable then that a depletion region within the PbS layer grows from nothing to about 70 nm (or even larger) as the cell is UV photodoped. The EQE spectrum would then be expected to show a peak at longer wavelengths that widens, extending back to shorter wavelengths as the depletion region grows. The entire peak position doesn't shift though since the PbS layer thickness doesn't change and the longer wavelength photons are still absorbed.

The doping dependent EQE spectrum shown in Figure 3.12 has two peaks that match well with the two peaks of the 190 nm thick PbS cell in Figure 3.11. Before any photodoping and at low doping times, only the peak near 600 nm is evident. With increased photodoping, the shorter wavelength EQE is seen to increase (EQE peak widening back to shorter wavelengths) and eventually the peak near 450 nm becomes clear. This gives evidence of a depletion region growing in the PbS layer which aids in the extraction of carriers generated by short wavelength photons further from the PbS/ZnO interface.

Initially, with basically no depletion region in the PbS layer (intrinsic ZnO), only charge carriers generated within a diffusion length of the PbS/ZnO interface have a good probability of being harvested. The junction behaviour is then initially excitonic. After the ZnO is photodoped such that the doping density is near or greater than that of the PbS, a significant portion of the depletion region lies within the PbS layer which increases the charge extraction region within the PbS layer (*p*-*n* operation).

Therefore the results suggest an initial excitonic junction behaviour before photodoping that transitions to a *p*-*n* junction mechanism as the ZnO layer becomes

doped. Capacitance measurements in section 3.7.3 also provide evidence of a depletion region for fully doped cells. The conclusions in section 3.8 provide more discussion on the topic taking into account these results and the capacitance results.

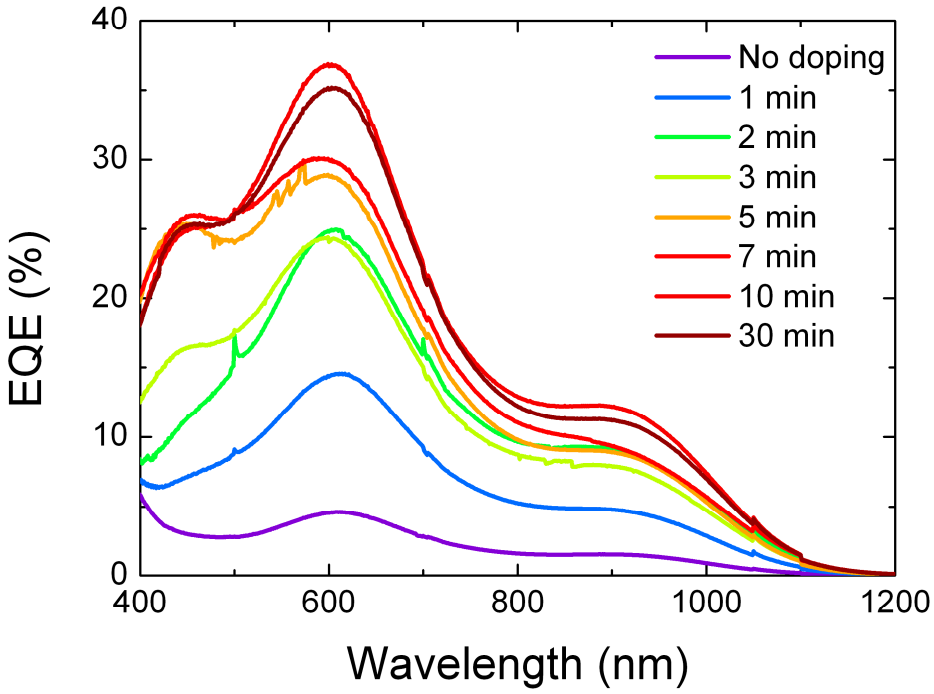

Figure 3.12. External quantum efficiency spectra as a function of UV photodoping. Initially, only the peak near 600 nm is evident. After sufficient doping, the peak near 450 nm becomes visible.

Finally, as mentioned in section 3.7.2.1, the relative magnitude of the two peaks varies with photodoping. Near 7 minutes of doping the 450 nm peak is close in magnitude to the 600 nm peak. After another 3 minutes of doping the 600 nm peak increased in magnitude while the 450 nm peak stayed the same. The reason for the extra increase in the 600 nm peak without an increase in the 450 nm peak requires further investigation.

3.7.2.3 Temperature Dependent EQE Results

Temperature dependent EQE measurements down to 77 K were also taken. Figure 3.13 shows that the peak location is constant for each peak indicating a constant bandgap in the material. This is another indicator of the quantum confinement controlling the PbS bandgap. The peak at ~500 nm and the excitonic EQE peak are both seen to have a maximum value near 200 K. This temperature matches well with the peak in J_{sc} as a function temperature in section 3.7.1.2 and the explanation offered there can account for the EQE behaviour as well: increased coupling between the QDs results from ligand contraction as the temperature is decreased. Near 200 K the ligands stop contracting[122].

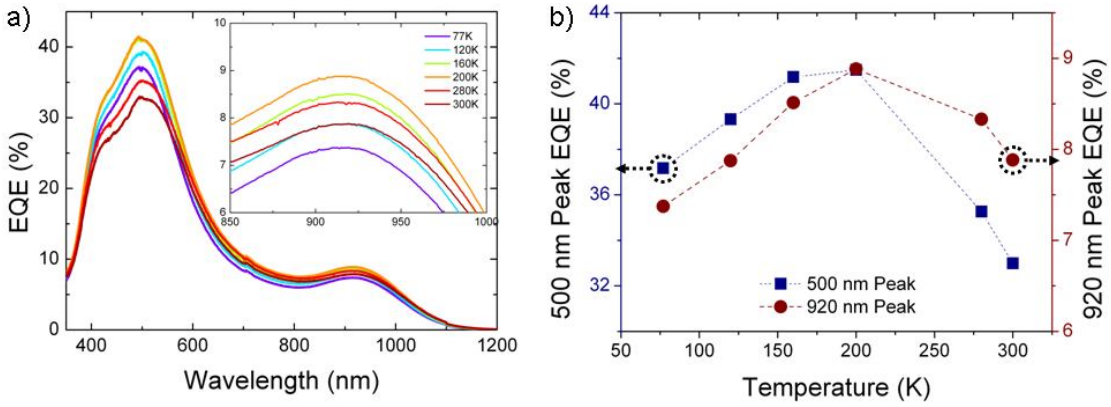

Figure 3.13. a) Temperature dependent EQE spectra. b) Peak temperature dependence comparison of the peaks located at 500 and 920 nm.

In section 2.3.2 it was stated that for the cells in this chapter an overall correction factor was applied to the EQE spectrum to match the integration of the EQE and solar spectrum to the measured J_{sc}, since not all of the monochromatic light could be focused onto the small cell. For the data presented in Figure 3.13 the correction factor was not applied. If the correction factor were to be applied to these specific measurements, any trend with temperature would be based on the temperature

dependent *JV* measurements. Therefore the absolute values in Figure 3.13a are not exactly correct, but the relative values and peak trends in Figure 3.13a-b are correct. During the temperature dependent EQE measurements, the position of the cell never moved. Therefore the number of incident photons is the same for each measured temperature.

3.7.3 Impedance Analysis

This section analyzes the impedance response of the PbS/ZnO CQD heterojunction under various conditions. First though, capacitance versus voltage, CV, measurements were performed on a PbS Schottky cell and a Mott-Schottky analysis was performed on the results in order to determine the PbS doping density. This is presented in section 3.7.3.1. Fabricating Schottky devices with ZnO is quite challenging, so literature values of $10^{18} - 10^{19}$ cm^{-3} were used when needed[104]. The results from the remaining sections are from tests performed on full devices instead of the PbS Schottky device. Section 3.7.3.2 examines the CV results from cells of all three doping variations (pre, post, GB) and the four PbS CQD layer thicknesses. Temperature dependent CV results are shown and discussed in section 3.7.3.3.

3.7.3.1 PbS Schottky Cell Analysis

CV measurements were used to determine the PbS CQD doping density by performing Mott-Schottky analysis on PbS CQD Schottky cells. Figure 3.14a shows a representative C^{-2} versus bias result for the ITO/PEDOT:PSS/PbS/Al device architecture. The linear fits from multiple devices resulted in a built-in voltage, V_{bi}, of 0.2 ± 0.01 V and a doping concentration, N_A, of $4 \pm 2 \times 10^{16}$ cm^{-3}. A relative permittivity of 18 was used for the PbS QDs based on values from literature[50,112] The V_{bi} and N_A results are in good agreement with reported values for PbS Schottky cells

with an aluminium electrode[50]. The results shown here are for a modulating frequency of 100 Hz and amplitude of 25 mV.

Modulating frequencies up to 5 kHz were also tested and the results were found to be very frequency dependent as seen in Figure 3.14b. This is not unexpected since a contribution of the measured capacitance comes from charging and discharging defect states within the bandgap of the material[55]. As the frequency is increased not all of the defect states are able to respond to the perturbation signal and hence no longer contribute to the junction capacitance. Therefore, low frequency measurement provides a better description of the junction which includes all the defect states.

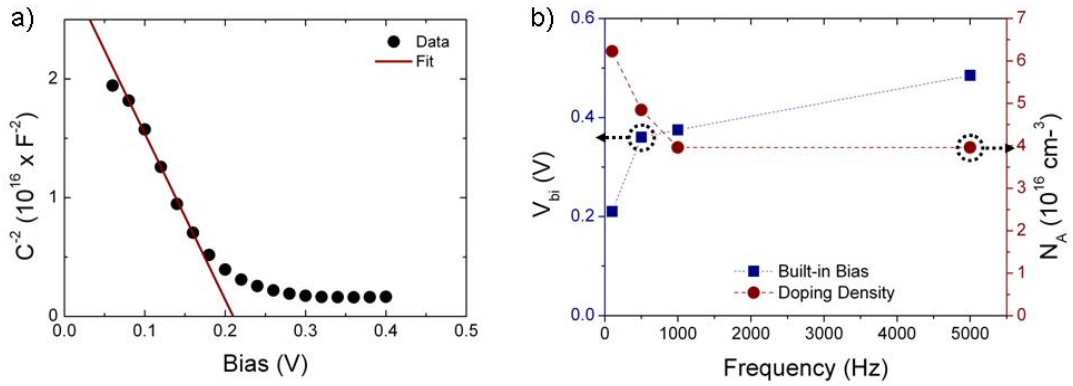

Figure 3.14. a) Mott-Schottky fit to the linear portion of the C^{-2} vs. bias curve of a PbS Schottky cell (modulation frequency of 100 Hz and amplitude of 25 mV). b) Frequency dependence of the fit parameters, V_{bi} (built-in bias) and N_A (doping density).

3.7.3.2 PbS-Layer Thickness Dependent Capacitance Results

The CV measurements on the heterojunction cells of different PbS thicknesses do not all show the simple shape associated with the depletion capacitance of a *p-n* junction described by equation (2.17).

For Schottky or *p-n* junction solar cells that have a bias-dependent depletion region, the capacitance is proportional to $1/(V_{bi} - V)^{1/2}$ where V_{bi} is the built in bias and V is the applied bias. The behaviour is easier to see by plotting C^{-2} versus the applied bias,

which produces a linear region with a slope proportional to the doping density and *x*-axis crossing equal to the built in bias. The $Cell_{post}$ batch (Figure 3.15) exhibits the best evidence of a bias-dependent depletion capacitance. The regions following this behaviour are indicated in Figure 3.15a for the CV curves and Figure 3.15b for the C^{-2} curves. The two thinnest devices show the strongest evidence.

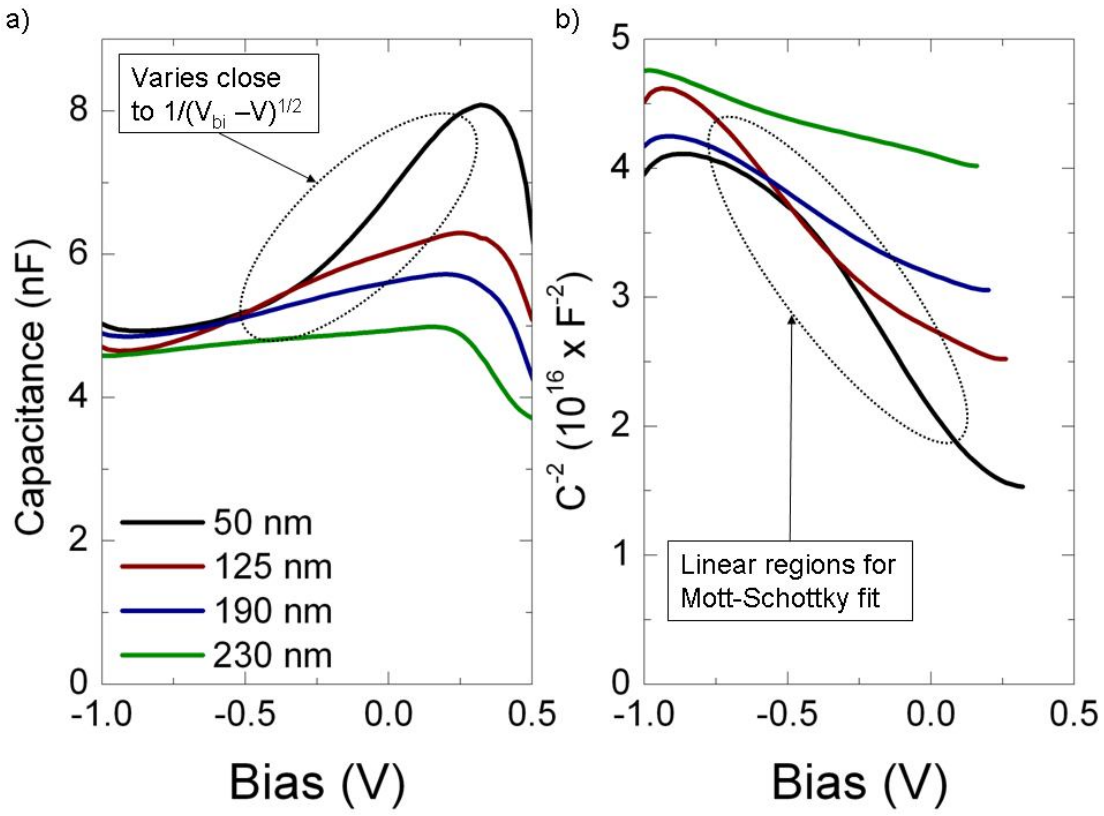

Figure 3.15. a) CV plots for the $Cell_{post}$ batch. The depletion capacitance should vary proportional to $1/(V_{bi} – V)^{1/2}$. b) The corresponding C^{-2} versus bias curves. The highlighted linear regions indicate the depletion capacitance.

Before UV photodoping ($Cell_{pre}$ batch) there is very little evidence of a depletion capacitance. Figure 3.16 shows the CV (a) and C^{-2} (b) curves for the $Cell_{pre}$ batch, with the post photodoped results (orange dashed lines) given for comparison. The capacitance remains fairly constant across the range of applied biases for the $Cell_{pre}$ batch, showing no depletion capacitance. In the $Cell_{post}$ batch there is a clear trend with PbS thickness such that the thicker cells show less evidence of a depletion

region. With a 230 nm thick PbS layer there is not much difference before and after photodoping in the capacitance curves.

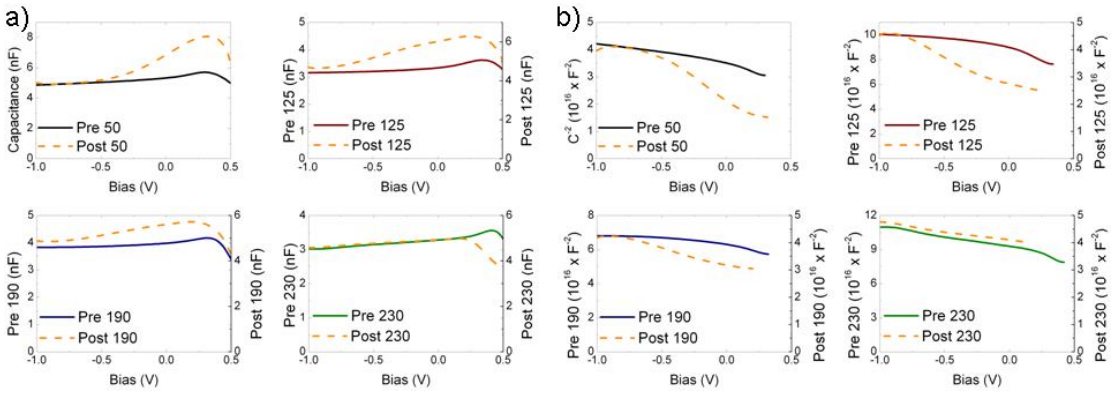

Figure 3.16. a) CV curves for Cell$_{pre}$ batch. b) The corresponding C^{-2} curves. In all the plots the dashed orange line corresponds to the cell after UV photodoping.

Figure 3.17 shows the capacitance results for the Cell$_{GB}$ batch. As with the other photodoped cells (Cell$_{post}$ batch), evidence of the depletion capacitance is seen by the linear regions in the C^{-2} versus bias curves (Figure 3.17b). The next step is to fit equation (2.17) to the linear regions in the C^{-2} curves to determine the V_{bi} and N_A. The fits however produce V_{bi} values (x-axis crossing) that are too large to attribute to any interface. This can be explained when other sources of capacitance are included in the cell that obscure the depletion capacitance. The temperature dependent behaviour in section 3.7.1.2 provided evidence of injection barriers at the electrodes (more evidence will be presented based on the temperature dependent capacitance results in section 3.7.3.3). A model that includes the effects of a constant capacitance due to injection barriers can explain why the Mott-Schottky fits produce V_{bi} values that are larger than the actual value.

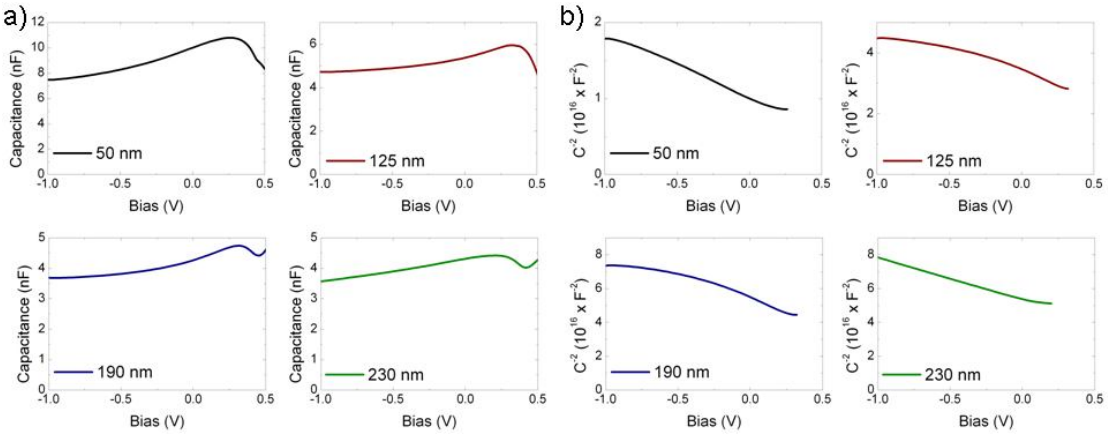

Figure 3.17. CV (a) and C^{-2} (b) curves for the $Cell_{GB}$ batch.

With injection barriers present, the overall capacitance is due to a combination of different capacitances. As an example, in Figure 3.18a, two capacitances are shown for the PbS/ZnO solar cell. C_1 corresponds to the bias-dependent depletion capacitance and C_2 corresponds to a constant capacitance that arises from injection barriers. The equivalent circuit of the depletion capacitance and constant capacitance is two capacitors in parallel[124] and is also shown in Figure 3.18a. The reference CV curve in Figure 3.18b is from a gallium arsenide *p-i-n* solar cell that is investigated in chapter 4. It was chosen for the simulation here because it has a very clear and well-behaved depletion capacitance. The other CV curves correspond to different values of constant capacitance added in parallel to the reference capacitance to create a simulated overall capacitance from C_1 and C_2. Values of constant capacitance between 1 and 7 nF were chosen for the simulation since these values are on the same order of the geometric capacitance of the cell structure. Figure 3.18c shows the resulting C^{-2} versus bias curves.

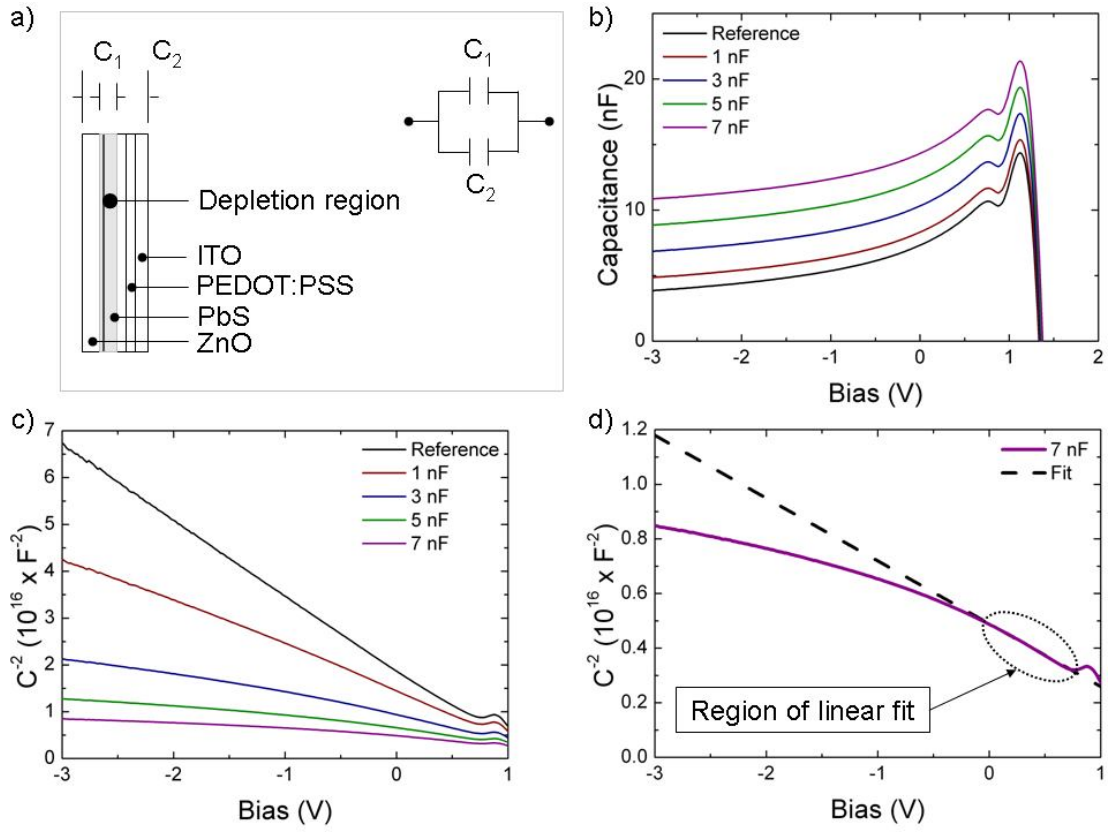

Figure 3.18. a) PbS/ZnO solar cell with the origin of depletion capacitance, C_1, and a constant capacitance, C_2, due to injection barriers. The equivalent circuit is two capacitors in parallel. b) CV curves for the reference data and different values of constant capacitance in parallel. c) C^{-2} versus bias curves for the reference data and different values of constant capacitance in parallel. d) Expanded view of the reference capacitance with 7 nF constant capacitance in parallel. Not only does the slope and x-axis crossing change, but the shape of the curve is distorted as well.

For larger values of the injection barrier capacitance, the C^{-2} curve is seen to deviate more from the reference curve. Mott-Schottky fits then produce larger V_{bi} (*x*-axis crossing) and N_A (inversely proportional to the slope) values than the reference data. The linear region of the C^{-2} slope itself also becomes distorted as is illustrated in Figure 3.18d for the case of a constant 7 nF capacitance added in parallel to the reference capacitance. Linear regions still exist however that can be fit with the Mott-Schottky equation (equation (2.17)). The fitting results though produce built-in bias and doping density values higher than the true value for the *p-i-n* junction. For the simulation here with a constant 7 nF capacitance due to injection barriers, the fit gives

V_{bi} = 2.1 V compared to the true value (no constant capacitance) of 1.1 V. Likewise, the fit gives N_A = 7.6 x 10^{16} cm^{-3} compared to the true value of 1.1 x 10^{16} cm^{-3}. Coupled with the evidence of injection barriers from the temperature dependent *JV* and CV measurements, this simulation provides a good explanation of how to interpret the CV results in Figure 3.15 - Figure 3.17.

An example of this model applied to the measured capacitances in this chapter is shown in Figure 3.19 for $Cell_{post,50}$.

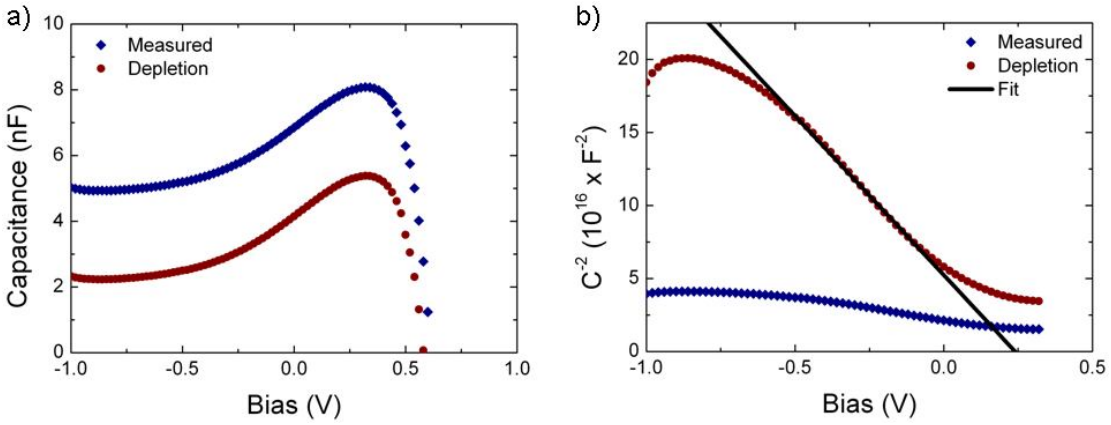

Figure 3.19. a) Measured capacitance from $Cell_{post,50}$ (blue diamonds). The depletion capacitance (red circles) was calculated based on the parallel capacitors equivalent circuit shown in Figure 3.18a with a constant capacitance of 2.7 nF. b) The corresponding C^{-2} curves with a Mott-Schottky fit to the depletion capacitance. V_{bi} = 0.24 V, N_A = 4 x 10^{16} cm^{-3}.

The difference in Fermi levels for the two materials is not exactly known since it depends on the ZnO doping level. However, assuming the ZnO is fully doped, the Fermi level difference should be near 0.2 V (see Figure 3.3a). The PbS doping level was found to be ~4 x 10^{16} cm^{-3} by taking CV measurements and fitting the C^{-2} curve with the Mott-Schottky equation (section 3.7.3.1). Using a value of 2.7 nF for the injection barrier constant capacitance then gives a good fit of the adjusted depletion capacitance with fit parameters of V_{bi} = 0.24 V and N_A = 4 x 10^{16} cm^{-3} (Figure 3.19b). Even though the actual values of V_{bi} and N_A are hard to extract, this does provide

qualitative evidence of a bias-dependent depletion width in the case of UV doped samples.

The change in the capacitance response between $Cell_{pre,50}$ and $Cell_{post,50}$ is the most dramatic of any thickness. This corresponds well to the largest increase in J_{sc} coming from the difference between $Cell_{pre,50}$ and $Cell_{post,50}$ in section 3.7.1.1. It is still hard to determine whether the improved J_{sc} results from a better depletion region aiding exciton separation or from better ZnO conductivity. Initially it appears the greatest determining factor comes from the improved ZnO conductivity since there is a good probability of excitons diffusing to the PbS/ZnO interface even without a large depletion region since the PbS layer is thin in $Cell_{pre,50}$.

3.7.3.3 Temperature Dependent Capacitance Results

As discussed in section 3.7.3.2, the CV measurements in some cases give linear regions in the C^{-2} versus bias curve that can be fit with the Mott-Schottky equation, but the resulting built-in bias seems to be too high to attribute to any of the junctions. Temperature dependent CV measurements down to 77 K were performed in an effort to find out more about the cell.

To start with, Figure 3.20a shows the capacitance as a function of bias for temperatures in the range of 77 – 300 K for a 125 nm PbS layer thickness cell photodoped using the post-fabricated method. This figure shows the results using a modulating frequency of 500 Hz and amplitude of 25 mV. The results are frequency dependent as discussed in section 3.7.3.1. The 500 Hz results are shown instead of 100 Hz because the measurements at 100 Hz were somewhat noisy. There are two items of initial interest. First, for the lower temperatures there is a sudden rise in capacitance (labelled V1), and second, for all temperatures there is a peak in

capacitance followed by rapid decrease (labelled V2). The bias location is somewhat difficult to see in Figure 3.20a, so in Figure 3.20b the capacitance values have been adjusted so that the capacitance for each temperature is equal at 0 V applied bias. Now it is easier to see a couple of trends. The sudden increase in capacitance at V1 stays stationary with changing temperature (77 K behaves a little differently at higher frequencies which needs further study), while the sharp drop in capacitance at V2 decreases in bias with increasing temperature. Near 130 K and above, it actually occurs before the rise in temperature such that the rise is not seen.

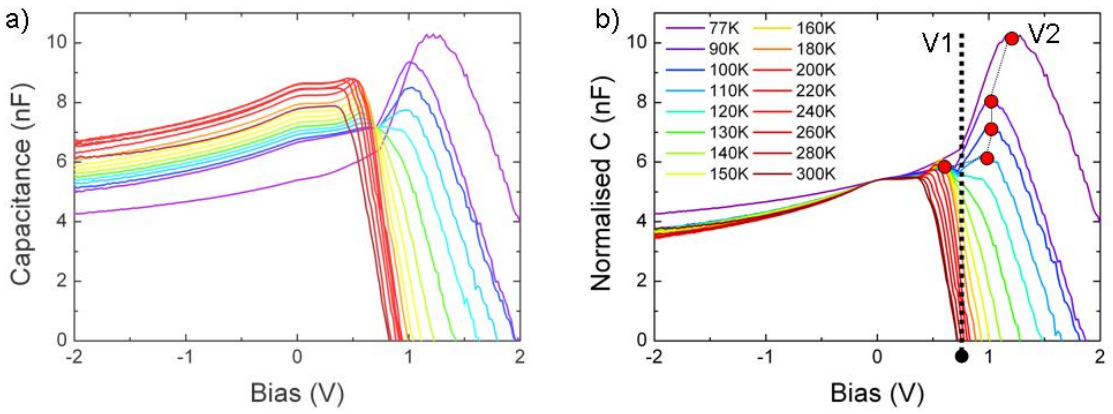

Figure 3.20. a) Temperature-dependent CV results for a 125 nm thick PbS layer cell. b) The data from (a) adjusted to coincide at 0 V bias. V1 is the onset of the excessive capacitance peak. V2 marks the peak in capacitance. The selected temperatures in the legend illustrate the direction of increasing temperature.

The excessive capacitance peak at forward bias has been reported in polymer light emitting diodes (PLEDs) of ITO/PEDOT:PSS/MEH-PPV/Metal (Ca, Al, Au) [125]. They argue that the increase in capacitance at V1 is due to majority charge carrier injection from the anode which causes an increase of charge in the polymer, and the drop in capacitance at V2 is due to minority carrier injection at the cathode which leads to recombination of electrons and holes causing a significant drop in charge carriers within the diode[125]. Rapid capacitance increases at forward biases above a

"turn on" bias have also been reported in silicon *p-n* junction solar cells. The increase in this case is due to minority carrier injection as the *p-n* junction reaches flat-band conditions resulting in a large increase in charge carriers within the material[58]. Since the diffusion length is much longer in silicon, recombination isn't as dominant as in the PLED, which explains why the capacitance doesn't drop rapidly when minority carriers cross the *p-n* junction. In both of these devices (polymer LED and silicon *p-n* solar cell), the increase in capacitance is attributed to an excess of charge carriers within the device.

Excessive capacitance peaks beyond the space-charge capacitance (similar to those observed here) have also been observed in Schottky diodes for many decades and have been shown to be due to minority carriers[63,124]. In this case, both the minority charge injection and extraction at the back contact are reported to have an effect on the capacitance peak. For a perfectly Ohmic back contact, the minority current has an inductive effect on the total capacitance resulting in a reduced or even negative capacitance since the minority current through the bulk is controlled by diffusion and flows out of phase with the applied voltage[124]. If the back contact is imperfect (resistance to minority carrier extraction), then the excessive capacitance peak is present. The excessive capacitance was concluded to be the result of excessive diffusion capacitance combined with increased conductivity modulation of the minority carriers within the bulk when there is a minority carrier extraction barrier[124]. Other work has viewed this in terms of injection barriers. For high injection barriers, the capacitance is found to first produce an increased capacitance peak before becoming inductive[63]. Again, the increase in capacitance is attributed to the presence of minority carriers, with the peak and subsequent drop in capacitance due to a limitation on the minority carrier injection rate. Recent results in P3HT:PCBM solar

cells have shown the same capacitance peak which was also attributed to minority carriers, and the drop after the peak was due to a limitation of the minority carrier concentration in the neutral region of the device[62].

The temperature dependent V_{oc} behaviour in section 3.7.1.2 suggested the presence of injection barriers, which compliments the idea that injection barriers are responsible for the temperature-dependent CV peak. The task is now to work out the details. Figure 3.20b shows two different regimes based on temperature. Above ~130 K the rise in capacitance at V1 is not seen and the capacitance peak is located at the same bias as the diode turn on voltage which increases with decreasing temperature from ~0.4 to ~0.6 V (see Figure 3.21a-b for correlation with the diode turn on voltage). In this regime the peak corresponds to electron transfer from the ZnO to the PbS where the effect of minority carrier injection into the PbS has an inductive effect on the overall capacitance since the electrons are either extracted at the PEDOT:PSS/PbS interface or combine with majority holes (hole transfer in the opposite direction is unlikely due to the large energy barrier at the heterojunction interface for holes as seen in Figure 3.3).

In the second regime, below ~130 K, the sharp rise in capacitance is seen and the peak no longer corresponds to the diode turn on voltage (Figure 3.21c). For low temperature then, injection barriers at each electrode come into play and display effects that are not seem at higher temperatures. V1 and V2 then correspond to injection of charge carriers with each overcoming the barrier at one of electrodes. For example, V1 most likely corresponds to hole injection at the PEDOT:PSS/PbS interface and V2 corresponds to electron injection at the Al/ZnO interface. At V1, holes are injected into the PbS which increases the amount of charge and hence the

capacitance. Since both V1 and V2 occur at biases beyond the diode turn-on voltage (see Figure 3.21c), once V2 is reached, electrons injected into the ZnO can pass easily into the PbS layer to be extracted at the PEDOT:PSS or combine with holes causing the decrease in capacitance.

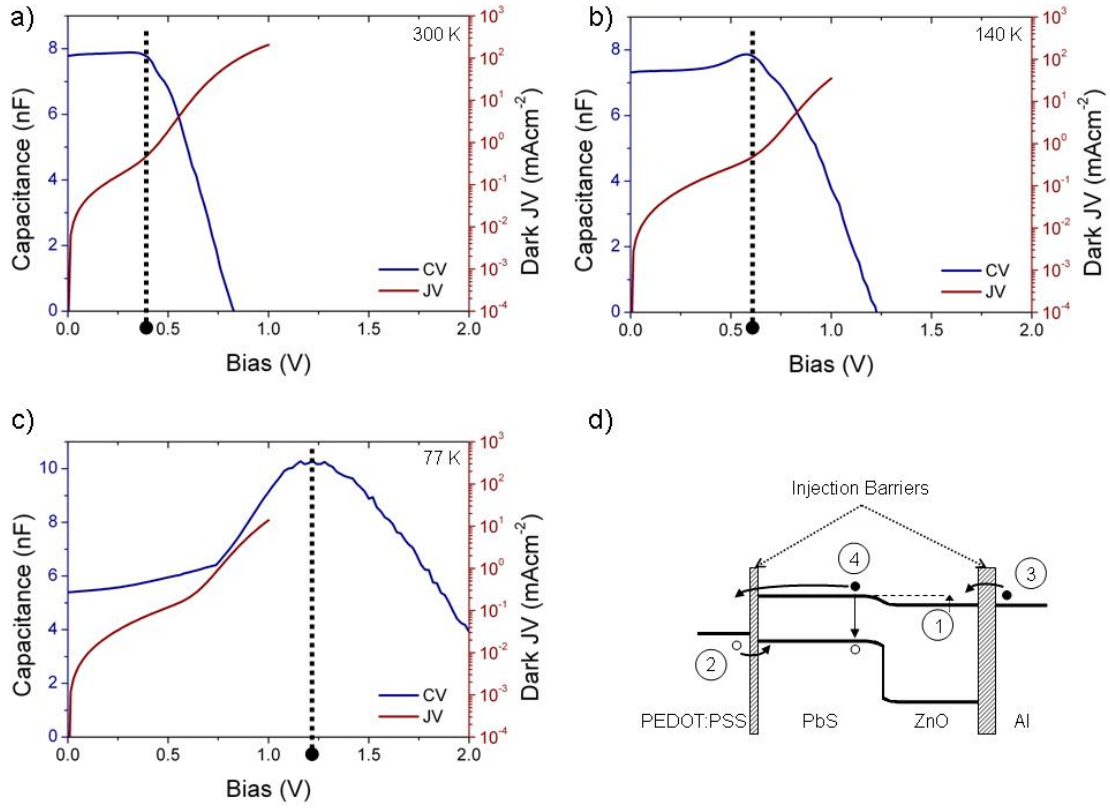

Figure 3.21. a) – b) CV peak and diode turn on voltage correspond in the regime above ~130 K. c) Below ~130 K the excessive capacitance onset and peak occur at biases higher than the diode turn on voltage. d) The steps forming the excessive capacitance peak with increasing forward bias. 1. Flat band is reached. 2. Hole injection into PbS. 3. Electron injection into ZnO. 4. Electron is extracted or recombines with a hole.

In the example, injection at V1 was correlated to the PEDOT:PSS/PbS interface. This is likely to be the case since, if flat-band conditions are already achieved before injection (step 1 in Figure 3.21d), any charge injection at the Al/ZnO interface would be able to go immediately into the PbS layer to be extracted or combine with the majority holes, reducing the overall amount of charge before an increase in

capacitance is observed. On the other hand, charge injection at the PEDOT:PSS/PbS interface (step 2 in Figure 3.21d) would cause an increase in capacitance due to an increased amount of charge because the charge is unable to pass into the ZnO layer, even at flat-band conditions, due to the large energy barrier to holes in that direction due to the heterojunction (see Figure 3.3). Then, once the injection barrier at the Al/ZnO electrode is overcome (step 3 in Figure 3.21d), electrons flood in and pass into the PbS layer to be extracted or combine with holes (step 4 in Figure 3.21d) decreasing the amount of charge.

The thermal activation energy of the capacitance peak can be determined by[126]

$$V = \frac{V_0}{1 + C\exp\left(\frac{-E_a}{kT}\right)} \qquad \textbf{(3.1)}$$

where E_a is the thermal activation energy, k is the Boltzmann constant, T is the temperature, and V_0 and C are fitting constants. Arrhenius plots at different modulating frequencies for the temperatures are shown in Figure 3.22. Equation (3.1) has been fit over the temperature range where the peak bias corresponds to the diode turn on voltage and the plot in Figure 3.22d shows the resulting activation energies as a function of modulation frequency. Again the results are seen to be frequency dependent with three energy level regimes appearing. The first is ~600 meV for 100 Hz. This value is difficult to pin down exactly because the noise level is quite high which could affect the actual peak bias locations and hence the fitting results. For 500 Hz and 1 kHz the activation energy is around 130 meV and for 5 and 10 kHz it is near 50 meV. An attempt to fit equation (3.1) over the temperature where the capacitance no longer corresponds to the diode turn on voltage was completed at

100 Hz and 500 Hz yielding activation energies of 3 meV and 80 meV respectively. These results are also included in Figure 3.22.

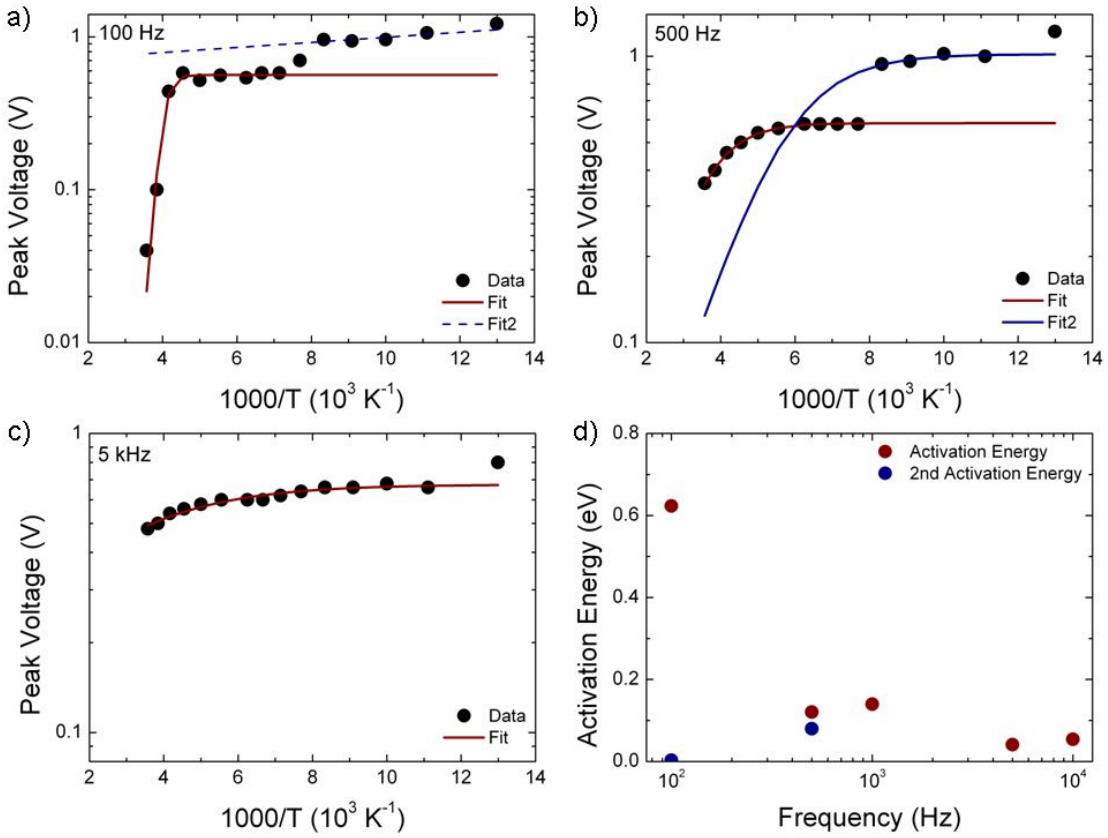

Figure 3.22. Capacitance peak voltage values fitted with equation (3.1) for modulation frequencies of a) 100 Hz, b) 500 Hz, and c) 5 kHz. d) The determined activation energy as a function of modulation frequency.

For the two high frequencies, the sharp rise in capacitance associated with V1 in Figure 3.20 is not visible even at low temperatures. As a result, equation (3.1) can be fitted down to 90 K (77 K still behaves differently) for the high modulation frequencies. The absence of the rise in capacitance for high frequencies can be explained by the ability of charge carriers to respond to the modulation frequency[53]. As the frequency is increased beyond a certain threshold, the injection of charge carriers can no longer respond fast enough to the changing potential and hence the two materials are not flooded with charges. The capacitance drop still exists though

because once flat-band conditions are reached at the PbS/ZnO junction, electrons and holes will still recombine depleting the cell of charges.

Linear regions in the C^{-2} versus bias plot are visible under reverse bias as shown in Figure 3.23. Mott-Schottky fits again give built-in voltages that are quite a bit higher than expected for any junction energy level differences. This again could be due to a complex capacitance due to the cell geometry as described in section 3.7.3.2. However, the nature of the capacitance change with bias between -2 and 0 V points towards a depletion region with a thickness that varies based on the applied bias.

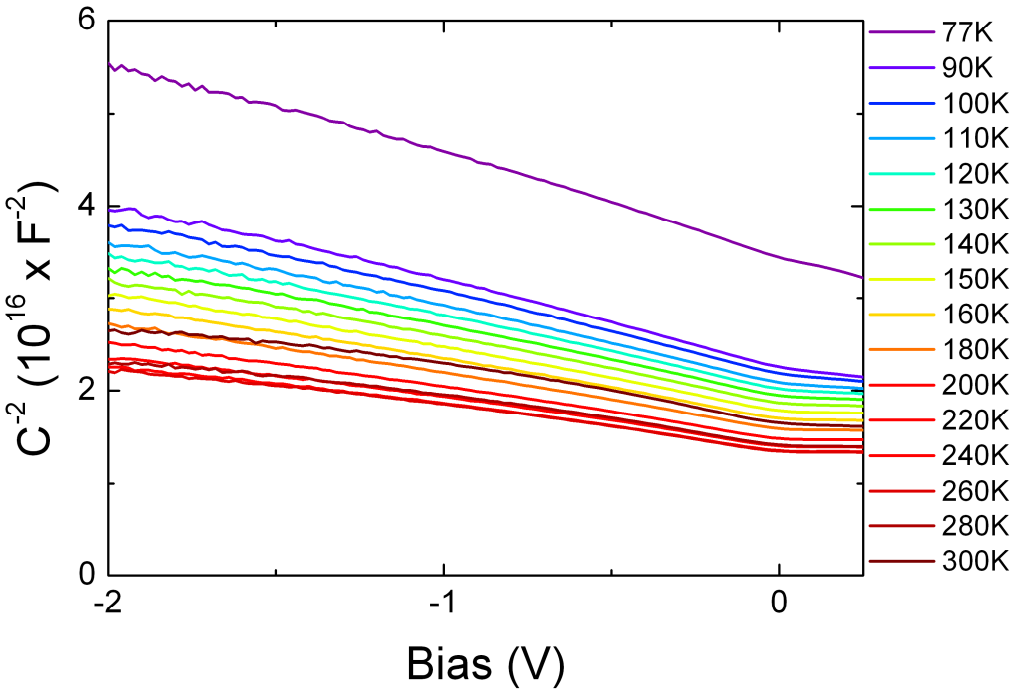

Figure 3.23. Temperature-dependent C^{-2} versus bias curve for the 125 nm thick PbS layer cell.

3.8 CQD Solar Cell Conclusions

Temperature dependent *JV* and CV results give evidence of injection barriers located at the electrodes that become evident at low temperatures (below about 130 K). The temperature dependent V_{oc} results in section 3.7.1.2 match well with what has been

reported for organic bulk heterojunction cells[120]. Injection barriers were proposed as the reason for V_{oc} saturation at low temperatures. At high temperatures, charges have enough thermal energy to overcome the barriers, but at low temperatures the effects become evident. The temperature dependent CV results in section 3.7.3.3 support this conclusion as well by the sharp rise and subsequent drop in capacitance with increasing forward bias at low temperatures which corresponds to the injection of charges across each barrier. Applying this to the PbS layer thickness CV results in section 3.7.3.2 gives a complex capacitance model that includes a depleted region at the PbS/ZnO interface and an overall capacitance due to the injection barriers. The combination of the two capacitances provides a reasonable explanation of the CV responses seen in the thickness dependent CV measurements.

Finally, there is the matter of whether the PbS/ZnO interface acts as an excitonic or depleted *p-n* junction. In PbS Schottky devices (section 3.7.3.1), electron flow from Al into the PbS layer to create the depletion region indicates there is no fundamental limitation to the PbS QDs forming a depletion region. CV measurements taken before photodoping ($Cell_{pre}$ batch) however display a near constant capacitance in reverse bias showing no evidence for a bias-dependent depletion region. The cell still operates in this case though, which means the junction must act excitonic. In other words, excitons created within a diffusion length of the heterojunction have a high probability of diffusing to the junction and dissociating without the presence of a depletion region. Photodoping the cell changes the behaviour and evidence of a depletion region becomes visible in the thickness and temperature dependent CV results as well as the doping dependent EQE results. A complex capacitance model that includes a constant capacitance due to injection barriers was used to describe the C^{-2} versus bias response. However, due to the complex capacitance interactions,

actual depletion width calculations aren't valid without a more advanced model. The appearance of a second peak at short wavelengths in the EQE spectrum with increased photodoping also demonstrated the appearance of a depletion region within the PbS layer. Therefore before photodoping, the junction is initially seen to lack a depletion region (excitonic behaviour) which requires electron-hole pairs to be created within a diffusion length from the junction to harvest the charge carriers. After photodoping the junction behaves as a depleted *p*-*n* junction which enhances the charge collection. It needs to be noted though that the majority of the increase in J_{sc} seen with photodoping is likely due to increased conductivity of the ZnO with some contribution coming from the increased charge collection region.

Estimates of the diffusion length in CQDs are generally in the 100 nm range[113,127]. However, for small CQDs (the size studied here), estimates near 20 nm have been reported[112]. In either case, the values are both less than the 190 and 230 nm-thick PbS layers presented here. The additional charge collecting region gained by the appearance of a depletion region is therefore significant for thicker PbS layer devices.

Previous reports of excitonic junction behaviour in CQD PbSe/ZnO solar cells have been concluded based on the rectification reversal of an inverted PbSe/ZnO region (see section 3.6)[100]. However, in this configuration they make no mention of a UV photodoping step. In the work presented in this thesis, the photodoping is a necessary step to create the *p*-*n* junction behaviour. Support for depleted *p*-*n* junction behaviour has come from cells fabricated with TiO_2 instead of ZnO which don't require photodoping to create an *n*-type electron acceptor material[93].

3.9 Further Work on CQD Solar Cells

Better understanding of the role ZnO plays in the cell is needed. Specifically, the effect photodoping has on doping density and the Fermi level position would help to further understand the interface mechanism at the PbS/ZnO junction. A Kelvin probe could be used to measure the Fermi level of un-doped ZnO QDs to verify whether the material is intrinsic or nearly intrinsic. If the ZnO is indeed intrinsic, support is given to the conclusion of the PbS/ZnO junction operating as an excitonic junction for un-doped ZnO. Finding the Fermi level location based on the amount of photodoping would also be helpful since this would help in determining any band bending at the heterojunction. However, Kelvin probe measurements on photodoped ZnO would need to be measured in an oxygen-free environment to prevent re-adsorption of oxygen at the ZnO surface. Creating Schottky devices from the ZnO QDs would allow the doping density to be determined using CV measurements for different photodoping amounts. This was tried in the work here using ITO and ZnO, but the results were difficult to understand and require more work.

Another area that needs to be investigated is to check for any effect of UV radiation on the PbS QDs. This work has assumed that there is no effect, and none has been reported by other workers. However, broad band illumination of PbSe QDs has been shown to *p*-dope the QDs and increase their conductivity[109]. A simple set of tests would be to fabricate PbS Schottky cells and run *JV* and CV analysis on them at different photodoping times. Any changes to the PbS performance or parameters (n, J_0, N_A, etc…) would need to be incorporated into the results presented here for the heterojunction cells.

The evolution of the cell characteristics and parameters as the photodoping time increases is also an interesting set of experiments. If the ZnO Fermi level is indeed lower than the PbS Fermi level and the doping density less than that of PbS before photodoping, then the cell should exhibit a transition between a depletion region located mainly in the ZnO layer to one that is located mainly in the PbS layer as the photodoping time is increased. Performance values based on the junction characteristics as they change would provide a great deal of information towards fully understanding the junction mechanism. These experiments with controlled levels of photodoping should also be performed on cells with a range of PbS thicknesses including layers thicker than those studied here to ensure the junction is further away than the exciton diffusion length for a large portion of absorbed photons. This would allow better observation of any increasing depletion region within the PbS layer.

A way to verify and study further the proposal of injection barriers at the contacts is to fabricate cells using metals of different work functions such as Au and Ca. These two metals have work functions greater and less than Al which provides a good set of parameters to test the injection barrier theory. Temperature dependent *JV* and CV measurements with the different cathode choices should reflect the different barrier heights. Larger barriers (such as that for Au) should show more V_{oc} saturation at low temperatures and possibly even an overall reduction at each temperature[125]. The location of the capacitance peak for low temperatures when the peak no longer corresponds to the diode turn on voltage should shift in voltage for different injection barriers as well.

The last piece of additional work offered here is modelling of the complex capacitance proposed in section 3.7.3.2. This would require determining the

capacitance caused by the overall cell due to injection barriers incorporating two materials of different dielectric constants. Also, the proposed equivalent circuit of two parallel capacitances might need refinement.

Chapter 4

Enhancing III-V Solar Cells: Investigating Defects in Quantum Dot and Dilute Nitride Solar Cells

4.1 Introduction

Currently the highest performing single-junction solar cells are fabricated from III-V semiconductors[128,129]. Two routes to increase the efficiency in these materials even further are the use of quantum dots (QD)s to create an intermediate band within the bandgap that harvests previously inaccessible low energy photons[130], and bandgap engineering of a 1 eV material that can be lattice matched to both GaAs and Ge for use in multi-junction cells[131]. In both cases defects induced during the material processing affect device performance. For GaAs cells with InAs QDs, defects form during the QD growth if the proper strain relieving techniques are not employed[132]. In GaInNAs, thermal annealing removes defects from the material, but annealing at too high of a temperature induces other defects[133].

The electrical characterisation techniques described in chapter 2 are very useful methods to study the effect of defects within the In(Ga)As QD and GaInNAs solar

cells. Temperature dependent EQE and *JV* measurements show that the dislocation defects in In(Ga)As QD cells which significantly degrade the cell performance actually improve the device performance at sub-bandgap wavelengths. In GaInNAs cells, CV and impedance measurements show that even though rapid thermal annealing at a higher temperature (910 ^{0}C compared to 825-875 ^{0}C) produces a larger depletion region, it also creates defects that are detrimental to the cell performance.

4.2 Work Collaboration

The In(Ga)As QD work was carried out in collaboration with Sharp Electronics (Dr Ian Sellers) and University College London (Dr Huiyun Liu and Mr Frank Tutu). The In(Ga)As cells were all grown by the collaborators at University College London. The photoluminescence measurements (Figure 4.5) and TEM images (Figure 4.8) were also taken by the collaborators at University College London.

The GaInNAs solar cell work in section 4.4 was done in collaboration with Sharp Electronics (Dr Ian Sellers). The GaInNAs cells were grown and fabricated by Sharp.

4.3 In(Ga)As Quantum Dot Solar Cells

4.3.1 In(Ga)As QD Solar Cell Introduction

Third generation processes may lead to improved solar cell efficiencies beyond the Shockley-Queisser limit. In this regard, quantum dots (QD)s have been proposed as a means to realize multiple exciton generation[83], hot carrier solar cells[134] and the intermediate band solar cell (IBSC) [130]. While none of these processes have yet demonstrated their predicted potential, progress towards their goal has been achieved. The IBSC receives special attention in this chapter since it is closely related to the cells studied here. Well known processing techniques allow InAs QDs to be grown in

a GaAs matrix[135]. Even though the end-product is not the ideal system for an IBSC and has not outperformed a traditional GaAs solar cell[130], it is a good test bed to study carrier dynamics in QD solar cells.

The idea that defect states could be created within a semiconductor's bandgap that allow photons of sub-bandgap energies to be harvested in a solar cell has been around for at least two decades[136]. Not long after it was presented, the proposed structure progressed to an isolated energy band within the bandgap and the introduction of the IBSC concept[137]. The attraction of such a solar cell is its potential for efficiencies above the Schokley-Queisser limit[16]. For example, under ideal concentration with a back mirror, the thermodynamic limit for an optimised IBSC is 63.1% versus 40.7% for a conventional cell under the same conditions[130,137,138] and is also higher than the 55.4% of a two-terminal tandem cell under these conditions[137]. The increased efficiency limit compared to the conventional single gap cell is the result of harvesting sub-bandgap photons through the two-step intermediate band process without decreasing the voltage[130]. It might be surprising that the efficiency limit is also higher than a two-terminal tandem cell. The reason is that a tandem cell needs two photons to deliver one electron to the external circuit resulting in an overall quantum efficiency of ½. For the IBSC, the same is true for low energy photons (sub-bandgap), but for photons with energy greater than the bandgap only one photon is needed to supply an electron to the external circuit. Therefore, the IBSC overall quantum efficiency is greater than ½, which translates to a higher efficiency limit than the tandem cell[137].

Some progress towards the realization of an IBSC has been made using QDs[139]. However, there is difficulty in fully demonstrating an IBSC stemming from the

current lack of ability to fabricate a QD solar cell with the optimum energy levels. The most common QD solar cell used to study IBSCs has InAs QDs grown in a GaAs matrix by molecular beam epitaxy using the Stranski-Krastanov self-assembly method (explained in section 4.3.3). Although the method is well known and relatively cheap and simple[130], it does not produce ideal energy levels[140]. Nevertheless, the In(Ga)As/GaAs QD array structure is frequently used[141,142,143,144], and the IBSC operating principles have been demonstrated with these cells[145,146].

Although the cells studied here are not true IBSCs (as the concept has been proposed) since the intermediate band is electronically coupled to the conduction band (explained in section 4.3.2), knowing the requirements for an IBSC aids in understanding the operating concepts behind the cells studied here. Therefore the next section gives an overview of the relevant IBSC principles since understanding the charge generation and escape mechanisms within the QDs are a piece of the puzzle towards achieving an IBSC.

The main focus of the In(Ga)As QD solar cell portion of this chapter is on the characterisation of GaAs *p-i-n* solar cells with InAs QD arrays grown in the intrinsic region. Special attention is given to the sub-bandgap performance of two QD cells of substantially different material quality. Previous reports have shown increased current due to sub-bandgap photons when more quantum dot layers were grown (50 compared to 10), but the overall performance suffered because of defects induced by the strain of the extra layers[130]. The increased sub-bandgap photocurrent was attributed to the extra QD layers. In this chapter the sub-bandgap photocurrent (and PCE) is studied in two QD cells having the same number of QD layers, but with different material quality (one with dislocation defects and one without). It is found

that the cell with the dislocation defects performs better when looking at just sub-bandgap illumination, without an increase in the number of QD layers.

4.3.2 IBSC Operating Principles

Figure 4.1a demonstrates the basic principle of an IBSC. Process 1 shows the conventional excitation path of an electron from the valence band to the conduction band via absorption of a single photon. If an intermediate band can be created within the bandgap, another pathway also becomes available by sequential absorption of photons 2 and 3 which excite an electron from the valence band to the intermediate band and then to the conduction band[147]. If the cell acts as a true IBSC, an increase in the photocurrent is expected while maintaining the same output voltage.

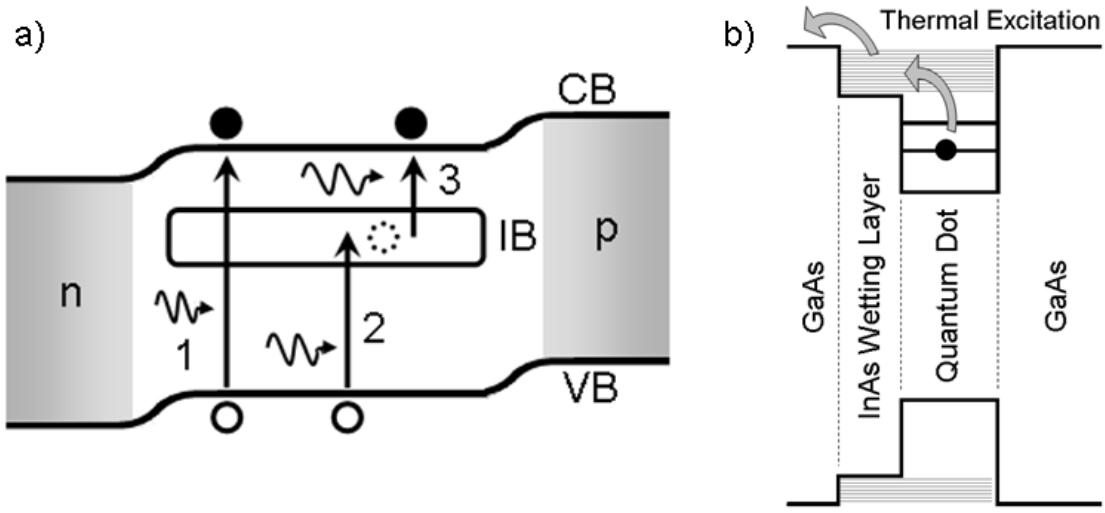

Figure 4.1. a) IBSC excitation processes (explanation in text). b) Energy diagram showing the thermal escape pathway from the QD to the conduction band via the InAs wetting layer.

There are two important constraints to consider when designing an IBSC that are also relevant to the cells discussed in this chapter. In order to prevent a reduction in the output voltage, the quasi-Fermi levels associated with each band must be isolated from each other and the intermediate band material must be isolated from the metal contacts with oppositely doped semiconductor material to prevent carrier extraction

from the intermediate band to the contacts[137,148]. There are other considerations for optimal performance that are not particularly significant for the cells studied here and are therefore not discussed. They can, however, be found in references 130 and 149.

The use of QDs to form the intermediate band[150] has received a lot attention due to their zero dimensionality, preventing thermal transfer of electrons between bands[139,148]. Unlike quantum wells or quantum wires that do not have three-dimensional confinement, QDs (at least ideally) create full tri-dimensional potential wells producing a zero density of states that isolates the intermediate band from the conduction band[130]. Such isolation is necessary to ensure the V_{oc} is not reduced. Any non-optical transitions, such as thermal excitation, from the intermediate band to the conduction band means the two Fermi levels are not electrically isolated and therefore must come to the same potential. This lowers the potential energy difference between carriers resulting in a lower V_{oc}. It is possible though to increase the J_{sc} since lower energy photons are also harvested. However, the increased J_{sc} has yet to overcome the loss due to the decreased V_{oc} which results in lower device efficiencies[130].

One of the problems with the In(Ga)As/GaAs system is a thin InAs wetting layer that forms when growing the QDs (described in section 4.3.3). The wetting layer acts as a quantum well with a near continuous set of states[148] that effectively lowers the GaAs bandgap[151]. This is thought to create a strong thermal escape pathway for holes and electrons out of the intermediate band into the conduction band[130] as shown in Figure 4.1b. It is this effect that has prevented this structure of QD solar cells from outperforming a comparable reference GaAs cell without the addition of QDs[130,148].

The work presented in this chapter studies the electrical properties of two In(Ga)As QD cells fabricated with and without strain relief techniques during the fabrication

process (discussed in the next section). A special focus is given to the carrier dynamics and transfer between the confined QD states, wetting layer states, and bulk GaAs states in the two QD cells.

4.3.3 In(Ga)As QD Solar Cell Fabrication

The Stranski-Krastanov self assembly method[152] was used to produce GaAs *p-i-n* solar cells with InAs QDs grown in the intrinsic layer. The following description of the growing method comes from reference 135. Using molecular beam epitaxy, InAs is grown on GaAs. After a couple monolayers are grown, the strain due to lattice mismatch causes the InAs to form three-dimensional nano-structures (typical heights are 2-5 nm and base widths are ~ 20 nm) that sit on the thin InAs layer. These nano-structures are the QDs. The thin InAs layer is the quantum well mentioned in section 4.3.2. GaAs is then grown on top of the InAs QDs and the process is repeated to grow multiple QD layers.

As multiple QD layers are grown, strain begins to build up, and if not relieved, defects are created that reduce the overall cell performance[132]. To avoid this problem, much work has gone into techniques to relieve the strain caused by stacking multiple QD layers[142,143,144,148]. For the cells grown here, 29 nm-thick GaAs spacer layers grown at different temperatures were used to compensate strain[153]. In one case the spacer layers were grown at a constant 510 ^{0}C which resulted in threading dislocations that propagated through the GaAs emitter to the surface. In this second case, the spacer layer was grown at 510 ^{0}C only for the first 3 nm and then at 580 ^{0}C for the remaining 26 nm which prevented the formation of the threading dislocations[154]. TEM images displaying the two cells with and without threading dislocations are shown in Figure 4.8. The overall QD density was approximately 5 x 10^{10} cm^{-2}. The solar cells were

grown using solid source molecular beam epitaxy and fabricated using standard III-V processing techniques. Figure 4.2 shows the entire cell structure for the cells in this study.

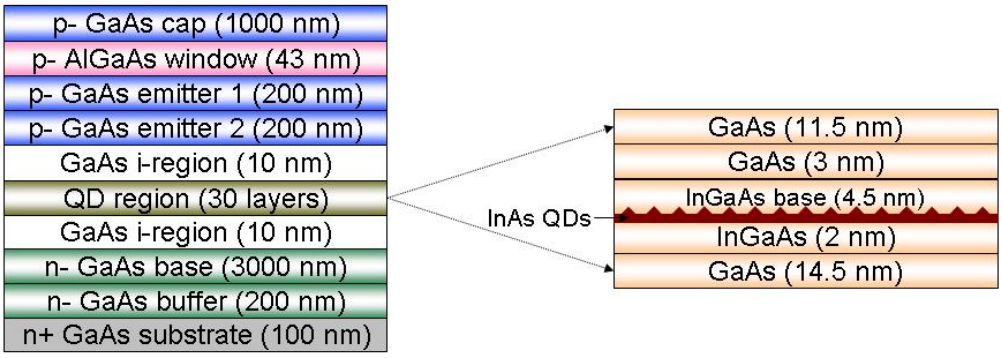

Figure 4.2. In(Ga)As QD solar cell structure. The expanded region on the right shows one layer of the QD growth region. The QD cells have 30 QD layers. The reference GaAs cell does not have the QD region.

4.3.4 In(Ga)As QD Solar Cell Results and Discussion

Three GaAs solar cell systems are considered in this analysis. The first is a GaAs *p-i-n* cell ($Cell_{Ref}$) that acts as the reference cell. The other two systems have 30 InAs QD layers grown in the intrinsic region using the methods described in section 4.3.3. The first QD cell ($Cell_{QD}$) was grown using high-temperature growth for the GaAs spacer layers while the second ($Cell_{QD+Defects}$) was grown using low-temperature growth for the GaAs spacer layers, which is again described in section 4.3.3. The growth temperatures resulted in the presence of threading dislocations within $Cell_{QD+Defects}$ and the prevention of threading dislocations in $Cell_{QD}$.

This section is organised according to characterisation technique with a small amount of discussion included in each technique section, followed by an overall discussion in the conclusion section (4.3.5).

4.3.4.1 *JV* Analysis

Room temperature AM1.5 illuminated JV curves for all three cells are shown in Figure 4.3a and the solar cell parameters are presented in Table 4.1.

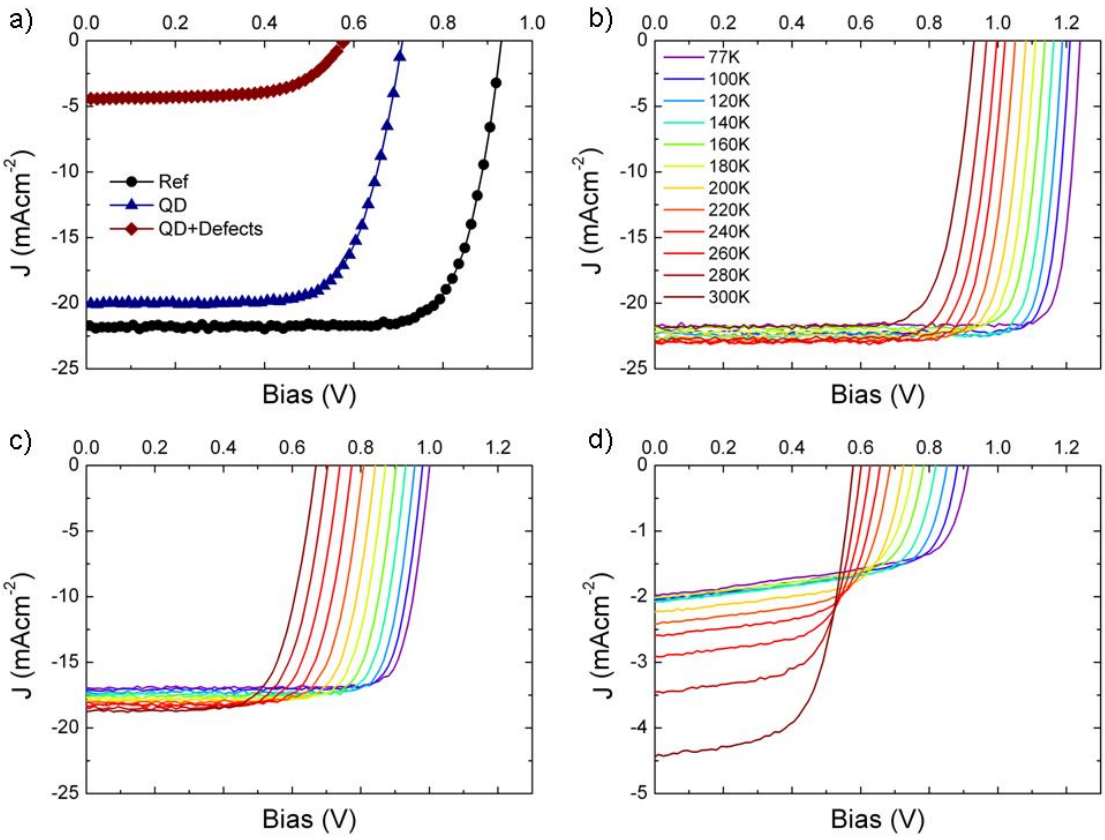

Figure 4.3. a) Room temperature *JV* curves for the three cells. b) – d) Temperature dependent *JV* curves for $Cell_{Ref}$ (b), $Cell_{QD}$ (c), and $Cell_{QD+Defects}$ (d).

The V_{oc} for $Cell_{QD}$ is reduced substantially compared to $Cell_{Ref}$ and for $Cell_{QD+Defects}$ it is reduced even further. As will be discussed in section 4.3.5 in conjunction with the EQE results, this gives strong indication that the quasi-Fermi level of the QDs is not electrically isolated from that of the GaAs. The J_{sc} for $Cell_{QD}$ is also lower than that of $Cell_{Ref}$. The goal of adding QDs to the cell is to harvest more photons leading to a higher J_{sc}, contrary to what is observed here. A likely possibility for the lower J_{sc} in $Cell_{QD}$ is due to a small amount of defects formed during the QD growth even though the high temperature growth strain relieving techniques were used. Figure 4.6c-d

show higher reverse saturation current and series resistance for $Cell_{QD}$ compared to $Cell_{Ref}$ that support this thought. In $Cell_{QD+Defects}$, there is a clear and very large reduction in J_{sc}. This will be discussed in more detail with consideration of the EQE results in section 4.3.5.

Table 4.1. Solar cell parameters of the three test cells at 300 K.

Cell	J_{sc} (mAcm^{-2})	V_{oc} (V)	FF	PCE (%)
Ref	21.7	0.93	0.78	15.6
QD	18.6	0.67	0.69	8.7
QD+Defects	4.5	0.58	0.61	1.65

The AM1.5 illuminated temperature dependent *JV* curves for the three cells are shown in Figure 4.3b-d, and the solar cell parameters are given in Figure 4.4. The V_{oc} for all three cells decreases at the same rate with increasing temperature, reflecting the change in bandgap of GaAs with temperature due to thermal expansion of the crystal lattice[155]. The FF of $Cell_{QD+Defects}$ does not follow the same trend as the other two cells though, and its lower values can be attributed to decreased carrier transport through the intrinsic and emitter regions[156]. Carrier lifetimes determined by impedance spectroscopy in section 4.3.4.3 support this conclusion since $Cell_{QD+Defects}$ has the lowest carrier lifetime.

There was no observable trend in J_{sc} for $Cell_{Ref}$ which had a standard deviation of 2.4% across the range of temperatures, even though a small J_{sc} increase is expected due to the decrease in bandgap as temperature increases. The reason for this is not fully understood yet. However, the thermal stability of the conductive paste used to adhere the cell to the back electrode needs to be investigated. Both QD cells on the other hand show an increase in J_{sc} with increasing temperature. The increase for

$Cell_{QD}$ is nearly linear across the temperature range, while the J_{sc} for $Cell_{QD+Defects}$ is relatively stable until ~200 K at which point it increases very rapidly. The percentage change in J_{sc} is quite small for $Cell_{QD}$ and is overshadowed by the change in V_{oc} such that the trend in PCE follows that of the V_{oc}. This is true of $Cell_{Ref}$ as well. However, even though $Cell_{QD+Defects}$ displays the same trend in V_{oc} as the other two cells, its PCE follows closely to the J_{sc}.

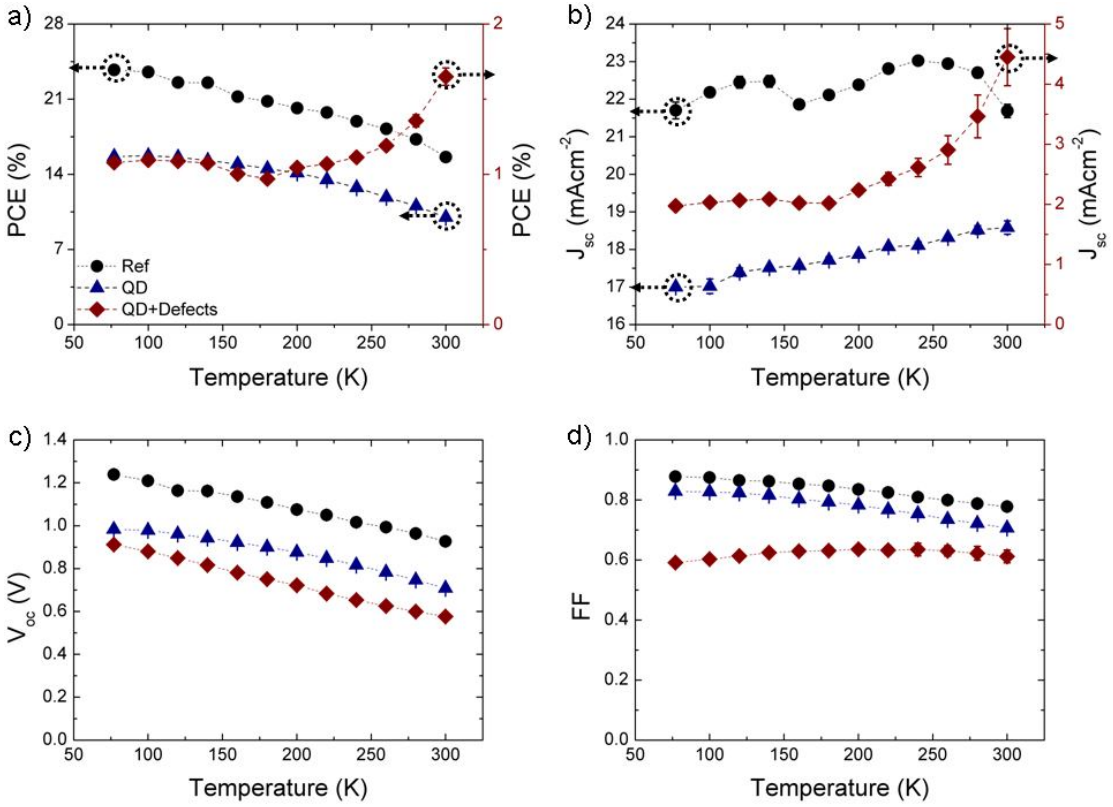

Figure 4.4. Temperature dependent solar cell parameters for the three cells. a) PCE. b) J_{sc}. c) V_{oc}. d) FF.

The J_{sc} behaviour of $Cell_{QD+Defects}$ suggests an escape energy for trapped or confined carriers near 220 K at which point carriers are released and contribute to the photocurrent. Temperature dependent photoluminescence (PL) results which were taken by the group at University College London support this conclusion. Figure 4.5 shows a consistent PL signal is observed over the complete range of temperatures for

$Cell_{QD}$, matching well with its V_{oc} trend. However, near 200 K the PL signal of $Cell_{QD+Defects}$ is quenched indicating carriers can escape and be extracted as photocurrent or recombine through non-radiative pathways.

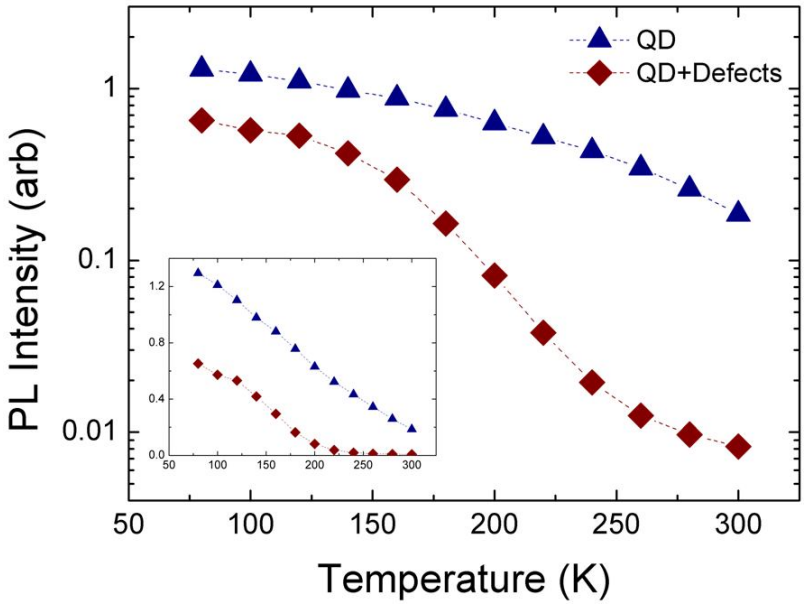

Figure 4.5. Temperature dependent photoluminescence measurements. Near 200 K the PL of $Cell_{QD+Defects}$ is quenched. The inset shows the plot on a linear *y*-axis. This data was taken by collaborators at UCL.

Figure 4.6a shows the dark *JV* curves for the three cells at 300 K, and Figure 4.6b-d presents the temperature dependent, n, J_0, and R_s results. J_0 seems to be the easiest to interpret in its correspondence to recombination. The threading dislocations located in $Cell_{QD+Defects}$ are expected to provide non-radiative recombination pathways for charge carriers which results in higher J_0 values as demonstrated in the figure. Even with the high-temperature strain relief layer growth in $Cell_{QD}$ which prevents the formation of threading dislocations, it is expected that the presence of QDs in the matrix produces some defects, which again promote some recombination. Evidence for this is seen in the increased J_0 value for $Cell_{QD}$ over that of $Cell_{Ref}$.

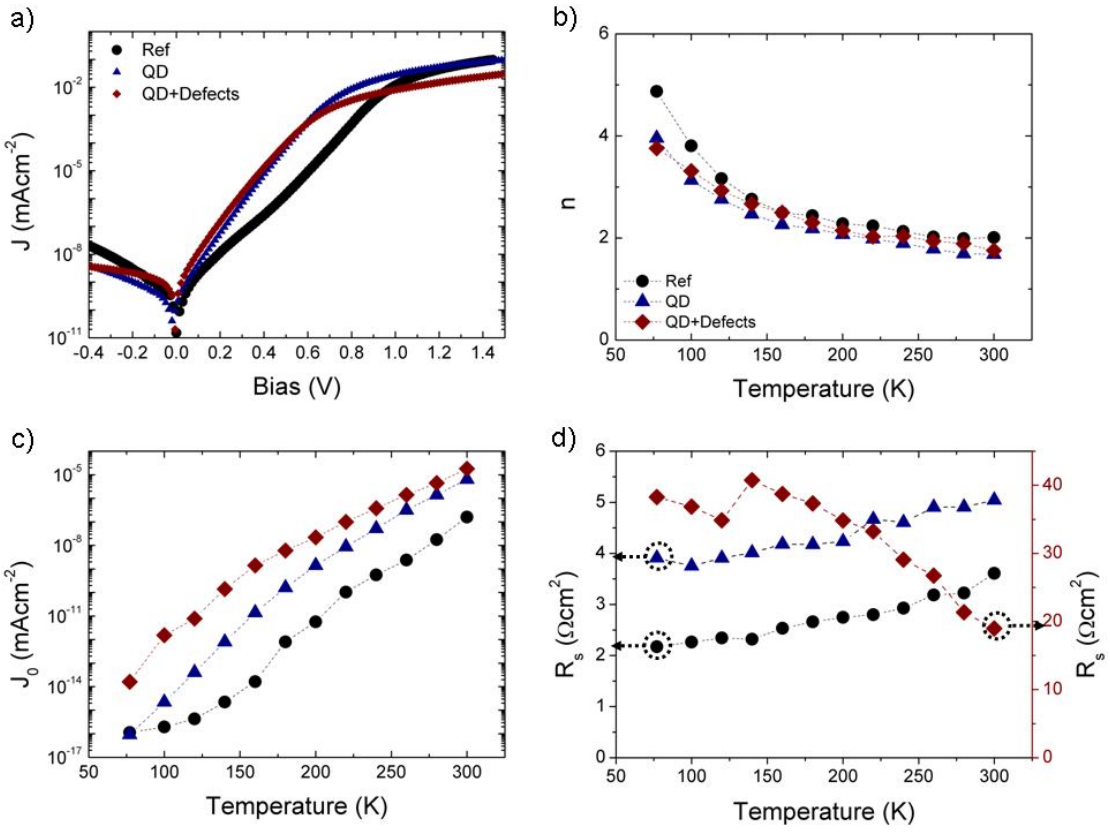

Figure 4.6. a) Dark *JV* curves at 300 K for the three cells. b) – d) Temperature dependent (b) *n*, (c), J_0, and (d) R_s for the three cells.

The ideality factor for the three cells shows very little difference between the three cells. $Cell_{QD+Defects}$ has a higher *n* value than $Cell_{QD}$ at all temperatures which seems to make sense since this would mean it is further from the ideal diode. However, $Cell_{Ref}$ is higher at all temperatures than both QD cells. This type of behaviour (higher ideality factor for the reference GaAs cell compared to the QD cell) has just reported by Lu *et al*[157]. They propose that there are two different recombination pathways in a QD cell that contribute differently to the overall ideality factor. Any injected minority carriers that recombine with majority carriers already occupying states within the quantum dot is similar to dark current outside the space charge region since it requires the transport of only one type of charge carrier. Thus, this type of recombination leads to a low ideality factor. When electrons and holes are captured simultaneously, the

recombination is similar to defect related recombination in the space charge region and leads to larger ideality factors[157]. This behaviour has been seen in GaAs/AlGaAs multiple quantum well solar cells too. The ideality factor of a GaAs/AlGaAs cell with 40 quantum wells was found to be lower over a range of temperatures compared to ideality factors of the control GaAs and AlGaAs *p-i-n* cells[158]. All three of the cells tested here have *n* values slightly less than two at 300 K and increase as the temperature decreases (*n* increases when the current decreases[159]) under the same trend, which seems to indicate the diode characteristics of each cell are very similar.

The series resistance, on the other hand, shows a clear distinction between $Cell_{QD+Defects}$ and the other two cells. While $Cell_{Ref}$ and $Cell_{QD}$ have slightly increasing R_s with increasing temperature, $Cell_{QD+Defects}$ has a fairly large reduction in R_s with increasing temperature. This is most likely due to carriers gaining enough energy as temperature increases to avoid becoming trapped (or escape easier) at the dislocations. This also explains the much higher R_s for $Cell_{QD+Defects}$, since the other two cells do not have the traps associated with the threading dislocations.

4.3.4.2 EQE Analysis

Figure 4.7 displays the room temperature EQE results for the three cells in (a) and the temperature dependent EQE results for each cell in (b) – (d). The peak near 980 nm in the two QD cells is due to the InAs wetting layer[148,135] and the peak near 1220 nm is due to the QDs. The QD peak is more evident in the temperature dependent EQE results (c) and (d). Both of these peaks are beyond the band edge of GaAs (near 870 nm) exhibiting a photocurrent for photons of less energy than the bulk GaAs bandgap. This needs to be considered with regard to the drop in V_{oc} between the samples and is discussed in section 4.3.5.

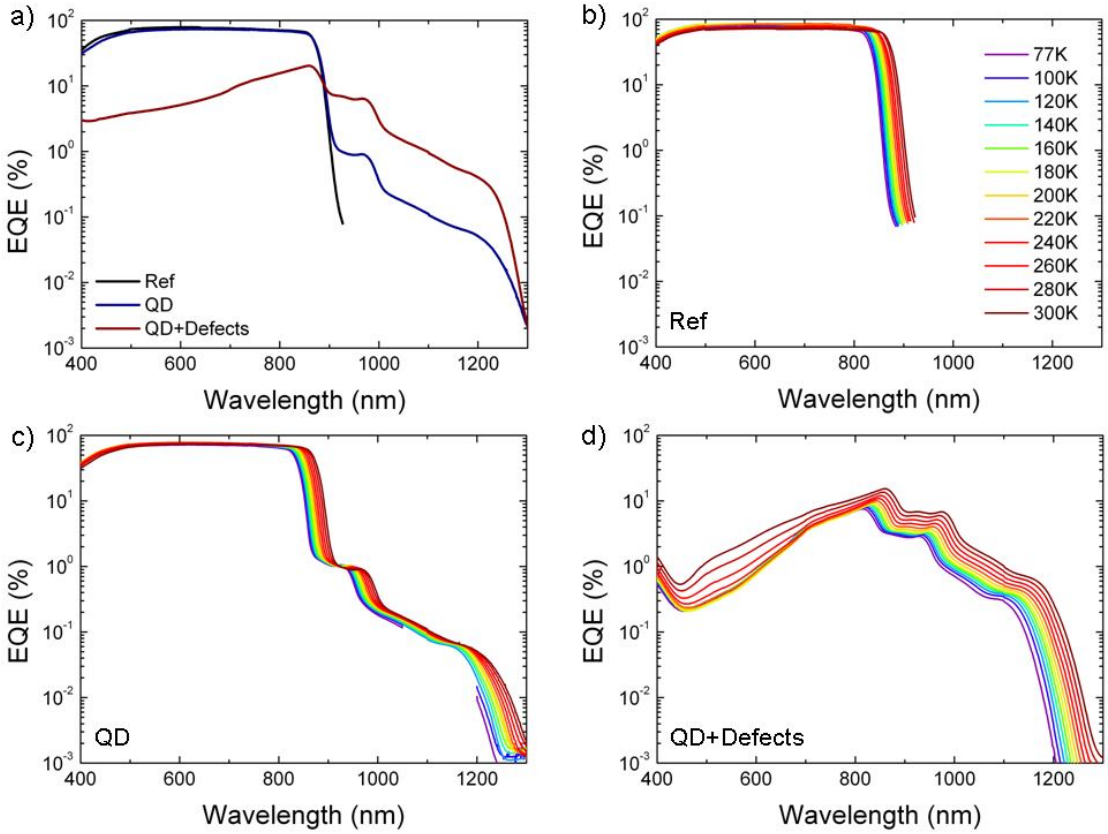

Figure 4.7. a) EQE at 300 K for the three cells. b) – d) Temperature dependent EQE for (b) $Cell_{Ref}$, (c) $Cell_{QD}$, (d) $Cell_{QD+Defects}$.

The additional EQE response beyond the GaAs band edge of $Cell_{QD}$ is expected to increase the J_{sc} of $Cell_{QD}$ compared to that of $Cell_{Ref}$. In fact, it has been reported that the addition of QDs can improve the J_{sc} compared to the reference GaAs cell[142,160]. However, as discussed in section 4.3.4.1, the J_{sc} for $Cell_{QD}$ is lower than that of $Cell_{Ref}$. The first thing to notice is that the sub-bandgap photocurrent for $Cell_{QD}$ is very small (Figure 4.7 is plotted as a semi-log plot) and doesn't contribute much. Any increase in J_{sc} due to the lower energy absorption of the QDs could be outweighed by small amounts of defects within $Cell_{QD}$ inducing recombination.

It is clear from the EQE results of $Cell_{QD+Defects}$ why its J_{sc} is much lower than the other two cells. In the bulk GaAs region (~400 to 900 nm) the cell shows severe degradation to the EQE. TEM images, take by the collaborators at University College

London, shown in Figure 4.8 display large amounts of threading dislocations that propagate up into the GaAs emitter. These dislocations extend all the way to the surface and result in strong surface recombination. This type of dislocation has been reported by others as well[130,132,156] and is discussed more in section 4.3.5.

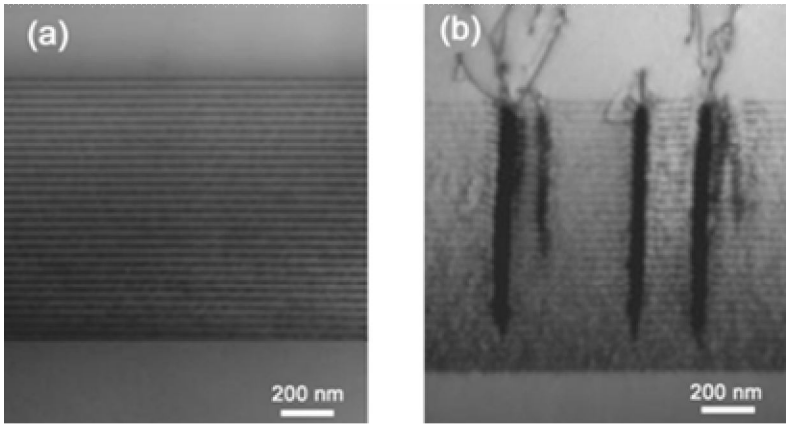

Figure 4.8. a) TEM image of the QD layers using the high temperature growth method for the GaAs spacer layers. b) TEM image of the QD layers when the high temperature growth method is not used, resulting in large dislocation defects. The TEM images were taken by the collaborators at University College London.

The temperature dependent EQE measurements for $Cell_{QD+Defects}$ in Figure 4.7d reflect the increase in J_{sc} near 220 K seen in Figure 4.4e. Both the bulk GaAs responding region and QD peak show strong EQE increases with increasing temperature above 220 K. In $Cell_{Ref}$, the effect of temperature is a shift in the band edge near 870 nm such that higher temperatures have a band edge at longer wavelengths. This means the cell should show an increase in J_{sc} with increasing temperature and a decrease in V_{oc} since a longer wavelength band edge translates to a smaller bandgap. The J_{sc} and V_{oc} temperature dependent results are discussed in the previous section (4.3.4.1). $Cell_{QD}$ shows the same band edge shift with temperature as $Cell_{Ref}$. However, the wetting layer and QD peaks don't exhibit the same magnitude increase with increasing temperature that is seen in $Cell_{QD+Defects}$. For $Cell_{QD}$, the wetting layer peak EQE

decreases with increasing temperature and the QD peak EQE has a maximum value near 220 K, decreasing at higher and lower temperatures. The departure in behaviour between the two QD cells near 220 K indicates a difference in the charge extraction mechanism and is discussed in the conclusions section (4.3.5). The large QD peak EQE increase in $Cell_{QD+Defects}$ compared to the QD peak EQE behaviour of $Cell_{QD}$ and the implications on overall efficiency are also discussed in the conclusions.

4.3.4.3 Impedance Analysis

CV measurements were taken from -3 to 2 V. The results were very consistent over a wide range of modulating frequencies which is expected in well-behaved crystalline cells (see section 2.2.3 for a discussion of the modulation frequency). The results given here are for a modulation frequency of 5 kHz and amplitude of 25 mV. Figure 4.9a shows the C^{-2} versus bias curve including the Mott-Schottky fit (solid lines) for the three cells. The fit values are given in Table 4.2. Interestingly, the built-in bias, V_{bi}, for each cell is very similar even though the V_{oc} varies considerably as shown in Figure 4.3 and Figure 4.4. As discussed in detail in section 2.2, the Mott-Schottky analysis determines the energy band barrier height between the *n*- and *p*-type materials. Since the only difference between the cells is the addition of quantum dot layers (*p* and *n* material layers are the same), the energy band barrier height should be the same for each cell yielding similar V_{bi} values. The V_{oc} on the other hand is lowered with the addition of QDs due to electrical conductivity between the wetting layer, QDs, and bulk GaAs region. Since the Fermi levels are not electrically isolated, the potential energy levels must come to the same value creating a smaller effective bandgap, and hence V_{oc}. Large recombination due to dislocation defects in $Cell_{QD+Defects}$ will decrease the V_{oc} even further. As expected, the doping density, N_A,

increases from $Cell_{Ref}$ to $Cell_{QD}$ and again to $Cell_{QD+Defects}$, since the QDs and dislocation defects contribute to the doping profile in this measurement technique.

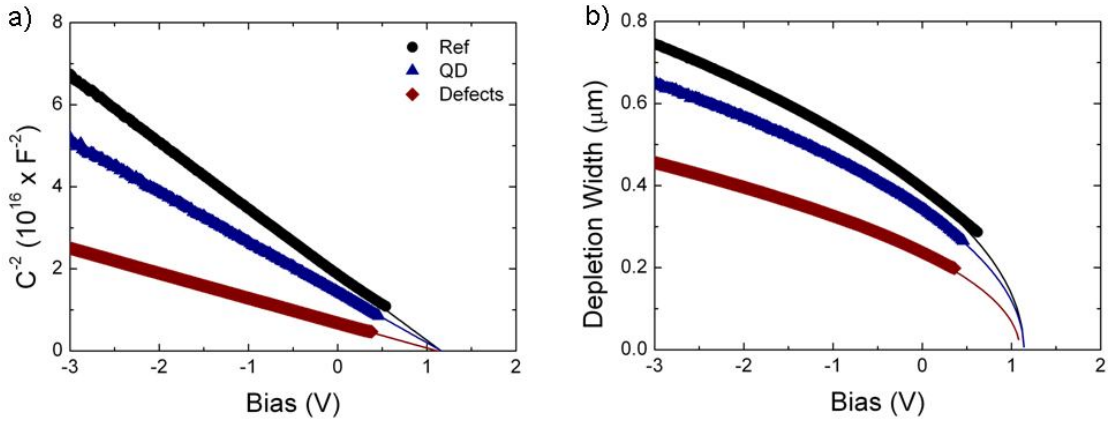

Figure 4.9. a) C^{-2} versus bias curve for the three cells. The solid lines show the Mott-Schottky fit. b) Bias dependent depletion width curves for the three cells. The symbols were calculated using the parallel plate capacitor model (equation (2.16)) and the solid lines were calculated using V_{bi} and N_A in equation (1.3).

Depletion width calculations based on the CV results are shown in Figure 4.9b and the value at zero bias is shown in Table 4.2. The symbols represent the depletion width calculated using the parallel plate capacitor model (equation (2.16)) and the solid lines are calculated from the V_{bi} and N_A values using equation (1.3).

Table 4.2. Built in bias (V_{bi}), doping density (N_A), and depletion width (D.W.) at zero volt bias for the three cells.

Cell	V_{bi} (V)	N_A (cm^{-3})	D.W. (0 V) (μm)
Ref	1.16	1.1 x 10^{16}	0.39
QD	1.16	1.4 x 10^{16}	0.34
QD+Defects	1.12	2.9 x 10^{16}	0.24

The addition of QDs decreases the depletion width which results in less charge collection. The decrease is largest in $Cell_{QD+Defects}$. This is not unexpected since the

doping density for the two QD cells is higher than the reference cell. The depletion width according to equation (1.3), decreases with increased doping.

Impedance measurements as a function of frequency over a range of applied biases were also taken to investigate minority carrier lifetimes. However, the interpretation of the lifetime in this case is more complex than the explanation in section 2.2.5 since in this *p*-*n* structure the *p*- and *n*-type materials are of comparable thicknesses and carriers from each doped material will be able to cross the junction under forward bias. Therefore the carrier lifetime takes into account both carriers using this method. This complication has been reported for carrier lifetimes determined by transient photoluminescence measurements in GaAs and AlGaAs, where the carrier lifetime was found to be a linear combination of the minority and majority carrier lifetimes depending on the illumination intensity[161].

Fitting the Nyquist plots with an equivalent RC circuit to determine the RC time constants yielded results very similar to calculating the lifetimes using the characteristic peak frequency (the methods are explained in section 2.2.5). Figure 4.11 shows example fits and the lifetime results are given in Figure 4.10b.

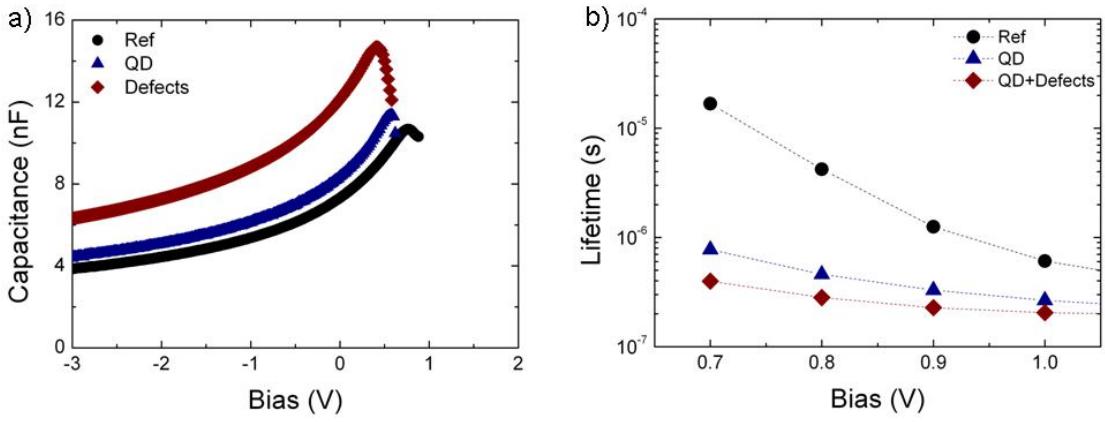

Figure 4.10. a) Capacitance versus bias for the three cells. b) Carrier lifetimes for the three cells.

The carrier lifetimes are shown down to biases of 0.7 V since this is the bias at which carriers are able to cross the depletion region in $Cell_{Ref}$ based on the peak in capacitance as a function of applied bias shown in Figure 4.10a. Carrier lifetimes for $Cell_{QD}$ and $Cell_{QD+Defects}$ are valid down to 0.6 and 0.5 V respectively based on the CV peak.

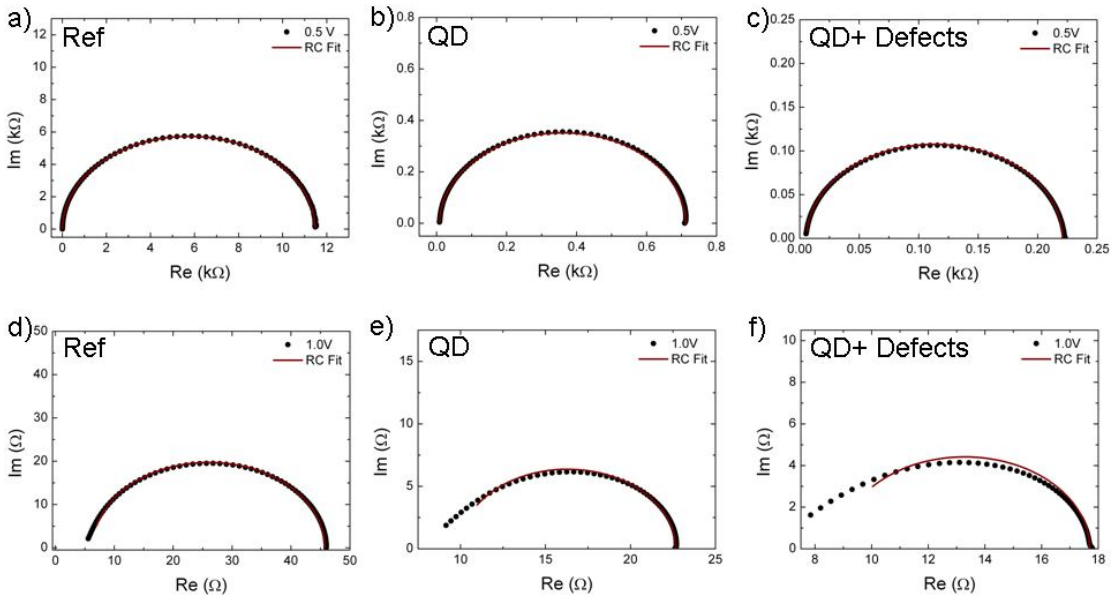

Figure 4.11. Nyquist plots with RC circuit fits at 0.5 V bias (a) – (c) and 1.0 V bias (d) – (f) for the three cells.

As might be expected, the carrier lifetimes decrease significantly when QDs are added to the cell. At 0.7 V bias, there is over an order of magnitude drop in lifetime from $Cell_{Ref}$ to $Cell_{QD}$, and the carrier lifetime in $Cell_{QD+Defects}$ is even lower. The values for carrier lifetimes are almost 3 orders of magnitude higher than what has been reported for minority carrier lifetimes in In(Ga)As QD cells[132]. However, majority carrier lifetimes in GaAs have been reported as long as[162,163] 10^{-6} s and 10^{-5} s. The longer lifetimes determined here compared to previous minority carrier lifetime reports is likely a result of the measurement technique used here, which yields a combination of

both carrier lifetimes. Taking this into account, the results are comparable to reported majority carrier lifetimes[162,163].

The shape of the Nyquist plots for $Cell_{QD}$ and $Cell_{QD+Defects}$ at 1 V bias (Figure 4.11e and f) is similar to that of an exponential distribution of traps seen in disordered organic and inorganic semiconductors[64,65]. This is not unexpected since both the QDs and the dislocation defects can act as recombination centres.

4.3.5 In(Ga)As QD Solar Cell Conclusions

The presence of a sub-bandgap photocurrent in the two QD cells suggests the formation of an intermediate band. However, the reduction in V_{oc} gives strong evidence that the transition of carriers from the intermediate band to the carrier band occurs through processes other than optical excitation. If the Fermi levels are electrically isolated, the only way to extract carriers from the intermediate band into the conduction band is by photon absorption, which excites the electron from the intermediate band to the conduction band. This would preserve the V_{oc} since carriers in the intermediate and conduction bands do not come to the same potential (it is assumed the intermediate band is also isolated from the electrodes so that charges cannot be extracted from the intermediate band at the electrodes). However, the presence of processes other than optical excitation that transfer charges from the intermediate band into the conduction band require non-isolated Fermi levels to allow charge flow, and hence reduce the V_{oc}. The V_{oc} reduction seen in these cells is not unexpected since the InAs wetting layer acts as a quantum well with a near continuous set of energy levels extending the valence and conduction bands, and effectively decreasing the bandgap[130]. In addition, the confined QD energy levels are

not much lower than those of the wetting layer which most likely creates a strong thermal pathway for carrier escape from the QDs to the conduction band[130,148].

As mentioned in section 4.1, the In(Ga)As QD system is not the ideal system for an intermediate band solar cell due to the energy level locations. However, the addition of threading dislocations provides for an interesting study. It's clear from Figure 4.3 that $Cell_{QD}$ far outperforms $Cell_{QD+Defects}$. If however, only sub-bandgap wavelength illumination is considered, the situation appears to be reversed. Figure 4.7 shows the sub-bandgap photocurrent of $Cell_{QD+Defects}$ to be larger than that of $Cell_{QD}$.

This has been reported by others as well when trying to improve the J_{sc} of a cell with 10 QD layers by growing 50 QD layers: dislocations formed due to the strain which caused the overall J_{sc} to decrease, but the sub-bandgap photocurrent increased[130,132]. In this case, the increase in sub-bandgap photocurrent was attributed to the increased number of QDs in the cell[132]. For the cells studied here though, the same number of QD layers was grown for $Cell_{QD}$ and $Cell_{QD+Defects}$.

To carry this study further, it is interesting to calculate the J_{sc} resulting from just sub-bandgap photon absorption in cells with the same number of QDs, but different defects ($Cell_{QD}$ and $Cell_{QD+Defects}$). This was done by integrating the EQE from the trough in EQE just before the wetting layer peak out to 1400 nm with the solar spectrum, as demonstrated in Figure 4.12a. In this manner, only the contribution of lower energy photons (wavelength greater than ~910 nm to ~950 nm depending on the temperature) is considered. Unlike under full AM1.5 illumination, the J_{sc} shown in Figure 4.12c calculated for sub-bandgap photons is nearly an order of magnitude larger in $Cell_{QD+Defects}$ than in $Cell_{QD}$. If this J_{sc} value is then used to calculate the PCE

for just sub-bandgap photons using the V_{oc} and FF from the AM1.5 measurements, $Cell_{QD+Defects}$ outperforms $Cell_{QD}$ as displayed in Figure 4.12d.

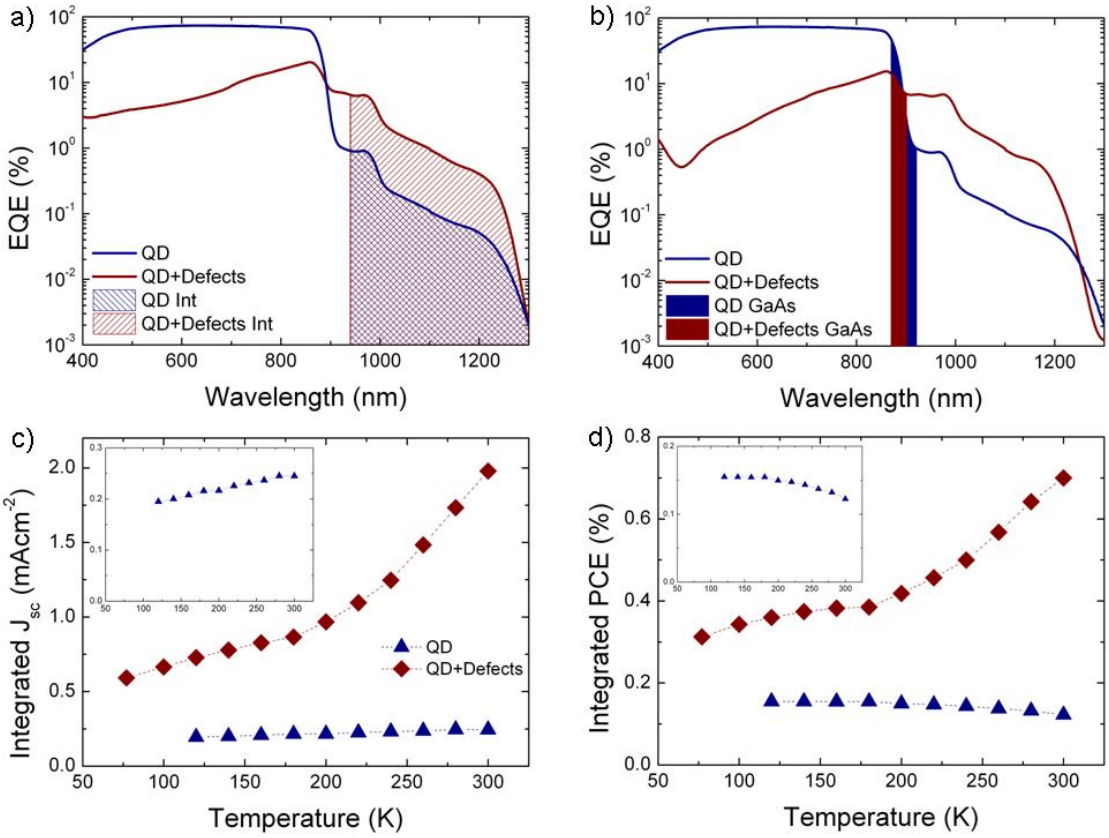

Figure 4.12. a) Integration at sub-bandgap wavelengths to determine J_{sc} due to just long wavelength photons. Hashed areas represent the integration region. b) Solid areas under the EQE curves represent the wavelengths beyond the 870 nm high-pass filter cutoff. For $Cell_{QD}$ more of the GaAs responding region is passed through the filter than for $Cell_{QD+Defects}$ since the GaAs is not degraded in $Cell_{QD}$. The data shown is at 300 K. c) J_{sc} calculated from integrating the EQE as in (a) with the AM1.5 spectrum. Inset shows the results for $Cell_{QD}$ magnified. d) PCE calculated using the J_{sc} from (c) with the V_{oc} and FF from full AM1.5 illumination. Inset shows the results for $Cell_{QD}$ magnified.

In an effort to check this experimentally, an 870 nm high-pass filter was used in front of the solar simulator to illuminate the QD cells with sub-bandgap photons only. However, the filter's cutoff wavelength was not an ideal choice for this experiment since as the temperature is increased, a larger portion of the bulk GaAs response crosses over the cutoff wavelength obscuring the response from just the QDs and

quantum well. This is illustrated Figure 4.12b by the solid areas under the EQE curves at 300 K. While this happens in both cells, the effect is greater in $Cell_{QD}$ since its GaAs response has not been degraded. Yet even considering the larger contribution from the bulk response in $Cell_{QD}$, $Cell_{QD+Defects}$ still performed better at low temperatures when measured using the 870 nm high-pass filter. This is seen in Figure 4.13.

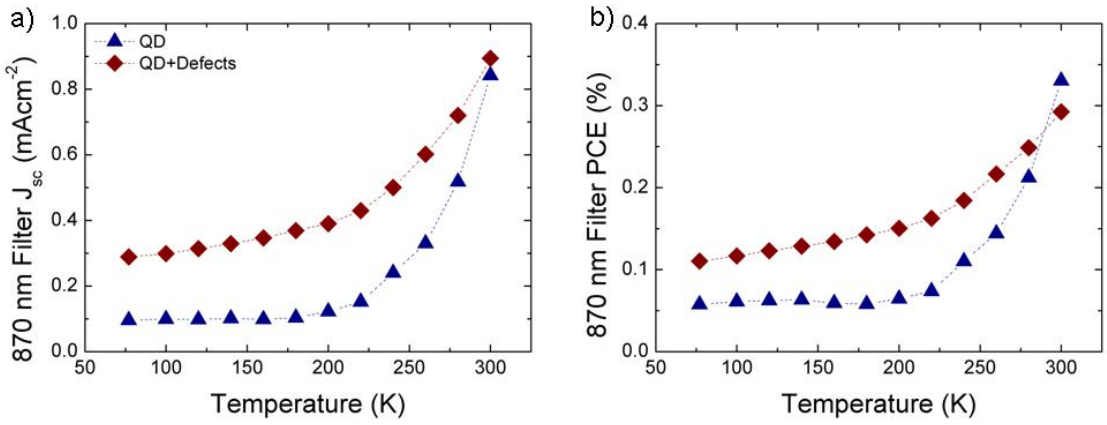

Figure 4.13. Temperature dependent J_{sc} (a) and PCE (b) for the QD cells illuminated through a 870 nm high-pass filter.

Room temperature *JV* measurements shown in Figure 4.14 were taken using a 1000 nm high-pass filter. The results in this case show a higher J_{sc} and higher PCE for $Cell_{QD+Defects}$ despite the lower V_{oc} and FF (Table 4.3).

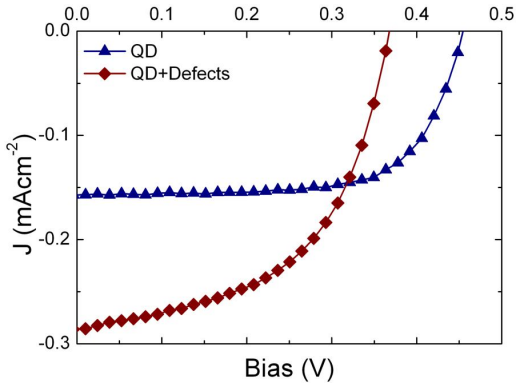

Figure 4.14. Room temperature *JV* curves for the QD cells illuminated through a 1000 nm high-pass filter.

Table 4.3. Room temperature solar cell parameters for the QD cells illuminated through a 1000 nm high-pass filter.

Cell	J_{sc} (mAcm^{-2})	V_{oc} (V)	FF	PCE (%)
QD	0.16	0.45	0.69	0.049
QD+Defects	0.29	0.37	0.53	0.056

Even though the results are not as dramatic when measured using the high-pass filters compared to integrating the long wavelength EQE with the solar spectrum, they do demonstrate that $Cell_{QD+Defects}$ does actually perform better for sub-bandgap photons. One possible reason for this is that the defects aid in carrier extraction from the confined QD states, allowing more charge carriers to contribute to the photocurrent. Another possibility, mentioned later in this section, is that the sub-bandgap absorption is increased due to the presence of the defects resulting in more charge carriers. Of course the penalty for the better sub-bandgap performance of $Cell_{QD+Defects}$ is quite high due to the threading dislocations degrading the GaAs emitter, and ultimately the cell's performance. However, it does open up the idea of selective defect addition to aid in absorption or carrier escape from the QDs in a QD solar cell if the defects can be prevented from propagating into the emitter. This would not be applied in an IBSC (or at least a traditional one) since the escape route provides a non-optical pathway for carriers to transition from the confined state into the conduction band. In other words, the two Fermi levels are not isolated which results in a reduced V_{oc}.

The next step is to consider the charge extraction mechanism in the two QD cells. It has been shown from thermal studies that the charge extraction mechanism depends on the spacer layer thickness between QD layers: thermally activated escape is the dominant mechanism in thick layers while tunnelling plays an important role when thin layers are used[148,164,165]. A spacer layer of ~85 nm was considered thick and one

of ~15 nm was considered thin[148]. The spacing between QD layers for the cells here is ~29 nm (see section 4.3.3). Consistent with results from Antolin *et al*. on cells with thin spacer layers[148], very little sub-bandgap photocurrent suppression was seen at low temperatures in EQE measurements (Figure 4.7c-d), which suggests tunnelling escape of charges in both QD cells at low temperatures. The relatively small change with temperature of the QD peak EQE compared to the complete suppression of the QD peak below ~100 K that has been reported for cells with thick spacer layers demonstrates the effects of different extraction mechanisms (tunnelling versus thermal).

Further evidence is seen in Figure 4.15 which shows an Arrhenius plot of the maximum EQE value of the peak near 1220 nm attributed to the absorption and extraction from the QDs. At low temperatures, very little temperature dependence is seen for either sample, again suggesting temperature independent tunnelling escape as the dominant escape mechanism. However, both cells exhibit transition points near 220 K. First, $Cell_{QD}$ drops off from its near linear trend as temperature increases (inverse temperature decreases). A drop from the linear trend in cells with thick spacer layers has been reported to be due to complete extraction of carriers from the QDs through thermal processes at temperatures above the drop from linear temperature[148]. That could be the case here for $Cell_{QD}$. However if that is true, the low sub-bandgap photocurrent compared to $Cell_{QD+Defects}$ needs to be addressed. The continued increase in the QD peak EQE of $Cell_{QD+Defects}$ with increasing temperature indicates that not all of the carriers have been extracted from the QDs at temperatures up to 340 K. Therefore if all the carriers have been extracted from the QDs in $Cell_{QD}$ by ~220 K, but in $Cell_{QD+Defects}$ they still have not all been extracted by 340 K, $Cell_{QD}$ might be expected to have a larger sub-bandgap photocurrent than $Cell_{QD+Defects}$ at

temperatures above 220 K (contrary to the results shown in Figure 4.7). One possible explanation is that not all of the extracted carriers in $Cell_{QD}$ contribute to the current. In other words, a larger fraction of carriers extracted from the QDs contribute to the current in $Cell_{QD+Defects}$ than in $Cell_{QD}$. Another more likely possibility is that $Cell_{QD+Defects}$ has stronger sub-bandgap absorption due to the dislocation defects and therefore produces a larger current. This is an area that needs further investigation. Another aspect that needs to be considered if all the charges are thermally extracted from the QDs in $Cell_{QD}$ is the PL results shown in Figure 4.5. The PL quenching in $Cell_{QD+Defects}$ near 200 K was attributed to charge extraction from the QDs (section 4.3.4.1). The reason the PL is not quenched for $Cell_{QD}$ if all the charges are extracted is the relatively small contribution from the QDs to the overall current. In $Cell_{QD+Defects}$ the contribution from the QDs is a much larger percentage of the overall current.

The response of $Cell_{QD+Defects}$ on the other hand exhibits a substantially different trend as temperature is increased over ~220 K. In this case thermal activation has not extracted all the carriers, even at temperatures up to 340 K. Carrier escape by thermal activation is proportional to $\exp(-E_A / kT)$ where E_A is the confined carrier activation energy, k is the Boltzmann constant, and T is the temperature[148]. A linear fit above 220 K for $Cell_{QD+Defects}$ gives an activation energy of 48 meV. The same fit applied to temperatures below ~220 K yields 1.8 and 2.3 meV for $Cell_{QD}$ and $Cell_{QD+Defects}$ respectively which again shows the very small temperature dependence in that regime.

The activation energy for $Cell_{QD+Defects}$ at temperatures over 220 K is in line with admittance spectroscopy results that have shown activation energies from 18 –

125 meV for hole extraction in InAs/GaAs QDs[166] and stress-induced traps in Au/*n*-GaAs Schottky diodes with embedded InAs QDs which have been determined to have activation energies as low as 24 meV[167]. Defects within GaAs have also been attributed with the creation of traps[168,169].

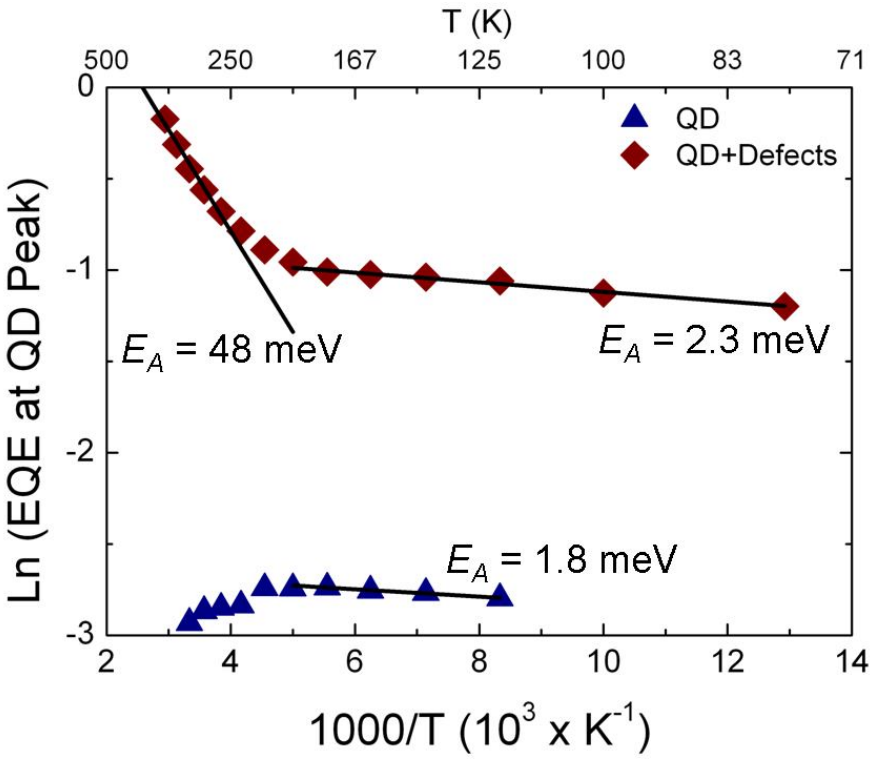

Figure 4.15. Arrhenius plot of the EQE value at the QD peak. The fits are used to determine the thermal activation energy.

This analysis shows tunnelling is significant at low temperatures in $Cell_{QD+Defects}$. As the temperature is increased over ~220 K, thermal excitation of carriers from defect induced traps becomes the dominant charge extraction mechanism.

4.3.6 In(Ga)As QD Solar Cell Further Work

Further investigation into trap assisted carrier escape from the QDs is of considerable interest. Much of this requires new cells grown by the group at University College London which could then be characterised using the techniques presented here. The

new cells need to be such that different defect compositions can be studied. Unfortunately it doesn't look possible to grow cells that include the same dislocations within the intrinsic region, but that do not propagate up into the emitter region due to strain on the crystal lattice. However, different growing temperatures during the spacer layer growth may allow for smaller defects within the intrinsic region that could be strain compensated near the top to prevent propagation into the emitter. Another possibility is lightly doping the intrinsic region or adding point defects. If a range of defect profiles can be created, this would present a good base to perform the same characterisations done in this chapter to investigate further if defects can be used to enhance QD solar cell performance.

Going a different direction, work towards an IBSC should be investigated. From a discussion with the collaborators at University College London, they believe they can fabricate the same type of QD cells as in this study, but without the InAs wetting layer. This could prove to be very interesting, since it might remove any non-optical pathways from the intermediate band to the conduction band by removing the quantum well (and the near continuous set of energy levels within it) making the energy difference between the QD confined energy levels and the conduction band greater. Such a system might prevent the reduction in V_{oc} due to Fermi level isolation between the intermediate and conduction bands. If these cells could be grown, the electrical characterisations done in this chapter would have the potential to yield a lot of information towards the realization of an IBSC that outperforms the reference cell.

A simple experiment that would be useful is to perform temperature dependent *JV* measurements with the 1000 nm high-pass filter to verify the higher QD performance in $Cell_{QD+Defects}$ to that of $Cell_{QD}$. One of the problems with doing that now is that the

thermal cycling from previous temperature measurements has taken its toll on the cells. The bonding method (conductive paste) does not do well with thermal cycling, and the cells have fallen off the copper cathode multiple times. Each time it has become harder to re-bond the connections. New cells will most likely need to be processed.

Another relatively simple set of experiments is absorption measurements. An absorption comparison between the QD cells at sub-bandgap wavelengths would determine whether a higher absorption in $Cell_{QD+Defects}$ is the reason for the increased sub-bandgap photocurrent.

4.4 Dilute Nitride Solar Cells

4.4.1 GaInNAs Introduction

It has been proposed that the maximum thermodynamic efficiency limit under the 500-sun low aerosol optical depth solar spectrum of a triple-junction GaInP/GaAs/Ge solar cell can be increased from ~40% to ~44% by replacing the Ge subcell with a dilute nitride such as GaInNAs (bandgap of 0.9 eV) to form the triple-junction cell illustrated in Figure 4.16a[170]. GaInNAs has also been suggested as a 1 eV bandgap material that has the potential to be lattice-matched to GaAs and Ge in order to produce the four junction cell shown in Figure 4.16b with an efficiency limit of ~52%[131].

Growing GaInNAs with enough nitrogen is challenging due to phase segregation[171]. In order to prevent phase segregation, low temperature growth conditions (near 410 ^{0}C to 470 ^{0}C) [172] are used which results in degradation to the material's optical properties[172,173] due to an increased number of nonradiative recombination

centres[174,175,176]. Therefore rapid thermal annealing is used to improve the material quality[177,178].

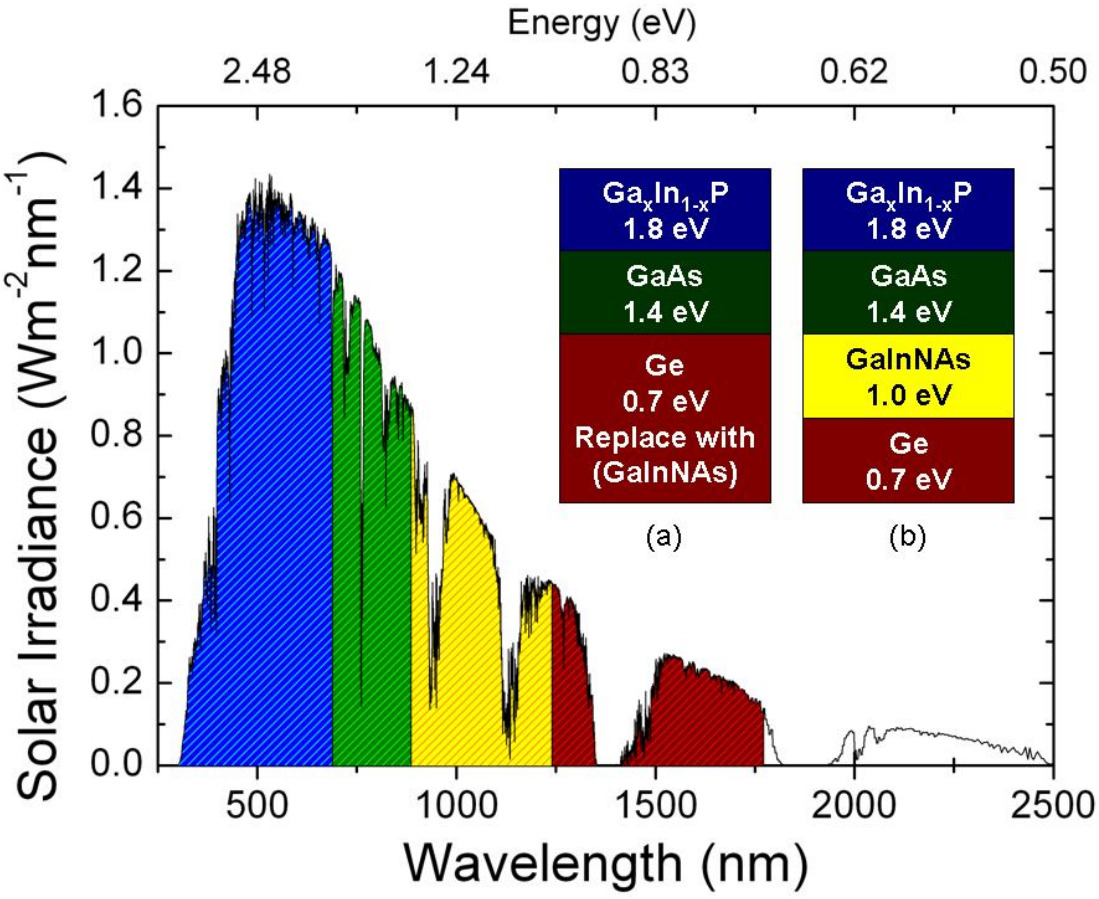

Figure 4.16. The maximum thermodynamic limit of the triple junction cell shown in (a) can be increased by replacing the Ge subcell with GaInNAs. The maximum efficiency can be increased even further with the four layer cell shown in (b).

Rapid thermal annealing at high temperature (910 ^{0}C) has been shown to increase the depletion region in GaInNAs solar cells with a bandgap of 1eV (the bandgap of interest for multi-junction cells)[179]. However, radiative recombination was concluded to limit the cell performance compared to cells annealed at lower temperatures. In the work presented here, capacitance and impedance measurements are used to show a higher presence of non-radiative recombination centres in the higher temperature annealed GaInNAs *p-i-n* cells as well.

Three different annealing temperature (825, 875, 910 ^{0}C) corresponding to $Cell_{825}$, $Cell_{875}$, and $Cell_{910}$ were performed on cells of the structure seen in Figure 4.17. $Cell_{875}$ deviates from this structure in the intrinsic region thickness. Instead of 1500 nm, the thickness is 1000 nm for $Cell_{875}$.

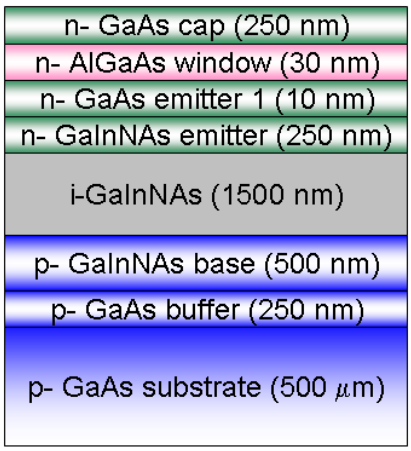

Figure 4.17. GaInNAs cell structure. The intrinsic region for $Cell_{875}$ is 1000 nm thick instead of 1500 nm.

4.4.2 GaInNAs Solar Cell Results and Discussion

Figure 4.18a-b shows the CV results and Mott-Schottky fits for the three anneal temperatures taken at 5 kHz modulation frequency. Both V_{bi} and N_A are affected by the anneal temperature, with higher temperatures causing both to decrease. At an annealing temperature of 910 ^{0}C , the drop is very significant as seen in Figure 4.18c-d which demonstrates the effectiveness of high-temperature annealing at removing the background doping.

The depletion width is also affected by the anneal temperature as shown in Figure 4.19a. The deviation of the calculated depletion width based on V_{bi} and N_A from that determined by the parallel plate capacitor model (explained in section 2.2.4) below

0 V for $Cell_{910}$ indicates it becomes fully depleted under reverse bias. At zero bias, the depletion width as a function of anneal temperature is shown in Figure 4.19b.

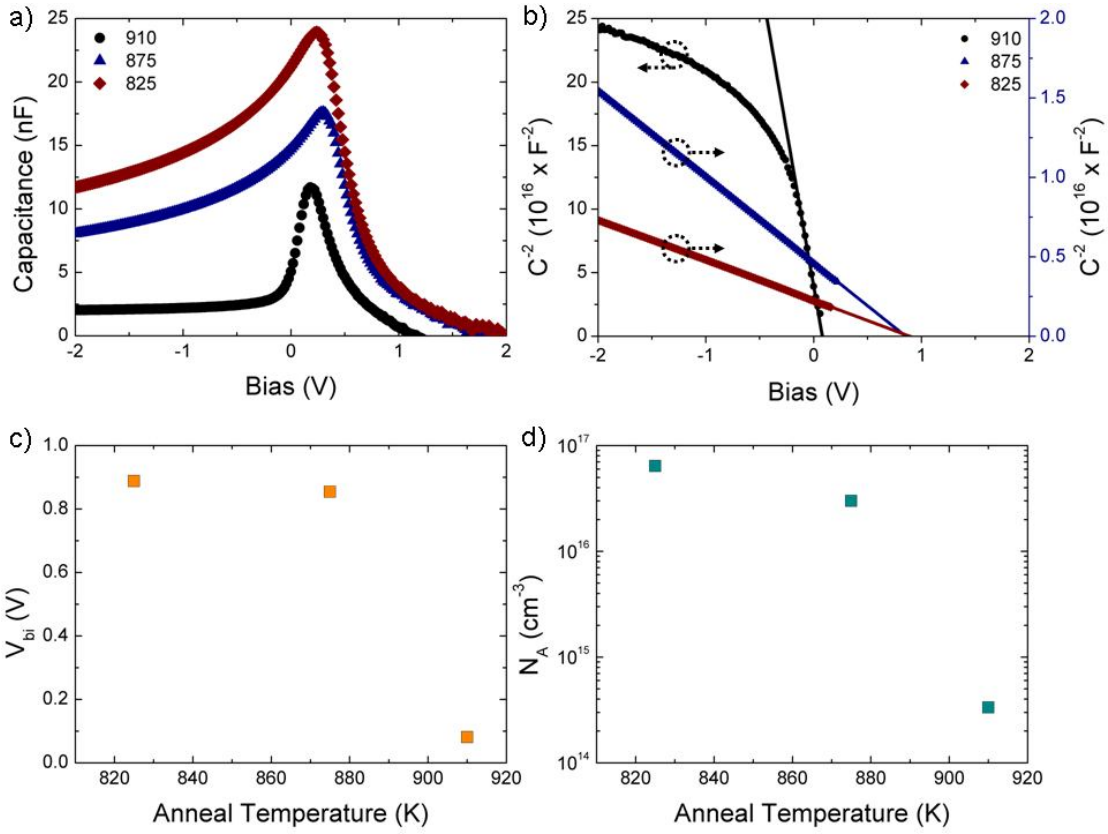

Figure 4.18. a) Room temperature CV results for the three GaInNAs cells. b) The symbols are the corresponding C^{-2} curves to the data in (a). The solid lines are the Mott-Schottky fits. c) Built in bias (V_{bi}) as a function of anneal temperature. d) Doping density (N_A) as a function of anneal temperature.

Higher temperature annealing produced a larger depletion width which aids in carrier extraction. This was confirmed by a larger J_{sc} for $Cell_{910}$ compared to the lower temperature annealed cells[179]. However, the V_{oc} for $Cell_{910}$ was significantly lower than the other cells negating any benefits from the increased J_{sc}[179]. Analysis of the V_{oc} and N_A frequency dependence can explain the drop in V_{oc} for $Cell_{910}$.

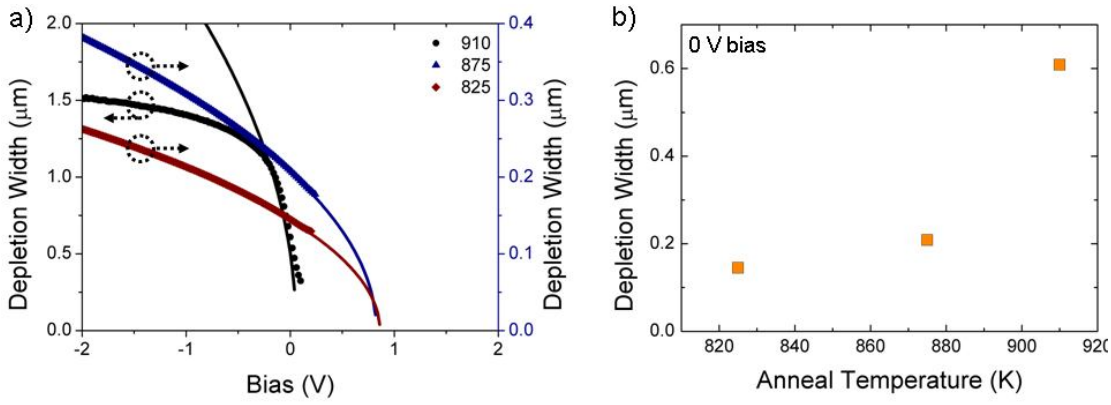

Figure 4.19. a) Bias dependent depletion widths. The symbols represent the value calculated using the parallel plate capacitor model and the solid lines represent the value calculated using V_{bi}, N_A, and equation (1.3). The deviation of the two methods for $Cell_{910}$ indicates the cell has become fully depleted. b) The depletion width at zero bias as a function of anneal temperature.

The V_{bi} and N_A values derived from the Mott-Schottky fits are very frequency dependent for $Cell_{910}$ compared to relatively stable values in $Cell_{825}$ and $Cell_{875}$ as seen in Figure 4.20. The large variation in values with frequency for $Cell_{910}$ is a good indicator of the presence of defect states that are not able to respond to higher frequency modulation[55]. It was previously stated that rapid thermal annealing is used in dilute nitrides to remove non-radiative recombination centres[177,178]. However, it has also been shown that over-annealing (annealing at higher temperatures than the optimum temperature) induces defects within the material[133,180,181,182,183]. These defects have been attributed to both propagation of arsenic vacancies created at the surface during the annealing process[180] and structural degradation of the dilute nitride material[183]. Although the mechanism of defect formation was not studied here, the large frequency dependence of the V_{bi} and N_A for $Cell_{910}$ agrees with the reports of defects forming due to high annealing temperatures. Further evidence is seen in the shape of the impedance Nyquist plots for $Cell_{910}$.

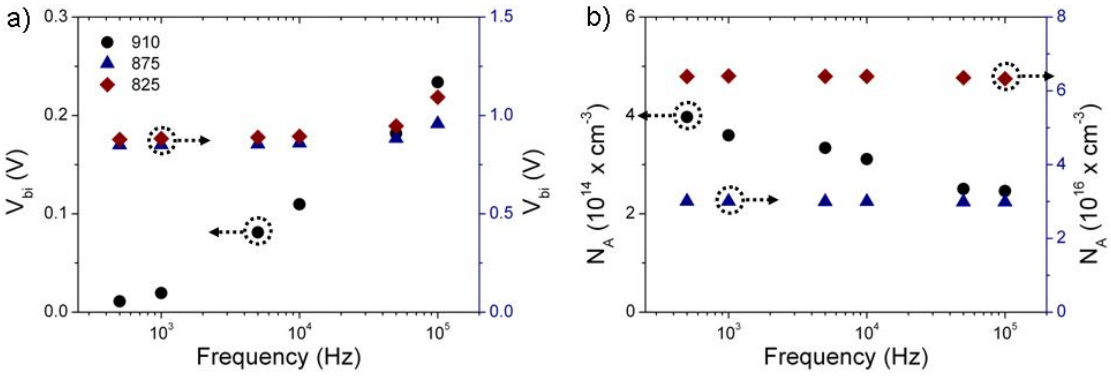

Figure 4.20. Frequency dependent V_{bi} (a) and N_A (b) for the three GaInNAs cells.

Figure 4.21 shows the Nyquist plots for each cell at two different biases (0.3 and 0.5 V) along with the fit result from an equivalent RC circuit (Figure 2.7).

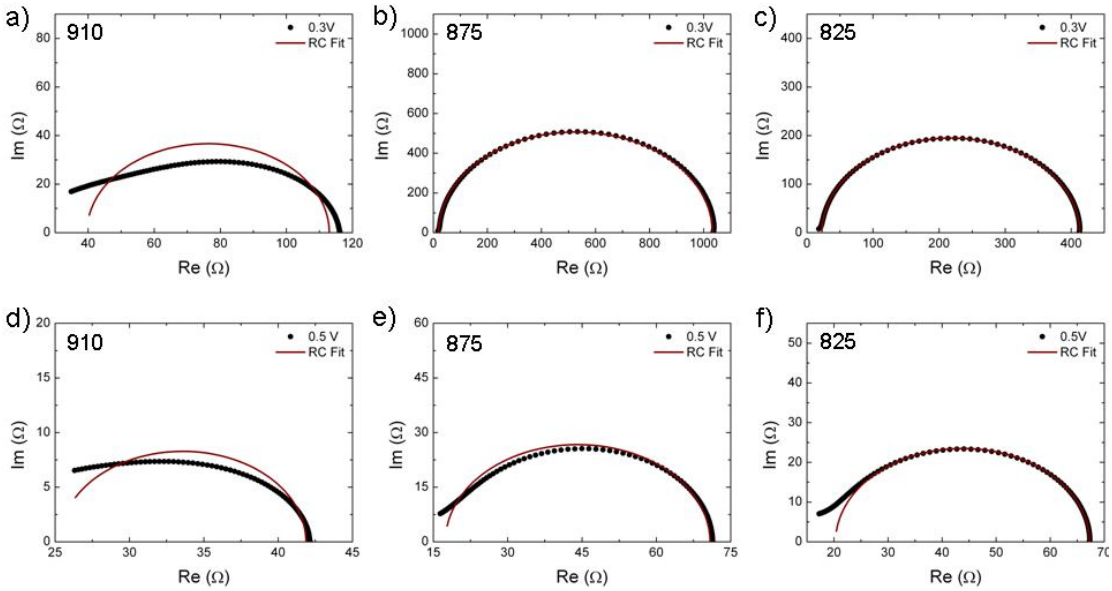

Figure 4.21. Nyquist plots with RC circuit fits at 0.3 V bias (a) – (c) and 0.5 V bias (d) – (f) for the three GaInNAs cells.

$Cell_{825}$ and $Cell_{875}$ have very good fits, although at 0.5 V the high frequency fit deviates a little from the data. $Cell_{910}$, on the other hand, doesn't exhibit a good RC response arc at either bias, which results in poor fits. The shape of the Nyquist plot for $Cell_{910}$ is characteristic of an exponential distribution of traps in disordered organic and inorganic semiconductors[64,65]. This agrees well with the frequency dependent CV

results for $Cell_{910}$, which indicated the presence of defect states that cannot respond to higher modulation frequencies.

Carrier lifetimes are given by the RC time constant of the equivalent circuit and can also be determined by the characteristic peak frequency (section 2.2.5). For $Cell_{825}$ and $Cell_{875}$ these two methods are comparable and the results are shown in Figure 4.22 for forward bias values of 0.3 V to 0.7 V. The minimum value of 0.3 V was chosen based on the location of the capacitance peak value in Figure 4.18a to ensure the devices are in the diffusion capacitance regime and not the depletion capacitance regime. The RC fit for $Cell_{910}$ is not that good due to the high frequency response. However, the RC arc is still partially viewable and the characteristic frequency can be extracted. It turns out the carrier lifetime of $Cell_{910}$ calculated from the characteristic frequency is not much different than that from the RC time constant. The results are also shown in Figure 4.22. As with the In(Ga)As QD cells in section 4.3.4.3, the method used here considers both carriers due to the cell architecture, and results in lifetimes that are a combination of the two carrier types.

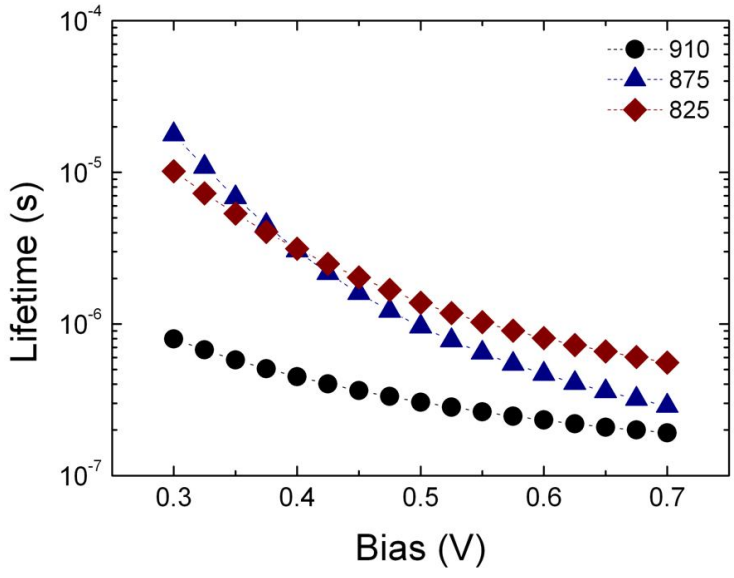

Figure 4.22. Carrier lifetimes for the three GaInNAs cells.

The carrier lifetimes of $Cell_{910}$ are about an order of magnitude less than the other two cells. This is also in agreement with the proposal that annealing at the higher temperature of 910 ^{0}C induces defects in the material. In this case the defects become recombination pathways leading to decreased lifetimes. The reason for the cross-over in lifetime values between $Cell_{825}$ and $Cell_{875}$ is not known at this time and requires further investigation.

4.4.3 GaInNAs Solar Cell Conlcusions

Rapid thermal annealing at 910 ^{0}C compared to lower temperatures of 825 and 875 ^{0}C produced a factor of three larger depletion widths in the GaInNAs *p-i-n* solar cells. However, the large frequency dependence of the CV measurements in the higher annealed cell indicated the presence of defects induced by the higher annealing temperature. This is supported by the shape of the Nyquist plots and lower carrier lifetime of the cell annealed at 910 ^{0}C. Recombination pathways created by the induced defects can account for the lower V_{oc} in $Cell_{910}$.

4.4.4 GaInNAs Solar Cell Future work

Optimisation of the annealing temperature should be accomplished in smaller annealing temperature steps. Although the cell annealed at 910 ^{0}C has a larger depletion width, it also shows the presence of defects which are detrimental to the cell performance. This is an indication that the cell has been over-annealed. Finer temperature steps could find the optimum balance of maximising the depletion width with minimum defect formation. To carry this out, more cells need to be fabricated followed by the characterisation techniques presented in this thesis.

4.5 Conclusion

The electrical characterisation techniques have proven to be very useful in studying the consequences of defect formation in both In(Ga)As QD and GaInNAs solar cells. In the first case, EQE measurements suggested that large dislocation defects within the QD cell actually improve the sub-bandgap performance even though the overall performance suffers significantly. This was further supported by simulation using the sub-bandgap EQE data, and then verified by temperature dependent *JV* measurements on cells illuminated through a high-pass filter.

The poor performance of GaInNAs cells annealed at high temperature was explained by the presence of defects induced by the annealing itself. This was made evident by the frequency dependence of the capacitance results and the behaviour of the impedance frequency response.

Chapter 5

Organic Solar Cells: Polymer Degradation Study and Capacitance Analysis of Thermally Evaporated Thiophene Solar Cells

5.1 Introduction

Research in organic photovoltaics has undergone incredible growth within the last decade. The first solution processed bulk-heterojunction (BHJ) solar cells were reported in 1995[184,185], but the field didn't show much growth until 1999, after which organic solar cell publications grew 65% per year for the next eight years[186]. This growth resulted in organic solar cell publications accounting for 10% of all photovoltaic publications in 2006[186]. Since then the rapid progress has continued and record polymer/fullerene efficiencies over 8% have recently been reported from Konarka[187]. Organic solar cells offer many attractive properties such as the ability to modify the bandgap, the molecular orbital energy level, the wetting and structural properties, and doping levels[25]. Also, organic materials open the way for flexible solar cells that could be incorporated into various consumer items[188]. Perhaps the most attractive quality is the possibility of cheap solar energy resulting from high-

throughput production using well established printing techniques in a roll-to-roll system[188,189,190]. Despite such promising possibilities, organic solar cells still have large hurdles to overcome. For one, exposure to oxygen, moisture, and ultra-violet illumination all seriously degrade the performance of organic solar cells[191]. Another problem is the difficulty in fabricating complex architectures using solution processing techniques due to the limitation of orthogonal solvents for each layer[192].

In this chapter capacitance and *JV* measurements prove to be useful methods for examining material interfaces in solution processed and thermally evaporated organic solar cells. In section 5.2, CV and *JV* measurements are used to monitor the performance, doping density, and formation of an Al_2O_3 layer in P3HT:PCBM bulk heterojunction solar cells as they degrade in air. Capacitance measurements on evaporated thiophene bi-layer solar cells in section 5.3 suggest different crystallization between small and large organic molecules, and may provide a way to investigate the thiophene/fullerene interface.

5.2 Degradation of Organic Solar Cells

5.2.1 Organic Solar Cell Degradation Introduction

Polymer solar cells are an exciting field of study right now with efficiencies rapidly climbing and the promise of novel solar cell applications. However, progress in efficiency is not the only area of concern and without an improvement in cell stability, implementation of polymer solar cells faces a tough challenge[191]. To this end, much work has been conducted studying the mechanics of cell degradation. From early studies, oxygen was known to be the prime cause of cell degradation[193,194]. Further

study has shown that oxygen can cause both reversible and irreversible degradation[195,196]. On the irreversible side, chemical reactions between oxygen and P3HT, for example, result in the formation of carbonyl and carboxyl groups due to covalent bonds between oxygen and carbon[197], which then act as charge traps[198]. The deep traps formed due to photo-oxidation in MDMO-PCBM solar cells have been reported to reduce charge-carrier mobility which ultimately leads to a reduction in J_{sc}[199]. Reversible degradation occurs through photo-assisted doping by oxygen[200] which increases the mobile hole concentration in thiophenes[201,202,203,204] and decreases conductivity in fullerenes[205,206,207] due to a decrease in mobile electrons[200]. Thermal annealing however can return the material to its former state[200,204,206]. Although the effects of oxygen are greatly enhanced under illumination, oxygen doping of P3HT has also been shown to occur in the dark[208]. Finally, with enough oxygen doping, P3HT and P3HT:PCBM have both been shown to form Schottky contacts with Al creating a bias dependent depletion region at the interface[62,201].

The amount of research studying degradation in polymer solar cells underscores the importance of understanding and extending the lifetime in organic cells. One of the simplest sources of information comes from *JV* curves as a function of time as the cell degrades since J_{sc}, V_{oc}, FF, PCE, R_{sh}, and R_s all come from these measurements[191]. However, many more techniques have been employed to understand organic cell degradation mechanisms. UV-visible spectroscopy has been used to study the rate of PPV degradation due to oxygen[193] and light-beam induced current measurements have produced 2-D maps of the cell's photoelectrical response over time in MDMO-PPV:PCBM cells using a xenon light source[209] and laser illumination[210]. The results showed uniform response initially, but as the cells degraded the response became very spatially inhomogeneous. Infrared spectroscopy and Fourier-transform infrared

spectroscopy have shown a decrease in vinylene bonds with a simultaneous increase in carbonyl groups when PPV cells degrade[211,212,213]. Energy dispersive X-ray reflectometry on MDMO-PPV:PCBM cells have shown possible reactions of the polymer and Al electrode to form aluminium oxide and/or indium migration into the polymer from the ITO[214,215], although further studies in this area have shown that the evaporated Al surface roughness is so large that x-ray reflections are most likely not seen from this layer[216].

One of the pathways for oxygen to enter the cell is through pinholes in the top metal electrode which leads to oxidation of the low work function metal[217]. Oxidation of the polymer from exposure to air was noted by Garcia-Belmonte *et al*. as the reason the polymer becomes doped *p*-type and subsequently forms a Schottky barrier with the aluminium electrode[62]. Using CV measurements and a Schottky analysis, they determined the built in bias and doping density of P3HT in a P3HT:PCBM bulk heterojunction cell that had been annealed prior to depositing the aluminium electrode. Seemann *et al*. investigated the degradation and formation of a Schottky barrier in P3HT:PCBM cells using the same capacitance methods, and found the Schottky barrier didn't form until the cell had sufficient exposure to air[200]. However, in their study they used 10 kHz as the modulation frequency, which neglects the contribution of slower responding charges.

In the work presented here, CV measurements are used to monitor the Schottky junction formed at the P3HT/Al interface in multiple cell configurations (P3HT, P3HT:PCBM annealed and non-annealed, and P3HT:PCBM/LiF) as the cell is allowed to degrade in air. This builds on the techniques described by Garci-Belmonte *et al*[62]. by monitoring the formation of the Schottky barrier, and extends the study of

Seeman *et al.*[200] by comparing the junction evolution in multiple cell configurations (and using a low modulation frequency).

5.2.2 Solution Processed Organic Solar Cell Fabrication

First the BHJ solution was prepared. P3HT from Reike Metals Inc. and PCBM from Nano-C were dissolved in chlorobenzene with a weight ratio of (1:0.8). The solution was continuously stirred overnight at ambient temperature. Once the BHJ solution was ready, ITO coated glass substrates were etched and cleaned. The cleaning process consisted of sonication for 6 minutes in a detergent solution, sonication for 6 minutes in de-ionized water, soaking for 5 minutes in 50 ^{0}C acetone, and finally soaking for 5 minutes in 50 ^{0}C isopropanol. After this the substrates were plasma etched in an oxygen plasma for 30 seconds. Next PEDOT:PSS was spin cast at 5000 RPM onto the substrates and annealed at 140 ^{0}C for 7 minutes. Following this the substrates were transferred to a nitrogen environment glovebox where the P3HT:PCBM solution was spin cast onto the substrates at 700 RPM. One set of cells was also fabricated from P3HT solution (no PCBM). From this point the fabrication varied depending on the specific cell. However, in general the cells were placed in a vacuum chamber and aluminium electrodes were thermally evaporated through a shadow mask. The specific cell differences are discussed in section 5.2.3.

The final cell geometry is shown in Figure 5.1. Each substrate contained three different cells determined by the overlap of the Al and ITO strips. The cell area was 0.03 cm^2. Also shown is a layer of LiF between the active layer and Al. This was only included in one set of cells.

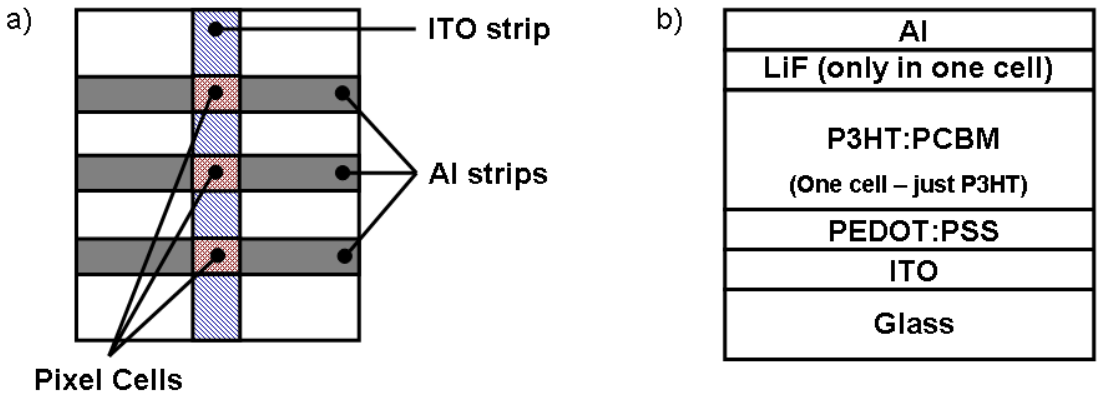

Figure 5.1. a) Three solar cells (termed pixel cells) per substrate are determined by the ITO and Al overlap. b) The solar cell layer structure. LiF was included in only one cell (P3HT:PCBM cell). One cell was fabricated from P3HT instead of P3HT:PCBM. The layers are not to scale.

5.2.3 Organic Solar Cell Degradation Results and Discussion

Five different cell configurations were investigated and are shown in Table 5.1. One device had an active material of P3HT instead of P3HT:PCBM, one had a 2 nm layer of LiF evaporated between the active layer and Al electrode, one was annealed prior to depositing the Al electrode, and one after.

Table 5.1. Degradation cell configurations.

Material	LiF	Pre-Anneal	Post-Anneal
P3HT			
P3HT:PCBM			
P3HT:PCBM			X
P3HT:PCBM		X	
P3HT:PCMB	X		

The focus of the work presented here is on capacitance measurements taken over time as the cells degraded in air. All capacitance measurements were taken in the dark, and the cells were maintained in the dark except when illuminated *JV* curves were taken. The *JV* data is presented in section 5.2.3.1 followed by the CV results.

5.2.3.1 *JV* Degradation

Although the main focus of this set of experiments was on the evolution of the CV characteristics while the cells degraded in oxygen, a brief look at the solar cell parameters compliments the results. In all cells the largest effect was seen in the J_{sc}. Figure 5.2 shows the *JV* curves and J_{sc} as functions of air exposure time, demonstrating the decrease in J_{sc}. The decrease is a well known phenomenon and agrees with what has been previously reported[196,218,219].

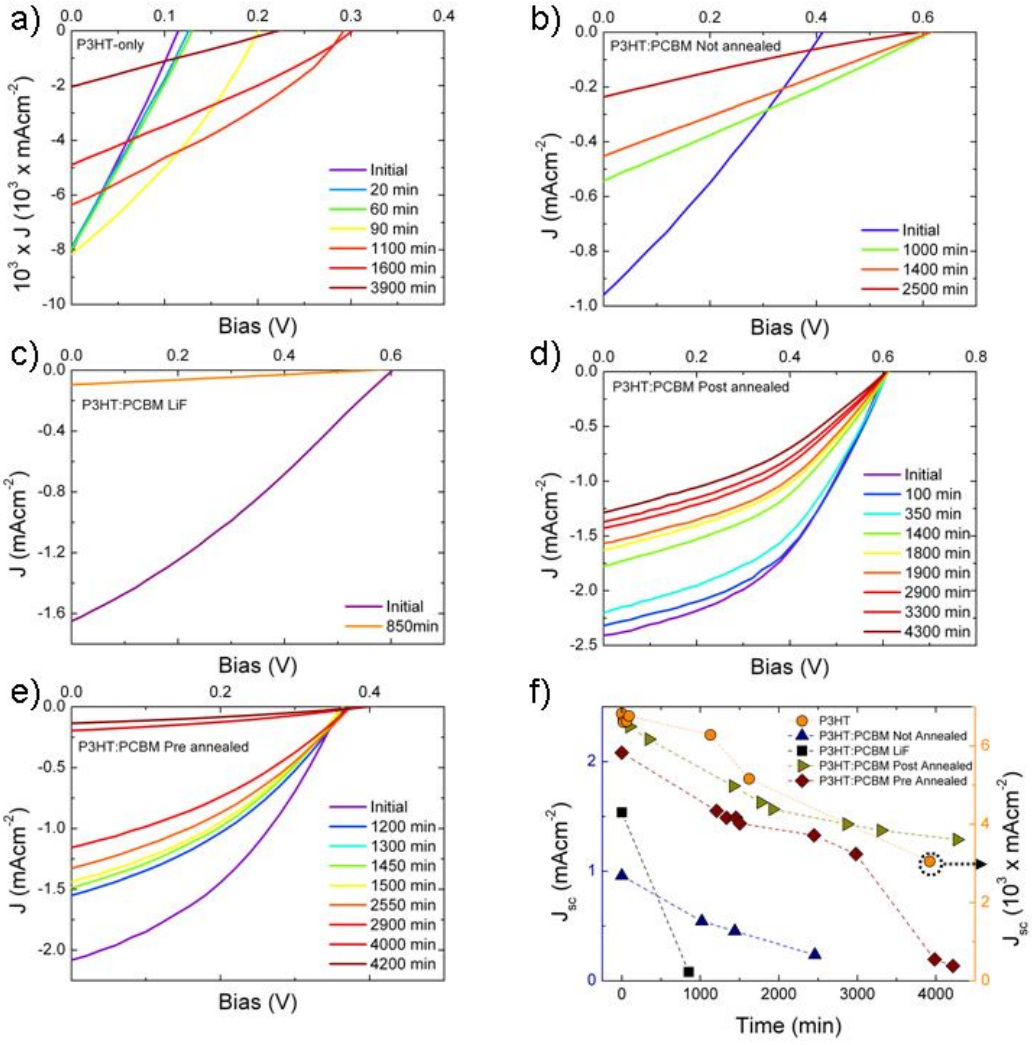

Figure 5.2. AM1.5 Illuminated *JV* curves as a function of exposure to air. Note the scales are different. a) P3HT-only. b) P3HT:PCBM not annealed. c) P3HT:PCBM with LiF. d) P3HT:PCBM post annealed. e) P3HT:PCBM pre annealed. f) J_{sc} as a function of exposure time for the five cells.

The V_{oc} on the other hand did not degrade over the entire exposure time period. Neglecting the cell with LiF since only two data points were taken (initial and final times), all the other cells show an initial increase followed by a decrease in V_{oc} (Figure 5.3). The pre-annealed cell actually showed an increasing trend over the entire time. The amount of V_{oc} change varied depending on the cell, ranging from very little change in the post-annealed cell (0.008 V difference between the maximum and minimum V_{oc}) to large changes in the non-annealed cell (0.2 V between maximum and minimum). This is depicted in Figure 5.3. Only the P3HT cell saw any increase in PCE due to the increased V_{oc} and that was only up to ~1000 minutes. After that the PCE decreased due to the decrease in both V_{oc} and J_{sc}. In all the other cells the decrease in J_{sc} was the dominant factor and directed the PCE as seen in Figure 5.4.

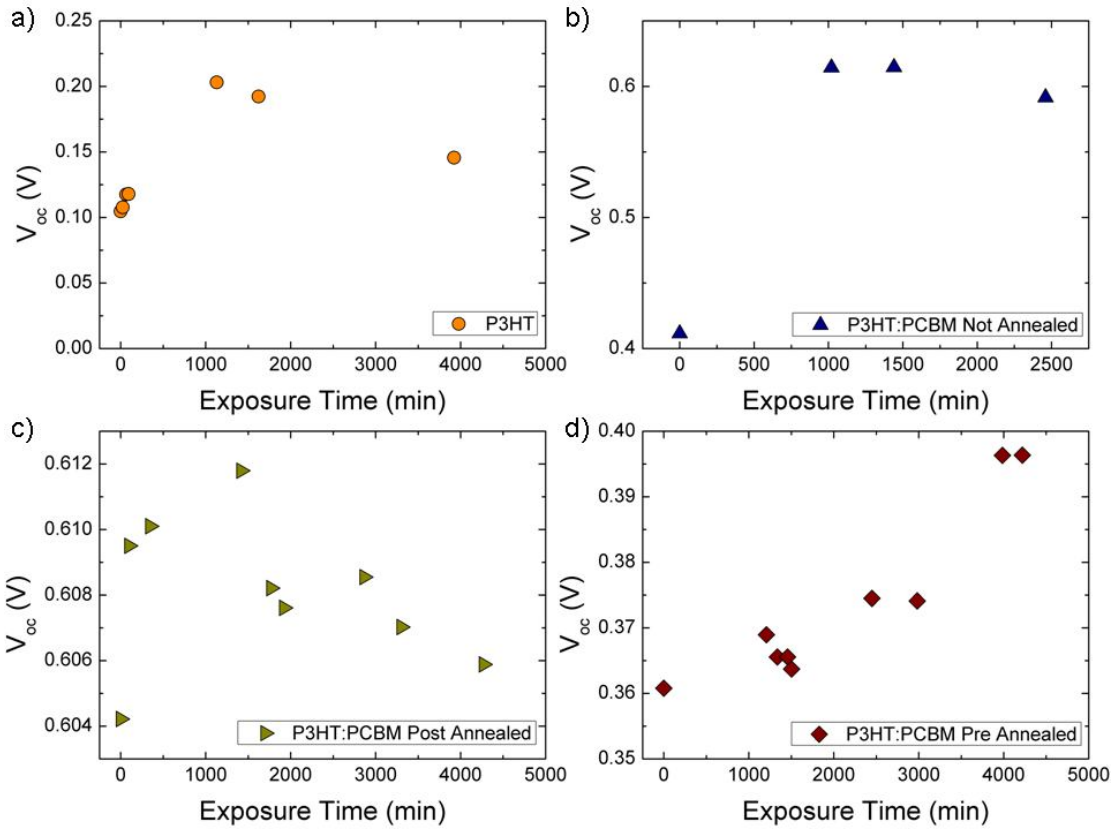

Figure 5.3. V_{oc} as a function of air exposure time. a) P3HT-only. b) P3HT:PCBM not annealed. c) P3HT:PCBM post annealed. d) P3HT:PCBM pre annealed.

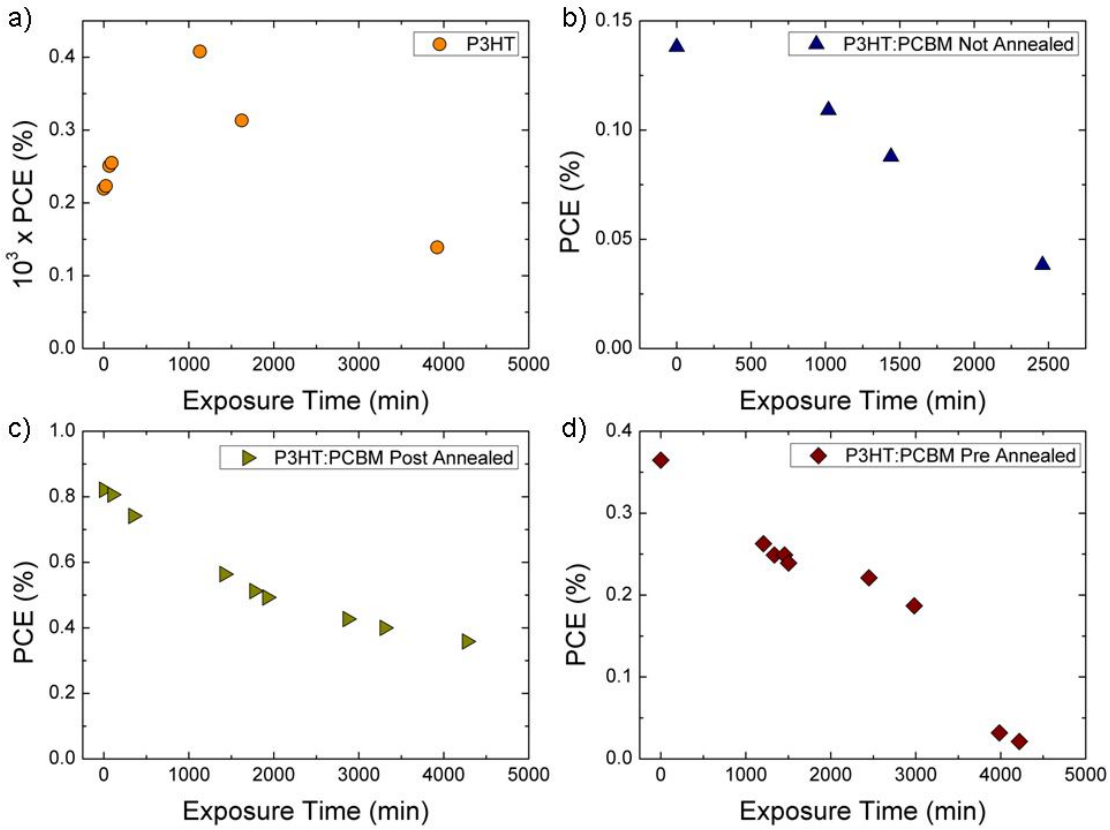

Figure 5.4. PCE as a function of air exposure time. a) P3HT-only. b) P3HT:PCBM not annealed. c) P3HT:PCBM post annealed. d) P3HT:PCBM pre annealed.

The V_{oc} increase is evidence of the formation of an Al_2O_3 hole blocking layer at the Al electrode interface. More evidence for this is presented in the CV analysis (section 5.2.3.2) accompanied by a discussion of the consequences related to capacitance measurements. In relation to *JV* performance, it has been reported in organic bulk heterojunction cells that shunt pathways initially exist through the interpenetrating network from one electrode to the other that reduce the V_{oc}[220,221]. However, annealing under the stress of an Al electrode that has already been deposited produces a vertical segregation of the blended material[28] that reduces the formation of shunt pathways resulting in an increase in V_{oc}[243]. In the results here, the V_{oc} increase seen in the post-annealed cell is much smaller than that in the non-annealed cell, suggesting many of the shunt pathways were removed during the annealing process. The formation of a

hole blocking layer however, brought the V_{oc} of the non-annealed cell up to the same level as the post-annealed cell. In addition to vertical segregation, annealing after the Al deposition has been shown to produce a different P3HT crystal orientation compared to annealing prior to the Al deposition which also increases the V_{oc} in the post-annealed process[242]. Finally, annealing prior to depositing the Al electrode may lead to overgrowth in the PCBM clusters, which degrades the morphology and can lower the V_{oc}[242,222,223].

In the case of the non-annealed cell presented here, a large initial V_{oc} increase is observed. The V_{oc} of two other non-annealed cells (not shown here) were monitored under degradation with initial increases of 0.05 V and 0.55 V. In all three of these cells the maximum V_{oc} value was slightly over 0.6 V (there was a very wide initial V_{oc} range between the cells). The initial increase in V_{oc} for the non-annealed cell demonstrates the formation of a hole blocking layer that reduces shunt pathways. This is seen in the other cells as well, although not as dramatically. In the case of the post-annealed cell, very little increase is observed followed by very little decrease. Interestingly, the pre-annealed sample never reached the V_{oc} value that the non-annealed and post-annealed cells reached (~0.4 V compared to ~0.6 V). Possible reasons for this may be due to different crystal orientation[242] or crystal overgrowth[242,222,223] in the pre-annealed cell as described in the previous paragraph. Reports for pre-annealed cells in annealing experiments have yielded V_{oc} values near 0.4-0.5 V compared to values above 0.6 V for post-annealed cells[242,243] which is consistent with the values found here. Non-annealed cells reported from the same set of experiments gave V_{oc} values ranging from 0.54 to 0.64 V showing a varied range (although not as dramatic as that shown here) of values[242,243]. Of course the cost of V_{oc} increase due to the hole blocking layer formation during degradation in the

experiments performed here is a large reduction in J_{sc} that ultimately lowers the PCE (except in the P3HT device that has a very low J_{sc}).

Following the initial increase in V_{oc}, it decreased for all cells except the pre-annealed cell. Most likely the pre-annealed cell would demonstrate the same behaviour with extended exposure to air. The decrease in V_{oc} with exposure to air is consistent with literature reports of V_{oc} decreasing when exposed to humid air conditions[218].

Included for completeness here, the FF is shown in Figure 5.5. In all cells, the FF trend was a decrease as the exposure time increased. However, small initial increases are seen in a couple of cells which correlates with the initial V_{oc} increase coupled with a small initial J_{sc} decrease over the same short time span.

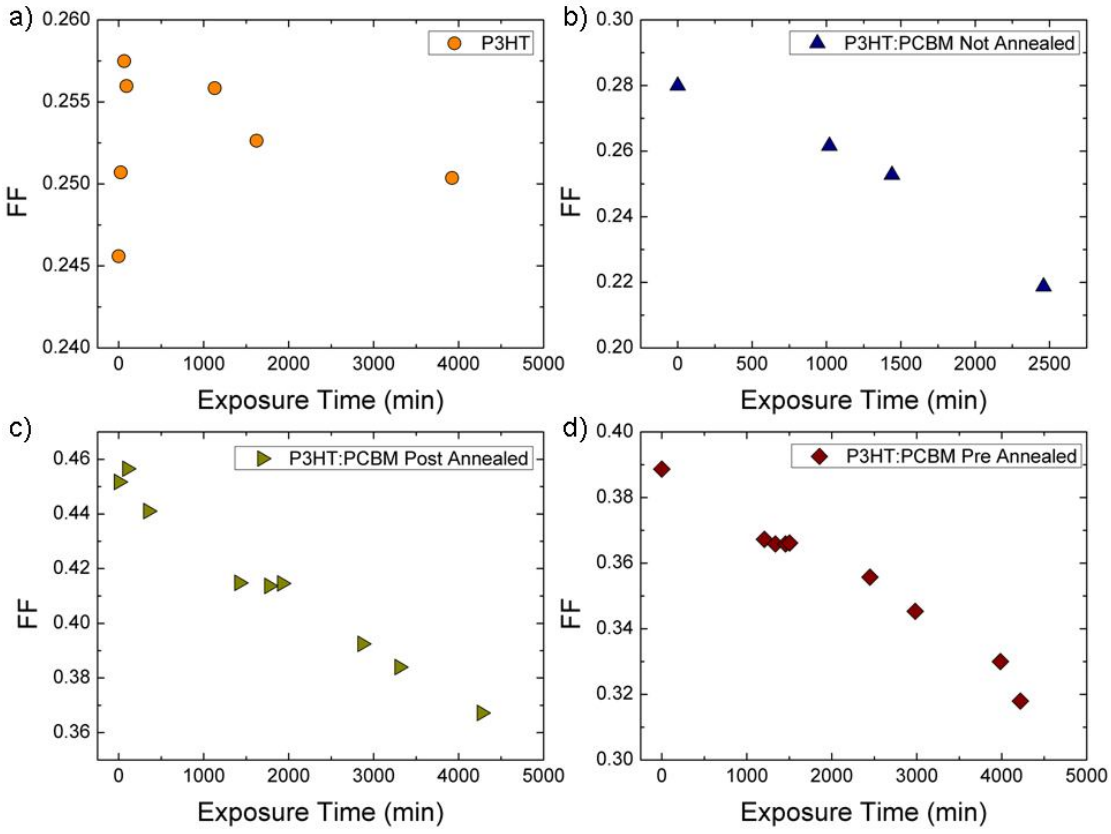

Figure 5.5. FF as a function of air exposure time. a) P3HT-only. b) P3HT:PCBM not annealed. c) P3HT:PCBM post annealed. d) P3HT:PCBM pre annealed.

5.2.3.2 Degradation CV

Example CV and C^{-2} versus bias plots at three different degradation times are shown in Figure 5.6 - Figure 5.10. Two items of interest are visible in the figures. First is the large capacitance peak at high forward bias (near 1 V) that is visible from the start in the cell with LiF and grows in the remaining cells with increased exposure to air. Second is the linear behaviour of the C^{-2} curve under reverse bias for all the cells. In the case of the post-annealed cell the linear region isn't clear until a lengthy exposure to air and it is quite noisy initially for the non-annealed and pre-annealed cells.

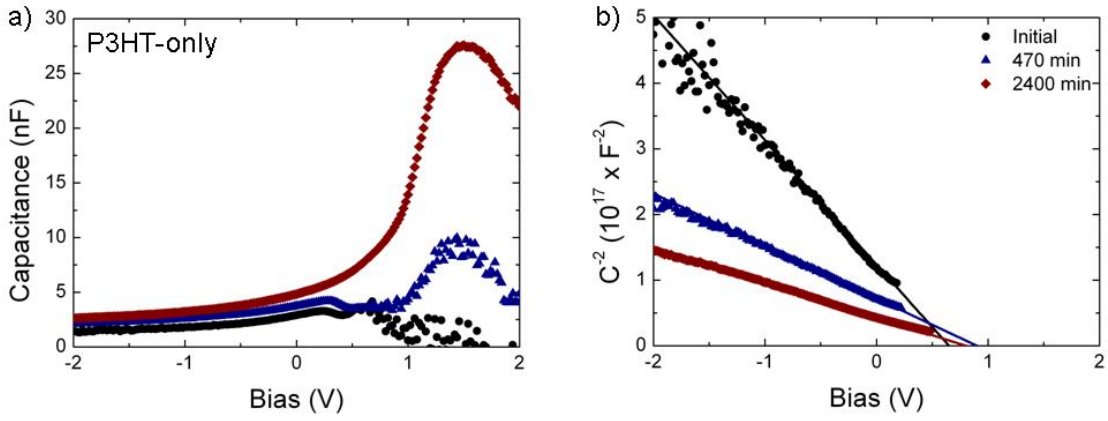

Figure 5.6. P3HT-only cell at three degradation times. a) CV results. b) The symbols represent the C^{-2} versus bias data points. The solid lines show the Mott-Schottky fits.

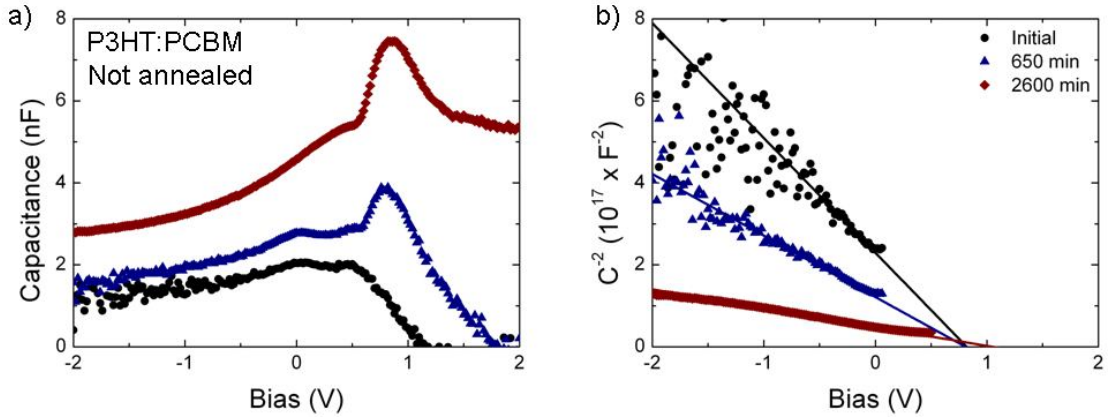

Figure 5.7. Non-annealed P3HT:PCBM cell at three degradation times. a) CV results. b) The symbols represent the C^{-2} versus bias data points. The solid lines show the Mott-Schottky fits.

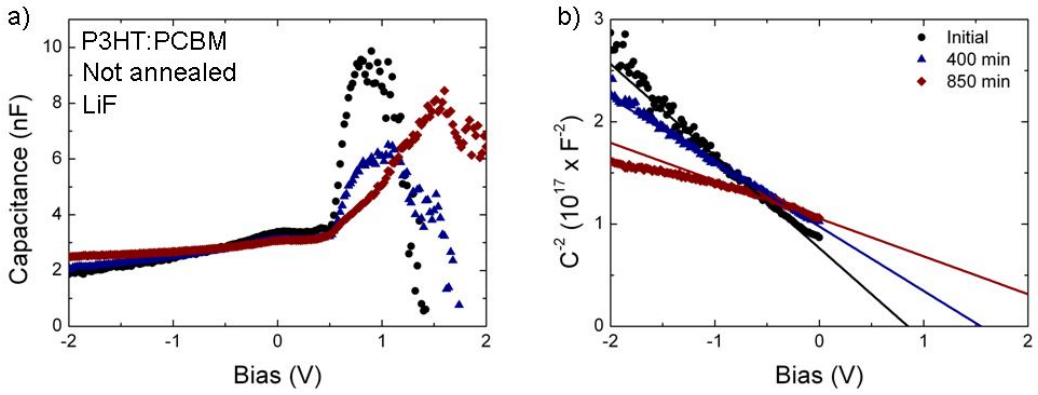

Figure 5.8. Non-annealed P3HT:PCBM cell with a 2 nm layer of LiF at three degradation times. a) CV results. b) The symbols represent the C^{-2} versus bias data points. The solid lines show the Mott-Schottky fits.

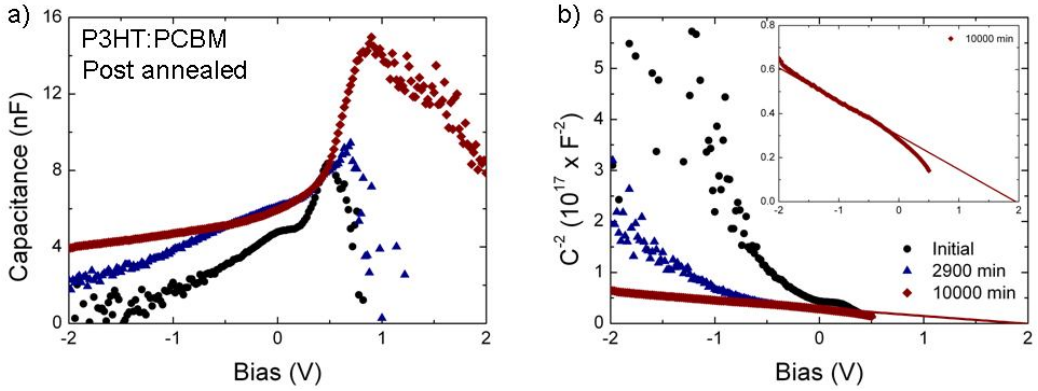

Figure 5.9. Post-annealed P3HT:PCBM cell at three degradation times. a) CV results. b) The symbols represent the C^{-2} versus bias data points. The solid line shows the Mott-Schottky fit for the longest degradation time. The inset shows an expanded view of the fit.

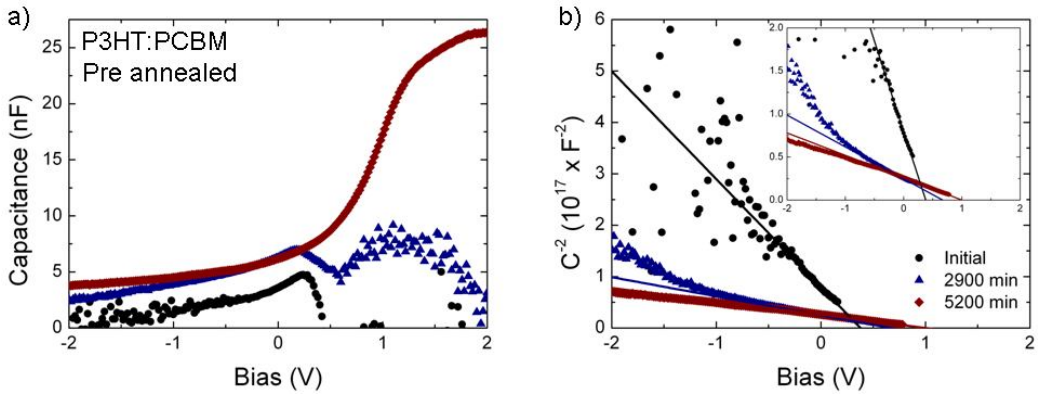

Figure 5.10. Pre-annealed P3HT:PCBM cell at three degradation times. a) CV results. b) The symbols represent the C^{-2} versus bias data points. The solid lines show the Mott-Schottky fits. The inset shows an expanded view of the fits.

5.2.3.2.1 Excessive Capacitance in Forward Bias

The first item considered here is the high forward bias capacitance peak that is strongly present from the initial measurement in the cell with LiF and gradually appears in the remaining cells. Excessive capacitance in forward bias has been attributed to the injection of minority carriers in Schottky diodes[63,124] , p-n junctions[58], and the P3HT/Al Schottky contact[62] in P3HT:PCBM bulk heterojunction solar cells. If however minority carrier injection becomes limited in some manner, the excessive capacitance reaches a peak value and can exhibit inductive behaviour[62]. In Schottky diodes, one of the effects of high minority carrier injection is a reduced rate of minority carrier injection increase due to the minority carrier density becoming comparable with the impurity concentration within the neutral region[63]. Another mechanism that reduces the minority carrier injection rate is the limited number of minority carriers that can be supplied by the contact[63].

In the cells studied here, only the cell fabricated with a LiF layer between the P3HT:PCBM and Al electrode shows excessive capacitance under forward bias at the initial measurement (before exposure to air). A thin layer of LiF deposited at the electron injecting electrode in organic electroluminescent devices has been shown to enhance electron injection into the device[224,225,226]. In addition, a thin layer of LiF has been shown to act as a hole blocking layer in organic LEDs and bulk heterojunction solar cells[227,228,229]. Therefore for the cell with a LiF layer, the LiF enhances electron injection into the P3HT:PCBM under forward bias causing the sharp increase in capacitance. At the same time, hole extraction at the Al electrode is suppressed by the layer of LiF which reduces the inductive effect of majority carrier extraction by the Al electrode. Then at sufficient forward bias minority carrier injection becomes limited,

possibly due to high minority carrier density or the limitation of the electrode as mentioned in the previous paragraph[63], and the capacitance drops off.

The excessive capacitance in the remaining cells is apparent only after the cells have degraded in air. In this case, exposure to air is expected to create a thin aluminium oxide layer between the P3HT:PCBM and Al electrode[62]. Aluminium oxide (Al_2O_3) layers in organic electroluminescent devices and LEDs have been shown to enhance minority carrier injection at the aluminium electrode[230,231]. For electroluminescent devices made with aluminium tris(8-hydroxyquinoline) (Alq_3) such that the interface is of the architecture $Alq_3/Al_2O_3/Al$, the enhanced minority carrier injection due to the Al_2O_3 layer was attributed to a shift in the HOMO level of the Alq_3 compared to that of a device without the oxide layer (Alq_3/Al)[230]. In LEDs based on amino-oxadiazole-fluorenes (AODF)s with Al_2O_3/Al cathodes, the increased minority carrier injection was concluded to be a result of the Al_2O_3 layer preventing the generation of carrier trapping and singlet exciton quenching centres created by the interaction of AODF and Al[231]. Besides enhancing minority carrier injection, Al_2O_3 has also been reported to act as a hole blocking layer in organic LEDs[232]. In the cells studied here without the LiF layer, the absence of an excessive capacitance at forward bias (the capacitance is actually negative in this case) suggests minority carrier injection is initially very low. Without the Al_2O_3 layer to assist with minority carrier injection, the ability of majority carriers to pass into the cathode under sufficient forward bias (flat-band) produces an inductive effect that causes the capacitance to drop sharply and go negative. As the cells are exposed to air, an Al_2O_3 layer forms which assists in minority carrier (electron) injection and reduces majority carrier (hole) extraction at the Al electrode. Now at forward bias the injection of minority carriers causes the capacitance to increase[58,62,63] until the injection again becomes limited and the

capacitance decreases. In terms of performance, this is good as long as the Al_2O_3 layer doesn't become too thick. In organic bulk heterojunction solar cells, the insertion of a thin layer of LiF (< 1.5 nm) increased the cell efficiency by over 20%[233,234]. This was the result of a significant increase in fill factor. The LiF layer also stabilized the V_{oc}. However, at thicknesses above 2 nm the positive effect of the LiF layer was lost due to its high resistivity[233]. This is expected to be the case with the formation of an Al_2O_3 layer as well (thin layers have a positive effect, but the high resistiviy of thicker layers reduces cell performance). At the end of the next section (5.2.3.2.2) a comparison of doping density and series resistance is given (Figure 5.13). The series resistance is found to increase with air exposure time, with the Al_2O_3 layer being a likely contributor.

The onset voltage of the capacitance peak, corresponds to the energy difference between the Al electrode and either the P3HT or PCBM LUMO. For the P3HT-only cell, the onset occurs near 1 V, which corresponds to the ~1 eV difference in energy between the Al electrode and P3HT LUMO level. For the other cells except the post-annealed cell, the onset occurs near 0.6 V, which corresponds to the 0.6 eV energy difference between the Al electrode and the PCBM LUMO level. In this case electrons injected into the PCBM actually become majority carriers within the PCBM, but the effect is the same. For the post-annealed cell, the capacitance peak never becomes fully evident. However, the last measurement in time (shown in Figure 5.9) appears to show the peak forming with an onset near 0.6 V.

The other contact also plays a role in the capacitance peak formation, since the presence of the peak was found to be determined by the minority carrier extraction resistance at the Ohmic contact[124] (discussed previously in section 3.7.3.3). Both the

P3HT and PCBM LUMO levels are at higher energy levels than the ITO electrode suggesting Ohmic extraction of electrons there. However, a hole selective layer of PEDOT:PSS[185] was spin cast on top of the ITO layer for all the cells studied here. This then acts as barrier to electron extraction at the ITO electrode and allows the capacitance peak to form.

5.2.3.2.2 Depletion Capacitance Analysis

Now the reverse bias depletion capacitance is discussed. Initially only the P3HT cell and the cell with a LiF layer show a fairly clear linear region in the C^{-2} trace under reverse bias. The non-annealed and pre-annealed cells initially appear to exhibit linear Schottky regions in the C^{-2} curves as well, but the data is very noisy which could be due to low initial doping values. The post-annealed cell however, doesn't show a clear (non-noisy) linear Schottky region until after a lengthy exposure to air (about 95 hours in this case). This is indicative of very low initial doping followed by slow *p*-doping with exposure to air caused by the post-anneal process.

In support of this idea for the post-annealed cell, Glatthaar *et al*. concluded, using impedance spectroscopy, that post-processed annealing in the presence of a forward bias reduced the doping level in P3HT[235]. However, instead of basing their conclusion on the standard impedance measurement technique to directly determine the doping density (fitting the linear C^{-2} curve linear region with the Mott-Schottky equation), they based their conclusion on a comparison of the impedance spectra of treated and untreated cells which is an indirect method to determine the doping level. The question arises as to why CV measurements were not shown since these are taken in the same manner and with the same equipment as the impedance spectra. Likely this is because a clear Schottky region was not visible in the C^{-2} curves for the annealed

cell (as in the initial post-annealed cell measurements presented here), but no discussion of this is offered in their report[235]. In any event, post-process annealing has been shown to increase the crystallinity of P3HT[236,237,238] and the stability and hence lifetime of P3HT:PCBM BHJ solar cells[239]. This provides another reason for the extended length of time exposed to air before the post-annealed cell shows clear indication of depletion region due to a Schottky barrier at the P3HT/Al interface.

This leads to question why the pre-annealed cell doesn't exhibit the same characteristics, since it is also annealed and appears to have enhanced stability over the non-annealed cells (although not as good as the post-annealed cell) based on the time it takes for the excessive capacitance to form. The differences from the capacitance measurements are a faster appearance of the excessive capacitance peak, the initial appearance of the depletion capacitance (although noisy), and differences in V_{bi} (shown in the next paragraph). Ma *et al*. showed significant differences existed between cells annealed before Al deposition and after Al deposition[240]. The cells annealed after depositing Al electrodes showed enhanced efficiency and thermal stability compared to the cells annealed prior to depositing the Al electrodes. The reason concluded for the better results of the post-annealed cells was a stronger interaction between the heterojunction material and the Al, possibly due to Al diffusion or chemical reactions leading to stronger contacts and increased contact area[240]. Further work in this area has also found Al diffusion into the heterojunction material, larger contact area, decreased contact resistance and the prevention of shunt pathways for cells annealed after Al electrodes have been deposited compared to being annealed prior to depositing the electrodes[241,242,243]. For the pre-annealed cell studied here, the weaker bond with Al compared to the post-annealed cell could lead to better oxygen penetration and faster degradation.

Figure 5.11 shows the V_{bi} and N_A values from fitting the Mott-Schottky equation to the depletion capacitance region in the C^{-2} versus bias curves (see section 2.2.3). Example fits at different degradation times are shown in Figure 5.6 to Figure 5.10. In each of the different cells, N_A increases with longer air exposure indicating the devices become more *p*-doped as expected since oxygen is known to *p*-dope P3HT[244,245]. The V_{bi} on the other hand is not as clear to interpret. Each cell's V_{bi} increases with increased air exposure up to a time where it drops down a little (the drop is not seen in the cell with LiF). A small increase might be expected since increased doping would shift the Fermi level and therefore the amount of band bending. However, the increases in V_{bi} seen here are too large to be due to solely to a shift in the Fermi level. For example, the V_{bi} of the cell with LiF increases to nearly 3 V and the P3HT bandgap is less than 2 eV. Also, many of the linear regions become distorted after long exposure to air.

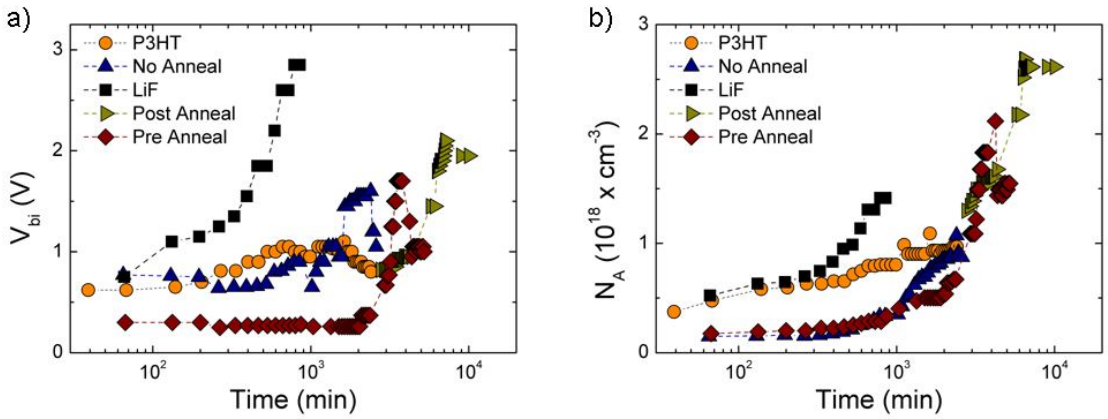

Figure 5.11. Built-in bias (a) and doping density (b) as functions of air exposure time.

The unexpectedly high V_{bi} could come from very slow deep-level thermalization of acceptor states which shift the entire CV and C^{-2} plots along the bias axis[53] or fixed charges at the interface which also shift the curves along the bias axis[246]. If the Al_2O_3 layer becomes thick enough, it could act as a thin insulator with a capacitance that

shifts the V_{bi} to higher values and also distort the linear C^{-2} curve (similar to the effects described in section 3.7.3.2 that were observed in the colloidal quantum dots solar cells) if its capacitance is large enough[53]. It has been reported that C_{60} can become *n*-doped and form a Schottky barrier with Al[247], which might suggest the same could happen with PCBM leading to more problems interpreting the Schottky results here. However, the description of the CV curve given in the C_{60} paper states the geometric capacitance was observed in reverse bias and only a very limited linear region in forward bias was seen in the C^{-2} curve[247]. This description leads one to question the validity of their results and not much weight is given to it here. The point is that many things can influence the Mott-Schottky analysis results to give inaccurate results.

Mott-Schottky analysis on organic solar cells also produces varied results based on the modulation frequency which affects both the V_{bi} and N_A results[248]. Since P3HT responds slowly to the applied signal, low frequency measurements have been applied to achieve the most accurate results[55]. However, there are still differences in reported Mott-Schottky analysis results and techniques. For example, one of the leading groups performing impedance analysis on polymer solar cells reported a V_{bi} of 0.43 V using a modulation frequency of 100 Hz on a P3HT:PCBM cell that was annealed before depositing the Al electrode[62]. Their C^{-2} curve showed a clear linear region in the reverse bias regime indicating the presence of a Schottky junction. However, when the same group performed the analysis on a P3HT:PCBM cell that was annealed after depositing the Al electrode, their C^{-2} curves showed a linear region only in low forward bias and not in reverse bias which was taken to mean the device was fully depleted at 0 V bias[55]. However, using their reported V_{bi} (near 0.4 V) and N_A values in equation (1.3) results in a depletion width of ~80 nm and their reported P3HT:PCBM

thickness was 150 nm. Finally, the same group again presented Mott-Schottky analysis on a P3HT:PCBM cell (in this case there was no annealing step mentioned), but this time the modulation frequency they used was 1 kHz[249]. This produced similar V_{bi} (0.36 V) and N_A values to their other reports, but again the linear region was only seen in the forward bias regime. An immediate question that comes to mind is why the larger modulation frequency was used and why it produced the same results. As an example of the frequency dependence from the tests reported here, Figure 5.12 shows how much V_{bi} and N_A vary as the probing frequency is increased. The data is for the P3HT-only cell after being exposed to air for 140 minutes. Another question is why the Schottky region was seen only in forward bias for some cells when the calculated depletion width was only about half of the reported thickness, although this could be due to one of the reasons listed in the previous paragraph to account for the large V_{bi}.

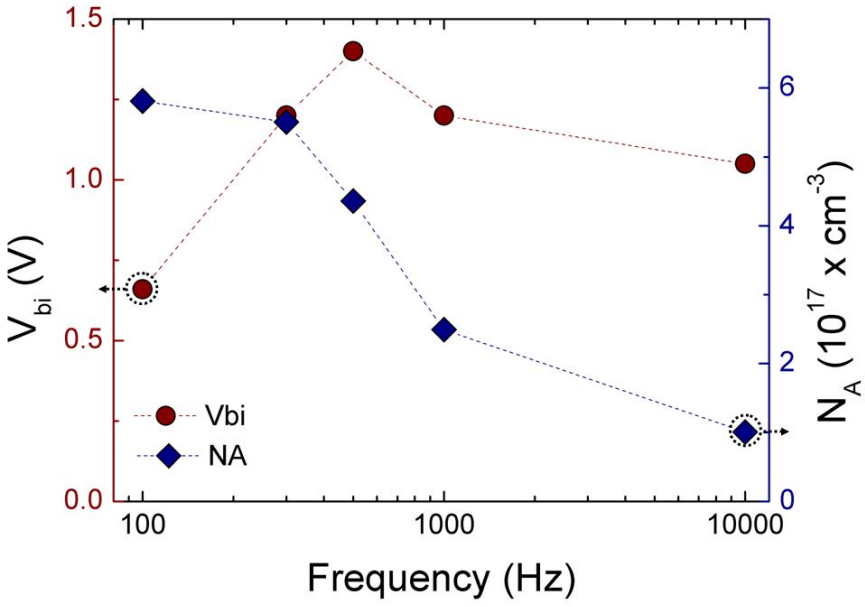

Figure 5.12. Frequency dependence of V_{bi} and N_A in the P3HT-only cell. This measurement was taken after 140 minutes exposure to air.

Previous degradation tests analyzed by Mott-Schottky analysis concluded that no Schottky characteristics were visible in the initial state, but after two hours exposed to oxygen while under illumination, the capacitance exhibited depletion characteristics in reverse bias enabling fitting of the data by the Mott-Schottky equation (equation (2.17))[200]. Exposure to oxygen while the device was illuminated was found to accelerate the degradation process. There are a couple items that make direct comparison to the work here difficult. First is the geometry. The cells tested in reference 200 used an inverted architecture of the structure ITO/organic hole blocking layer/P3HT:PCBM/PEDOT:PSS/Ag grid. The other problem is they used a modulation frequency of 10 kHz which will shift the V_{bi} to higher values and the N_A to lower values (see Figure 5.12). For example, they found V_{bi} = ~0.8 V and N_A = ~7 x 10^{17} cm^{-3} after two hours of degradation[200]. A better comparison is the trend in N_A between their results and the results presented here. In both cases exposure to oxygen increased the doping density. They don't report the trend in V_{bi}. However, the two C^{-2} curves they show at different degradation times have significantly different V_{bi}, suggesting the difficulties with V_{bi} mentioned here.

The final set of data presented here is a comparison of the series resistance and doping density trends of each cell, except the cell with LiF since that cell only had two series resistance data points. Figure 5.13 shows a correlation between the two values for each cell. With increased doping, the series resistance might be expected to decrease due to better conductivity. However, the irreversible degradation that results from the formation of carbonyl groups creates charge-carrier traps[197,198] that can increase R_s. Also, the formation of an Al_2O_3 layer can increase R_s. These latter two factors appear to outweigh any potential conductivity increase due to increased doping.

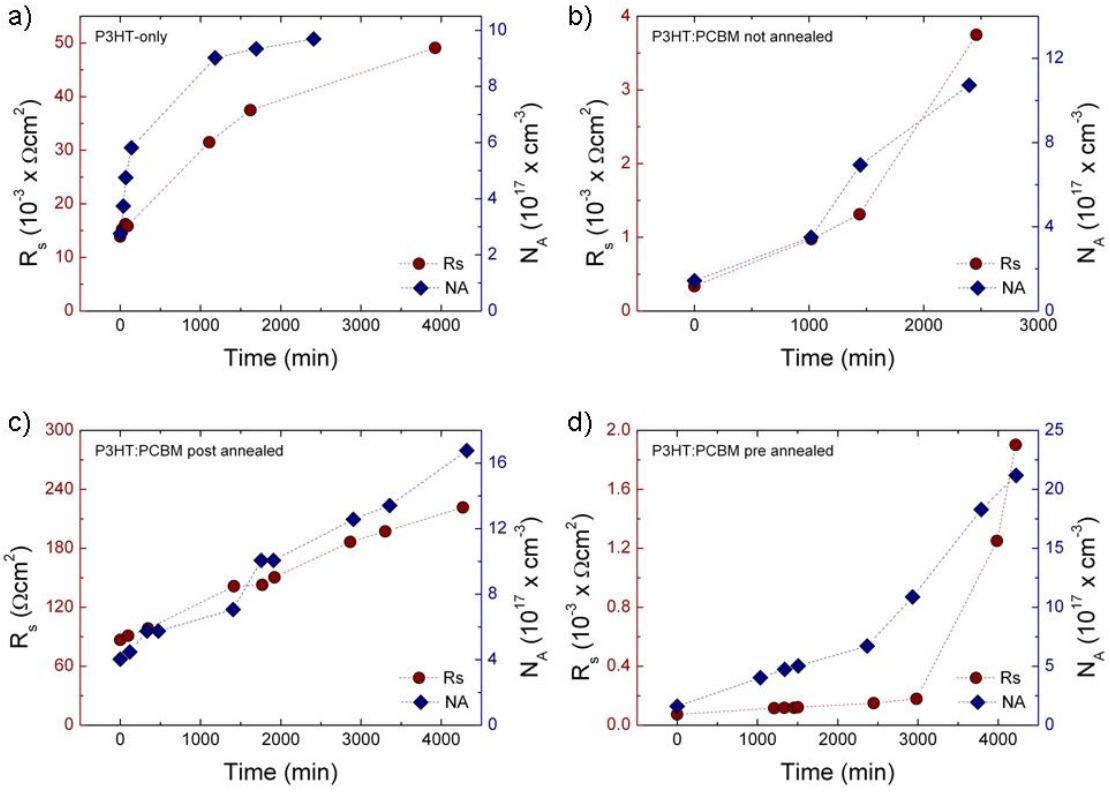

Figure 5.13. Comparison of the series resistance and doping density for each cell as a function of air exposure time. a) P3HT-only. b) P3HT:PCBM not annealed. c) P3HT:PCBM post annealed. d) P3HT:PCBM pre annealed.

5.2.4 Organic Solar Cell Degradation Conclusions

Capacitance measurements over extended time periods proved to be a useful method for investigating the P3HT/Al and P3HT:PCBM/Al interface as the cells degraded with exposure to air. An excessive capacitance peak was seen to form with prolonged air exposure (in the cell with LiF it existed from the initial measurement). Based on previous literature[62,63,124], the peak was attributed to minority carrier injection. Both LiF and Al_2O_3 have been shown to enhance minority carrier injection in organic electroluminescent devices[224,225,226,230,231] and act as hole blocking layers[227,228,229,232]. In the cells studied here, this explains the mechanism for the excessive capacitance under forward bias. The formation of the Al_2O_3 layer also explains the initial increase

in V_{oc} with exposure to air that is observed in all the cells without LiF by forming a hole blocking layer which reduces shunt pathways.

Mott-Schottky analysis on the reverse bias capacitance demonstrated the formation of a Schottky barrier at the Al interface. However, clear evidence of a Schottky region in the post-annealed cell under reverse bias was only observed after extended exposure to air, indicating increased stability due to thermal annealing. This is also seen by the slower J_{sc} degradation in the post-annealed cell. The doping density was found to increase with increased air exposure for each cell as expected, but the built in bias was more difficult to interpret. The formation of the Al_2O_3 hole blocking layer may create a junction capacitance that can distort the Mott-Schottky curve and shift the built in bias to higher values[53,221].

The importance of annealing after aluminium deposition as opposed to before aluminium deposition was also made evident. The V_{oc} for the pre-annealed cell was more than 0.2 V less than for the post-annealed cell. Exposure to air increased the V_{oc} for each cell, but for the pre-annealed cell it never surpassed 0.4 V whereas the post-annealed cell had a V_{oc} greater than 0.6 V. In contrast, the non-annealed cell started with a very low V_{oc}, but increased to the same V_{oc} as the post-annealed cell. Therefore it is concluded that a reduction of shunt pathways is not the only aspect that needs to be addressed to increase the V_{oc}. Possible reasons for the decreased V_{oc} in the pre-annealed cell are different crystal orientations and P3HT:PCBM crystal overgrowth due annealing without the metal electrode cap[242,222,223].

5.2.5 Future Work in Organic Solar Cell Degradation

The first area for future work could be to compare these results with an annealed P3HT-only and an annealed LiF cell. Stability comparisons of annealed versus non-

annealed P3HT devices would be interesting to compare with annealed and non-annealed P3HT:PCBM cells. PCBM has been shown to decrease the degradation rate of MDMO-PPV when added to the polymer[213,250]. Under the assumption that PCBM also reduces the degradation rate of P3HT, a comparison of the reduction in degradation rate due to annealing and due to the addition of PCBM could be investigated.

Another item for study is to perform CV degradation measurements on P3HT and P3HT:PCBM cells that have electrodes of different work functions. According to the ideas presented in this section, the onset of the excessive capacitance peak should shift in bias value to match the difference between the electrode work function and P3HT or PCBM LUMO level. In that same regard, cells constructed without the PEDOT:PSS electron blocking layer are of interest to see whether the excessive capacitance peak can be eliminated by enabling electron extraction at the ITO electrode. During these tests, possible Fermi level pinning would need to be considered since that could affect the energy level differences.

Collaboration work with students working on barrier layers would be a good partnership. CV measurements conducted on cells that have a barrier layer could show the amount of doping change that takes place as the cell sits in air. This in turn yields information about how the barrier performs when actually applied to a solar cell.

5.3 Comparison of Thermally Evaporated Sexithiophene and Polythiophene

5.3.1 Thermally Evaporated Thiophene Introduction

Vacuum thermally evaporated materials are relatively easy to deposit in parallel and sequential applications, enabling complex multilayered structures to be fabricated[251]. On the other hand, solution processed materials require orthogonal solvents for each layer since using non-orthogonal solvents damages the previously deposited material[192], resulting in less complex architectures. The application of vacuum processing to large molecular weight organic material however is challenging and generally results in decreased molecular weight and changes to the local chemistry[252,253]. Recently though, P3HT was shown to be vacuum processable and still maintain most of its original chemical composition and structure[254]. In this context, a study of two vacuum processed organic thiophenes of different molecular weight is presented in this section. Polythiophene, Pth, was chosen for the large molecule and sexithiophene, 6T, for the small molecule.

The work presented in this section was done in collaboration with a fellow DPhil student, Peter Kovacik. Peter completed all the device fabrication (section 5.3.2) and the author performed all the device testing and analysis presented here.

5.3.2 Thiophene Solar Cell Fabrication

ITO coated glass substrates were cleaned, PEDOT:PSS was spin cast, and the substrates were annealed as described in section 5.2.2. Following this, a 35 nm layer of thiophene and 100 nm layer of C_{60} were sequentially deposited by thermal vacuum evaporation. Finally, a 90 nm Al electrode was evaporated through a shadow mask.

The cells were stored and tested in a nitrogen environment. A more detailed description of the device fabrication and materials property analysis is given in references 251 and 255.

5.3.3 Evaporated Thiophene Results and Discussion

Bilayer solar cells of C_{60} and a thiophene (either Pth or 6T) were compared. For each thiophene material, annealed and non-annealed variations were studied. There was also one device fabricated of pristine 6T (no C_{60}) which was not annealed. The results begin with a discussion of which material interface is being probed by CV measurements in Section 5.3.3.1. Following that in section 5.3.3.2, the CV and *JV* results are presented and discussed.

5.3.3.1 Determining the Depletion Capacitance Interface

Figure 5.14 shows the cell architecture of each cell used in this study except the pristine 6T cell. For that cell there is no C_{60} layer.

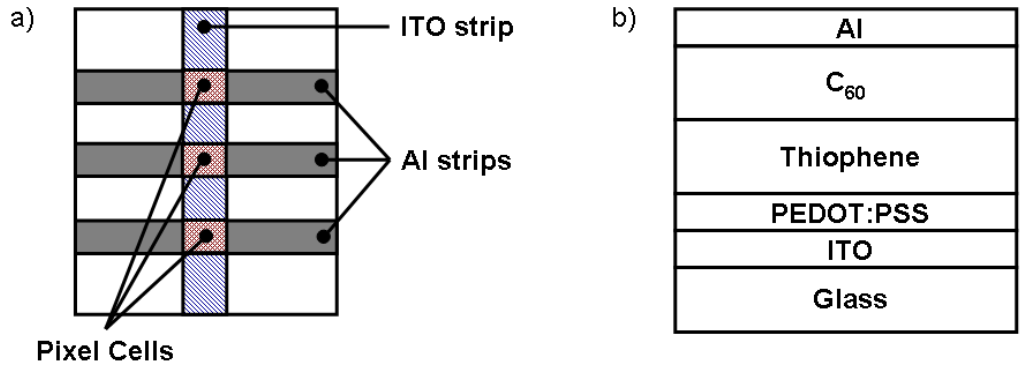

Figure 5.14. a) Three solar cells (termed pixel cells) per substrate are determined by the ITO and Al overlap. b) The solar cell layer structure.

Much of the analysis later in this section is a Mott-Schottky analysis which relies on bias-dependent depletion capacitance. In the degradation study presented in section 5.2, the depletion capacitance is a result of the Schottky junction formation between

the polymer and Al electrode. However, with the exception of the pristine 6T cell, the cells studied in this section do not have a thiophene/Al interface to create such a junction. Figure 5.17 in the next section does show good evidence of a depletion capacitance though. The question then arises as to what junction is responsible for the depletion capacitance. The three possibilities are the C_{60}/Al, C_{60}/thiophene, and thiophene/ITO interfaces.

The pristine 6T CV results in Figure 5.15a shows that the depletion capacitance does not occur at the thiophene/ITO interface (at least for the 6T cells) since the capacitance is relatively constant with applied bias until ~1.5 V where it then starts to increase. The corresponding C^{-2} curve is shown in Figure 5.15b and displays no evidence of a linear region to fit the Mott-Schottky curve (see section 2.2.3). In other words, no bias-dependent depletion capacitance evidence is seen in the range of -2 V to 1.5 V. However, the depletion capacitance in the bilayer cells (Figure 5.17) is observed from small negative to small positive voltages. The increase in capacitance near 1.5 V in the pristine 6T cell corresponds to the diode turn-on voltage (Figure 5.15a) and is most likely caused by injection of minority charge carriers at the diode turn-on voltage. The CV results also imply that no Schottky junction is formed at the 6T/Al interface. In previous studies on ITO/6T/Al cells, Kouki *et al*. argued that the most likely model for this system is a metal-insulator-metal structure rather than a Schottky junction at the 6T/Al interface due to the low thickness and carrier concentration of the 6T film[256]. The metal-insulator-metal model would explain the results seen here.

That leaves either the C_{60}/Al or C_{60}/thiophene interfaces to form the depletion capacitance observed in the thiophene/C_{60} cells. Forward bias for the cells was

connected such that the positive bias was connected to the ITO electrode. In this configuration, Figure 5.16 shows a rectification ratio greater than one for positive biases compared to negative biases in each of the different cells. Now, if C_{60} formed a Schottky contact with Al, the C_{60} is expected to be an *n*-type semiconductor since it is an electron transporter. Therefore, forward bias would require a positive bias applied to the Al electrode, in opposition to what was observed here.

That leaves the C_{60}/thiophene interface. If a *p*-*n* junction formed at this interface with the thiophene *p*-type and C60 *n*-type as expected, the forward bias configuration (positive bias connected to ITO electrode) matches what is observed in the *JV* curves. Therefore, the most likely interface for the observed depletion capacitance is at the C_{60}/thiophene interface.

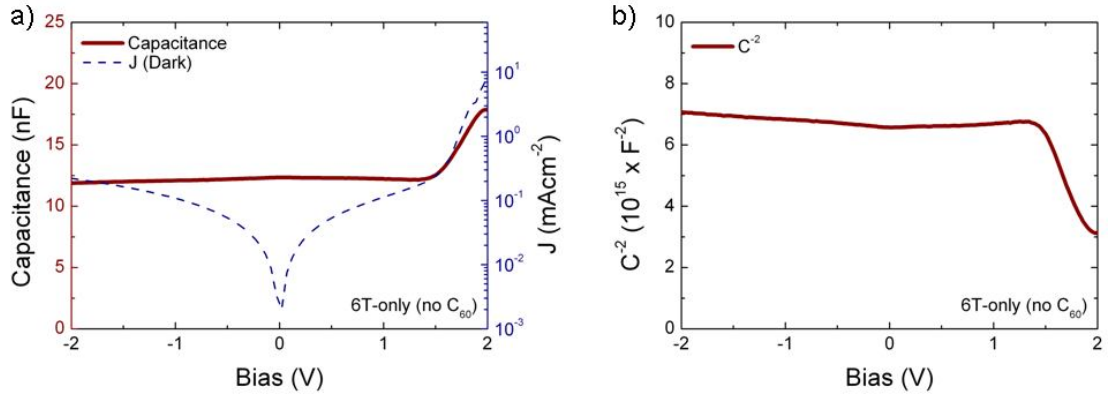

Figure 5.15. 6T-only CV (a) and C^{-2} (b) results. The dark *JV* curve is included in (a) to show the correspondence between the increase in capacitance and the diode turn-on voltage.

The *JV* curves for the pristine 6T in Figure 5.16 exhibit a diode turn-on voltage near 1.5 V. In previous reports this has been shown to be near 1.2 V[256] which corresponds to the difference in energy difference between the Al work function and 6T LUMO level[257]. The larger than expected turn-on voltage seen here requires further investigation, but is expected to correspond to the energy level differences as well.

Injection of minority carriers at the diode turn-on voltage near 1.5 V is the likely cause of the capacitance increase in Figure 5.15a.

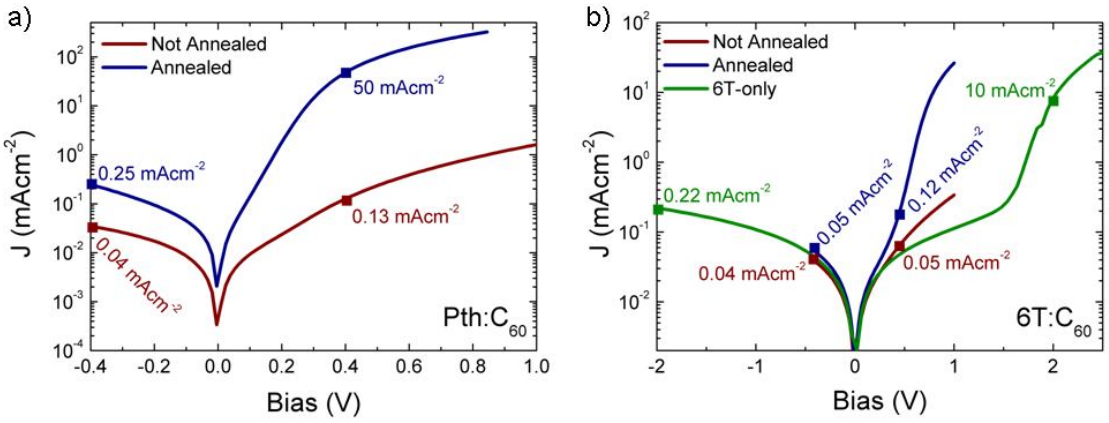

Figure 5.16. Dark *JV* curves for Pth:C_{60} (a) and 6T:C_{60} (b) before and after thermal annealing. Also included in (b) is the dark *JV* curve for the pristine 6T cell. The marked points show the current density at symmetric biases around zero bias. Each cell has a rectification ration greater than one.

5.3.3.2 CV and *JV* Analysis

Sample CV and C^{-2} versus bias curves are shown in Figure 5.17 for both the 6T and Pth cells. In both cells annealing affects the forward bias capacitance. Prior to annealing, the capacitance increases rapidly in forward bias without a subsequent drop. However, after annealing the capacitance of both cells drops sharply in forward bias displaying inductive behaviour. In the Pth cell an excessive capacitance peak is seen after annealing while in the 6T cell the capacitance drops without first showing the excessive capacitance peak

Before annealing, the excessive capacitance is likely due to the injection of minority carriers[58,62]. After annealing there are a couple of possibilities. Either minority carrier injection becomes limited[62,63], or the carriers are more easily extracted at the opposite contact[124]. Further investigation is needed to determine the exact cause of the change in CV behaviour.

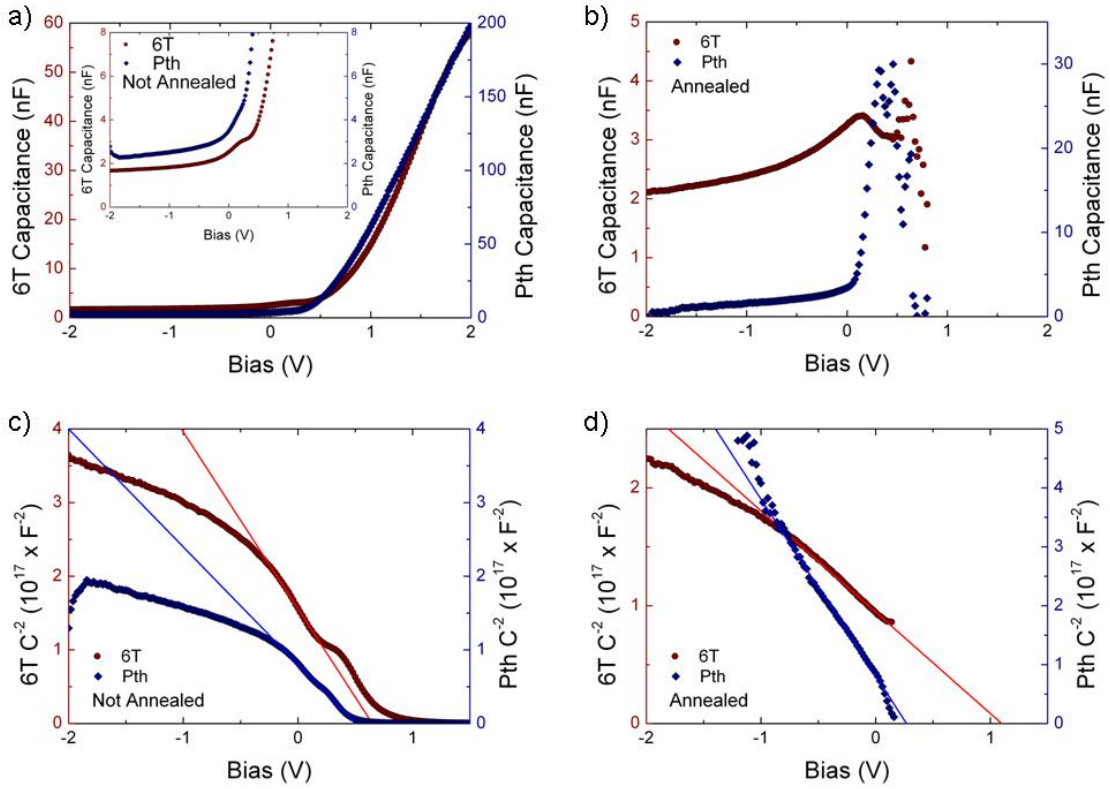

Figure 5.17. CV and C^{-2} curves for the 6T and Pth cells. a) Not-annealed CV. b) Annealed CV. c) Not annealed C^{-2}. d) Annealed C^{-2}.

Mott-Schottky analysis of the C^{-2} curves show different trends between the non-annealed and annealed cells for the two different materials. For the Pth cell, annealing causes a decrease in V_{bi} and N_A, whereas annealing causes an increase in V_{bi} and N_A for the 6T cell. This was unexpected, but analysis of the V_{oc} for non-annealed and annealed cells showed similar trends for each cell as depicted in Figure 5.18a. The V_{oc} increase of the 6T cell is not that dramatic, but this could be due to Fermi level pinning which has been shown to limit the V_{oc} is organic solar cells[258,259,260,261]. The trend in N_A is the same as that for V_{bi} in each cell as depicted in Figure 5.18b.

It is difficult at this stage to determine the exact reason for the different V_{bi} and V_{oc} trends between the two materials. However, the thiophene crystallization may play an important role. 6T is a relatively small molecule compared to Pth causing it to crystallize and aggregate easily[257,262]. Annealing Pth increases its crystallinity and

improves the coherence length within crystal regions, indicating growth of the polymer chain[263]. The P3HT crystal alignment in solution processed P3HT:PCBM bulk-heterojunction cells has been suggested as a reason for the V_{oc} differences between cells annealed before and cells annealed after Al electrode deposition[242] as mentioned in section 5.2.3.1. A similar phenomenon could be happening here, causing one cell to increase in V_{oc} after annealing and the other to decrease.

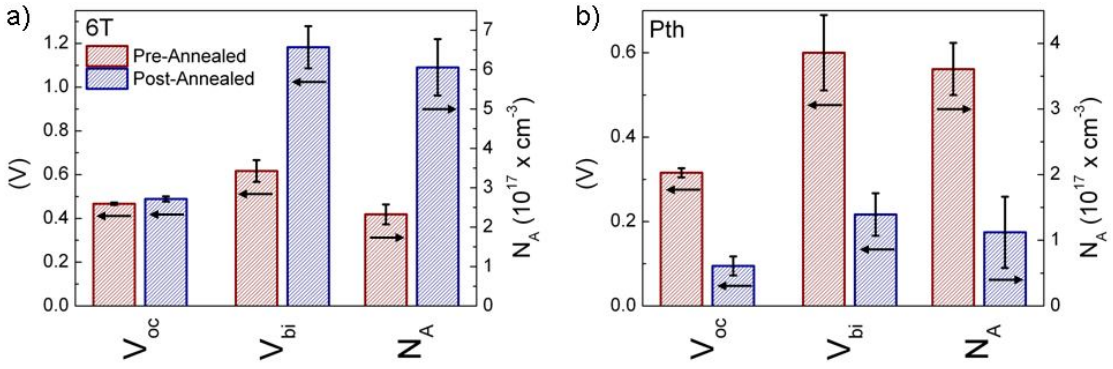

Figure 5.18. a) V_{bi} and V_{oc} trend comparison between the 6T and Pth cells before and after thermal annealing. b) N_A trend comparison between the 6T and Pth cells before and after annealing.

The parasitic resistances shown in Figure 5.19 show shunt resistances changes with annealing that correspond to the direction of change in the respective V_{oc} values.

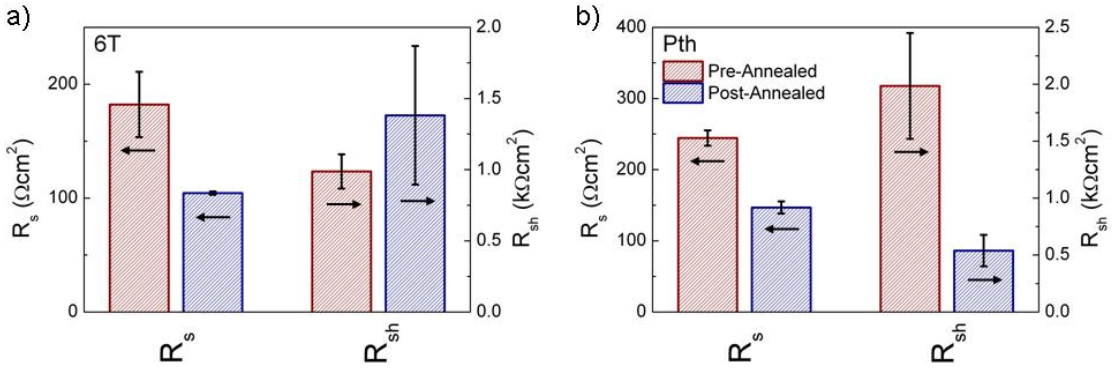

Figure 5.19. Series and shunt resistances before (red) and after (blue) annealing for 6T in (a) and Pth in (b).

This suggests another possible explanation for the change in V_{oc} upon annealing which is due to the removal (in the 6T case) and formation (in the Pth case) of shunt pathways. However, it should be noted that the standard deviation between post annealed 6T cells is very high.

Added for comparison to R_s is the effect of annealing on J_{sc} shown in Figure 5.20. For the 6T cells the decrease in R_s correlates with the increase in J_{sc}. However, this is not the case for the Pth cells. The J_{sc} measurements were not very consistent between cell samples for either material, as evidenced by the large standard deviations. Further trials need to be accomplished before any conclusions can be made in this regard.

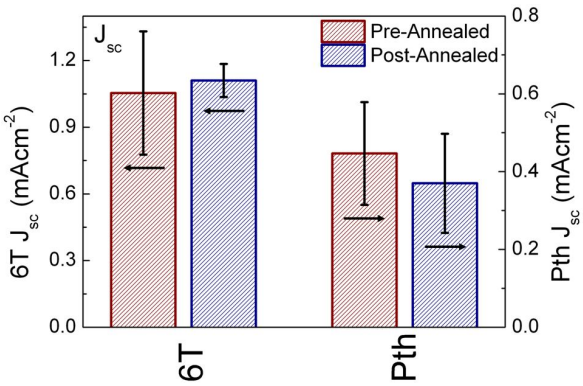

Figure 5.20. Short circuit current before (red) and after (blue) annealing for 6T and Pth cells.

5.3.4 Thermally Evaporated Thiophene Conclusions

The work performed in this section is in the preliminary stages. However, there are a couple interesting results that could prove to be fruitful and also suggest the importance of CV measurements in these cells. The first is the decrease in V_{bi}, N_A, and V_{oc} for the Pth cell upon annealing compared to an increase in the parameters for the 6T cell. Definitive reasons for this behaviour are not possible yet, but a good possibility is the differences in crystallisation on annealing between small molecules

(6T) and larger molecules (Pth). It is these differences which make the evaporation of polymeric materials of potential interest for bulk heterojunction cells.

Another interesting outcome is the possibility of probing the C_{60}/thiophene interface using bias-dependent capacitance measurements. In solution processed bulk-heterojunction cells, bias-dependent capacitance measurements probe the Schottky junction formed at the polymer/Al interface instead of the polymer/fullerene interface[55,62]. Evaporating bilayers may provide a method to probe the C_{60}/thiophene junction, which is of interest since this is where exited electron-hole pairs should be separated. However, more work needs to be accomplished in order to confirm this.

5.3.5 Future Work in Evaporated Thiophene Solar Cells

Further investigation into the depletion capacitance is very interesting due to the possibility of probing the C_{60}/thiophene interface. Evaporation of a thin layer of intrinsic semiconductor between the two materials could change the junction characteristics to *p-i-n* which might be detectable with CV measurements. Also, evaporating a thin layer of 6T between the C_{60} and Pth should change the junction characteristics and be detectable with CV measurements. These tests could help determine whether the depletion capacitance is truly from the C_{60}/thiophene interface. In addition, changing the metal electrode to one with a different work function should give further evidence to the origin of the depletion capacitance. If no change is noticed, this would support the depletion capacitance coming from the C_{60}/thiophene interface.

Finally, more study of the effects of annealing on the CV measurements should be conducted. A comparison of non-annealed and annealed pristine Pth and pristine 6T should be added. Other iterations to try are annealing prior to Al deposition and after

Al deposition for the pristine and bilayer cells. In solution processed organic cells, annealing with and without the Al electrode deposited has been shown to affect material segregation, crystal orientation, and crystal overgrowth[242,28,222]. Annealing with and without the Al electrode in a bilayer configuration would help in understanding any interaction between C_{60} and Al during annealing.

5.4 Conclusion

Capacitance-voltage measurements proved to be a good tool for analysing the P3HT/Al interface during degradation in air. Analysis of the excessive forward capacitance between the different cell architectures combined with the initial increase in V_{oc} during degradation demonstrated the formation of an Al_2O_3 layer that aids in electron injection and acts as a hole blocking layer. In the thermally evaporated thiophenes, capacitance measurements look promising as a method to investigate the thiophene/C_{60} interface.

Chapter 6

Conclusions and Future Work

6.1 Conclusions

Material and solar cell system specific conclusions are included in the respective chapters (3.8, 4.3.5, 4.4.3, 5.2.4, 5.3.4). Given here is a broad assessment of the electrical characterisation techniques used in this thesis and described in chapter 2.

Efficiency drives the advancement of solar PV. The basic metric for solar cell quality is current–voltage measurements under illumination. The advancement of efficiency does not come from a series of efficiency measurements alone, but from understanding the mechanisms that affect efficiency. Using a combination of AC and DC electrical characterisation techniques, this thesis generates a deeper understanding of the optoelectronic processes within the cell and hopefully can be used to guide future cell improvements.

Material conductivity is reflected in the series resistance and becomes especially important at high current densities where its effect on performance is more pronounced. Determining R_s from the inverse slope of the illuminated *JV* curve at V_{oc} then sheds light on material or barrier layers that reduce cell performance. For

example, in the CQD cells R_s was found to decrease after UV photodoping, confirming the increased conductivity of the ZnO QDs. On the other hand, R_s of the P3HT:PCBM cells was found to increase with increased exposure to air, indicating the formation of an Al_2O_3 layer at the P3HT:PCBM/Al interface.

The reverse saturation current describes the amount of recombination within a cell which in turn limits the V_{oc}. Both J_0 and n can be determined by fitting the diode equation to the dark *JV* curve. In the In(Ga)As QD cells, J_0 demonstrated increased recombination with the addition of QDs and a further increase when defects were formed. Charge transport is different in QDs than in a bulk semiconductor due to quantum confinement. Temperature dependent J_{sc} measurements on the In(Ga)As QD cells showed that when defects were allowed to propagate through the QD system, more charges were extracted from the QDs. Another example of how temperature dependent measurements extend the *JV* capabilities is the temperature dependent V_{oc} behaviour of the CQD cells indicating the presence of injection barriers which were not detectable with a single temperature measurement.

Photocurrent measured under monochromatic illumination describes how a material responds to different photon energies. The performance difference between the In(Ga)As QD and QD with defects cells demonstrates the negative impact of defects. However, the purpose of adding QDs to the solar cell is to harvest sub-bandgap photons, and in this regime EQE measurements tell a different story. Due to the wavelength specific photocurrent from EQE measurements, the superior sub-bandgap performance of the defect cell was found. In the case of the CQD cells, the PbS/ZnO junction mechanism impacts the useable absorber material thickness. By examining the evolution of the peak EQE value extending back to shorter wavelengths as a

function of UV photodoping, a transition from excitonic behaviour to *p-n* behaviour of the PbS/ZnO heterojunction with increased photodoping was made known. This highlighted the importance of photodoping not only to increase the ZnO conductivity, but also to increase the exciton harvesting regime.

The built-in bias quantifies the barrier height at a Schottky or *p-n* junction. Fitting the Mott-Schottky equation to the linear portion of the C^{-2} versus bias curve yields both V_{bi} and N_A. In dilute nitride cells that have undergone rapid thermal annealing at 910 ^{0}C, the large frequency dependence of V_{bi} and N_A compared to that of cells annealed at 825 and 875 ^{0}C indicated defects were induced in the material due to the higher annealing temperature. Even though high temperature annealing produced a larger depletion width, the advantage was offset by the detrimental impact of induced defects. The Mott-Schottky analysis was straight forward for the GaAs based cells. However, the CV results for the CQD cells were more complex. Based on injection barriers determined by temperature dependent *JV* and CV analysis, an equivalent circuit model incorporating the depletion capacitance with a constant capacitance was able to describe the CQD CV measurements, demonstrating a transition from excitonic to *p-n* junction behaviour with UV photodoping. CV measurements showed increased *p*-doping of P3HT with exposure to air, which demonstrated that oxygen diffuses into the material and explains how the Al_2O_3 layer forms at the P3HT/Al interface.

Analysis of the impedance spectrum with an equivalent circuit leads to carrier lifetimes. In the dilute nitride cells, the lower carrier lifetime of the 910 ^{0}C annealed cell coupled with qualitative evidence based on the shape of the impedance Nyquist plot supported the conclusion from the frequency dependent CV parameters that the

higher temperature annealing induced defects into the material. The negative effect of the defects prevented any increase in efficiency that might come from a larger depletion region.

The electrical characterisation techniques employed in this thesis go beyond the standard efficiency measurements, but have the ultimate goal of improving solar cell performance. A better understanding of the operating mechanisms involved and their contribution to cell performance is needed to continue enhancing solar cell efficiency. The techniques presented here are tools that provide this understanding, directing the path to better solar cells.

6.2 Future Work

As in the conclusions, material and solar cell system specific future work is presented in each chapter. This section focuses on the experimental techniques used in this thesis and complimentary techniques that can be added.

First, the impedance analysis should be extended to the polymer degradation study using an equivalent circuit that incorporates the full transmission line element to determine minority carrier lifetime and mobility as a function of air exposure time. Further extension of the impedance analysis should be accomplished using the differential susceptance, similar to that done in polymer LEDs to simultaneously determine the hole and electron mobilities[264,265,266]. Charge carrier mobility is a metric of how well charges are transported through the material. Understanding how this is affected by material degradation provides insight into the degradation mechanisms

which guides research to mitigate the degradation and has the potential to be used as a metrology method in production environments.

Internal quantum efficiency should be determined in addition to external quantum efficiency by adding absorption measurements to the suite of characterisations. Once this has been accomplished, poor performance can be attributed to either low absorption or poor electrical characteristics. This provides direction towards understanding the mechanisms that limit the cell's overall performance.

Further experimental techniques that have been setup by the author, but were not used due to time restraints, should be added to the analysis suite. The first is charge extraction by linearly increasing voltage, which produces the carrier mobility and material dielectric constant[267]. The second is transient current decay using time of flight, which also gives carrier mobility[267]. The combination of carrier lifetime and mobility determines the best material thickness for electrical performance. This can then be balanced with the thickness needed for optimal photon absorption to convert the most photons into useable electricity.

Finally, a V_{oc} decay experiment[268], which yields carrier lifetime, should be built using the time of flight equipment. This would be a straight forward extension to an existing experimental setup. Lifetime is a key element in balancing material thickness (as previously stated) for optimum performance.

All but one of the areas of work are either extensions to an existing measurement system or utilization of an existing (but currently unused) system. These straight forward additions to the suite of electrical characterisations will provide added confidence to parameters determined by a single method and support any weaknesses in a given technique. Taken together with the existing methods, even further

understanding of the electro-optical mechanisms within a solar cell can be gained leading to enhanced solar cells.

References

[1] World Coal Association, Where is Coal Found? http://www.worldcoal.org/coal/where-is-coal-found/ (accessed 9 August 2011).

[2] trillionthtonne.org, Explaining the need to limit cumulative emissions of carbon dioxide. http://trillionthtonne.org/ (accessed 9 August 2011).

[3] NASA, Earth Observatory, Global Warming. http://earthobservatory.nasa.gov/Features/GlobalWarming/ (accessd 9 August 2011).

[4] Lewis, N.S., *Powering the Planet*. MRS Bulletin, 2007, 32, 808.

[5] REN21. 2008. "Renewables 2007 global Status Report" (Paris: REN21 Secretariat and Washington, DC: Worldwatch Institue). Copyright © 2008 Deutsche Gesellschaft fur Technishe Zusammenarbeit (GTZ) GmbH.

[6] Pure Energy Systems, PESWiki, Directory:Cents Per Kilowatt-Hour. http://peswiki.com/index.php/Directory:Cents_Per_Kilowatt-Hour (accessed 9 August 2011).

[7] Kamat, P. V. Quantum Dot Solar Cells. Semiconductor Nanocrystals as Light Harvesters. *J. Phys. Chem. C.* **2008**. 112, 18737-18753.

[8] Hoppe, H.; Sariciftci, N. S. Organic solar cells: An overview. *J. Mater. Res.* **2004**. 19, 1924-1945.

[9] Wadia, C.; Alivisatos, A. P.; Kammen, D. M. Materials Availability Expands the Opportunity for Large-Scale Photovoltaics Deployment. *Environ. Sci. Technol*. **2009**. 43, 2072-2077.

[10] Nelson, J. *The Physics of Solar Cells.* Imperial College Press: London, 2003.

[11] Wurfel, P. *Physics of Solar Cells: From Basic Principles to Advanced Concepts.* Wiley-VCH, 2009.

[12] Fonash, S. *Solar Cell Device Physics, Second Edition.* Academic Press, 2010.

[13] Kitai, A. *Principles of Solar Cells, LEDs and Diodes: The role of the PN junction.* Wiley-Blackwell, 2011.

[14] PVCDROM http://pveducation.org/pvcdrom (accessed 9 August 2011).

[15] Araujo, G. L.; Marti, A. Absolute limiting efficiencies for photovoltaic energy conversion. *Sol. Energy Mater. Sol. Cells.* **1994**. 33, 213-240.

[16] Shockley, W.; Queisser, H. J. Detailed Balance Limit of Efficiency of *p-n* Junction Solar Cells. *J. Appl. Phys.* **1961**. 32, 510-519.

[17] Henry, C. H. Limiting efficiencies of ideal single and multiple energy gap terrestrial solar cells. *J. Appl. Phys.* **1980**. 51, 4494-4500.

[18] Saleh, B. E. A.; Teich, M. C.. *Fundamentals of Photonics.* John Wiley & Sons, Inc: New York, 1991.

[19] Rhoderick, E. H.; Williams, R. H. *Metal-Semiconductor Contacts, 2nd ed.* Oxford University Press: USA, 1988.

[20] Sze, S. M. *Physics of Semiconductor Devices, 2nd ed.* Wiley-Interscience: New York, 1981.

[21] Bhattacharya, P. *Semiconductor Optoelectronic Devices, 2nd ed.* Prentice Hall: New Jersey, 1997, p. 128.

[22] Gregg, B. A. Excitonic Solar Cells. *J. Phys. Chem. B*. **2003**. 107, 4688-4698.

[23] Mayer, A. C.; Scully, S. R.; Hardin, B. E.; Rowell, M. W.; McGehee, M. D. Polymer-based solar cells. *Mater. Today*. **2007**. 10, 28-33.

[24] Markov, D. E. Excitonic processes in polymer-based optoelectronic devices. *University of Groningen, The Netherlands, PhD Thesis.* **2006**.

[25] Blom, P. W. M.; Mihailetchi, V. D.; Koster, L. J. A.; Markov, D. E. Device Physics of Polymer:Fullerene Bulk Heterojunction Solar Cells. *Adv. Mater.* **2007**. 19, 1551-1566.

[26] Gunes, S.; Neugebauer, H.; Sariciftci, N. S. Conjugated Polymer-Based Organic Solar Cells. *Chem. Rev*. **2007**. 107, 1324-1338.

[27] Sun, S.; Sariciftci, N. S. *Organic Photovoltaics: Mechanism, Materials, and Devices*. CRC Press, 2005.

[28] Peumans, P.; Uchida, S.; Forrest, S. R. Efficient bulk heterojunction photovoltaic cells using small-molecular-weight organic thin films. *Nature.* **2003**. 425, 158-162.

[29] Markov, D. E.; Hummelen, J. C.; Blom, P. W. M.; Sieval, A. B. Dynamics of exciton diffusion in poly(*p*-phenylene vinylen)/fullerene heterostructures. *Phys. Rev. B.* **2005**. 72, 045216.

[30] Scully, S. R.; McGehee, M. D. Effects of optical interference and energy transfer on exciton diffusion length measurements in organic semiconductors. *J. App. Phys.* **2006**. 100, 034907.

[31] PVCDROM, Recombination mechanisms. http://pvcdrom.pveducation.org/CELLOPER/IDEALITY.HTM (accessed 5 Sep 2011).

[32] European Photovoltaic Industry Association. *Solar Generation 6 Solar Photovoltaic Electricity Empowering the World*. **2011**.

[33] Zhao, J.; Wang, A.; Green, M. A.; Ferrazza, F. 19.8% efficient "honeycomb" textured multicrystalline and 24.4% monocrystalline silicon solar cells. *Appl. Phys. Lett.* **1998**. 73, 1991-1993.

[34] Schultz, O.; Glunz, S. W.; Willeke, G. P. Multicrystalline Silicon Solar Cells Exceeding 20% Efficiency. *Prog. Photovolt: Res. Appl*. **2004**. 12, 553-558.

[35] Benagli, S.; Borrello, D.; Vallat-Sauvain, E.; Meier, J.; Kroll, U.; Hotzel, J.; Spitznagel, J.; Steinhauser, J.; Castens, L.; Djeridane, Y. High-efficiency Amorphous Silicon Devices on LPCVD-ZNO TCO Prepared in Industrial KAI-M R&D Reactor. *24th European Photovoltaic Solar Energy Conference*. Hamburg, September, 2009.

[36] Kayes, B.M; Nie, H.; Twist, R.; Spruytte, S. G.; Reinhardt, F.; Kizilvalli, I. C.; Higashi, G. S.; 27.6% Conversion Efficiency, a New Record for Single-Junction Solar Cells Under 1 Sun Illumination. *Proceedings, 37th IEEE Photovoltaic Specialist Conferenece*, Seattle, June 2011.

[37] Venkatasubramanian, R.; O'Quinn, B. C.; Hills, J. S.; Sharps, P. R.; Timmons, M. L.; Hutchby, J. A.; Field, H.; Ahrenkiel, A.; Keyes, B. 18.2% (AM1.5) efficient GaAs solar cell on optical-grade polycrystalline Ge substrate. *Conference Records, 25th IEEE Photovoltaic Specialists Conference*. Washington, May 1997; 31-36.

[38] Keavney, C. J.; Haven, V. E.; Vernon, S. M.; Emitter structures in MOVCVD InP solar cells. *Conference Record, 21st IEEE Photovoltaic Specialists Conference*. Kissimimmee, May 1990, 141-144.

[39] Repins, I.; Contreras, M. A.; Egaas, B.; DeHart, C.; Scharf, J.; Perkins, C. L.; To, B.; Noufi, R. 19.9%-efficient ZnO/CdS/CuInGaSe^2 Solar Cell with 81.2% Fill Factor. *Prog. Photovolt: Res. Appl.* **2008**. 16, 235-239.

[40] Wu, X.; Keane, J. C.; Dhere, R. G.; DeHart, C.; Duda, A.; Gessert, T. A.; Asher, S.; Levi, D. H.; Sheldon, P. 16.5%-efficient CdS/CdTe polycrystalline thin-film solar cell. C*onf. Proceedings, 17th European Photovoltaic Solar Energy Conference*, Munich, 22-26 October 2001. 995-1000.

[41] Todorov, T. K.; Reuter, K. B.; Mitzi, D. B. High-efficiency solar cell with earth-abundant liquid-processed absorber. *Adv. Energy Mater.* **2010**. 22, E156-E159.

[42] Koide, N.; Yamanaka, R.; Katayama, H. Recent advances of dye-sensitized solar cells and integrated modules at SHARP. *MRS Proceedings 2009.* **2009**. 1211, 1211-R12-02.

[43] Konarka, Konarka's Power Plastic Achieves World Record 8.3% Efficiency Certification from National Energy Renewable Laboratory (NREL) http://www.konarka.com/index.php/site/pressreleasedetail/konarkas_power_plastic_achieves_world_record_83_efficiency_certification_fr (accessed 1 September 2011).

[44] Fath, P. Latest developments in crystalline silicon based photovoltaics manufacturing process technologies. *Proceedings, 7th Photovoltaic Science Applications and Technology (PVSAT-7).* Edinburgh, April, 2011.

[45] Razkov, T. M.; Ferekides, C. S.; Morel, D.; Stefanakos, E.; Ullal, H. S.; Upadhyaya, H. M. Solar photovoltaic electricity: Current status and future prospects. *Sol. Energy*. **2011**. 85, 1580-1608.

[46] Jimbo, K.; Kimura, R.; Kamimura, T.; Yamada, S.; Maw, W. S.; Araki, H.; Oishi, K.; Katagiri, H. Cu_2ZnSnS_4-type thin film solar cells using abundant materials. *Thin Solid Films.* **2007**. 515, 5997-5999.

[47] Katagiri, H.; Jimbo, K.; Maw, W. S.; Oishi, K.; Yamazaki, M.; Araki, H.; Takeuchi, A. Development of CZTS-based thin film solar cells. *Thin Solid Films*. **2009**. 2455-2460.

[48] Wang, K; Gunawan, O.; Todorov, T.; Shin, B.; Chey, S. J.; Bojarczuk, N. A.; Mitzi, D.; Guha, S. Thermally evaporated Cu_2ZnSnS_4 solar cells. *Appl. Phys. Lett.* **2010**. 97, 143508.

[49] Gunawan, O.; Todorov, T. K.; Mitzi, D. B. Loss mechanisms in hydrazine-processed $Cu_2ZnSn(Se,S)_4$ solar cells. *Appl. Phys. Lett.* **2010**. 97, 233506.

[50] Clifford, J. P.; Johnston, K. W.; Levina, L.; Sargent, E. H. Schottky barriers to colloidal quantum dot films. *Appl. Phys. Lett.* **2007**. 91, 253117.

[51] Barsouka, E.; Macdonald, J. R. *Impedance Spectroscopy Theory, Experiment, and Application, Second Edition*. John Wiley & Sons, Inc.: Hoboken, New Jersey, 2005.

[52] Macdonald, D. D. Reflections on the history of electrochemical impedance spectroscopy. *Electrochimica Acta*. **2006**. 51, 1376-1388.

[53] Stallinga, P. *Electrical Characterization of Organic Electronic Materials and Devices*. John Wiley and Sons Ltd: West Sussex, UK, 2009, p95.

[54] Schroder, D. K. *Semiconductor Material and Device Characterization, Third Edition.* Wiley – IEEE Press, 2006, p62.

[55] Boix, P. P.; Garcia-Belmonte, G.; Munecas, U.; Neophytou, M.; Waldauf, C.; Pacios, R. Determination of gap defect states in organic bulk heterojunction solar cells from capacitance measurements. *Appl. Phys. Lett.* **2009**. 95, 233302.

[56] Mora-Sero, I.; Luo, Y.; Garcia-Belmonte, G.; Bisquert, J.; Munoz, D.; Voz, C.; Puigdollers, J.; Alcubilla, R. Recombination rates in heterojunction silicon solar cells analyzed by impedance spectroscopy at forward bias and under illumination. *Sol. Energy Mater. Sol. Cells.* **2008**. 92, 505-509.

[57] Bisquert, J.; Cahen, D.; Hodes, G.; Ruhle, S.; Zaban, A. Physical Chemical Principles of Photovoltaic Conversion with Nanoparticulate, Mesoporous Dye-Sensitized Solar Cells. *J. Phys. Chem. B*. **2004**. 108, 8106-8118.

[58] Mora-Sero, I.; Garcia-Belmonte, G.; Boix, P. P.; Vazquez, M. A; Bisquert, J. Impedance spectroscopy characterisation of highly efficient silicon solar cells under different light illumination intensities. *Energy & Environ. Sci.* **2009**. 2, 678-686.

[59] Bisquert, J. Chemical capacitance of nanostructured semiconductors: its origin and significance for nanocomposite solar cells. *Phys. Chem. Chem. Phys.* **2003**. 5, 5360-5364.

[60] Sah, C. –T. *Fundamentals of Solid State Electronics*. World Scientific Pub Co Inc: Singapore, 1991.

[61] Mora-Sero, I.; Bisquert, J.; Fabregat-Santiago, F.; Garcia-Belmonte, G. Zoppi, G.; Durose, K.; Proskuryakov, Y. Y.; Oja, I.; Belaidi, A.; Dittrich, T.; Tena-Zaera, R.; Katty, A.; Levy-Clement, C.; Barrioz, V.; Irvine, S. J. C. Implications of the Negative Capacitance Observed at Forward Bias in Nanocomposite and Polycrystalline Solar Cells. *Nano Lett.* **2006**. 6, 640-650.

[62] Garcia-Belmonte, G.; Munar, A.; Barea, E. M.; Bisquert, J.; Ugarte, I.; Pacios, R. Charge carrier mobility and lifetime of organic bulk heterojunctions analyzed by impedance spectroscopy. *Organic Electronics.* **2008**. 9, 847-851.

[63] Green, M. A.; ShewChun, J. Minority Carrier Effects Upon the Small Signal and Steady-State Properties of Schottky Diodes. *Solid State Electron.* **1973**. 16, 1141-1150.

[64] Bisquert, J. Beyond the quasistatic approximation: Impedance and capacitance of an exponential distribution of traps. *Phys. Rev. B.* **2008**. 77, 235203.

[65] Bisquert, J. Theory of the Impedance of Electron Diffusion and Recombination in a Thin Layer. *J. Phys. Chem. B*. **2002**. 106, 325-333.

[66] Pitarch, A.; Garcia-Belmonte, G.; Mora-Sero, I.; Bisquert, J. Electrochemical impedance spectra for the complete equivalent circuit of diffusion and reaction under steady-state recombination current. *Phys. Chem. Chem. Phys.* **2004**. 6, 2983-2988.

[67] Park, S.; Yoo, J. Electrochemical impedance spectroscopy for better electrochemical measurements. *Anal. Chem.* **2003**. 75, 455a-461a.

[68] Tzabari, L.; Tessler, N. Shockley-Read-Hall recombination in P3HT:PCBM solar cells as observed under ultralow light intensities. *J. Appl. Phys.* **2011**. 190, 064501.

[69] Hillhouse, H. W.; Beard, M. C. Solar cells from colloidal nanocrystals: Fundamentals, materials, devices, and economics. *Current Opinions in Colloid & Interface Science*. **2009**. 14, 245-259.

[70] Sargent, E. H. Infrared photovoltaics made by solution processing. *Nat. Photonics*. **2009**. 3, 325-331.

[71] Tang, J.; Sargent, H. Infrared Colloidal Quantum Dots for Photovoltaics: Fundamentals and Recent Progress. *Adv. Mater.* **2011**. 23, 12-29.

[72] Jabbour, G. E.; Doderer, D. Quantum Dot Solar Cells The best of both worlds. *Nat. Photonics*. **2010**. 4, 604-605.

[73] Emin, S.; Singh, S. P.; Han, L,; Satoh, N.; Islam, A. Colloidal quantum dot solar cells. *Sol. Energ.* **2011**. 85, 1264-1282.

[74] Haverinen, H. M.; Myllyla, R. A.; Jabbour, G. E. Inkjet printing of light emitting quantum dots. *Appl. Phys. Lett.* **2009**. 94, 073108.

[75] Singh, M.; Haverinen, H. M.; Dhagat, P.; Jabbour, G. E; Inkjet Printing – Process and Its Applications. **2010**. 22, 673-685.

[76] Alivisatos, A. P. Semiconductor Clusters, Nanocrystals, and Quantum Dots. *Science*. **1996**. 271, 933-937.

[77] Wise, F. W. Lead Salt Quantum Dots: the Limit of Strong Quantum Confinement. *Acc. Chem. Res.* **2003**. 33, 773-780.

[78] Brus, L. E. A simple model for the ionization potential, electrons affinity, and aqueous redox potentials of small semiconductor crystallites. *J. Chem. Phys.* **1983**. 79, 5566-5571.

[79] Brus, L. E. Electron-electron and electron-hole interactions in small semiconductor crystallites: The size dependence of the lowest excited electronic state. *J. Chem. Phys.* **1984**. 80, 4403-4409.

[80] Luther, J. M.; Gao, J.; Lloyd, M. T.; Semonin, O. E.; Beard, M. C.; Nozik, A. J. Stability Assessment on a 3% Bilayer PbS/ZnO Quantum Dot Heterojunction Solar Cell. *Adv. Mater.* **2010**. 22, 3704-3707.

[81] Hines, M.; Scholes, G. D. Colloidal PbS Nanocrystals with Size-Tunable Near-Infrared Emission: Observation of Post-Synthesis Self-Narrowing of the Particle Size Distribution. *Adv. Mater.* **2003**. 15, 1844-1849.

[82] Nozik, A. J. Quantum dot solar cells. *Physica E*. **2002**. 14, 115-120.

[83] Nozik, A. J. Nanoscience and Nanostructures for Photovoltaics and Solar Fuels. *Nano Lett.* **2010**. 10, 2735-2741.

[84] Schaller, R. D.; Klimov, V. I. High Efficiency Carrier Multiplication in PbSe Nanocrystals: Implications for Solar Energy Conversion. *Phys. Rev. Lett.* **2004**. 92, 186601.

[85] Ellingson, R. J.; Beard, M. C.; Johnson, J. C.; Yu, P.; Micic, O. I.; Nozik, A. J.; Shabaev, A.; Efros, A. L. Highly Efficient Multiple Exciton Generation in Colloidal PbSe and PbS Quantum Dots. *Nano Lett.* **2005**. 5, 865-871.

[86] Sukhovatkin, V.; Hinds, S.; Brzozowski, L.; Sargent, E. H. Exploiting Multiexciton Generation. *Science*. **2009**. 324, 1542-1544.

[87] Pijpers, J. J. H.; Ulbricht, R.; Tielrooij, K. J.; Osherov, A.; Golan, Y.; Delerue, C.; Allan, G.; Bonn, M. Assessment of carrier-multiplication efficiency in bulk PbSe and PbS. *Nat. Phys.* **2009**. 5, 811-814.

[88] Beard, M. C.; Midgett, A. G.; Law, M.; Semonin, O. E.; Ellingson, R. J.; Nozik, A. J. Variations in the Quantum Efficiency Generation for a Series of Chemically Treated PbSe Nanocrystal Films. *Nano Lett.* **2009**. 9, 836-845.

[89] Ben-Lulu, M.; Mocatta, D.; Bonn, M.; Bannin, U.; Ruhman, S. On the Absence of Detectable Carrier Multiplication in a Transient Absorption Study of InAs/CdSe/ZnSe Core/Shell1/Shell2 Quantum Dots. *Nano Lett.* **2008**. 8, 1207-1211.

[90] Nair, G.; Bawendi, M. G. Carrier multiplication yields of CdSe and CdTe nanocrystals by transient photoluminescence spectroscopy. *Phys. Rev. B.* **2007**. 76, 081304(R).

[91] Trinh, M. T.; Houtepen, A. J.; Schins, J. M.; Hanrath, T.; Piris, J.; Knulst, W.; Goossens, A. P. L. M.; Siebbeles, L. D. A. In Spite of Recent Doubts Carrier Multiplication Does Occur in PbSe Nanocrystals. *Nano Lett.* **2008**. 8, 1716-1718.

[92] McGuire, J. A.; Joo, J.; Pietryga, J. M.; Schaller, R. D.; Klimov, V. I. New Aspects of Carrier Multiplication in Semiconductor Nanocrystals. *Acc. Chem. Res.* **2008**. 41, 1810-1819.

[93] Pattantyus-Abraham, A. G; Kramer, I. J.; Barkhouse, A. R.; Wang, X.; Konstantatos, G.; Debnath, R.; Levina, L.; Raabe, I.; Nazeeruddin, M.; Gratzel, M.; Sargent, E. H. Depleted-Heterojunction Colloidal Quantum Dot Solar Cells. *ACS Nano*. **2010**. 4, 3374-3380.

[94] Barkhouse, D. A. R.; Debnath, R.; Kramer, I. J.; Zhitomirsky, D.; Pattantyus-Abraham, A. G.; Levina, L.; Etgar, L.; Gratzel, M.; Sargent, E. H. Depleted Bulk Heterojunction Colloidal Quantum Dot Photovoltaics. *Adv. Mater.* **2011**. 23, 3134-3138.

[95] Choi, J. J.; Wenger, W. N.; Hoffman, R. S.; Lim, Y.; Luria, J.; Jasieniak, J.; Marohn, J. A.; Hanrath, T. Solution-Processed Nanocrystal Quantum Dot Tandem Solar Cells. *Adv. Mater*. **2011**. 23, 3144-3148..

[96] Wang, X.; Koleilat, G. I.; Tang, J.; Liu, H.; Kramer, I. J.; Debnath, R.; Brzozowski, L.; Barkhouse, D. A. R.; Levina, L.; Hoogland, S.; Sargent, E. H. Tandem colloidal quantum dot solar cells employing a graded recombination layer. *Nat. Photon.* **2011**. 5, 480-484.

[97] Kramer, I. J.; Levina, L.; Debnath, R.; Zhitomirsky, D.; Sargent, E. H. Solar Cells Using Quantum Funnels. *Nano Lett*. In press. dx.doi.org/10.1021/nl201682h.

[98] Debnath, R.; Tang, J.; Barkhouse, D. A.; Wang, X. H.; Pattantyus-Abraham, L; Brzozowski, L; Levina, L.; Sargent, E. H. Ambient Processed Colloidal Quantum Dot Solar Cells via Individual Pre-Encapsulation of Nanoparticles. *J. Am. Chem. Soc.* **2010**, 132, 5952-5953.

[99] Leschkies, K. S.; Beatty, T. J.; Kang, M. S.; Norris, D. J.; Aydill, E. S. Solar Cells Based on Junctions between Colloidal PbSe Nanocrystals and Thin ZnO Films. *ACS Nano.* **2009**. 11, 3683-3648.

[100] Choi, J. J.; Lim, Y.; Santiago-Berrios, M. B; Oh, M.; Hyun, B.; Sun, L.; Bartnik, A. C.; Goedhart, A.; Malliaras, G. G.; Abruna, H. D.; Wise, F. W.; Hanrath, T. PbSe Nanocrystal Excitonic Solar Cells. *Nano Lett.* **2009**. 11, 3749-3755.

[101] Gao, J.; Luther, J. M.; Semonin, O. E.; Ellingson, R. J.; Nozik, A. J.; Beard, M. C. Quantum Dot Size Dependent J-V Characteristics in Heterojunction ZnO/PbS Quantum Dot Solar Cells. *Nano Lett.* **2011**. 11, 1002-1008.

[102] Verbakel, F.; Meskers, S. C. J.; Janssen, R. A. J. Electronic memory effects in diodes from a zinc oxide nanoparticle-polystyrene hybrid materia. *Appl. Phys. Lett.* **2006**. 89, 102103.

[103] Gilot, J.; Wienk, M. M.; Janssen, R. A. J. Double and triple junction polymer solar cells processed from solution. *Appl. Phys. Lett.* **2007**. 90, 143512.

[104] Lakhwani, G.; Roijmans, R. F. H.; Kronemeijer, A. J.; Gilot, J.; Janssen, R. A. J.; Meskers, S. C. J. Probing Charge Carrier density in a Layer of Photodoped ZnO Nanoparticles by Spectroscopic Ellipsometry. *J. Phys. Chem. C.* **2010**. 114, 14804-14810.

[105] Collins, R. J.; Thomas, D. G Photoconduction and Surface Effects with Zinc Oxide Crystals. *Phys. Rev*. **1958**. 112, 388-395.

[106] Verbakel, F.; Meskers, S. C. J.; Janssen, R. A. J. Electronic memory effects in diodes of zinc oxide nanoparticles in a matrix of polystyrene or poly(3-hexythiophene). *J. Appl. Phys.* **2007**. 102, 083701.

[107] Liu, W. K.; Whitaker, K. M; Kittilstved, K. R.; Gamelin, D. R. Stable Photogenerated Carriers in magnetic Semiconductor Nanocrystals. *J. Am. Chem. Soc.* **2006**. 128, 3910-3911.

[108] Pacholski, C.; Kornowski, A.; Weller, H. Self-Assembly of ZnO: From Nanodots to Nanorods. *Angewandte Chemie International Edition.* **2002**. 47, 1188-1191

[109] Luther, J. M.; Law, M.; Song, Q.; Perkins, C. L.; Beard, M. C.; Nozik, A. J. Structural, Optical, and Electrical Properties of Self-Assembled Films of PbSe Nanocrystals Treated with 1,2-Ethanedithiol. *ACS Nano*. **2008**. 2, 271-280.

[110] Tang, J.; Wang, X.; Brzozowski, L,; Barkhouse, D. A. R.; Debnath, R,; Levina, L.; Sargent, E. H. Schottky Quantum Dot Solar Cells Stable in Air under Solar Illumination. *Adv. Mater*. **2010**. 22, 1398-1402.

[111] Johnston, K. W.; Pattantyus-Abraham, A. G.; Clifford, J. P.; Myrskog, S. H.; Hoogland, S.; Shukla, H.; Klem, E. J. D.; Sargent, E. H. Efficient Schottky-quantum-dot photovoltaics: The roles of depletion, drift, and diffusion. *Appl. Phys. Lett.* **2008**. 92, 122111.

[112] Tang, J.; Brzozowski, L.; Barkhouse, D. A. R.; Wang, X.; Debnath, R.; Wolowiec, R.; Palmiano, E.; Levina, L.; Pattantyus-Abraham, A. G.; Jamakosmanovic, D.; Sargent, E. H. Quantum Dot Photovoltaics in the Extreme Quantum Confinement Regime: The Surface-Chemical Origins of Exceptional Air- and Light-Stability. *ACS Nano*. **2010**. 4, 869-878.

[113] Luther, J. M.; Law, M.; Beard, M. C.; Song, Q.; Reese, M. O.; Ellingson, R. J.; Nozik, A. J. Schottky Solar Cells Based on Colloidal Nanocrystal Films. *Nano Lett.* **2008**. 10, 3488-3492.

[114] Choi, J. J.: Luria, J.; Hyun, B.; Bartnik, A. C.; Sun, L.; Lim, Y.; Marohn, J. A.; Wise, F. W.; Hanrath, T. Photogenerated Exciton Dissociation in Highly Coupled Lead Salt Nanocrystal Assemblies. *Nano Lett.* **2010**. 10, 1805-1811.

[115] Sheng, S. L. *Semiconductor Physical Electronics*. Springer. 1993.

[116] Hyun, B.; Zhong, Y.; Bartnik, A. C.; Sun, L.; Abruna, H. D.; Wise, F. W.; Goodreau, J. D.; Matthews, J. R.; Leslie, T. M.; Borrelli, N. F. Electron Injection from Colloidal PbS Quantum Dots into Titanium Dioxide Nanoparticles. *ACS Nano*. **2008**. 2, 2206-2212.

[117] Clark, S. W.; Harbold, J. M.; Wisw, F. W. Resonant Energy Transfer in PbS Quantum Dots. *J. Phys. Chem. C*. **2007**. 111, 7302-7305.

[118] Warner, J. H.; Thomsen, E.; Watt, A. R.; Heckenberg, N. R.; Rubinsztein-Dunlop, H. Time-resolved photoluminescence spectroscopy of ligand-capped PbS nanocrystals. *Nanotechnology*. **2005**. 16, 175-179.

[119] Dissanayake, D. M. N. M.; Lutz, T.; Curry, R. J.; Silva, S. R. P. Measurement and validation of PbS nanocrystal energy levels. *Appl. Phys. Lett.* **2008**. 93, 043501.

[120] Rauh, D.; Wagenpfahl, A; Deibel, C.; Dyakonov, V. Relation of open circuit voltage to charge carrier density in organic bulk heterojunction solar cells. *Appl. Phys. Lett.* **2011**. 98, 133301.

[121] Wagenpfahl, A.; Deibel, C.; Dyakonov, V. Organic Solar Cell Efficiencies Under the Aspect of Reduced Surface Recombination Velocities. *IEEE Journal of Selected Topics in Quantum Electronics*. **2010**. 16, 1759-1763.

[122] Ju, T.; Graham, R. L.; Zhai, G.; Rodriguez, Y. W.; Breeze, A. J.; Tang, L.; Alers, G. B.; Carter, S. A. High efficiency mesoporous titanium oxide PbS quantum dot solar cells at low temperatures. *Appl. Phys. Lett.* **2010**. 97, 043106.

[123] Law, M.; Beard, M. C.; Choi, S.; Luther, J. M.; Hanna, M. C.; Nozik, A. J. Determining the Internal Quantum Efficiency of PbSe Nanocrystal Solar Cells with the Aid of an Optical Model. *Nano Lett.* **2008**. 8, 3904-3910.

[124] Werner, J.; Levi, A. F. J.; Tung, R. T.; Anzlowar, M.; Pinto, M. Origin of the Excess Capacitance at Intimate Schottky Contacts. *Phys. Rev. Lett.* **1988**. 60, 53-56.

[125] Shrotriya, V.; Yang, Y. Capacitance-voltage characterization of polymer light-emitting diodes. *J. Appl. Phys.* **2005**. 97, 054504.

[126] Leroux, M.; Grandjean, N.; Beaumont, B.; Nataf, G.; Semond, F.; Massies, J.; Gibart, P. Temperature quenching of photoluminescence intensities in undoped and doped GaN. *J. Appl. Phys.* **1999**. 86, 3721-3728.

[127] Clifford, J. P.; Konstantatos, G.; Johnston, K. W.; Hoogland, S.; Levina, L.; Sargent, E. H. Fast, sensitive and spectrally tuneable colloidal-quantum-dot photodetectors. *Nature Nanotech.* **2009**. 4, 40-44.

[128] Green, M. A.; Emery, K.; Hishakawa, Y.; Warta, W.; Dunlop, E. D. Solar cell efficiency tables (Version 38). *Prog. Photovolt: Res. Appl.* **2011**. 19, 565-572.

[129] NREL Best Research-Cell Efficiencies table. http://en.wikipedia.org/wiki/File:PVeff(rev110826).jpg (accessed 1 September 2011).

[130] Luque, A.; Marti, A., The Intermediate Band Solar Cell: Progress Toward the Realization of an Attractive Concept. *Adv. Mater.* **2010**. 22, 160-174.

[131] Volz, K.; Lackner, D.; Nemeth, I.; Kunert, B.; Stolz, W.; Baur, C.; Dimroth, F.; Bett, A. W. Optimization of annealing conditions of (GaIn)(NAs) for solar cell applications. *J. Cryst. Growth*. **2008**. 310, 2222-2228.

[132] Marti, A.; Lopez, N.; Antolin, E.; Canovas, E.; Luque, A.; Stanley, C. R.; Farmer, C. D.; Diaz, P. Emitter degradation in quantum dot intermediate band solar cells. *Appl. Phys. Lett.* **2007**. 90, 233510.

[133] Bank, S. R.; Yuen, H. B.; Bae, H.; Wistey, M. A.; Harris, J. S. Jr. Overannealing effects in GaInNAs(Sb) alloys and their importance to laser applications. *Appl. Phys. Lett.* **2006**. 88, 221115.

[134] Shrestha, S. K.; Aliberti, P.; Conibeer, G. J. Energy selective contacts for hot carrier solar cells. *Sol. Energy Mater. Sol. Cells*, **2010**. 94, 1546-1550.

[135] Mowbray, D. J.; Skolnick, M. S. New physics and devices based on self-assembled semiconductor quantum dots. *J. Appl. Phys. D.* **2005**. 38, 2059-2076.

[136] Li, J.; Chong, M.; Zhu, J.; Li, Y.; Xu, J.; Wang, P.; Shang, Z.; Yang, Z.; Zhu, R.; Cao, X. 35% efficient nonconcentrating novel silicon solar cell. *Appl. Phys. Lett.* **1992**. 60, 2240-2242.

[137] Luque, A.; Marti, A. Increasing the Efficiency of Ideal Solar Cells by Photon Induced Transitions at Intermediate Levels. *Phys. Rev. Lett.* **1997**. 78, 5014-5017.

[138] Araujo, G. L.; Marti, A. Absolute limiting efficiencies for photovoltaic energy conversion. *Sol. Energy Mater. Solar Cells*. **1994**. 33, 213-240.

[139] Marti, A; Cuadra, L.; Luque, A. Quantum Dot Intermediate Band Solar Cell. *Conference Record of the 28th IEEE Photovoltaics Specialists Conference* (IEEE, New York, USA) **2000**. 940-943.

[140] Popescu, V.; Bester, G.; Hanna, M. C.; Norman, A. G.; Zunger, A. Theoretical and experimental examination of the intermediate-band concept for strain-balanced (In,Ga)As/Ga(As,P) quantum dot solar cells. *Phys. Rev. B.* **2008**. 87, 205321.

[141] Marti, A.; Lopez, N.; Antolin, E.; Canovas, E.; Stanley, C.; Farmer, C.; Cuadra, L.; Luque, A. Novel semiconductor solar cell structures: The quantum dot intermediate band solar cell. *Thin Solid Films*. **2006**. 511-512, 638-644.

[142] Hubbard, S. M.; Cress, C. D.; Bailey, C. G.; Raffaelle, R. P.; Bailey, S. G.; Wilt, D. M. Effect of strain compensation on quantum dot enhanced GaAs solar cells. *Appl. Phys. Lett.* **2008**. 92, 123512.

[143] Laghumavarapu, R. B.; El-Emawy, M.; Nuntawong, N.; Moscho, A.; Lester, L. F.; Huffaker, D. L. Improved device performance of InAs/GaAs quantum dot solar cells with GaP strain compensation layers. *Appl. Phys. Lett.* **2007**. 91, 243115.

[144] Oshima, R.; Takata, A.; Okada, Y. Strain-compensated InAs/GaNAs quantum dots for use in high-efficiency solar cells. *Appl. Phys. Lett.* **2008**. 93, 083111.

[145] Luque, A.; Marti, A.; Lopez, N.; Antolin, E.; Canovas, E.; Stanley, C.; Farmer, C.; Caballero, L. J.; Cuadra, L.; Balenzategui, J. L. Experimental analysis of the quasi-Fermi level split in quantum dot intermediate-band solar cells. *Appl. Phys. Lett.* **2005**. 87, 083505.

[146] Marti, A.; Antolin, E.; Stanley, C. R.; Farmer, C. D.; Lopez, N.; Diaz, P. Canovas, E.; Linares, P. G.; Luque, A. Production of Photocurrent due to Intermediate-to-Conduction-Band Transitions: A Demonstration of a Key Operating Principle of the Intermediate-Band Solar Cell. *Phys. Rev. Lett.* **2006**. 97, 247701.

[147] Luque, A.; Marti, A. A Mettalic Interband High Efficiency Solar Cell. *Prog. Photovoltaics: Research and Applications.* **2001**. 9, 73-86.

[148] Antolin, E.; Marti, A.; Farmer, C. D.; Linares, P. G.; Hernandez, E.; Sanchez, A. M.; Ben, T.; Molina, S. I.; Stanley, C. R.; Luque, A. Reducing carrier escape in the InAs/GaAs quantum dot intermediate band solar cell. *J. Appl. Phys.* **2010**. 108, 064513.

[149] Aroutiounian, V.; Petrosyan, S.; Khachatryan, A.; Touryan, K. Quantum Dot Solar Cells. *J. Appl. Phys.* **2001**. 89, 2268-2271.

[150] Marti, A.; Cuadra, L.; Luque, A. Partial Filling of a Quantum Dot Intermediate Band for Solar Cells. *IEEE Trans. Electron. Dev.* **2001**. 48, 2394-2399.

[151] Marti, A.; Cuadra, L.; Luque, A. *Next Generation Photovoltaics: High Efficiency through Full Spectrum Utilization.* (Institute of Physics, Bristol) **2003**. 140-162.

[152] Stranski, I. N.; Krastanov, L. V. Akad. Wiss. Lit. Mainz Abh. Math. Naturwiss. Kl. **1939**. 146, 797-810. There is question as to the correctness of this reference. It is given here as a reference to Stranski and Krastanov. Descriptions of the method come from other references.

[153] Liu, H. Y.; Sellers, I. R.; Gutierrez, M.; Groom, K. M.; Soong, W. M.; Hopkinson, M.; David, J. P. R. Influence of the spacer layer growth temperature on multilayer InAs/GaAs quantum dot structures. *J. Appl. Phys.* **2004**. 96, 1988-1992.

[154] Tutu, F. K.; Sellers, I. R.; Peinado, M. G.; Willis, S. M.; Assender, H. E.; Watt, A. A. R.; Wang, T.; Liu, H. Y. Improved performance of multilayer InAs/GaAs quantum-dot solar cells using a high-growth-temperature GaAs spacer layer. Submitted to *Appl. Phys. Lett.*

[155] University of Colorado Department of Electrical, Computer, and Energy Engineering. Principles of Semiconductor Devices. Temperature dependence of the energy bandgap. http://ecee.colorado.edu/~bart/book/eband5.htm (accessed July 22, 2011).

[156] Hubbard, S. M.; Bailey, C. G.; Cress, C. D.; Polly, S.; Clark, J.; Forbes, D. V.; Raffaelle, R. P.; Bailey, S. G.; Wilt, D. M. Short Circuit Current Enhancement of GaAs Solar Cells Using Strain Compensated InAs Quantum Dots. *33 IEEE Photovoltaic Specialist Conference* (IEEE, San Diego, USA). **2008**.

[157] Lu, H. F.; Fu, L.; Jolley, G.; Tan, H. H.; Tatavarti, S. R.; Jagadish, C. Temperature dependence of dark current properties of InGaAs/GaAs quantum dot solar cells. *Appl. Phys. Lett.* **2011**. 98, 183509.

[158] Aperathitis, E.; Scott, C. G.; Sands, D.; Foukaraki, V.; Hatzopoulos, Z.; Panayotatos, P. Effect of temperature on GaAs/AlGaAs multiple quantum well solar cells. *Mater. Sci. Eng.* **1998**. B51, 85-89.

[159] PVCDROM http://www.pveducation.org/pvcdrom/pn-junction/diode-equation (accessed 23 August 2011).

[160] Guimard, D.; Morihara, R.; Bordel, D.; Tanabe, K.; Wakayama, Y.; Nishioka, M.; Arakawa, Y. Fabrication of InAs/GaAs quantum dot solar cells with enhanced photocurrent and without degradation of open circuit voltage. *Appl. Phys. Lett.* **2010**. 96, 203507.

[161] Marvin, D. C.; Halle, L. F. Intensity Effects in Minority Carrier Lifetime Measurements. *Photovoltaic Specialists Conference, 1990., Conference Record of the Twenty First IEEE.* (Kissimmee, FL, USA) **1990**. 1, 353-356.

[162] Kladis, D. I.; Euthymiou, P. C. Carrier Lifetimes in Low-Resistivity GaAs upon Electron Bombardment and Annealing. *Phys. Stat. Sol. A.* **1972**. 10, 479-485.

[163] Blakemore, J. S. *Gallium Arsenide*. American Institute of Physics: 1993, p399.

[164] Fox, A. M.; Ispasoiu, R. G.; Foxon, C. T.; Cunningham, J. E.; and Yan, W. Y. Carrier escape mechanisms from GaAs/$Al_xGa_{1-x}As$ multiple quantum wells in an electric field. *Appl. Phys. Lett.* **1993**. 63, 2917-2919.

[165] Loef, R.; Houtepen, A. J.; Talgorn, E.; Schoonman, J.; Goossens, A. Temperature Dependence of electron Transport in CdSe Quantum Dot Films. *J. Phys. Chem. C* **2009**. 113, 15992-15996.

[166] Chang, W. –H.; Chen, W. Y.; Hsu, T. M.; Yeh, N. –T.; Chyi, J. I. Hole emission processes in InAs/GaAs self-assembled quantum dots. *Phys. Rev. B.* **2002**. 66, 195337.

[167] Tsormpatzoglou, A.; Tassis, D. H.; Dimitriadis, C. A.; Frigeri, P.; Franchi, S.; Gombia, E.; Mosca, R. Stress-Induced Local Trap Levels in Au/n-GaAs Schottky Diodes With Embedded InAs Quantum Dots. *IEEE Elec. Dev. Lett.* **2006**. 27, 320-322.

[168] Stievenard, D.; Boddaert, X.; Bourgoin, J. C.; von Bardeleben, H. J. Behavior of electron-irradiation-induced defects in GaAs. *Phys. Rev. B*. **1990**. 41, 5271-5279.

[169] Siyanbola, W. O.; Palmer, D. W. Electronic Energy Levels of Defects That Anneal in the 280-K Stage in Irradiated *n*-Type Gallium Arsenide. *Phys. Rev. Lett.* **1991**. 66, 56-59.

[170] Jackrel, D. B.; Bank, S. R.; Yuen, H. B.; Wistey, M. A.; Harris, J. S.; Ptak, A. J.; Johnston, S. W.; Friedman, D. J.; Kurtz, S. R. Dilute nitride GaInNAs and GaInNAsSb solar cells by molecular beam epitaxy. *J. Appl. Phys.* **2007**. 101, 114916.

[171] Tu, K.N.; Mayer, J. W.; Feldman, L. C. *Electronic Thin Film Science for Electrical Engineers and Materials Scientists.* Macmillian: USA, 1992.

[172] Damilano, B.; Barjon, J.; Duboz, J. –Y; Massies, J.; Hierro, A.; Ulloa, J. –M.; Calleja, E. Growth and *in situ* annealing conditions for long-wavelength (Ga, In)(N, As)/GaAs lasers. *Appl. Phys. Lett.* **2005**. 86, 071105.

[173] Geelhaar, L.; Galluppi, M.; Jaschke, G.; Averbeck, R.; Riechert, H.; Remmele, T.; Albrecht, M.; Qworzak, M.; Hildebrandt, R.; Hoffman, A. Influence of structural nonuniformity and nonradiative processes on the luminscence efficiency of InGaAsN quantum wells. *Appl. Phys. Lett.* **2006**. 88, 011903.

[174] Toivonen, J.; Hakkarainen, T.; Sopanen, M.; Lipsanen, H.; Oila, J.; Saarinen, K. Observation of defect complexes containing Ga vacancies in GaAsN. *Appl. Phys. Lett.* **2003**. 82, 40-42.

[175] Spruytte, S. G.; Coldren, C. W.; Harris, J. S.; Wampler, W.; Krispin, P.; Ploog, K.; Larson, M. C. incorporation of nitrogen in nitride-arsenides: Origin of improved luminescence efficiency after anneal. *J. Appl. Phys.* **2001**. 89, 4401-4406.

[176] Tanaka, S.; Moto, A.; Takahashi, M.; Tanabe, T.; Takagishi, S. Spatial distribution of deep level traps in GaNAs crystals. *J. Cryst. Growth*. **2000**. 221, 467-474.

[177] Hierro, A.; Ulloa, J. –M.; chauveau, J.; -M. Trampert, A.; Pinault, M. –A.; Tournie, E.; Guzman, A.; Sanchez-Rojas, J. L.; Calleja, E. Annealing effects on the crystal structure of GaInNAs quantum wells with large In and N content grown by molecular beam epitaxy. *J. Appl. Phys.* **2003**. 94, 2319-2324.

[178] Geelhaar, L.; Galluppi, M. Averbeck, R.; Jaschke, G.; Riechert, H. Annealing of InGaAsN quantum wells in hydrogen. *Appl. Phys. Lett.* **2007**. 90, 071913.

[179] Sellers, I. R.; Tan, W-S.; Smith, K.; Hooper, S.; Day, S.; Kauer, M. Effects of Thermal Annealing on GaInNAs Solar Cells: The effect of radiative recombination. Submitted to *Appl. Phys. Lett.*

[180] Govindaraju, S.; Reifsnider, J. M.; Oye, M. M.; Holmes, A. L. Jr. Rapid Thermal Annealing Effects on the Photoluminescence Propterties of Molucular Beam Epitaxy-Grown GaIn(N)As Quantum Wells with Ga(N)As Spacers and Barriers. *J. Electron. Mater.* **2004**. 33, 851-860.

[181] Liu, H. F.; Chua, S. J.; Xiang, N. On overannealing of GaIn(N)As/Ga(N)As multiple quantum wells grown by molecular beam epitaxy. *J. Appl. Phys.* **2007**. 102, 013504.

[182] Bae, H. P.; Bank, S. R.; Yuen, H. B.; Sarmiento, T.; Pickett, E. R.; Wistey, M. A.; Harris, J. S. Temperature dependencies of annealing behaviors of GaInNAsSb/GaNAs quantum wells for long wavelength dilute-nitride lasers. *Appl. Phys. Lett.* **2007**. 90, 231119.

[183] Mussler, G.; Chauveau, J. –M.; Trampert, A.; Ramsteiner, M.; Daweritz, L.; Ploog, K. H. Nitrogen-dependent optimum annealing temperature of Ga(As,N). *J. Cryst. Growth*. **2004**. 267, 60-66.

[184] Yu, G.; Gao, J.; Hummelen, J. C.; Wudl, F.; Heeger, A. J. Polymer Photovoltaic Cells: Enhanced Efficiencies via a Network of Internal Donor-Acceptor Heterojunctions. *Science*. **1995**. 270, 1789-1791.

[185] Dennler, G.; Scharber, M. C.; Brabec, C. J. Polymer-Fullerene Bulk-Heterojunction Solar Cells. *Adv. Mater*. **2009**. 21, 1323-1338.

[186] Ameri, T.; Dennler, G.; Lungenschmied, C.; Brabec, C. J. Organic tandem solar cells: A review. *Energy Environ. Sci.* **2009**. 2, 347-363.

[187] PVTECH, NREL validates Konarka's 8.3% 'Power Plastic' efficiency record. http://www.pv-tech.org/news/nrel_validates_konarkas_8.3_power_plastic_efficiency_record (accessed 29 July 2011).

[188] Nelson, J. Organic photovoltaic films. *Curr. Opin. Solid State Mat. Sci.* **2002**. 6, 87-95.

[189] Shaheen, S. E.; Radspinner, R.; Peyghambarin, N.; Jabbour, G. E. Fabrication of bulk heterojunction plastic solar cells by screen printing. *Appl. Phys. Lett.* **2001**. 79, 2996-2998.

[190] Gustafsson, G.; Cao, Y.; Treacy, G. M.; Klavetter, F.; Colaneri, N.; Heeger, A. J. Flexible light-emitting diodes made from soluble conducting polymers. *Nature*. **1992**. 357, 477-479.

[191] Jorgensen, M.; Norrman, K.; Krebs, F. C. Stability/degradation of polymer solar cells. *Sol. Energy Mater. Sol. Cells*. **2008**. 92, 686-714.

[192] Forrest, S. R. The path to ubiquitous and low-cost organic electronic appliances on plastic. *Nature*. **2004**. 428, 911-918.

[193] Dam, N.; Scurlock, R. D.; Wang, B.; Ma, L.; Sundahl, M.; Ogilby, P. Singlet Oxygen as a Reactive Intermediate in the Photodegeneration of Phenylenevinylene Oligomers. *Chem. Mater*. **1999**. 11, 1302-1305.

[194] Chawdhurry, N.; Kohler, A.; Harrison, M. G.; Hwang, D. H.; Holmes, A. B.; Friend, R. H. The Effects of H_2O and O_2 on the Photocurrent Spectra of MEH-PPV. *Synth. Met.* **1999**. 102, 871-872.

[195] Kawano, K.; Adachi, Chihaya, A. Evaluating Carrier Accumulation in Degraded Bulk Heterojunction Organic Solar Cells by a Thermally Stimulated Current Technique. *Adv. Funt. Mater.* **2009**. 19, 3934-3940.

[196] Seemann, A.; Egelhaaf, H. –J.; Brabec, C. J.; Hauch, J. A. Influence of oxygen on semi-transparent organic solar cells with gas permeable electrodes. *Org. Electron.* **2009**. 10, 1424-1428.

[197] Manceau, M.; Rivaton, A.; Gardette, J.; Guillerez, S.; Lemaitre, N. The mechanism of photo- and thermooxidation of poly(3-hexylthiophene) (P3HT) reconsidered. *Polym. Degrad. Stab.* **2009**. 94, 898-907.

[198] Ficker, J.; von Seggem, H.; Rost, H.; Clemens, W.; McCulloch, I. Influence of intensive light exposure on polymer field-effect transistors. *App. Phys. Lett.* **2004**. 85, 1377-1379.

[199] Pacios, R.; Chatten, A.; Kawano, K.; Durrant, J. R.; Bradley, D. D. C.; Nelson, J. Effects of Photo-oxidation on the Performance of Poly[2-methoxy-5-(3',7'-dimethyloctyloxy)-1,4-phenylenevinylene]:6,6]-Phenyl C_{61}-Butyric Acid Methyl Ester Solar Cells. *Adv. Funct. Mater.* **2006**. 16, 2117-2126.

[200] Seemann, A.; Sauermann, T.; Lungenschmied, C.; Armbruster, O.; Bauer, S.; Egelhaaf, H. –J.; Hauch, J. Reversible and irreversible degradation of organic solar cell performance by oxygen. *Sol. Energy*. **2011**. 85, 1238-1249.

[201] Dennler, G.; Lungenschmied, C.; Saiciftici, N. S.; Schwodiauer, R.; Bauer, S.; Reiss, H. Unusual electromechanical effects in organic semiconductor Schottky contacts: Between piezoelectricity and electrostriction. *Appl. Phys. Lett.* **2005**. 87, 163501.

[202] Zhuo, J.; Zhao, L.; Png, R.; Wong, L.; Chia, P.; Tang, J.; Sivaramakrishnan, S.; Zhou, M.; Ou, E. C. –W.; Chua, S.; Sim, W.; Chua, L.; Ho, P. K. –H. Direct Spectroscopic Evidence for a Photodoping Mechanism in Polythiophene and Poly(bithiophen-*alt*-thienothiophene) Organic Semiconductor Thin Films Involving Oxygen and Sorbed Moisture. *Adv. Mater.* **2009**. 21, 4747-4752.

[203] Engelhaaf, H. –J.; Luer, L.; Oelkrug, D.; Winter, G.; Haisch, M.; Hanack, M. Influence of Oxygen Doping on the Photoconductivity of π-Conjugated Molecules. *Synth. Met.* **1997**. 84, 897-898.

[204] Liao, H.; Yang, C.; Liu, C.; Horng, S.; Meng, H.; Shy, J. Dynamics and reversibility of oxygen doping and de-doping for conjugated polymers. *J. Appl. Phys.* **2008**. 130, 104506.

[205] Jarret, C. P.; Pichler, K.; Newbould, R.; Friend, R. H. Transport studies in C_{60} and C_{60}/C_{70} thin films using metal-insulator-semiconductor field-effect-transistors. *Synth. Met.* **1996**. 77, 35-38.

[206] Kaiser, M.; Maser, W. K.; Byrne, H. J.; Mittelbach, A.; Roth, S. Photoconductivity of Thin Film Fullerenes: Effect of Oxygen and Thermal Annealing. *Solid State Commun.* **1993**. 87, 281-284.

[207] Arai, T.; Murakami, Y.; Suematsu, H.; Kikuchi, K.; Achiba, Y.; Ikemoto, I. Resistivity of Single Crystal C_{60} and Effect of Oxygen. *Solid State Commun.* **1992**. 84, 827-829.

[208] Meijer, E. J.; Detcheverry, C.; Baesjou, P. J.; van Veenendaal, E.; de Leeuw, D. M.; Klapwijk, T. M. Dopant density determination in disordered organic field-effect-transistors. *J. Appl. Phys.* **2003**. 93, 4831-4835.

[209] Kroon, J. M.; Wienk, M. M.; Verhees, W. J. H.; Hummelen, J. C. Accurate efficiency determination and stability studies of conjugated polymer/fullerene solar cells. *Thin solid Films*. **2002**. 403-404, 223-228.

[210] Jeranko, T.; Tributsch, H.; Sariciftci, N. S.; Hummelen, J. C. Pattern of efficiency and degradation of composite polymer solar cells. *Sol. Energ. Mater. Sol. Cells*. **2004**. 83, 247-262.

[211] Scurlock, R. D.; Wang, B.; Ogilby, P. R.; Sheats, J. R.; Clough, R. L. Singlet Oxygen as a Reactive Intermediate in the Photodegradation of an Electroluminescent Polymer. *J. Am. Chem. Soc.* **1995**. 117, 10194-10202.

[212] Bianchi, R. F.; Balogh, D. T.; Tinani, M.; Faria, R. M.; Irene, E. A. Ellipsometry Study of the Photo-Oxidation of Poly[(2-methoxy-5-hexyloxy)-p-phenylenevinylene]. *J. Polym. Sci. Part B: Polym. Phys.* **2004**. 42, 1033-1041.

[213] Neugebauer, H.; Brabec, C. J.; Hummelen, J. C.; Janssen, R. A. J.; Sariciftci, N. S. Stability Studies and Degradation Analysis of Plastic Solar Cell Materials by FTIR Spectroscopy. *Synth. Met.* **1999**. 102, 1002-1003.

[214] Paci, B.; Generosi, A.; Albertini, R.; Perfetti, P. *In situ* energy dispersive x-ray reflectometry measurements on organic solar cells upon working. *Appl. Phys. Lett.* **2005**. 87, 194110.

[215] Paci, B.; Generosi, A.; Albertini, V. R.; Perfetti, P.; de Bettignies, R.; Leroy, J.; Firon, M.; Sentein, C. Controlling photoinduced degradation in plastic photovoltaic cells: A time-resolved energy dispersive x-ray reflectometry study. *Appl. Phys. Lett.* **2006**. 89, 043507.

[216] Andreasen, J. W.; Gevorgyan, S. A.; Schleputz, C. M.; Krebs, F. C. Applicability of X-ray reflectometry to studies of polymer solar cell degradation. *Sol. Energy Mater. Sol. Cells*. **2008**. 92, 793-798.

[217] Krebs, F. C.; Norrman, K. Analysis of the Failure Mechanism for a Stable Organic Photovoltaic During 10 000h of Testing. *Prog. Photovolt: Res. Appl.* **2007**. 15, 697-712.

[218] Hauch, J. A.; Schilinsky, P.; Choulis, S. A.; Rajoelson, S. Brabec, C. J. The impact of water vapor transmission rate on the lifetime of flexible polymer solar cells. *Appl. Phys. Lett.* **2008**. 93, 103306.

[219] Schafferhans, J.; Baumann, A.; Wagenpfahl, A.; Deibel, C.; Dyakonov, V. Oxygen doping of P3HT:PCBM blends: Influence on trap states, charge carrier mobility and solar cell performance. *Org. Electron.* **2010**. 1693-1700.

[220] Snaith, H. J.; Greenham, N. C.; Friend, R. C. The Origin of Collected Charge and Open-circuit Voltage in Blended Polyfluorene Photovoltaic Devices. *Adv. Mater.* **2004**. 16, 1640-1645.

[221] Sun, B.; Snaith, H. J.; Dhoot, A. S.; Westenhoff, S.; Greenham, N. C. Vertically segregated hybrid blends for photovoltaic devices with improved efficiency. *J. Appl. Phys.* **2005**. 97, 014914.

[222] Jo, J.; Kim, S.; Na, S.; Yu, B.; Kim, D. Time-Dependent Morphology Evolution by Annealing Processes on Polymer:Fullerene Blend Solar Cells. *Adv. Funct. Mater*. **2009**. 19, 866-874.

[223] Tsoi, W. C.; Spencer, S. J.; Yang, L.; Ballantyne, A. M.; Nicholson, P. G.; Turnbull, A.; Shard, A. G.; Murphy, C. E.; Bradley, D. D. C.; Nelson, J.; Kim, J. Effect of Crystallization on the Electronic Energy Levels and Thin Film Morphology of P3HT:PCBM Blends. *Macromolecules*. **2011**. 44, 2944-2952.

[224] Hung, L. S.; Tang, C. W.; Mason, M. G. Enanced electron injection in organic electroluminescence devices using an Al/LiF electrode. *Appl. Phys. Lett.* **1997**. 70, 152-154.

[225] Mori, T.; Fujikawa, H.; Tokito, S.; Taga, Y. Electroni Structure of 8-hydroxyquinoline aluminum/LiF/Al interface for organic electroluminescent device studied by ultraviolet photoelectron spectroscopy. *Appl. Phys. Lett.* **1998**. 73, 2763-2765.

[226] Jabbour, G. E.; Kawabe, Y.; Shaheen, S. E.; Wang, J. F.; Morrell, M. M.; Kippelen, B.; Peyghambarian, N. Highly efficient and bright organic electroluminescent devices with an aluminum cathode. *Appl. Phys. Lett.* **1997**. 71, 1762-1764.

[227] Lian, J.; Yuan, Y.; Zhou, X. Organic Light-Emitting Devices with a LiF Hole Blocking Layer. *Chin. Phys. Lett.* **2007**. 24, 828-830.

[228] Gao, D.; Helander, M. G.; Wang, Z. B.; Puzzo, D. P.; Greinger, M. T.; Lu, Z. C60:LiF Blocking Layer for Environmentally Stable Bulk Heterojunction Solar Cells. *Adv. Mater.* **2010**. 22, 5404-5408.

[229] Zhou, E.; Deng, Z.; Lv, Z.; Chen, Z.; Xu, D.; Wang, Y. Enhancing properties of organic light-emitting diodes with LiF inside the hole transport layer. *Curr. Appl. Phys.* **2009**. 9, 1365-1368.

[230] Wang, K. L.; Lai, B.; Lu, M.; Zhou, X.; Liao, L. S.; Ding, L. S.; Ding, X. M.; Hou, X. Y.; Lee, S. T. Electronic structure and energy level alignment of $Alq_3/Al_2O_3/Al$ and Alq_3/Al interfaces studied by ultraviolet photoemission spectroscopy. *Thin Solid Films*. **2000**. 363, 178-181.

[231] Tang, H.; Shinar, J. Bright high efficiency blue organic light-emitting diodes with Al_2O_3/Al cathodes. *Appl. Phys. Lett.* **1997**. 71, 2560-2562.

[232] Niu, L.; Zhang, F. The effect of Al_2O_3 nanolayers on the efficiency of organic light-emitting devices. *Semicond. Sci. Technol.* **2006**. 21, 1639-1642.

[233] Spanggaard, H.; Krebs, F. C. A brief history of the development of organic and polymeric photovoltaics. *Sol. Energy Mater. Sol. Cells*. **2004**. 83, 125-146.

[234] Brabec, C. J.; Shaheen, S. E.; Winder, C.; Sariciftci, N. S.; Denk, P. Effect of LiF/metal electrodes on the performance of plastic solar cells. *Appl. Phys. Lett.* **2002**. 80, 1288-1290.

[235] Glatthaar, M.; Mingirulli, N.; Zimmermann, B.; Ziegler, T.; Kern, R.; Niggemann, M.; Hinsch, A.; Gombert, A. Impedance spectroscopy on organic bulk-heterojunction solar cells. *Phys. Stat. Sol. A.* **2005**. 202, R125-R127.

[236] Vanlaeke, P.; Swinnen, A.; Haeldermans, I.; Vanhoyland, G.; Aernouts, T.; Cheyns, D.; Deibel, C.; D'Haen, J.; Heremans, P.; Poortmans, J.; Manca, J. V. P3HT/PCBM bulk heterojunction solar cells: Relation between morphology and electro-optical characteristics. *Sol. Energy Mater. Sol. Cells*. **2006**. 90, 2150-2158.

[237] Huang, Y.; Liao, Y.; Li, S.; Wu, M.; Chen, C.; Su, W. Study of the effect of annealing process on the performance of P3HT/PCBM photovoltaic devices using scanning-probe microscopy. *Sol. Energy Mater. Sol. Cells*. **2009**. 93, 888-892.

[238] Brabec, C. J.; Gowrisanker, S.; Halls, J. J. M.; Laird, D.; Jia, S.; Williams, S. P. Polymer-Fullerene Bulk-Heterojunction Solar Cells. *Adv. Mater.* **2010**. 22, 3839-3856.

[239] Yang, X.; Loos, J.; Veenstra, S. C.; Verhees, W. J. H.; Wienk, M. M.; Kroon, J. M.; Michels, M. A. J.; Janssen, R. A. J. Nanoscale Morphology of High-Performance Polymer Solar Cells. *Nano Lett.* **2005**. 5, 579-583.

[240] Ma, W.; Yang, C.; gong, X.; Lee, K.; Heeger, A. J. Thermally Stable, Efficient Polymer Solar Cells with Nanoscale Control of the Interpenetrating Network Morphology. *Adv. Funct. Mater.* **2005**. 15, 1617-1622.

[241] Kim, H. J.; Lee, H. H.; Kim, J. Real Time Investigation of the Interface between a P3HT:PCBM Layer and an Al Electrode During Thermal Annealing. *Macromol. Rapid Commun.* **2009**. 30, 1269-1273.

[242] Kim, H. J.; Park, J. H.; Lee, H. H.; Lee, D. R.; Kim, J. The effect of Al electrodes on the nanostructure of poly(3-hexylthiophene): Fullerene solar cell blends during thermal annealing. *Organic Electronics*. **2009**. 10, 1505-1510.

[243] Kim, H.; So, W.; Moon, S. The importance of post-annealing process in the device performance of poly(3-hexylthiophene): Methanofullerene polymer solar cell. *Sol. Energy Mater. Sol. Cells*. **2007**. 91, 581-587.

[244] Abdou, M. S. S.; Orfino, F. P.; Son, Y.; Holdcroft, S. Interaction of Oxygen with Conjugated Polymers: Charge Transfer Complex Formation with Poly(3-alkylthiophenes). *J. Am. Chem. Soc*. **1997**. 119, 4518-4524.

[245] Hoshino, S.; Yoshida, M.; Uemura, S.; Kodzasa, T.; Takada, N.; Kamata, T.; Yase, K. Influence of moisture on device characteristics of polythiophene-based field-effect transistors. *J. Appl. Phys*. **2004**. 95, 5088-5093.

[246] Stallinga, P.; Gomes, H. L.; Rost, H.; Holmes, A. B.; Harrison, M. G.; Friend, R. H. Minority-carrier effects in poly-phenylenevinylene as studied by electrical characterization. *J. Appl. Phys*. **2001**. 89, 1713-1724.

[247] Melzer, C.; Krasnikov, V. V.; Hadziioannou, G. Organic donor/acceptor photovoltaics: The role of C_{60}/metal interfaces. *Appl. Phys. Lett*. **2003**. 82, 3101-3103.

[248] Jarosz, G. On doubts about Mott-Schottky plot of organic planar heterojunction in photovoltaic cell. *J. Non-Cryst. Solids*. **2008**. 354, 4338-4340.

[249] Bisquert, J.; Garcia-Belmonte, G.; Munar, A.; Sessolo, M.; Soriano, A.; Bolink, H. J.; Band unpinning and photovoltaic model for P3HT:PCBM organic bulk heterojunctions under illumination. *Chem. Phys. Lett*. **2008**. 465, 57-62.

[250] Neugebauer, H.; Brabec, C.; Hummelen, J. C.; Sariciftci, N. S. Stability and photodegradation mechanisms of conjugated polymer/fullerene plastic solar cells. *Sol. Energy Mater. Sol. Cells*. **2000**. 61, 35-42.

[251] Kovacik, P.; Sforazzini, G.; Cook, A. G.; Willis, S. M.; Grant, P. S.; Assender, H. E.; Watt, A. A. R. Vauum-Deposited Plana Heterojunction Polymer Solar Cells. *Appl. Mater. Interf*. **2011**. 3, 11-15.

[252] Gritsenko, K. P.; Krasovsky, A. M. Thin-Film Deposition of Polymers by Vacuum Degradation. *Chem. Rev*. **2003**. 103, 3607-3649.

[253] Inganas, O.; Salaneck, W. R. Thermochromic and Solvatochromic Effects in Poly(3-Hexylthiophene). *Synth. Met*. **1988**. 22, 395-406.

[254] Wei, H.; Scudiero, L.; Eilers, H. Infrared and photoelectron spectroscopy study of vapor phase deposited poly (3-hexylthiophene). *Appl. Surf. Sci*. **2009**. 255, 8593-8597.

[255] Kovacik, P.; Willis, S. M.; Matichak, J. D.; Assender, H. E.; Watt, A. A. R. Effect of side Groups on the Vacuum Thermal Evaporation of Polythiophenes for Organic Electronics. Submitted to ACS Macromolecules.

[256] Kouki, F.; Horowitz, G.; Ganier, F.; Bouchriha, H. Photogeneration process in pristine sexithiophene based photovoltaic cells. *Org. Electr*. **2010**. 11, 1439-1444.

[257] Sakai, J.; Taima, T.; Yamanari, T.; Saito, K. Annealing effect in the sexithiophene:C_{70} small molecule bulk heterojunction organic photovoltaic cells. *Sol. Energy Mater. Sol. Cells*. **2009**. 93, 1149-1153.

[258] Mihailetchi, V. D.; Blom, P. W. M.; Hummelen, J. C.; Rispens, M. T. Cathode dependence of the open-circuit voltage of polymer:fullerene bulk heterojunction solar cells. *J. Appl. Phys.* **2003**. 94, 6849-6854.

[259] Rusu, P. C.; Giovannetti, G.; Weijtens, C.; Coehoorn, R.; Brocks, G. Work Function Pinning at Metal-Organic Interfaces. *J. Phys. Chem. C*. **2009**. 113, 9974-9977.

[260] Tengstedt, C.; Osikowicz, W.; Salaneck, W. R.; Parker, I. D.; Hsu, C.; Fahlman, M. Fermi-level pinning at conjugated polymer interfaces. *Appl. Phys. Lett.* **2006**. 88, 053502.

[261] Xu, Z.; Chen, L.; Chen, M.; Li, G.; Yang, Y. Energy level alignment of poly(3-hexylthiophene):[6,6]-phenyl C_{61} butyric acid methyl ester bulk heterojunction. *Appl. Phys. Lett.* **2009**. 95, 013301.

[262] Sakai, J.; Taima, T.; Saito, K. Efficient oligothiophene:fullerene bulk heterojunction organic photovoltaic cells. *Org. Electron.* **2008**. 9, 582-590.

[263] Mo, Z.; Lee, K. –B.; Moon, Y. B.; Kobayashi, M.; Heeger, A. J.; Wudl, F. X-ray Scattering from Poythiophene: Crystallinity and Crystallographic Structure. M*acromol.* **1985**. 18, 1972-1977.

[264] Martens, H. C. F.; Huiberts, J. N.; Blom, P. W. M. Simultaneous measurement of electron and hole mobilities in polymer light-emitting diodes. *Appl. Phys. Lett.* **2000**. 77, 1852-1854.

[265] Tsang, S. W.; So, S. K.; Xu, J. B. Application of admittance spectroscopy to evaluate carrier mobility in organic transport materials. *J. Appl. Phys.* **2006**. 99, 013706.

[266] Martens, H. C. F.; Pasveer, W. F.; Brom, H. B.; Huiberts, J. N.; Blom, P. W. M. Crossover from space-charge-limited to recombination-limited transport in polymer light-emitting diodes. *Phys. Rev. B.* **2001**. 63, 125328.

[267] Pivrikis, A.; Sariciftci, N. S.; Juska, G.; Osterbacka, R. A Review of Charge Transport and Recombination in Polymer/Fullerene Organic Solar Cells. *Prog. Photovolt: Res. Appl.* **2007**. 15, 677-696.

[268] Zhao, N.; Osedach, T. P.; Chang, L.-Y.; Geyer, S. M.; Wanger, D.; Binda, M. T.; Arango, A. C.; Bawendi, M. G.; Bulovic, V. Colloidal PbS Quantum Dot Solar Cells with High Fill Factor. *ACS Nano.* **2010**. 4, 3743-3752.